Phase-and-Defect Diagrams for Polycrystalline Grain Boundary Segregation

By
Thomas P. Matson

B.S. Materials Science and Engineering
Carnegie Mellon University, 2019

SUBMITTED TO THE DEPARTMENT OF MATERIALS SCIENCE & ENGINEERING IN PARTIAL FULFILLMENT OF THE REQUIREMENTS FOR THE DEGREE OF

DOCTOR OF PHILOSOPHY IN MATERIALS SCIENCE & ENGINEERING AT THE MASSACHUSETTS INSTITUTE OF TECHNOLOGY

May 2024

Author **Thomas P. Matson**

Department of Materials Science and Engineering

Certified By **Christopher A. Schuh**

John G. Searle Professor, Northwestern University
Materials Science and Engineering

Dean, Northwestern University Robert R. McCormick
School of Engineering and Applied Sciences

Accepted By **Robert J. MacFarlane**

Associate Professor of Materials Science and Engineering

Chair, Departmental Committee on Graduate Studies

Abstract

Defect engineering provides access to a much larger range of material properties and is particularly necessary when designing any high-defect density material such as nanocrystalline (NC) alloys. Traditionally, bulk equilibrium phases have been considered in a decoupled manner from defects, such as solute and segregated atoms, dislocations, and grain boundaries. In recent years, a push has been made to treat defects as "defect states" in a manner analogous to bulk phases so they can be analyzed alongside existing bulk equilibrium phase diagrams – a treatment I refer to here as "phase-and-defect" diagrams. Segregated grain boundaries (GBs) are one such defect phase, and recent progress has indicated that spectral information, which describes the full distribution of available atomic environments, is required to rigorously understand segregated polycrystalline grain boundaries. However, models proposed prior to this work are primarily thermodynamic isotherms, which suffer from several limitations that prevent their use in the development of phase-and-defect diagrams. Existing spectral isotherms often use scalar assumptions to address solute-solute interactions, or are not atomistically informed, and have not been constructed from analytical free energy functions. For this reason, they cannot be used to construct fully spectral phase-and-defect diagrams. Furthermore, existing databases of spectral parameters contain only dilute limit information, limiting the accessibility of spectral segregation predictions at finite concentrations.

In this work, I take the following steps to address this need. First, I present a thermodynamic model that captures the spectral nature of both the segregation and solute interaction energies, and I describe an atomistic, physically motivated method to measure the full spectrum of GB solute interaction energies in a polycrystal. Then, I present the analytical framework for a spectral regular solution model of segregated polycrystals. I use this framework to derive a fully spectral free energy function and demonstrate how it can be used to develop a self-consistent phase-and-defect diagram which considers the bulk regular solution and the segregated polycrystalline defect state, and which shows significant improvement of the spectral model over traditional scalar representations. Finally, I develop an accelerated framework for predicting spectral solute-solute interactions, using a modified "bond-focused" local atomic environment (LAE) representation to construct descriptors for nearest neighbor pairs in the GB. I rigorously demonstrate its use for multiple binary alloys, and I then apply this accelerated framework to approximately 200 available embedded atom method (EAM) potentials to construct a large-scale database of spectral parameters for binary alloys beyond the dilute limit.

This work makes accessible, for the first time, fully spectral segregation parameters at finite concentrations. Additionally, it provides a framework for incorporating those estimates into existing CALPHAD methodology, allowing the production of phase-and-defect diagrams for segregated polycrystals. In doing so, I hope that this work will improve the community's ability to engineer stable nanocrystalline alloys and other defect states in the future.

Thesis Advisor: Christopher A. Schuh
Title: John G. Searle Professor, Northwestern University Materials Science and Engineering; Dean, Northwestern University Robert R. McCormick School of Engineering and Applied Sciences

Graphical Abstract

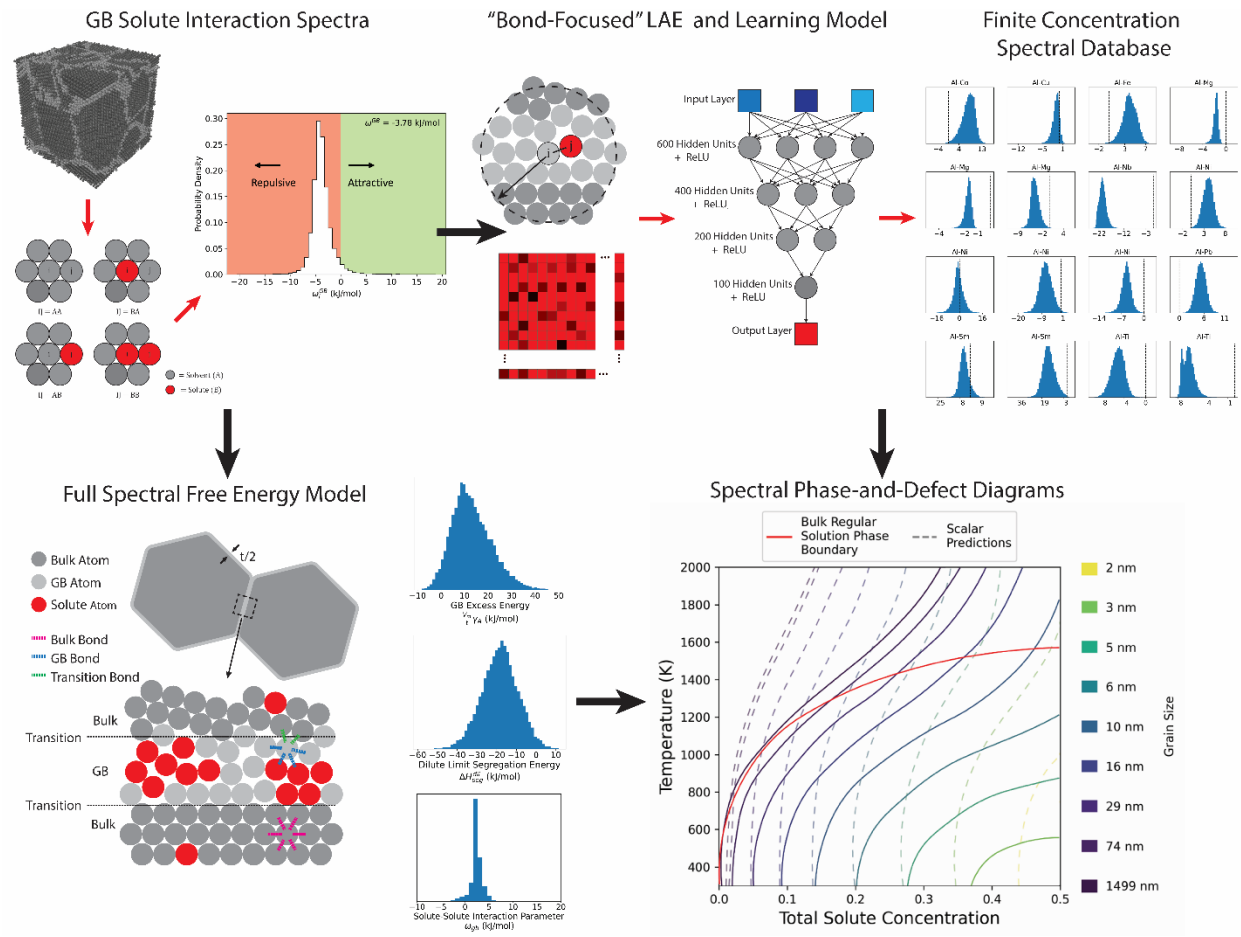

Acknowledgements

I would like to thank my thesis advisor, Professor Christopher A. Schuh, without whose support and mentorship this work would not have been possible.

I would also like to thank my thesis committee, Professor Craig. W. Carter and Professor Alfredo Alexander-Katz, who provided invaluable guidance throughout this work.

The members of the Schuh group made this an unforgettable experience. Many valuable discussions with Dr. Nutth Tuchinda and Dr. Malik Wagih in particular helped to bring this work to fruition.

Additionally, I would like to give a huge thank you to the many people throughout my life who helped me in starting this journey. Specifically, I would like to thank Professor Elizabeth Holm, my undergraduate research advisor at Carnegie Mellon University, who helped provide one the first of many great research experiences I've had, and Timothy Chelednik and Donald Allenbaugh, my high school teachers who helped set me on the path towards an academic career.

Finally, I would like to extend an incredible thank you to my family, whose support from afar made all this possible, and to all my friends near and far who have been with me throughout this journey.

This work was supported by the National Science Foundation Graduate Research Fellowship [grant number 2141064], the National Science Foundation [grant number DMR2002860], and the Department of Energy [grant number DE-SC0020180].

Table of Contents

1. Introduction…….. 8
2. Background……... 14
   2.1. Scalar Representation of GB Segregation……. 14
   2.2. The Spectral Representation of GB Segregation……... 16
3. The Solute-Solute Interaction Spectrum…….. 18
   3.1. Atomistic Simulations……... 18
   3.2. Measuring the Solute-Solute Interaction Spectrum……... 23
   3.3. The Fully Spectral Segregation Isotherm…….. 24
4. A Spectral Free Energy Representation for Segregated Polycrystals……... 29
   4.1. The Spectral Nanocrystalline Regular Solution Model……. 30
   4.2. Spectral Solution Model ……... 32
   4.3. Spectral Bond Distributions…….. 34
   4.4. Spectral Free Energy Functions……. 37
   4.5. Spectral Equilibrium Conditions and the Spectral Isotherm Model…….. 40
   4.6. Conversion of Site-Specific Spectra to Bond Energy Spectra…….. 41
5. Phase-and-Defect Diagram Construction……. 43
   5.1. The Nanocrystalline Free Energy at Fixed Grain Size…….. 44
   5.2. The Nanocrystalline Phase-and-Defect Diagram…….. 47
6. A Large-Scale Database of Spectral Parameters Beyond the Dilute Limit…….. 51
   6.1. Background on LAE Representations……... 51
   6.2. Atomistic Assessment of the Site Spectra……. 52
   6.3. Representation of the LAE…… 55
   6.4. A High-Fidelity Learning Model Based on the LAE……. 57
   6.5. Accelerated Predictions – Automatic Selection of Training Data……. 58
   6.6. Model Validation……... 60
   6.7. A Full Tri-Variate Database of Spectral Segregation Parameters…….. 63

Conclusion…….. 66

Future Outlook…… 69

Appendix A – The Scalar NCRS Model……. 71

Appendix B – Solute Interaction Predictions from a “Site-Focused” LAE…… 79
Appendix C – Accelerated Model Validation……. 79
Appendix D – Full Tri-Variate Database of Spectral Segregation Parameters……... 82
References…….. 150

List of Figures

Figure 1.1. Components of the free energy of segregation, ΔG^{seg}, separated into dilute and non-dilute terms…….. 12
Figure 3.1: Visualization of the grain boundary network of the pure Al polycrystal after relaxation and annealing…… 19
Figure 3.2. Dilute limit segregation energy distribution for Al-Mg…….. 20
Figure 3.3. Al-Mg polycrystal equilibrated via MC/MS and corresponding site occupation distribution, GB concentration, and GB excess, up to 10 percent total solute... 22
Figure 3.4. Example 2d atomic configurations used to calculate the per-bond solute interaction parameter……. 24
Figure 3.5. Site-wise solute interaction spectrum for Al-Mg…… 25
Figure 3.6. 2d Histogram and bivariate normal spectrum of the segregation and solute interaction energy for Al-Mg……. 25
Figure 3.7. Top-down view of Figure 3.6 with covariance…… 27
Figure 3.8. Predicted occupation distribution for Al-Mg using the bivariate spectrum…… 28
Figure 4.1. Visual overview of the spectral NCRS model…… 30
Figure 5.1. Hypothetical spectral system parameters to construct a phase-and-defect diagram……... 43
Figure 5.2. Free energy predictions for the hypothetical system at a fixed grain size…….... 44
Figure 5.3. Minimum energy convex hulls of the polycrystalline free energy function…… 47
Figure 5.4. Polycrystalline phase-and-defect diagram……... 49
Figure 6.1. Spectral quantities for GB segregation in Ag-Cu…… 54
Figure 6.2. Schematic depiction of SOAP LAE descriptors…….. 56
Figure 6.3. Feed-forward neural network architecture…….. 58
Figure 6.4. Schematic depiction of automatic training set selection……. 59

Figure 6.5. Model predictions for Ag-Cu……... 61
Figure 6.6. Occupation predictions for Ag-Cu with each model……... 62
Figure 6.7. Predicted solute interaction spectra for Al-based alloys…….. 64
Figure B1. Site-wise solute interaction parameter predicted using a site-focused LAE…… 79

List of Tables

Table 4.1. Bond types in each region of the spectral NCRS model…….. 32
Table 4.2. Concentration-dependent probabilities for each bond type in the spectral NCRS model……. 36
Table A1. Bond types in each region of the scalar NCRS model…….. 71
Table A2. Concentration-dependent probabilities for each bond type in the scalar NCRS model…….. 74
Table C1. Accelerated model validation on Al-Mg, Nb-Ni, Ni-Pt, and Pt-Au…….. 79
Table D1. Database of spectral GB parameters beyond the dilute limit…… 83

1. Introduction

Defect engineering has become a central focus in the design of materials in recent years, including the study of grain boundary complexions [1–3], dislocations [4–6], and point defects [7–9], encompassing a wide variety of applications. Grain boundary complexions in particular are known to be responsible for discontinuous transitions in many properties, such as mobility, diffusivity, cohesive strength, as well as various phenomena such as activated sintering, liquid-metal embrittlement, and abnormal grain growth [1–3,10–14]. The increased design space afforded by the structural and chemical variation of defects enables access to combinations of properties that are otherwise unattainable. This is particularly true in high defect density materials, such as nanocrystalline alloys. Due to the large volume fraction of grain boundaries present, the nanocrystalline state provides access to a broad range of improved mechanical [15–19] and functional [20–24] properties, such as hardness, magnetic and electronic behavior, corrosion resistance, etc.

Unfortunately, the nanocrystalline state is generally unstable against grain growth in pure metals, even at low temperatures [25–28], due to the large driving force for grain growth. Thermodynamic stabilization via grain boundary segregation offers an alloying approach to stability by reducing the excess energy of the grain boundary, and thus reducing the driving force for grain growth [25,29–43], as well as offering secondary kinetic pinning advantages against grain boundary motion [44–49]. Weissmüller first offered a stability criterion in which the enthalpic benefit of grain boundary segregation, ΔH^{seg}, competes with the enthalpic penalty of the grain boundary, $\frac{\gamma}{\Gamma}$ (where γ is the grain boundary energy of the solvent, and Γ is the solute excess at the boundary), and the entropic effect of bulk mixing [42], as shown in Equation (1.1).

$$\Delta H^{seg} > \frac{\gamma}{\Gamma} - k_B T ln(X) \tag{1.1}$$

If the enthalpic benefit of segregation is larger than the competing processes, then there exists a segregated state that is stable with respect to grain size.

This criterion was later expanded by other investigators to account for a broader range of compositions and to access a larger configurational space, using a variety of regular solution, lattice Monte Carlo, and phase field techniques [12,37,39,41,50,51]. One benefit of these expanded formulations is their ability to approximate total free energy functions for the nanocrystalline state, which allows for the construction of what I am terming here "phase-and-defect diagrams" for nanocrystalline alloys. These expand existing phase diagrams with additional information about the stable defect states. This approach was first applied to grain boundaries and nanocrystalline structures in the form of nanocrystalline alloy phase-and-defect diagrams [52] and can of course also be extended to other segregation states involving, e.g., dislocations, stacking faults, or special high symmetry boundaries [1,53–58]. To be clear, a "phase-and-defect" diagram as defined here refers to a diagram that contains information about a system containing both the phases defined by bulk equilibrium thermodynamics as well as potential defects that are not rigorously considered phases. Defects can experience phase-like behavior, as commonly observed for grain boundary complexions [1–3,10,11,13] however, the full system containing these defects will be referred to here as a "defect state" to ensure clarity.

While some experimental techniques exist to construct phase-and-defect diagrams (particularly in the case of complexion engineering, which has produced equilibrium complexion diagrams and time-temperature-transformation (TTT) diagrams for select systems), most of these diagrams are constructed via observation, using techniques such as high-angle annular dark-field (HAADF)-STEM, atom prove tomography (APT), or by tracking changes in the structure or composition, or in properties such as diffusivity and mobility [11,59–63,63]. Furthermore, while the free energy of certain structurally simple complexions can be computed from atomistics [57,63–65], this approach cannot be extended to segregated polycrystalline defect states, furthering the need for an analytical free energy representation for segregated polycrystals.

The above approaches to modeling grain boundary segregation can provide such a free energy representation; however, they have typically elected, just as in Equation (1.1), to simplify the segregation problem to one with a scalar segregation enthalpy or energy. This simplification is in opposition to studies providing atomic-level understanding of segregation as a spectral problem that involves a multitude of sites with significant anisotropy from one site, and one boundary, to

the next [66–71]. Recent studies that explicitly compare the use of scalar assumptions against the use of a full spectrum have revealed that spectral information is necessary to accurately understand and describe grain boundary segregation. Such demonstrations have so far been achieved in the form of thermodynamic segregation isotherms [67–69], and show the necessity of a fully spectral approach in many cases: beyond the dilute limit [69], at elevated temperatures either with [68] or without [67] excess vibrational entropy considered, or in nanocrystalline materials where the populations of grain boundaries and triple junctions can compete for solute [72].

These spectral models provide a framework to capture the complex, anisotropic energetics of grain boundaries, in a manner comparable to other models, such as Wynblatt and Chatain's layer model [73], or Cahn's lattice gas model [74]. However, while these alternatives to the spectral approach provide a similar framework, they are generally useful when modeling only one grain boundary character at a time and often require many energetic parameters that are difficult to pair with experimental data, particularly when considering many different grain boundaries in a polycrystalline grain boundary network. Spectral models simplify the complex geometry and energetics of the grain boundary network into random variables described by energetic distributions, thus generalizing the geometric constraints and providing a simpler method for future efforts to fit alloyed grain boundary energetics to experimental data.

Despite the observation that a full spectrum of segregation sites and energies must be accounted for in a rigorous understanding of defect chemistry, no spectral formulation currently exists that provides a total free energy function that could be used in the construction of a nanocrystalline phase-and-defect diagram. Wagih and Schuh took an initial step in this direction by applying the spectral model at 0 K in the dilute limit to develop a stability criterion [75] that is a spectral analog of Equation (1.1), but did not formulate a spectral free energy function. The focus of this thesis, therefore, is to derive an analytical spectral free energy model for grain boundary segregation and provide computational methods to efficiently measure the required inputs, allowing for the accessible production of phase-and-defect diagrams.

Assuming a finite volume fraction of the grain boundaries, f_{gb}, such a spectral free energy should have the following form:

$$\Delta G_{mix} = \left(1 - f_{gb}\right)\Delta G^{b}_{mix} + f_{gb} \int_{i} F_{gb,i} \Delta G^{gb}_{mix,i} dS \tag{1.2}$$

where the Gibbs free energy of mixing, ΔG_{mix}, is given as a rule of mixtures between a bulk free energy of mixing, ΔG^{b}_{mix}, and an integral over the spectral contributions due to the grain boundary, $\Delta G^{gb}_{mix,i}$, where i denotes available site types, $F_{gb,i}$ are the corresponding site probabilities, and S represents the spectral parameter space (which is generally multidimensional, and will be further developed in Chapter 4). In the limit where the spectrum collapses to a scalar, the resulting free energy function in Equation (1.2) should devolve to a conventional scalar solution model.

To begin construction of such a spectral free energy representation, consider the free energy of segregation [76], ΔG^{seg}, given as the sum of the segregation internal energy, ΔE^{seg}, a work term, $-P\Delta V$ (with pressure P, and volume change ΔV), and an excess entropy term $-T\Delta S^{seg}_{xs}$ [77].

$$\Delta G^{seg} = \Delta E^{seg} - P\Delta V - T\Delta S^{seg}_{xs}. \tag{1.3}$$

In metals, the work term is often negligible, so the enthalpy of segregation, ΔH^{seg} can be approximated as ΔE^{seg} [78]. The excess entropy of segregation can have many contributions, including configurational, ΔS^{seg}_{conf}, and vibrational, ΔS^{seg}_{vib}, which may or may not be negligible. These components are illustrated schematically in Figure 1.1, with components that were addressed with a spectral representation prior to this work shown in green, components that are not considered here shown in red, and the components still required to construct a minimally viable spectral free energy function at finite concentrations shown in yellow.

In the dilute limit, the spectral segregation energy, $\Delta E^{seg,dil}_{i}$, and ideal spectral configurational entropy, $\Delta S^{config}_{ideal}$, have already been addressed by the work of White and Stein [79], Kirchheim

[80,81], and Wagih and Schuh [67]. Recent work by Tuchinda and Schuh has addressed the spectrum of vibrational entropies, $\Delta S_{i,ideal}^{vib}$, involved in grain boundary segregation [68]; however, it is a minor contribution up to moderate temperatures, and can be neglected for simplicity and consistency with prior work in modeling of segregating systems. It may be added back in future work with little difficulty based on the work presented here. As such, all derivations throughout this work will assume that $\Delta G^{seg} \approx \Delta E^{seg}$.

The impact on the excess entropy at finite concentrations (given by a configurational component, ΔS^{config}, and a vibrational component, ΔS_i^{vib}) has not yet been studied; however, a viable non-dilute spectral free energy can be derived neglecting these components. This leaves the solute-solute interactions, ω_{i-j}^{GB}, as a necessary component of the spectral free energy of segregation that will be addressed in this work.

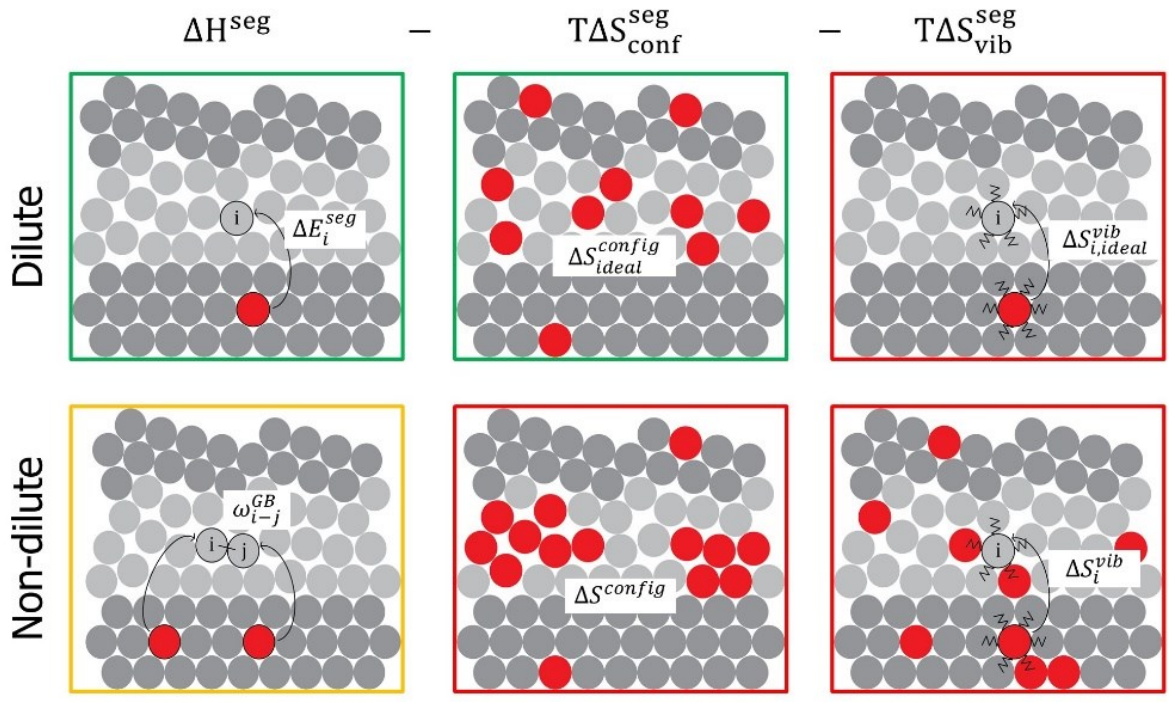

Figure 1.1. Components of the free energy of segregation, ΔG^{seg}, separated into dilute and non-dilute terms. Components addressed with a spectral representation prior to this work are shown in green, components neglected here or not yet addressed are shown in red, and components

required for a minimally viable spectral free energy function at finite concentrations are highlighted in yellow.

In the spectral model, one would expect a wide range of solute-solute interactions, due to the range of local atomic environments. Prior to this work, Wagih and Schuh showed that the addition of a single, fitted interaction energy (assumed relevant to all sites) could account for non-dilute interactions in an average sense, with good agreement to the overall segregated solute concentrations of full atomistic simulations of Al-Mg polycrystals [82]. However, because the parameter calculated by Wagih and Schuh was simply fitted to the results of atomistic simulations, it is not derived from atomistic-level physics directly. As a result, it is not generalizable without expensive computations on each individual alloy, and it does not provide the spectral energetics one would require for the fully spectral free energy given above. Furthermore, while Wagih and Schuh [83,84] and Tuchinda and Schuh [68] have developed large-scale databases for the dilute limit segregation spectra and vibrational entropy spectra of binary alloys, no such resource exists for spectral parameters beyond the dilute limit, making spectral predictions of nanocrystalline phase-and-defect diagrams generally inaccessible.

In this thesis, I will therefore take three necessary steps towards developing spectral phase-and-defect diagrams for segregated polycrystalline alloys, and towards making them accessible for the broader community. These steps will be addressed in the following chapters, and are as follows:

1) In Chapter 3, I will develop a physically motivated atomistic method to assess solute interactions during grain boundary segregation, in a way that acknowledges the wide diversity of local atomic environments in the GB. Additionally, I will propose a bivariate thermodynamic model which incorporates both the spectral segregation energies and spectral solute interactions.

2) In Chapter 4, I will derive a spectral regular solution model describing the segregated polycrystalline state and its corresponding free energy, in a manner that uses the energetics measured in (1) as inputs. In Chapter 5, I will use this free energy

representation to demonstrate a framework for creating phase-and-defect diagrams for the segregated polycrystalline state.

3) In Chapter 6, I will produce a high-throughput method for measuring the spectral energetics in (1), using a modified "bond-focused" descriptor for the local atomic environment, and I will use this method to construct a database of spectral parameters for binary alloys beyond the dilute limit from approximately 200 EAM potentials.

In the following chapters, each of these steps will be addressed primarily in the form of excerpts from existing manuscripts [69,85,86], both published and under review for publication, that I have written as the primary author alongside Professor Schuh, and which I have edited together here to give a concise presentation of this thesis.

2. Background

2.1. Scalar Representations of GB Segregation

The first isotherm for grain boundary segregation was proposed by McLean [87], in which the segregation energy is taken to be a single average parameter, $\Delta\bar{E}^{seg}$, given as the difference in energy of the full system when a solute, B, occupies a grain boundary site, E_{gb}^{B}, vis-à-vis a bulk site, E_{c}^{B}:

$$\Delta\bar{E}^{seg} = E_{gb}^{B} - E_{c}^{B}. \tag{2.1}$$

This approach assumes that the segregation energy, $\Delta\bar{E}^{seg}$, is independent of grain boundary character (or the site occupied by the solute), solute concentration, and temperature (T), resulting in McLean's isotherm [87]:

$$\frac{\bar{X}_{gb}}{1-\bar{X}_{gb}} = \frac{X_c}{1-X_c}\exp\left(-\frac{\Delta\bar{E}^{seg}}{kT}\right) \tag{2.2}$$

where $\bar{X}_{gb}$ is the average solute concentration in the grain boundary, X_c is the concentration in the bulk, and k is Boltzmann's constant.

To extend this treatment beyond the dilute limit, Fowler and Guggenheim accounted for concentration dependence of the segregation energy via the addition of a single interaction parameter based on a heat of mixing in the grain boundary, Ω_{gb} [88]:

$$\frac{\bar{X}_{gb}}{1-\bar{X}_{gb}} = \frac{X_c}{1-X_c}\exp\left(-\frac{\Delta\bar{E}^{seg}+2\Omega_{gb}\bar{X}_{gb}}{kT}\right) \tag{2.3}$$

which assumes that solute interactions in the bulk are negligible, due primarily to the assumption of relatively large, dilute grains, and thus relatively constant, dilute values of $X_c \approx X_{tot}$, where X_{tot} is the total system solute concentration. This assumption can be corrected with the addition of a term that includes the bulk heat of mixing, Ω_c [69,89]. This term appears consistently in more recent models that explicitly consider the nanocrystalline grain sizes [37,40,41,50,75], and when combined with the mixture rule, where X_{tot} is fixed and X_c and $\bar{X}_{gb}$ can vary dependently as [90]:

$$X_{tot} = \left(1-f_{gb}\right)X_c + f_{gb}\bar{X}_{gb}, \tag{2.4}$$

results in the complete scalar isotherm for nanocrystalline alloys:

$$X_{tot} = \left(1-f_{gb}\right)X_c + f_{gb}\left[1-\frac{1-X_c}{X_c}\exp\left(\frac{\Delta\bar{E}^{seg}-2\Omega_{gb}\bar{X}_{gb}+2\Omega_c X_c}{kT}\right)\right]^{-1} \tag{2.5}$$

where f_{gb} is the volume fraction of the grain boundary and is typically related to the grain size, d, and grain boundary thickness, t, by the equation:

$$f_{gb} = 1-\left(\frac{d-t}{d}\right)^3. \tag{2.6}$$

Assuming only nearest-neighbor contributions for solvent A and solute B, the heat of mixing can be represented as:

$$\Omega_s = \frac{1}{2} z_s \omega_s = \frac{1}{2} z_s \left(E_s^{AB} - \frac{E_s^{AA} + E_s^{BB}}{2} \right) \tag{2.7}$$

where s refers to either the GB or the bulk, z is the atomic coordination, and E_s^{AB}, E_s^{AA}, and E_s^{BB} are the bond energies of AB, AA, and BB bonds, respectively.

This model for scalar grain boundary segregation closely resembled that of Trelewicz and Schuh [41], who derived a nanocrystalline regular solution (NCRS) model and corresponding scalar free energy function for the segregated nanocrystalline state. This scalar NCRS formed the basis of many regular solution stability criteria and lattice Monte Carlo models that followed [39,43,52]. In Chapter 4 I will develop a spectral polycrystalline regular solution model, and I reproduce the corresponding scalar derivation in Appendix A.

2.2. The Spectral Representation of GB Segregation

Following the density of sites approach introduced by White and Stein [79], Wagih and Schuh developed a spectral model for grain boundary segregation, which assumes that each atomic grain boundary site has its own dilute limit segregation energy, $\Delta E_i^{seg,dil}$, defined as the difference between the energy of the system with a solute, B, populating that grain boundary site, $E_{gb,i}^B$, relative to the energy of the system with B on a bulk site surrounded by solvent, E_c^B:

$$\Delta E_i^{seg,dil} = E_{gb,i}^B - E_c^B. \tag{2.8}$$

Assuming a McLean-type contribution from each site type i with dilute limit segregation energy $\Delta E_i^{seg,dil}$, and accounting for the mixture rule of Equation (2.4), Wagih and Schuh's spectral isotherm is given as an integral over segregation energies [67]:

$$X_{tot} = \left(1 - f_{gb}\right)X_c + f_{gb}\int_{-\infty}^{\infty} F_{gb,i}\left[1 + \frac{1 - X_c}{X_c}\exp\left(\frac{\Delta E_i^{seg,dil}}{kT}\right)\right]^{-1} d\left(\Delta E_i^{seg,dil}\right) \quad (2.9)$$

where $F_{gb,i}$ is the density of sites of type i, and was shown by Wagih and Schuh to follow a roughly skew-normal distribution for general polycrystals:

$$F_{gb,i} = \frac{1}{\sqrt{2\pi}\sigma}\exp\left[-\frac{(\Delta E_i^{seg} - \mu)^2}{2\sigma^2}\right]\mathrm{erfc}\left[-\frac{\alpha\left(\Delta E_i^{seg} - \mu\right)}{\sqrt{2}\sigma}\right] \quad (2.10)$$

where α, μ, and σ are the fitted shape, location, and breadth of the dilute limit segregation energy distribution, respectively. The values of these parameters for several hundred binary alloys have been presented in Ref. [83].

Following from Equation (2.3), this spectral isotherm can be adapted to account for solute interactions in the grain boundary with a single Fowler-type interaction parameter:

$$X_{tot} = \left(1 - f_{gb}\right)X_c + f_{gb}\int_{-\infty}^{\infty} F_{gb,i}\left[1 - \frac{1 - X_c}{X_c}\exp\left(\frac{\Delta E_i^{seg} - 2\Omega_{gb}\bar{X}_{gb}}{kT}\right)\right]^{-1} d\left(\Delta E_i^{seg}\right). \quad (2.11)$$

Wagih and Schuh showed that for the Al-Mg system, the grains remain dilute even as the GB segregation raises the concentration locally at the boundary, leading to a significant effect via Ω_{gb}; thus, a single fitted value of Ω_{gb} provided a reasonably accurate description of full atomistic simulations beyond the dilute limit [82]. For other nanocrystalline alloys, the bulk concentration may vary more significantly, particularly at higher total concentrations, so for completeness it is appropriate to account for both GB and bulk contributions to the interactions, as in Equation (2.5).

3. The Solute-Solute Interaction Spectrum

In this chapter, I present a thermodynamic model which captures the spectral nature of solute-solute interactions, and develop an atomistically-informed method to measure the solute interaction spectra, providing a case study on Al-Mg [91]. This chapter has been modified from work previously published in Ref. [69].

Following from the derivations above, the isotherm of Equation (2.9) can be extended to account for non-dilute interactions as follows:

$$X_{tot} = \left(1 - f_{gb}\right)X_c + f_{gb} \int_{-\infty}^{\infty} F_{gb,i}\left[1 - \frac{1 - X_c}{X_c}\exp\left(\frac{\Delta E_i^{seg} - 2\bar{\Omega}_{gb}\bar{X}_{gb} + 2\Omega_c X_c}{kT}\right)\right]^{-1} d\left(\Delta E_i^{seg}\right) \quad (3.1)$$

where $\bar{\Omega}_{gb}$ and X_c are the average heat of mixing parameters of the grain boundary and bulk, respectively. The overbar on the former term is introduced to acknowledge that this $\bar{\Omega}_{gb}$ is no longer formally a single parameter in the spectral model, as there are many sites with unique behaviors. Assessing this value over many sites from atomistic information will be the major focus of my efforts below, with the goal of constructing a fully spectral representation of this model.

3.1. Atomistic Simulations

To study the solute-solute interactions, I produced an Al-Mg polycrystal with dimensions of (10 nm)^3, 60,367 total atoms, and 10 grains of random orientation with an average diameter of 6 nm. The polycrystal was randomly initialized via Voronoi tessellation using the toolkit Atomsk [92], followed by structural relaxation with conjugate gradient minimization. The polycrystal was then thermally annealed in an isothermal isobaric ensemble with a Nose-Hoover thermostat/barostat, at zero pressure and a temperature of 600 K for 0.5 ns. Finally, the polycrystal was cooled to 0 K over 0.25 ns, followed by a final conjugate gradient minimization. An image of the grain boundary network is shown in Figure 3.1, using polyhedral template matching to identify non-

FCC regions in the visualization tool OVITO [93]. All simulations here and in the remainder of this chapter were performed with the LAMMPS simulation package [94] and use the embedded atom method (EAM) potential by Mendelev for Al-Mg [91].

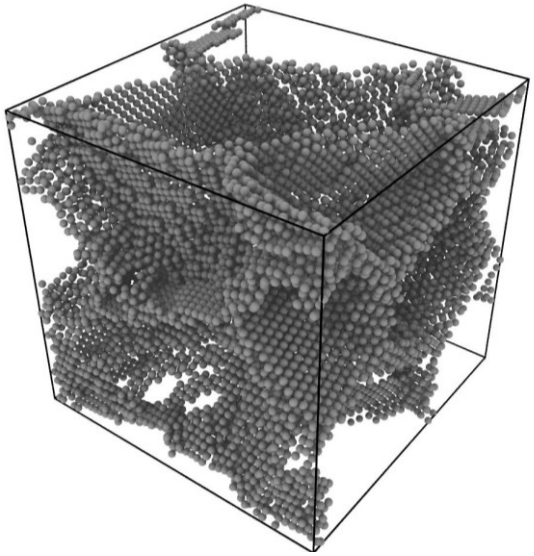

Figure 3.1: Visualization of the grain boundary network of the pure Al polycrystal after relaxation and annealing, with dimensions of (10 nm)^3, 10 randomly oriented grains of average diameter 6 nm, and 60,367 total atoms.

The Al-Mg system studied in this work was chosen for the strong agreement between its available interatomic potential [91] and density functional theory [95] when calculating segregation energies, and because it has been previously used for spectral grain boundary segregation analysis [82]. To compute the dilute limit segregation energy distribution of the Al polycrystal, I follow the procedure of Wagih and Schuh [67], and compute the dilute limit segregation energy, $\Delta E_i^{seg,dil}$, as given by Equation (2.8), for every site lacking FCC coordination. The resulting discrete distribution for Al-Mg is thus shown in Figure 3.2, with a skew-normal function fitted to Equation (2.10) overlaid. The distribution calculated here is skew-left, spans from approximately -60 to 40 kJ/mol, and has a mean of -6.82 kJ/mol, all of which are in excellent agreement with the distribution calculated previously by Wagih and Schuh for a (36 nm)^3 polycrystal [67].

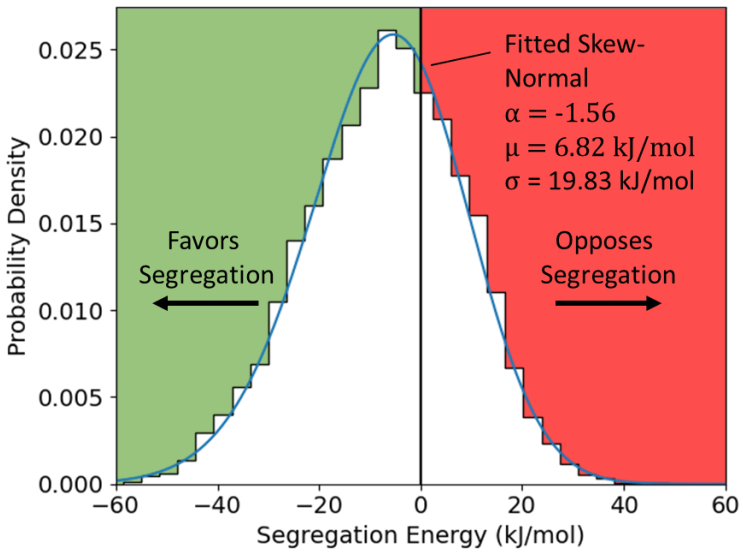

Figure 3.2. Dilute limit segregation energy distribution for Al-Mg, calculated from the (10 nm)^3 polycrystal, with a fitted skew-normal distribution overlaid.

To evaluate the predictions of the procedure proposed in this work, it is necessary to obtain the equilibrated segregation state of the Al-Mg polycrystal with finite solute content. This is done using a standard Monte Carlo (MC) procedure at a finite temperature to sample configurational space, in combination with molecular statics relaxations [12,30,96–102]. The Al polycrystal shown in Figure 3.1 was randomly populated with Mg solute, at concentrations of X_{tot} up to 10 percent. One step in the hybrid MC/MS procedure, referred to as one MC step, was conducted as a series of micro-MC steps at finite temperature, followed by a full-system relaxation at 0 K and constant pressure. Each micro-MC step consisted of a Monte-Carlo swap, attempted with a probability given by the metropolis criterion at 600 K, using the EAM potential for all energy evaluations. 6,000 micro-MC steps were attempted per MC step in the hybrid MC/MS procedure. 1,000 to 2,000 MC steps, scaling linearly with total solute concentration, were conducted to reach adequate convergence in both system energy and solute distribution.

The final state of the system after this process is taken as the true equilibrium segregation state, from which the final solute distribution is measured. An example equilibrated polycrystal of Al-Mg at X_{tot} = 0.05 is shown in Figure 3.3(a). The distribution of occupied sites is shown in red in

Figure 3.3(b), and resembles prior work on this system from Ref. [82]. These occupation distributions represent the true equilibrium segregation state, which I intend to understand in terms of Equation (3.1).

The resulting average equilibrium grain boundary solute concentration, $\bar{X}_{gb}$ is plotted as a function of X_{tot}, shown as red points in Figure 3.3(c). Here, it is important to note that $\bar{X}_{gb}$ defines the concentration in the grain boundary volume, determined by the geometric methods described above. For this reason, $\bar{X}_{gb}$ is not invariant to changes in the position or thickness of the grain boundary, and depends entirely on how the grain boundary is defined, as noted in many prior GB models such as those of Gibbs and Cahn [103,104]. For this reason, I have also plotted the grain boundary excess, Γ_{gb}, defined as the area normalized number of excess solute atoms due to the presence of the grain boundary region, in Figure 3.3(d). However, while I note that $\bar{X}_{gb}$ is subjectively defined, it does provide a more convenient means of interpreting these results in the context of the isotherms defined above and is a necessary parameter in the models developed in Chapter 4. For this reason, I will continue using $\bar{X}_{gb}$ throughout the following sections.

To extract the solute interaction parameter from the results of MC/MS, Wagih and Schuh [82] fitted Equation (3.1) to simulation results such as these, treating the solute interaction parameter(s) as unknown constants. Following this same approach here, as shown in Figure 3.3(c), results in a value of Ω_{gb} = -22.86 kJ/mol. For comparison, a McLean-style isotherm is plotted in green, using an effective segregation energy, $\Delta\bar{E}_{eff}^{seg}$ = -26.5 kJ/mol, fitted from Equation (2.2) in the dilute limit. Equation (2.9), which includes the effect of the segregation energy spectrum in the dilute limit, is also shown in blue.

This result, while physically motivated by the work of Fowler and Guggenheim [88], is ultimately a fitted parameter that is not derived from atomistic-level physics directly, and requires relatively expensive simulations to compute. Additionally, the use of a single interaction parameter does not explicitly separate the interaction contributions from the bulk and grain boundary, which may become relevant at high concentrations for some systems. My goal here is

to instead seek a direct atomistic assessment of those parameters, and success will be measured by my ability to reproduce the true segregation state in Figures 3.3(b) and 3.3(c).

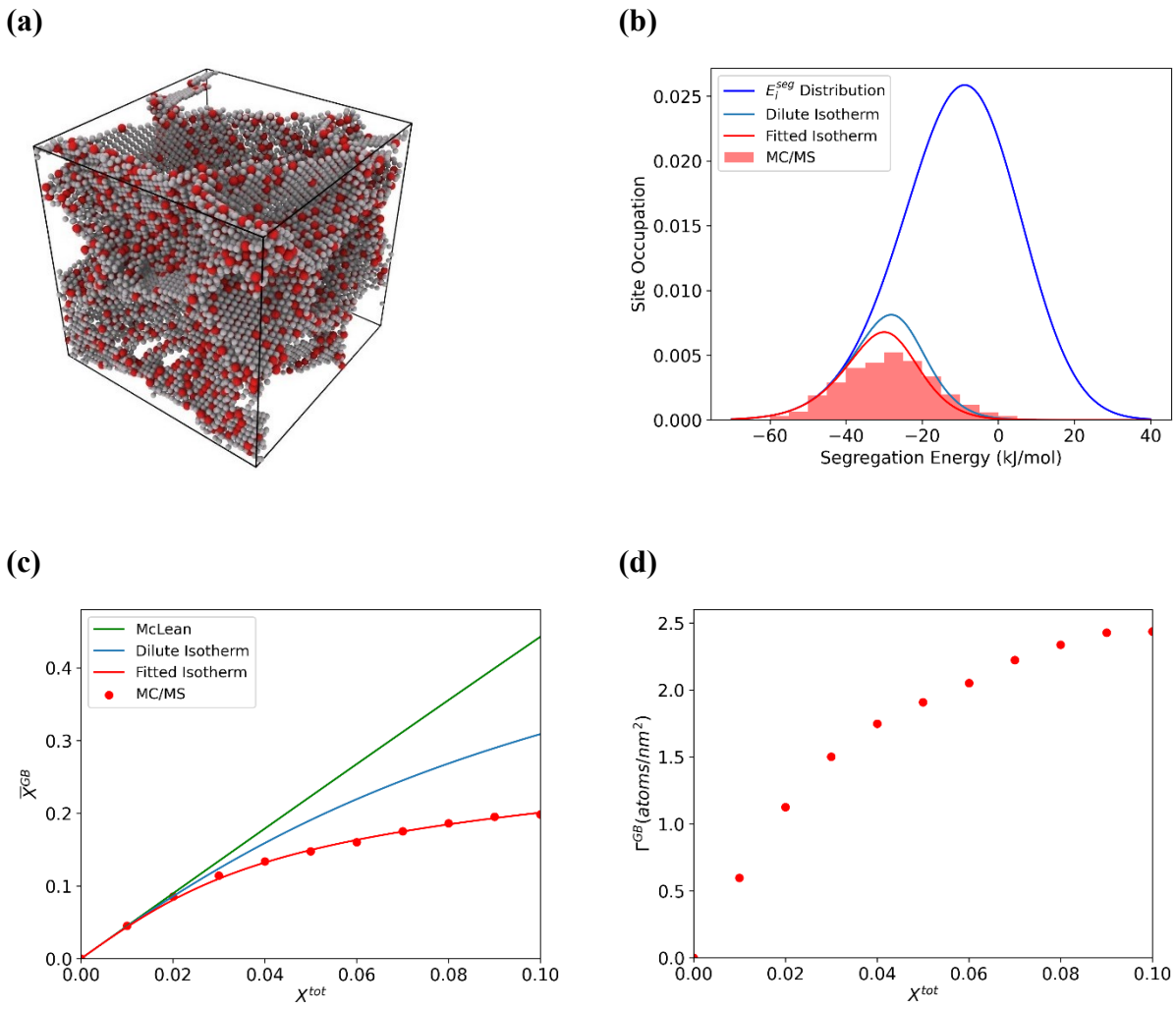

Figure 3.3. (a) Al-Mg polycrystal with 5 percent total solute, equilibrated with hybrid MC/MS at 600 K. (b) Segregation energy distribution with the equilibrium occupied distribution shown in red. Predicted occupied distribution is shown for the dilute case (Equation (2.8) (blue)). (c) For the (10nm)^3 Al-Mg polycrystal: McLean-style isotherm with effective segregation energy $\Delta\bar{E}_{eff}^{seg}$ = -26.5 (Equation (2.2) (green)), dilute limit spectral isotherm (Equation (2.8) (blue)), and polycrystal equilibrated via MC/MS, with a fitted linear interaction parameter Ω_{gb} = -22.86 kJ/mol (Equation (2.10) (red)). (d) Grain boundary excess solute, Γ_{gb}, converted from (c).

3.2. Measuring the Solute-Solute Interaction Spectrum

I am not aware of any measurement of the full distribution of solute-solute interactions in a polycrystalline grain boundary prior to this work, so I proceed to make one here. To begin, consider the site-wise version of the interaction parameter given in Equation (2.7), $\omega_{gb,i}$. To calculate this site-wise parameter, one must first calculate its pairwise equivalent for each nearest neighbor of a given site, as follows.

The coordination and nearest neighbors of each grain boundary site are calculated via Voronoi analysis in the OVITO visualization tool. The pair-wise parameter $\omega_{gb,i-j}$, where i is the site and j is one of its nearest neighbors, is then extracted for each nearest neighbor bond of each grain boundary site, including grain boundary to bulk bonds, via the following definition:

$$\omega_{gb,i-j} = \left(E^{gb}_{ij,A-B} - \frac{E^{gb}_{ij,A-A} + E^{gb}_{ij,B-B}}{2} \right) = E^{gb}_{ij,BA} - E^{gb}_{ij,BB} + E^{gb}_{ij,AB} - E^{gb}_{ij,AA} \tag{3.2}$$

where $E^{GB}_{ij,I-J}$ refers to a bond energy, $E^{GB}_{ij,IJ}$ refers to the local atomic energy of site i, I and J denote whether solute (B) or solvent (A) is present at sites i and j, and the local atomic energy of the site is related to the bond energies via:

$$E^{gb}_{ij,IJ} = \frac{1}{2}\left[(z-1)E^{gb}_{ij,I-J} + E^{gb}_{ij,I-J}\right]. \tag{3.3}$$

The necessary atomic configurations required to calculate $\omega_{gb,i-j}$ are shown schematically in Figure 3.4. Once obtained via molecular statics measurements, $\omega_{gb,i-j}$, can then be averaged over each nearest neighbor for a given grain boundary site i to obtain the average per-site parameter $\mathrm{w}_{gb,i}$. This value can in turn be combined with the atomic coordination of the site to obtain the per-site heat of mixing parameter, $\Omega_{gb,i}$, and thus the full heat of mixing distribution of the grain boundary. It should be noted that the heat of mixing calculated here assumes the

structure of the pure solvent A – in either the grain boundary or bulk, respectively – as the reference state for both components A and B.

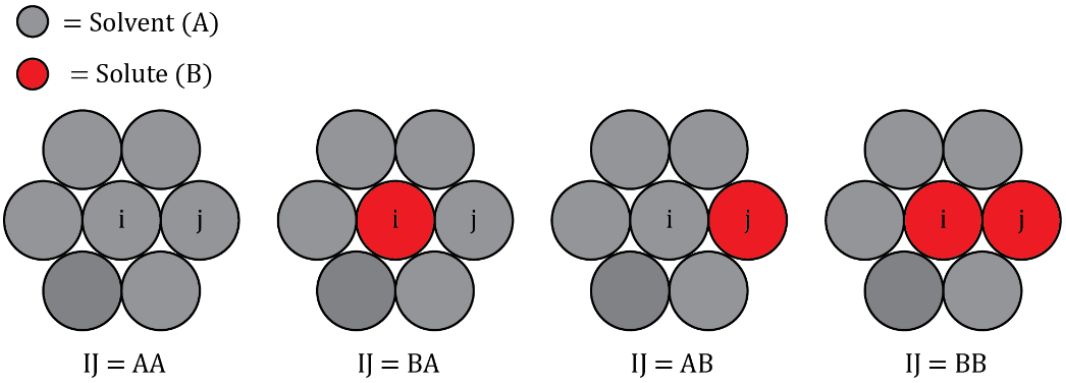

Figure 3.4. Example 2d atomic configurations used to calculate the per-bond parameter $\omega_{gb,i-j}$ *for bond* ij*, by measuring the per-atom energy of atom* i *in the fully relaxed polycrystal,* $E_{gb,ij}^{IJ}$*, where atoms I and J can be either solvent A or solute B.*

Following this procedure for a bulk site in the interior of a fully relaxed 16x16x16 supercell of FCC Al, values for the grain interior of $z_c = 12$, ω_c = -4.72 kJ/mol, and Ω_c = -28.32 kJ/mol were obtained. Then, following this procedure for the grain boundaries achieves the distribution shown in Figure 3.5. This per-site interaction parameter exhibits a roughly skew-normal distribution, similar to the segregation energy spectrum itself, with an average value of $\overline{\omega}_{gb}$ = -3.78 kJ/mol. The average grain boundary coordination was measured as z_{gb} = 14.3.

3.3. The Fully Spectral Segregation Isotherm

The results in Figure 3.5 represent what I believe to be the first atomistic measurement of the full spectrum of solute-solute interaction effects during grain boundary segregation in a polycrystal. As such, they permit a very detailed level of analysis of the grain boundary segregation state beyond the dilute limit.

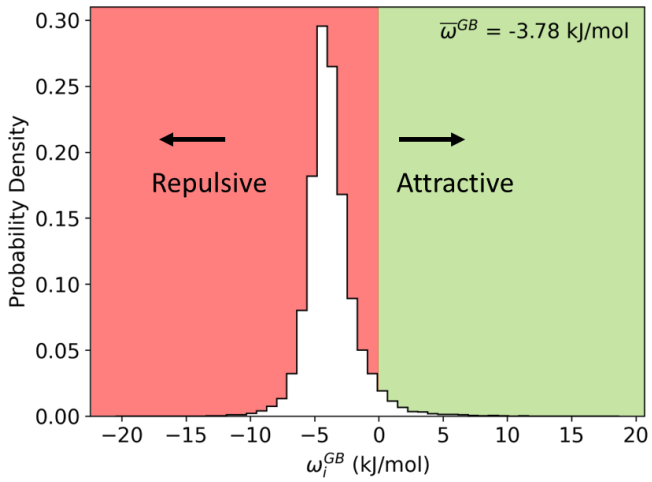

Figure 3.5. For every GB site in the (10nm)^3 Al-Mg polycrystal, the average per-site parameter, $\omega_{gb,i}$, measured via the atomistic method given in Equations (3.2) and (3.3).

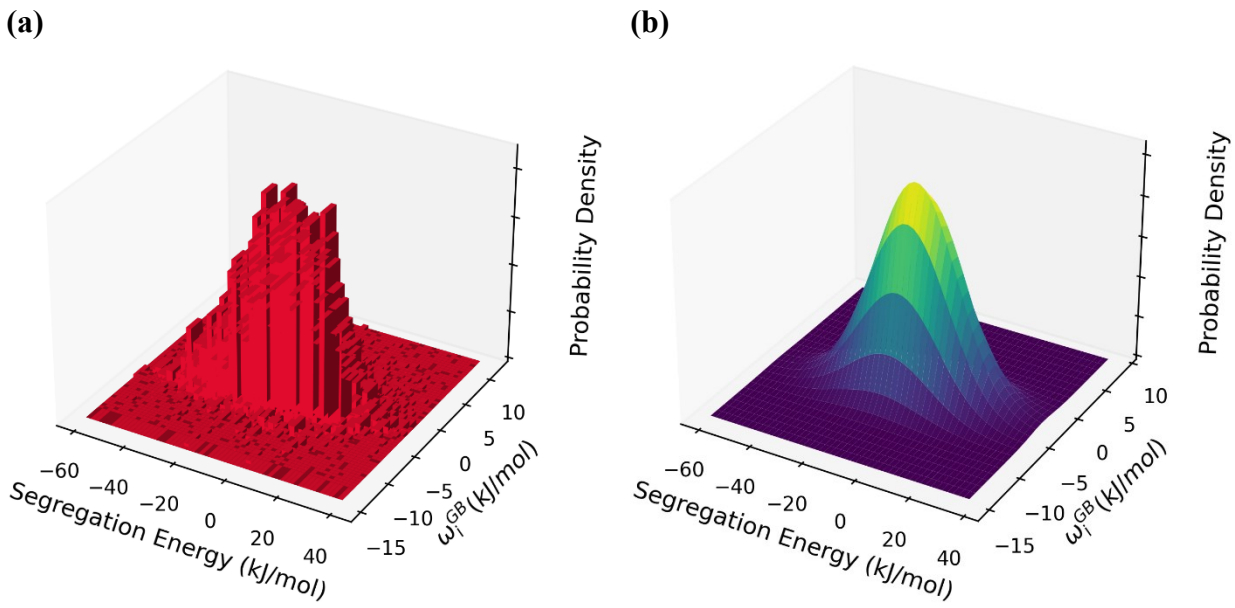

Figure 3.6. (a) 2D histogram of the dilute limit segregation energy and per-site interaction parameter $\omega_{gb,i}$, exhibiting a bivariate skew-normal distribution. (b) Bivariate normal distribution fitted to the data depicted in Figure 3.6(a).

For example, in the spirit of exhaustive rigor, consider an isotherm analysis based on both the spectrum of segregation energies and the spectrum of solute interactions across the grain

boundary, combined in a self-consistent probabilistic model. This is explored in Figure 3.6(a), where the per-site dilute limit segregation energy and interaction parameter are cross-compared, and together apparently constitute a single 2D distribution function with a single central peak.

Such a distribution could be modeled by, e.g., a bivariate normal (or skew-normal) distribution [105]. Equation (3.1) might therefore be modified to include an integral over the joint probability density of the segregation and interaction energies. The skewness is small in the present case, so a bivariate normal distribution is appropriate, and has the following form:

$$F_{gb,i} = \frac{1}{\sqrt{(2\pi)^2|\Sigma|}} \exp\left[-\frac{1}{2}(x-\mu)^T \Sigma^{-1}(x-\mu)\right] \tag{3.4}$$

where $F_{gb,i}$ now varies with the vector quantities x and μ, where x contains the segregation and interaction energies and μ their means, and Σ is their covariance matrix. For Al-Mg, I find the bivariate normal parameters to be $\mu = [\Delta\bar{E}^{seg}, \quad \bar{\omega}_{gb}]$, where $\Delta\bar{E}^{seg}$ = -7.10 kJ/mol is the mean segregation energy and $\bar{\omega}_{gb}$ = -3.78 kJ/mol is the mean interaction energy, with a covariance matrix given by:

$\Sigma = \begin{bmatrix} 244.04 & 4.76 \\ 4.76 & 3.86 \end{bmatrix}$ kJ/mol.

Combining Figures 3.6(a) and (b) into a top-down view provides a clear picture of a covariant relationship between the dilute limit segregation energy and solute interaction energy, as shown by the dashed black line in Figure 3.7. This representation makes clear that sites with more negative segregation energies (that more heavily favor segregation) also tend to experience more repulsive solute interactions. The implications of this relationship can be explored by comparing thermodynamic predictions based on these bivariate spectral energetics to prior scalar models.

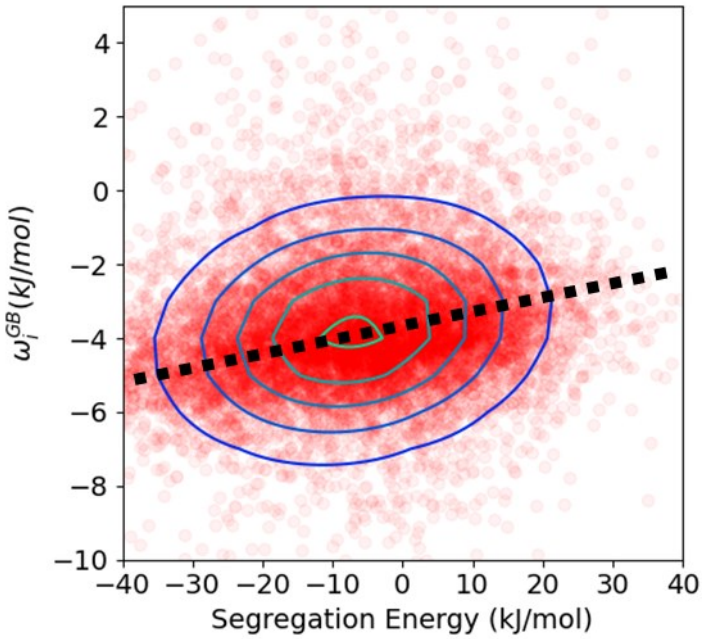

Figure 3.7. Top-down view of Figure 3.6, with the covariance shown as a dashed black line.

Performing an integration over both the segregation energy and interaction energy produces the following isotherm:

$$X_{tot} = (1 - f_{gb})X_c + f_{gb} \int_{-\infty}^{\infty}\int_{-\infty}^{\infty} F_{gb,i}\left[1 - \frac{1 - X_c}{X_c}\exp\left(\frac{\Delta E_i^{seg} - \bar{\Omega}_{gb,i}\bar{X}_{gb} + 2\Omega_c X_c}{kT}\right)\right]^{-1} d\left(\bar{\Omega}_{gb,i}\right)d\left(\Delta E_i^{seg}\right). \quad (3.5)$$

Equation (3.5) can be readily solved numerically, and the resulting occupation distribution and isotherm are shown in magenta in Figure 3.8 for Al-Mg. When this fully atomistic solution is compared with the single-parameter Fowler-like fit in the details of the atomic site distributions (Figure 3.8(a)), it is clear that the full bivariate distribution more accurately captures the distribution at equilibrium. This is largely due to its ability to correctly incorporate the covariant behavior exhibited in Figure 3.7; because sites with more negative segregation energies tend to experience more repulsive interactions, the distribution shifts to the right relative to the single parameter fit, which overpredicts occupation in strongly segregating sites.

The bivariate isotherm also credibly reproduces the trend of the isotherm in Figure 3.8(b) with no fitting parameters. Interestingly, though, the conformity in Figure 3.8(b) is not better than can be achieved with direct fitting. Thus, even though the full bivariate distribution approach may be more rigorous, it may not dramatically improve predictive power over a simple linear interaction term, if one is concerned only with the average grain boundary solute concentration and does not care about the details of site occupation. Since the full bivariate spectrum approach adds significantly more computational complexity, an atomistically-informed single parameter model may be a preferred solution. Introducing the directly atomistically measured average values of $\overline{\Omega}_{gb}$ and Ω_c into Equation (3.1) achieves the results shown by black lines in Figure 3.8; the result is a reasonable compromise between accuracy and speed.

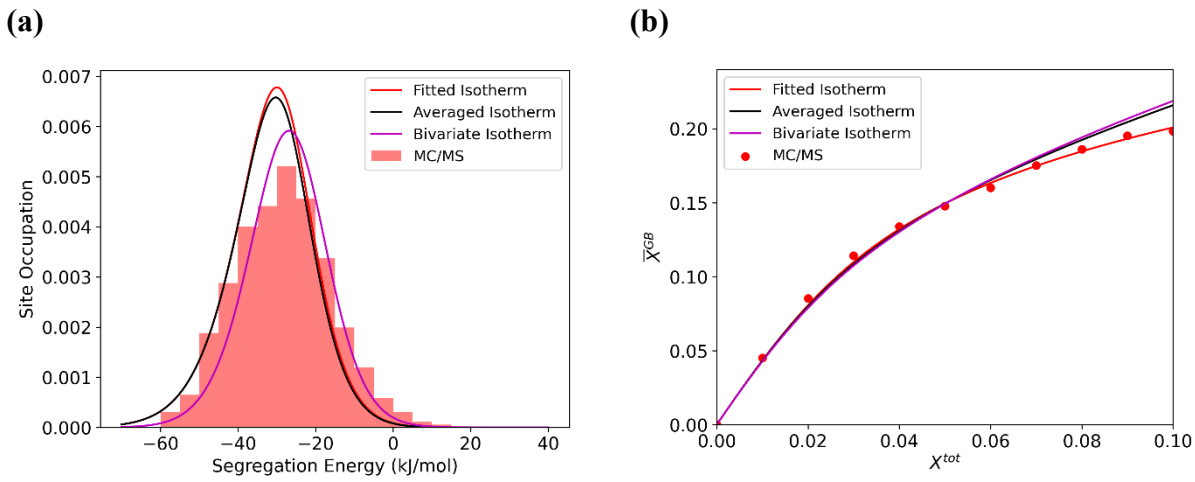

Figure 3.8. For the (10 nm)^3 Al-Mg polycrystal: (a) the occupied site distribution at 600 K and 5 percent total solute, equilibrated via MC/MS (red), with predicted occupation distributions, and (b) average grain boundary occupation as a function of total solute concentration, equilibrated via MC/MS at 600K, with predicted averages via isotherms. Both use the fitted isotherm with an interaction parameter Ω_{gb}= -22.86 kJ/mol (Equation (2.11) (red)), the measured isotherm with the average bulk interaction parameter Ω^c = -28.32 kJ/mol and average grain boundary interaction parameter $\overline{\Omega}_{gb}$ = -27.10 kJ/mol (Equation (3.1) (black)), and the full spectral isotherm with the fitted bivariate normal distribution (Equation (3.5) (magenta)).

The above analysis shows that the general approach of using a Fowler-like composition-dependent correction to the spectral model, as proposed by Wagih and Schuh, is indeed an excellent compromise between simplicity and accuracy to capture grain segregation beyond the dilute limit in the case when only knowledge of an average grain boundary solute concentration is required. However, the manner of its use proposed by those authors is computationally cumbersome and may not provide rigorously correct energetic predictions for the sake of developing a spectral free energy representation of segregated polycrystals. While the methodology proposed in this chapter also suffers from a high computational cost, it is readily adjustable to a high throughput method, which is discussed in Chapter 6. The fully spectral representation proposed here is therefore tractable to measure atomistically and enables a more rigorous approach for constructing a spectral free energy function, which I will address in the following chapter.

4. A Spectral Free Energy Representation for Segregated Polycrystals

The isotherm developed in Equation (3.5) was constructed assuming behavior similar to existing scalar Fowler-Guggenheim isotherms used for both surfaces and grain boundaries [88], which assume a regular solution model of both the bulk and grain boundary, and as such are physically based on bond counting. The above equations are all written with a spectrum of sites, and site energies; this in turn implies the existence of a spectrum of bond energies. Thus, to map the above progress on grain boundary segregation spectra into a regular-solution-based free energy in the form of Equation (1.2), we need to map site-wise spectra to bond-wise spectra. Trelewicz and Schuh [41] developed a similar mapping of scalar segregation energetics in their nanocrystalline regular solution model. Therefore, the focus of this chapter will be to construct a similar mapping in a fully spectral representation, by first using bond counting to develop a spectral regular solution model, and subsequently fitting that model to the site-wise spectral representation used in Equation (3.5) above. The work presented in this chapter was previously published in Ref. [85].

4.1. The Spectral Nanocrystalline Regular Solution Model

In this section I derive an analytical framework for the spectral nanocrystalline regular solution model, considering solvent atoms A and solute atoms B, with standard reference states of phases α and β, respectively. To begin, consider the nanocrystalline configuration shown schematically in Figure 4.1, in which a finite volume fraction of grain boundary, defined by spectral bond energetics, is attached to a standard bulk regular solution of B in A, in the α phase.

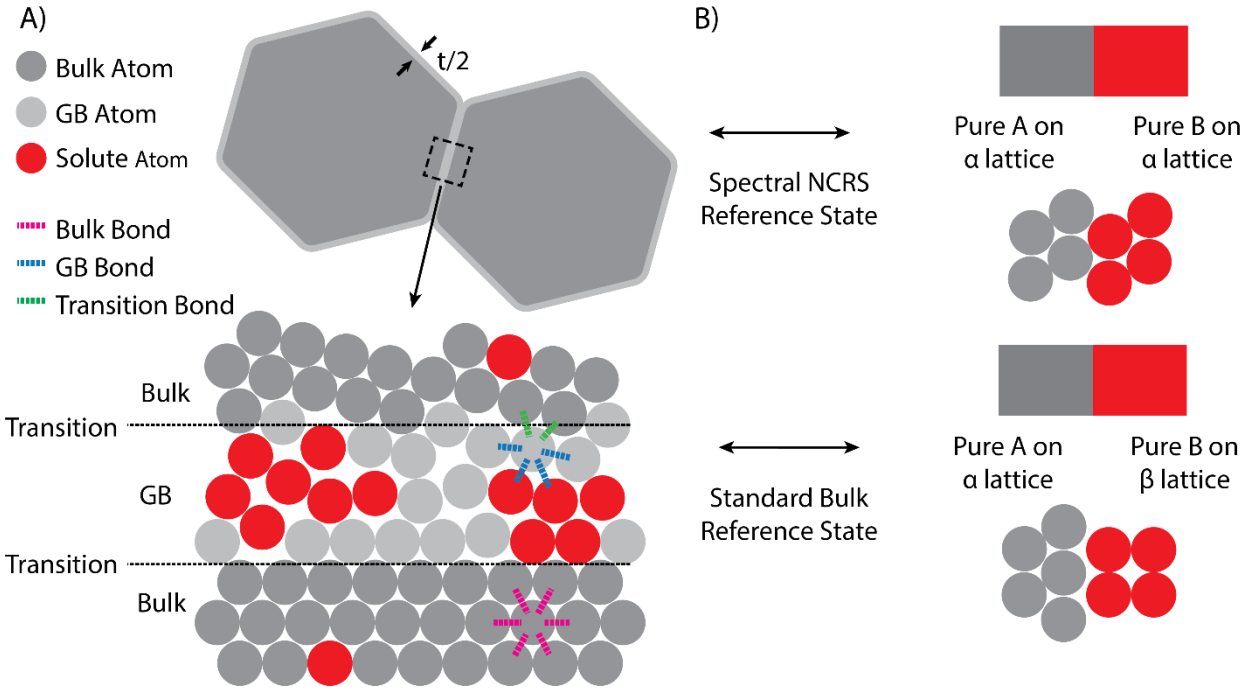

Figure 4.1. Visual overview of the spectral NCRS model. (a) Schematic of the spectral NCRS model, with bulk, GB, and transitional bonds labeled in pink, blue, and green, respectively. (b) Schematic reference states – the single lattice spectral NCRS reference state (top), and a more general standard reference state (bottom).

The enthalpy of mixing is formulated as a solution model assuming spectral bond energies in the grain boundary, and hence spectral concentrations at the grain boundary. The spatial distribution of bond energies in the grain boundary is assumed random, allowing for random mixing assumptions at the nearest-neighbor shell. While this assumption may be questionable for highly

symmetric grain boundaries or strongly interacting species, prior work by Wagih and Schuh [67], as well at that presented in Chapter 3 [69], on a general, primarily high angle grain boundary network in polycrystalline Al-Mg demonstrated reasonable conformity to a random mixing assumption. The enthalpy of mixing is then combined with an ideal configurational entropy of mixing for the bulk, and the spectral configurational entropy of mixing formulated by White and Stein [79] for the grain boundary to produce the total free energy of mixing for the nanocrystalline state.

In the absence of grain boundaries, the system should be a bulk regular solution defined by a heat of mixing parameter, E_{BinA} and total concentration X_{tot}, given by the molar free energy function G_{BinA}^{mix}:

$$G_{BinA}^{mix} = E_{BinA}X_{tot}(1 - X_{tot}) + RT(X_{tot}\ln(X_{tot}) + (1 - X_{tot})\ln(1 - X_{tot})) \tag{4.1}$$

where T is the temperature in Kelvin and R is the ideal gas constant. Here, I note that the conventional bulk heat of mixing, E_{BinA}, is defined as the energy of dissolving one mol of B from the β phase into the α phase. However, the regular solution formulation presented here considers only B in the α phase, as shown in the top of Figure 4.1(b). Therefore, in the general case, a shift in reference state must be accounted for, given as $E_{\beta to\alpha}^{ref}$:

$$E_{\beta to\alpha}^{ref} = \frac{X_{tot}}{2}\left(z^{\alpha}E_{BB}^{\alpha} - z^{\beta}E_{BB}^{\beta}\right) \tag{4.2}$$

where z^i is the coordination number, and E_{BB}^{i} is the bond energy of a BB bond in phase i. This standard reference state is depicted in the bottom of Figure 4.1(b).

For simplicity, the derivation in this section will proceed with the α phase as reference state, and this additional correction will be assumed negligible for the hypothetical systems shown in the following parametric study and construction of phase and defect diagrams. However, it should be stressed that it must be included in the general case. Additionally, no competing ordered phases

will be considered in this work, though I note that they may be added using existing models and similar energetic considerations [106].

4.2. Spectral Solution Model

Table 4.1. Bond types in each region of the spectral NCRS model – bulk (grain interior), grain boundary, and transition – along with the corresponding notation for the number of bonds and bond energies of each type.

Bond Type	**Number of Bonds**	**Bond Energies**
Bulk	$\boldsymbol{N_b^{AA}}$	$\boldsymbol{E_b^{AA}}$
	$\boldsymbol{N_b^{AB}}$	$\boldsymbol{E_b^{AB}}$
	$\boldsymbol{N_b^{BB}}$	$\boldsymbol{E_b^{BB}}$
GB-GB (Site Type i)	$\boldsymbol{N_{gb,i}^{AA}}$	$\boldsymbol{E_{gb,i}^{AA}}$
	$\boldsymbol{N_{gb,i}^{AB}}$	$\boldsymbol{E_{gb,i}^{AB}}$
	$\boldsymbol{N_{gb,i}^{BB}}$	$\boldsymbol{E_{gb,i}^{BB}}$
Transition (Site Type i)	$\boldsymbol{N_{t,i}^{AA}}$	$\boldsymbol{E_{gb,i}^{AA}}$
	$\boldsymbol{N_{t,i}^{AB}}$	$\boldsymbol{E_{gb,i}^{AB}}$
	$\boldsymbol{N_{t,i}^{BB}}$	$\boldsymbol{E_{gb,i}^{BB}}$

The binary nanocrystalline mixture of solvent A and solute B on the α phase lattice is described using pairwise bond energies in a manner similar to a regular solution model. As shown schematically in Figure 4.1(a), the system is divided into separate bulk and grain boundary regions, with the grain boundary region defined using spectral bond energies, where a specific atomic site, i, is described with its own unique set of bond energies.

Here it is necessary to define a third, transitional bond type that represents the bonds that bridge the grain boundary and bulk regions, so that the number of bonds can be calculated correctly in the following sections. In this derivation, I treat the energetics of transitional bonds the same as GB-GB bonds, however they are counted with the appropriate combination of grain boundary

and bulk concentrations, as will be shown in the following section [41]. The range of available grain boundary site types considered here follow a tri-variate distribution, $F_{gb,i}$, where i denotes a site type, and the corresponding GB bond energies connected to that site, $E_{gb,i}^{AA}$, $E_{gb,i}^{AB}$, and $E_{gb,i}^{BB}$ are all spectral, and constitute a parameter space denoted here as S. Presently, I assume that the number of each site type, and thus the number of each bond type, can take on any value; in later sections, I will explore the actual form of this distribution for general polycrystalline grain boundaries.

Given the numbers and energies of each bond type as listed in Table 4.1, the total solution energy, U_{soln}, can be written as a sum over all the bond types, s, in each region, which for the spectral approach here includes a summation over every site type i in the grain boundary:

$$U_{soln} = \sum_{s} \left[N_b^s E_b^s + \sum_i N_{gb,i}^s E_{gb,i}^s + N_{t,i}^s E_{t,i}^s \right] \tag{4.3}$$

where N and E represent the bond numbers and energies, and b, gb, and t denote the bulk, grain boundary, and transitional bonds, respectively. In addition to the solution energy, this model must also incorporate the interfacial energy resulting from the grain boundary and transitional bonds by defining the mixing energy, ΔU_{mix}, with respect to the unmixed, interface-free α phase of the same composition, as depicted in the top of Figure 4.1(b):

$$\Delta U_{mix} = U_{soln} - U_{ref} \tag{4.4}$$

where the reference state, U_{ref}, is given as:

$$U_{ref} = \frac{zN^A}{2} E_b^{AA} + \frac{zN^B}{2} E_b^{BB}. \tag{4.5}$$

Here, N^A and N^B are the total number of A and B atoms, respectively, and z is the coordination number of the α phase. The coordination number and total number of A and B atoms are related to the number of bonds given in Table 4.1 via:

$$zN^A = 2N_b^{AA} + N_b^{AB} + \sum_i 2N_{gb,i}^{AA} + 2N_{t,i}^{AA} + N_{gb,i}^{AB} + N_{t,i}^{AB} \tag{4.6}$$

$$zN^B = 2N_b^{BB} + N_b^{AB} + \sum_i 2N_{gb,i}^{BB} + 2N_{t,i}^{BB} + N_{gb,i}^{AB} + N_{t,i}^{AB}\,. \tag{4.7}$$

Combining these relationships with Equations (4.3) – (4.5), the change in internal energy upon mixing becomes:

$$\begin{aligned}\Delta U_{mix} = \quad & N_b^{AB}\left(E_b^{AB} - \frac{E_b^{AA} + E_b^{BB}}{2}\right) \\ & + \sum_i \left[\begin{matrix}\left(N_{t,i}^{AA} + N_{gb,i}^{AA}\right)\left(E_{gb,i}^{AA} - E_b^{AA}\right) + \left(N_{t,i}^{BB} + N_{gb,i}^{BB}\right)\left(E_{gb,i}^{BB} - E_b^{BB}\right) \\ + \left(N_{t,i}^{AB} + N_{gb,i}^{AB}\right)\left(E_{gb,i}^{AB} - \frac{E_b^{AA} + E_b^{BB}}{2}\right)\end{matrix}\right]\end{aligned} \tag{4.8}$$

where terms containing like bonds in the bulk have cancelled with those of the reference state, and spectral bond energies in the grain boundary region are paired with the corresponding bulk reference energies.

4.3. Spectral Bond Distributions

To determine the value of ΔU_{mix} in Equation (4.8), I must determine the number of each bond type listed in Table 4.1. The number of bonds in the bulk, grain boundary, and transition region can be assessed geometrically, assuming a volume fraction of grain boundary, f_{gb}, as given by Equation (2.4). Additionally, the number of transitional bonds can be defined with respect to the number of grain boundary atoms via a geometric parameter, v, which determines the fraction of bonds connected to grain boundary atoms which are transitional (GB-bulk) bonds. The number of bulk, transition, and grain boundary bonds, P_r, where r is the region, are thus given as:

$$P_b = \left(\frac{z}{2}\left(1 - f_{gb}\right) - \frac{zv}{2} f_{gb}\right) N \tag{4.9}$$

$$P_{gb} = \left(\frac{z}{2} f_{gb} - \frac{zv}{2} f_{gb}\right) N \tag{4.10}$$

$$P_t = \left(\frac{zv}{2} f_{gb}\right) N \tag{4.11}$$

where N is the total number of atoms, and the number of transitional bonds is subtracted from both the bulk and grain boundary to prevent double counting. For the case of the spectral grain boundary, the number of bonds for site type i are given by Equations (4.10) and (4.11) weighted by the site type probability, $F_{gb,i}$. It is important to note that v is not necessarily a constant and should converge to zero in the amorphous limit. Prior work has demonstrated the important effect of triple junctions and quadruple nodes on the spectral segregation energies [72]. Here, I neglect this energetic change, which is relatively small except at very small grain sizes, and I model the triple junctions geometrically by scaling v with the volume fraction of triple junctions and quadruple nodes, f_{tj}, given relative to the total intergranular volume fraction f_{gb} by the Palumbo polynomial [31,107–110]:

$$f_{tj} = f_{gb} - \frac{3t(d-t)^2}{d^3} \tag{4.12}$$

The fraction of grain boundary bonds that are then transitional bonds can be given as:

$$v = v_0 \left(1 - \frac{f_{tj}}{f_{gb}}\right) \tag{4.13}$$

where v_0 is the value of v for a grain boundary with no triple junctions or quadruple nodes, which I approximate here as 0.33 by fitting to the results of the atomistic simulations from Chapter 3 [69].

To calculate the number of each bond type, the number of bonds in each region from Equations (4.9)-(4.11) must be scaled by the probability of each bond type in that region. Here, in the spirit of a regular solution model, I assume random mixing in the bulk region, and random mixing at the nearest-neighbor level in the grain boundary, resulting in spectral probabilities for the grain boundary and transition regions, as shown in Table 4.2.

Table 4.2. Bond types in each region of the spectral NCRS model – bulk (grain interior), grain boundary, and transition. Additionally, the corresponding notation for the number of bonds and bond energies of each type, the concentration-dependent probabilities assigned of each bond type, and the total number of bonds in each region.

Bond Type	**Number of Bonds**	**Bond Energies**	**Probabilities**	**Bonds in Region**
Bulk	$\boldsymbol{N_b^{AB}}$	$\boldsymbol{E_b^{AB}}$	$\boldsymbol{2X_b(1-X_b)}$	$\boldsymbol{P_b}$
GB-GB	$\boldsymbol{N_{gb,i}^{AA}}$	$\boldsymbol{E_{gb,i}^{AA}}$	$\boldsymbol{(1-X_{gb,i})(1-\bar{X}_{gb})}$	$\boldsymbol{F_{gb,i}(P_{gb})}$
(Site Type i)	$\boldsymbol{N_{gb,i}^{AB}}$	$\boldsymbol{E_{gb,i}^{AB}}$	$\boldsymbol{X_{gb,i}\left(1-\bar{X}_{gb}\right)+\bar{X}_{gb}(1-X_{gb,i})}$	
	$\boldsymbol{N_{gb,i}^{BB}}$	$\boldsymbol{E_{gb,i}^{BB}}$	$\boldsymbol{X_{gb,i}(\bar{X}_{gb,i})}$	
Transition	$\boldsymbol{N_{t,i}^{AA}}$	$\boldsymbol{E_{gb,i}^{AA}}$	$\boldsymbol{(1-X_b)(1-X_{gb,i})}$	$\boldsymbol{F_{gb,i}(P_t)}$
(Site Type i)	$\boldsymbol{N_{t,i}^{AB}}$	$\boldsymbol{E_{gb,i}^{AB}}$	$\boldsymbol{X_b\left(1-X_{gb,i}\right)+X_{gb,i}(1-X_b)}$	
	$\boldsymbol{N_{t,i}^{BB}}$	$\boldsymbol{E_{gb,i}^{BB}}$	$\boldsymbol{X_b(X_{gb,i})}$	

The total solute concentration, X_{tot}, bulk solute concentration, X_b, and average grain boundary solute concentration, $\bar{X}_{gb}$, are related to the site-specific solute concentrations, $X_{gb,i}$, via the relationships:

$$X_{tot} = \left(1 - f_{gb}\right)X_b + f_{gb}\bar{X}_{gb} \tag{4.14}$$

$$\bar{X}_{gb} = \int_i F_{gb,i}(X_{gb,i})\, dS. \tag{4.15}$$

The probabilities and number of bonds in the region, as given in Table 4.2, can thus be combined to determine the number of bonds of each type and populate Equation (4.8) to determine the total change in internal energy upon mixing.

4.4. Spectral Free Energy Functions

The free energy of mixing, ΔG_{mix}, can be determined from the combination of the enthalpic, ΔH_{mix}, and entropic, ΔS_{mix}, contributions upon mixing, given as:

$$\Delta G_{mix} = \Delta H_{mix} - T\Delta S_{mix}. \tag{4.16}$$

Here, it should be noted that the geometric construction of the grain boundary used above and in prior spectral work [67–69,72,83] resembles that of the finite-thickness layer model previously developed by Cahn [104] as an extension of the dividing plane approach of Gibbs [111]. Under this construction, many of the energetic parameters describing the segregated grain boundary must be reported as properly constructed excess quantities to avoid dependence on the chosen grain boundary thickness and location of the dividing plane, as noted in Chapter 3 above. However, in the following construction of phase-and-defect diagrams, I will only consider the total free energy of mixing of the defect state, which encapsulates the whole system and is independent of the chosen grain boundary thickness or location of the dividing plane. Additionally, while the free energy of the defect state rigorously contains a work term corresponding to the excess volume of the grain boundary, I choose here to approximate the enthalpy of mixing as the internal energy of mixing given by Equation (4.8), using the same condensed phase assumptions as for the internal energy of segregation, ΔE_{seg}, discussed in Equation (1.3). The entropic term follows the same mixing assumptions discussed in the above section, and matches the dilute limit spectral formulation by White and Stein [79]:

$$\begin{aligned}\Delta S_{mix} = -RN[&\left(1 - f_{gb}\right)\left(X_b \ln(X_b) + (1 - X_b)\ln(1 - X_b)\right)\\ &+ f_{gb}\int_i F_{gb,i}\left(X_{gb,i}\ln\left(X_{gb,i}\right) + \left(1 - X_{gb,i}\right)\ln\left(1 - X_{gb,i}\right)\right)dS].\end{aligned} \tag{4.17}$$

Combining Equations (4.8) and (4.17) with (4.16), and normalizing by N results in the molar, fully functional form for the free energy of mixing for the spectral nanocrystalline state, which can be conveniently represented in three components that speak to the unique physical regions of the structure:

$$\Delta G_{mix} = (1 - f_{gb})\Delta G^{b}_{mix} + f_{gb}\Delta G^{gb}_{mix} + v f_{gb} \int_{i} F_{gb,i} \begin{bmatrix} \frac{z}{2}\omega_{gb,i}\left(X_b - \bar{X}_{gb}\right)\left(2X_{gb,i} - 1\right) \\ -z\omega_b X_b (1 - X_b) \\ +\frac{1}{2}\frac{V_m}{t}\left(\gamma_{B,i} - \gamma_{A,i}\right)\left(X_b - \bar{X}_{gb}\right) \end{bmatrix} dS \,. \quad (4.18)$$

The first term here, ΔG^{b}_{mix}, is the bulk mixing energy and is the only term present in the limit when grain size, d, is infinite. In this regime, the free energy of mixing follows that of a standard regular solution, and is derived as:

$$\begin{aligned} \Delta G^{b}_{mix} = zX_b(1 - X_b)\left(E_b^{AB} - \frac{E_b^{AA} + E_b^{BB}}{2}\right) \\ +RT(X_b \ln(X_b) + (1 - X_b)\ln(1 - X_b)) \end{aligned} \quad (4.19)$$

and the bulk regular-solution interaction parameter, ω_b, emerges as:

$$\omega_b = \left(E_b^{AB} - \frac{E_b^{AA} + E_b^{BB}}{2}\right). \quad (4.20)$$

The second term in Equation (4.18), ΔG^{gb}_{mix}, corresponds to the grain boundary mixing free energy, and is the only term present in the so-called "amorphous limit" where $f_{gb} \to 1$:

$$\Delta G^{gb}_{mix} = \int_{i} F_{gb,i} \begin{bmatrix} \frac{z}{2}\{\left(1 - X_{gb,i}\right)\left(E^{AA}_{gb,i} - E^{AA}_{b}\right) + X_{gb,i}\left(E^{BB}_{gb,i} - E^{BB}_{b}\right) \\ +\left(E^{AB}_{gb,i} - \frac{E^{AA}_{gb,i} + E^{BB}_{gb,i}}{2}\right)\left(\bar{X}_{gb} + X_{gb,i} - 2\bar{X}_{gb}X_{gb,i}\right)\} \\ +RT\left(X_{gb,i}\ln\left(X_{gb,i}\right) + \left(1 - X_{gb,i}\right)\ln\left(1 - X_{gb,i}\right)\right) \end{bmatrix} dS. \quad (4.21)$$

This formulation requires an integral over all grain boundary site types, and that the enthalpic contributions generally contain both spectral concentrations, $X_{gb,i}$, and the average grain boundary concentration, $\bar{X}_{gb}$. Additionally, this free energy term reveals a spectral regular-solution interaction parameter analogous to the bulk parameter above:

$$\omega_{gb,i} = \left(E_{gb,i}^{AB} - \frac{E_{gb,i}^{AA} + E_{gb,i}^{BB}}{2} \right). \tag{4.22}$$

The first two terms of Equation (4.21) consider the difference in like-bond energies between the bulk and the grain boundary, and are related to the conventional grain boundary energies of the solvent, $\gamma_{A,i}$, and of the solute, $\gamma_{B,i}$, by the relationship:

$$\gamma_{A,i} = \frac{z}{2}\frac{t}{V_m}\left(E_{gb,i}^{AA} - E_b^{AA}\right) \tag{4.23}$$

$$\gamma_{B,i} = \frac{z}{2}\frac{t}{V_m}\left(E_{gb,i}^{BB} - E_b^{BB}\right) \tag{424}$$

where $\frac{t}{V_m}$ converts the grain boundary excess energy to a molar quantity by normalizing with the thickness of the boundary, t, and the molar volume, V_m.

Introducing these definitions into Equation (4.21), the free energy contribution due to the grain boundary region can be written in a more familiar form as:

$$\Delta G_{mix}^{gb} = \int_i F_{gb,i} \begin{bmatrix} \left(1 - X_{gb,i}\right)\frac{V_m}{t}\gamma_{A,i} + X_{gb,i}\frac{V_m}{t}\gamma_{B,i} \\ +\frac{z}{2}\omega_{gb,i}\left(\bar{X}_{gb} + X_{gb,i} - 2\bar{X}_{gb}X_{gb,i}\right) \\ +RT\left(X_{gb,i}\ln\left(X_{gb,i}\right) + \left(1 - X_{gb,i}\right)\ln\left(1 - X_{gb,i}\right)\right) \end{bmatrix} dS \tag{4.25}$$

where the top row is now seen to be the excess energy of the alloyed grain boundary (a composition-weighted average of the excess energies of the two components), the second row speaks to mixing enthalpy in the grain boundary, and the third row is a configurational entropy. This is the correct assemblage of terms for a grain boundary mixing energy [41], formulated here in a spectral version integrated over all site types for the first time.

The first two terms of Equation (4.18) are thus described by Equations (4.19) and (4.25) and represent a rule of mixtures between the bulk and grain boundary regions. The remaining, third

term of Equation (4.18) handles the transitional bonds between the grain boundary and bulk region, bridging the two limiting cases considered here. Due to the assumption of a sharp interface between the bulk and grain boundary, this term includes both the addition of the correctly counted transitional bonds, and the removal of any double-counted bonds from the grain boundary and bulk.

Equation (4.18) is thus a complete free energy function for polycrystals and is ready for evaluation if spectral inputs about the grain boundary sites are available. Importantly, if all the spectral parameters in Equation (4.18) are replaced with their non-spectral counterparts, this model properly devolves into a standard scalar nanocrystalline regular solution model in the form derived by Trelewicz and Schuh [41]. This derivation is shown in Appendix A.

4.5. Spectral Equilibrium Conditions and the Spectral Isotherm Model

At this stage, the equilibrium condition of the nanocrystalline state could generally be solved by finding the minimum energy configuration across the possible space of solute configurations and grain sizes. In the case of a scalar, single-parameter segregation state, this problem is reduced to a simple minimization of Equation (4.18) with respect to the grain size, d (or equivalently, the grain boundary volume fraction, f_{gb}), and the average solute concentration at the grain boundary, $\bar{X}_{gb}$, assuming a closed system with constant total concentration, X_{tot}.

In the case of a spectral model such as this, such a minimization is non-trivial, because it must span the full configuration space of site-wise concentrations, $X_{gb,i}$, which results in a recursive definition, where knowledge of the equilibrium isotherm is necessary to populate the spectral concentrations in Equations (4.18) and (4.25). For that reason, a closed-form analytical solution of the spectral isotherm is not forthcoming. Instead, I use a modified version of the isotherms proposed in Chapter 3 that allows for a solution to this inverse problem in a reduced, yet physically reasonable, parameter space. These can be mapped to the form of the non-spectral solution given in Appendix A and have been shown to give reasonable agreement with the results of fully atomistic simulations. With this approach, I can populate the spectral concentrations of

Equations (4.18) and (4.25) to solve for an equilibrium condition. I elaborate this mapping in what follows.

Comparing the form of my previously proposed isotherm in Equation (3.5) to that of the non-spectral regular solution isotherm derived in Appendix A (A19) reveals that a similar set of dilute terms, as well as non-dilute terms modified by average solute concentrations, appear in both. Carrying the terms that account for transitional bonds, and converting non-spectral terms in Equation (A19) to spectral terms matching the present derivation, the following site-specific spectral isotherm is achieved:

$$\frac{X_{gb,i}}{1-X_{gb,i}} = \frac{X_b}{1-X_b}\exp\left(\frac{-\Delta H_i^{seg}}{kT}\right) \tag{4.26}$$

where the spectral site-specific segregation energy, ΔH_i^{seg}, is derived as:

$$\begin{aligned}\Delta H_i^{seg} = & \left(\frac{vf_{gb}}{1-f_{gb}}-1\right)z\omega_b + \left(1+\frac{v}{2}\left(1+\frac{f_{gb}}{1-f_{gb}}\right)\right)z\omega_{gb,i} \\ & + \frac{V_m}{t}\left(1-\frac{v}{2}\left(1+\frac{f_{gb}}{1-f_{gb}}\right)\right)(\gamma_{B,i}-\gamma_{A,i}) \\ & + 2z\left(\left(1-\frac{vf_{gb}}{1-f_{gb}}\right)w_bX_b - \left(1+\frac{v}{2}\left(1+\frac{f_{gb}}{1-f_{gb}}\right)\right)\omega_{gb,i}\bar{X}_{gb} + \frac{v}{2}\omega_{gb,i}(X_b-\bar{X}_{gb})\right)\end{aligned} . \tag{4.27}$$

The first two lines of Equation (4.27) are derived from the dilute-limit contributions to the segregation energy, and the third line of terms correspond to the effects of solute-solute interactions in the bulk and grain boundary. Note again that the convention here is that negative segregation energies favor segregation [67].

4.6. Conversion of Site-Specific Spectra to Bond Energy Spectra

Prior derivations of the spectral segregation energy have considered only site-specific energies in which the bulk site considered in Equation (2.2) is assumed to be far in the grain interior [67,69].

As such, prior spectral measurements do not account for any grain boundary effects on the bulk energetics – an assumption which this model does not support, due to the necessary transition region, potentially large values of f_{gb}, and arbitrary choice of grain boundary thickness. This can be noted by the modification terms containing v and f_{gb} in Equation (4.27) that adjust the segregation energy as a function of grain size, to account for the relative fraction of transitional bonds contributing to the bulk energy in Equation (4.1). For the sake of comparison with past measurements of the dilute limit segregation energy spectrum, and to allow for the conversion between site-specific and bond-based spectra, one can neglect the transition bond terms in the first two lines of Equation (4.27) and write the dilute limit segregation energy for the case of a perfect bulk, $\Delta H_i^{seg,dil}$, simply as:

$$\Delta H_i^{seg,dil} = \left[-z\omega_b + z\omega_{gb,i} + \frac{V_m}{t}\left(\gamma_{B,i} - \gamma_{A,i}\right)\right]. \tag{4.28}$$

This simplified form of the dilute limit segregation energy given in Equation (4.28) can be used to solve for $\gamma_{B,i}$: given measurements of site-specific spectra, such as those computed in Chapter 3, for the dilute limit segregation energy $\Delta H_i^{seg,dil}$, solute-solute interaction energy, $\omega_{gb,i}$, and the molar excess energy of the pure solvent grain boundary, $\frac{V_m}{t}\gamma_{A,i}$, to solve for the remaining term $\frac{V_m}{t}\gamma_{B,i}$. These site-specific spectra can then be used in combination with the definitions of $\gamma_{A,i}$, $\gamma_{B,i}$, and $\omega_{gb,i}$ given in Equations (4.22)-(4.24) to map the site-specific spectral description of the grain boundary to the corresponding bond energy spectra, by assuming asymmetric half bonds connected to each site. An example of this approach is shown in Figure 5.1 below.

5. Phase and Defect Diagram Construction

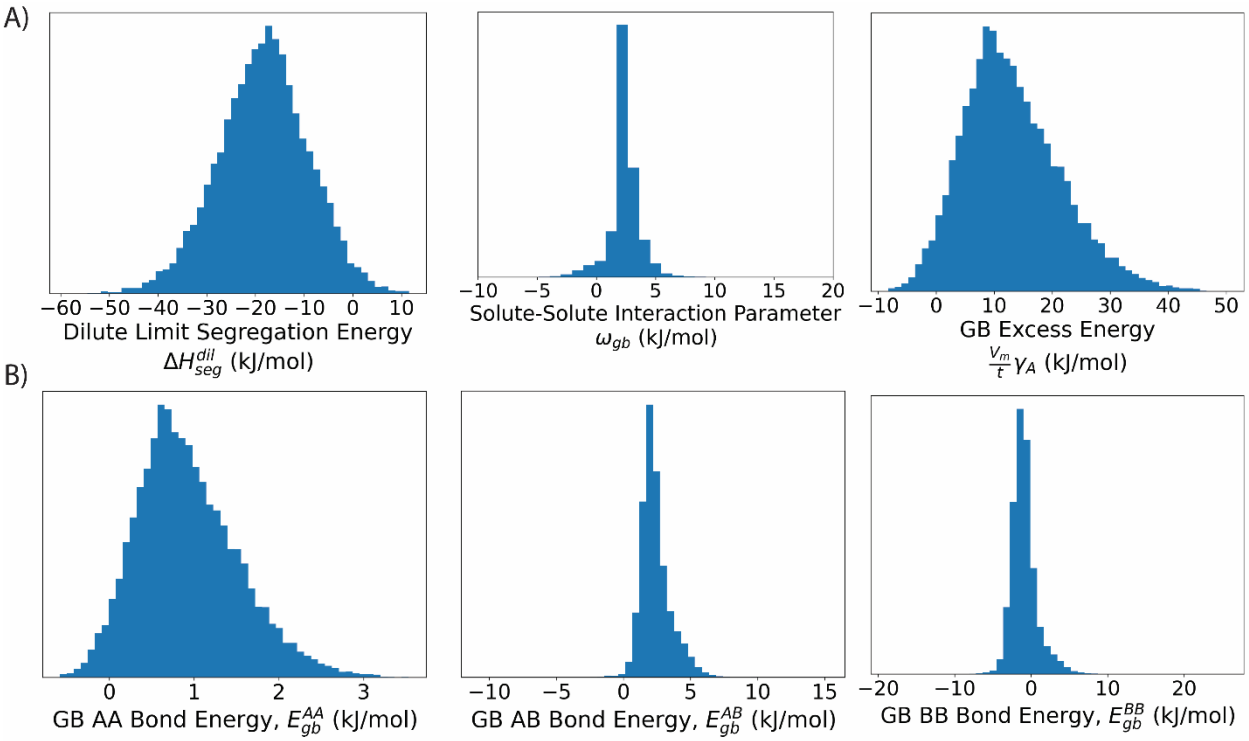

Figure 5.1. Hypothetical spectral system parameters. (a) Site-wise distributions for the hypothetical system used in this work, including the dilute limit segregation energy, solute-solute interaction parameter, and grain boundary excess energy of the solvent. (b) Bond-wise distributions for the grain boundary AA, AB, and BB bond energies, corresponding to the site-wise distributions in (a).

In this chapter, I consider a hypothetical system, given by the spectral parameters shown in Figure 5.1, and using a bulk interaction parameter, ω_b, of 2.17 kJ/mol. Given the assumed α phase reference state, the heat of mixing of B in A, E_{BinA}, is thus 26.04 kJ/mol. These parameters were chosen for the physically reasonable breadths and shapes of the spectra, with characteristic energies that favor nanocrystalline states and exhibit the interesting behavior first visualized by Weissmueller in the context of Equation (1.1). The integrals in the free energy equations are solved with discrete summation of the energetic distributions shown in Figure 5.1. The content of this chapter was previously published in Ref. [85] alongside Chapter 4.

5.1. The Nanocrystalline Free Energy at Fixed Grain Size

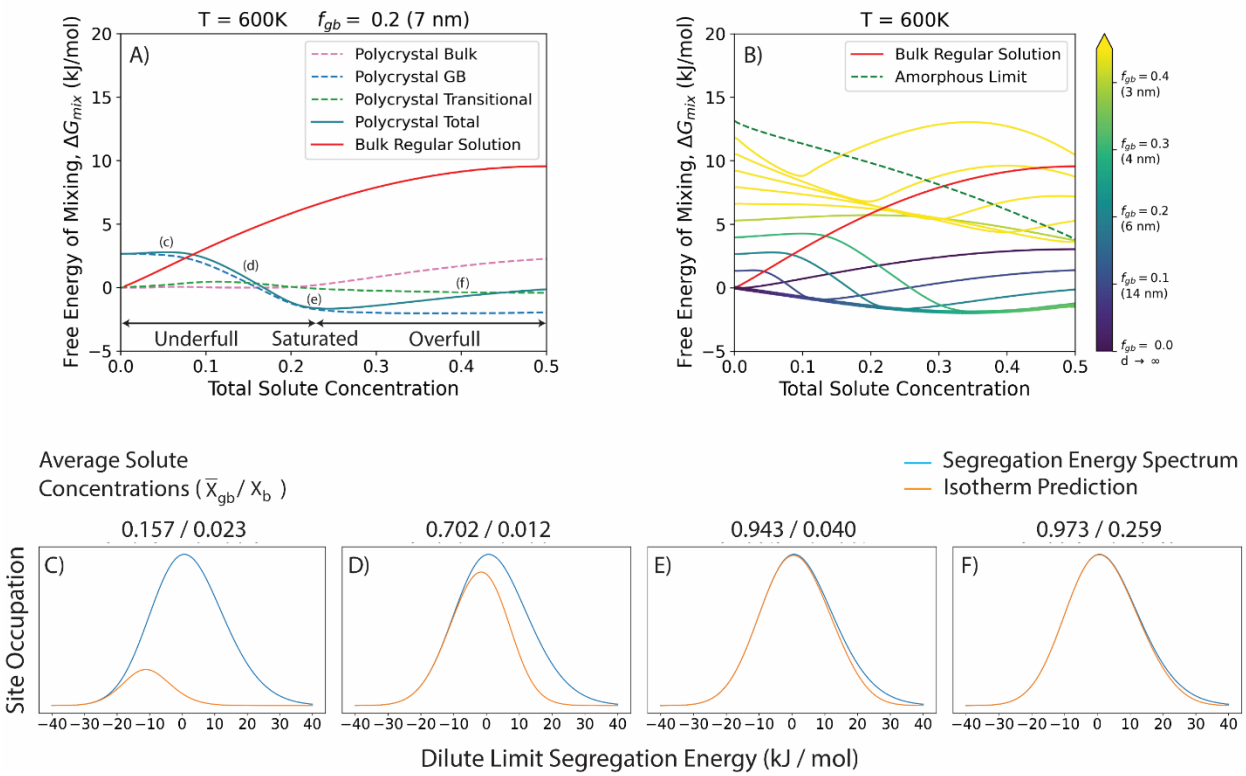

Figure 5.2. Free energy predictions for the hypothetical system at a fixed grain size. (a) Free energy of mixing of the polycrystalline state (dark blue – Equation (4.18)) at a grain size of 7 nm ($f_{gb} \approx 0.2$) and temperature of 600 K, as well as the corresponding polycrystalline bulk (light blue – Equation (4.19)), polycrystalline grain boundary (orange – Equation (4.25)), and remaining transitional terms (green), alongside the free energy of mixing for the bulk regular solution (red – Equation (4.1). (b) The free energy of mixing of the polycrystalline state at several grain sizes (dark blue), and the corresponding minimum energy hull (magenta). (c)-(f) The occupied grain boundary distribution as a function of dilute limit segregation energy for total solute concentrations of 0.05, 0.15, 0.22, and 0.4, respectively.

To construct a phase and defect diagram in concentration-temperature space for the segregated polycrystalline state, one can solve for the equilibrium condition of Equation (4.18) at a fixed

temperature. To do so, I sample across many grain sizes and total concentrations (including the infinite grain size, or bulk, limit) to numerically find the minimum energy configuration.

As an initial analysis of the form of this solution, observe the free energy of mixing as a function of total concentration at a fixed grain size of 7 nm ($f_{gb} \approx 0.2$) and a temperature of 600 K, given in Figure 5.2(a). The total free energy of mixing for the polycrystalline state is given by Equation (4.18) and shown in dark blue. To determine the dominant behavior in the system, I separate the contributions due to the bulk (light blue – Equation (4.19), the grain boundary (orange – Equation (4.25)), and the remaining transitional terms (green). The bulk free energy of mixing, given by Equation (4.1), or equivalently, the infinite grain size limit given by Equation (4.19), is plotted in red.

Plots showing the predicted solute occupation of the grain boundary as a function of the dilute limit segregation energy are shown in Figure 5.2(c)-(e), for total concentrations of 0.05, 0.15, 0.22, and 0.4, respectively. Note that the dilute limit segregation energies shown in these figures are not the simplified segregation energies given by Equation (4.28), rather they are the segregation energies after transitional bond corrections are taken into account, as in Equation (4.27).

From Figure 5.2(a), note that the free energy of mixing of the polycrystalline state is generally a complex form with various inflections as different terms attain prominence. In this example set of conditions, it initially rises to a maximum of about 9 percent total solute, before decreasing to a minimum at about 22 percent total solute and then rising again. Examining the sub-contribution lines, these changes correspond, respectively, to behavior dominated by the grain boundary (up to about 22% solute) and then by the bulk. This is confirmed by the occupation of the grain boundary at the plotted concentrations in Figure 5.2(c)-(f) – below 22 percent total solute, the spectrum of available sites in the grain boundary gradually fills, resulting in an asymmetric regular solution curve until saturation at 22 percent total solute, at which point the polycrystalline bulk begins to fill and a secondary peak in free energy emerges.

This behavior agrees well with prior models of grain boundary segregation which demonstrate "overfull" and "underfull" behavior [36,37,41], in which a fixed grain size achieves its minimum energy when there is enough solute to saturate the amount of available grain boundary, but not excess such that the bulk begins to fill. However, in this case it should be noted that the saturated grain boundary for this fixed grain size, as shown in Figure 5.2(e) and labeled in Figure 5.2(a), is not pure solute. Rather, appropriately accounting for temperature and solute interaction effects, the spectrum of available sites fills until the remaining sites are so unfavorable that the competing bulk sites are energetically preferred.

While Figure 5.2(a) demonstrates the behavior of this model at a single grain size, a convex hull construction across many grain sizes is required to find the equilibrium condition. Figure 5.2(b) shows the free energy of mixing of several grain sizes, sampled with uniformly spaced grain boundary volume fractions. In total, 100 different grain sizes were calculated, as well as the hypothetical "fully amorphous" (d = t, $f_{gb} = 1$) state. Taking the free energies sampled across many grain sizes, as well as the calculated amorphous limit, a convex hull construction can be used to construct the minimum energy hull for the polycrystalline state, shown as the multicolor line in Figure 5.2(b), where the color corresponds to the grain size at that point on the hull. This minimum energy hull can be used as a free energy function in temperature-concentration space to determine the minimum energy grain size and produce a phase and defect diagram, as will be demonstrated in the following section.

Here, I stress that the model presented here is asymmetric, and assumes only the segregated polycrystalline defect state with a randomly mixed solvent-based bulk; it does not account for two phase grains, nor the segregated polycrystalline defect state with a solute-based bulk. For that reason, I only consider concentrations below 50 percent total solute in this analysis. Additionally, the amorphous state presented in Equation (4.25) is a theoretical limit; it is non-physical and cannot exist outside of the geometric constraints of the grain boundary.

5.2. The Nanocrystalline Phase and Defect Diagram

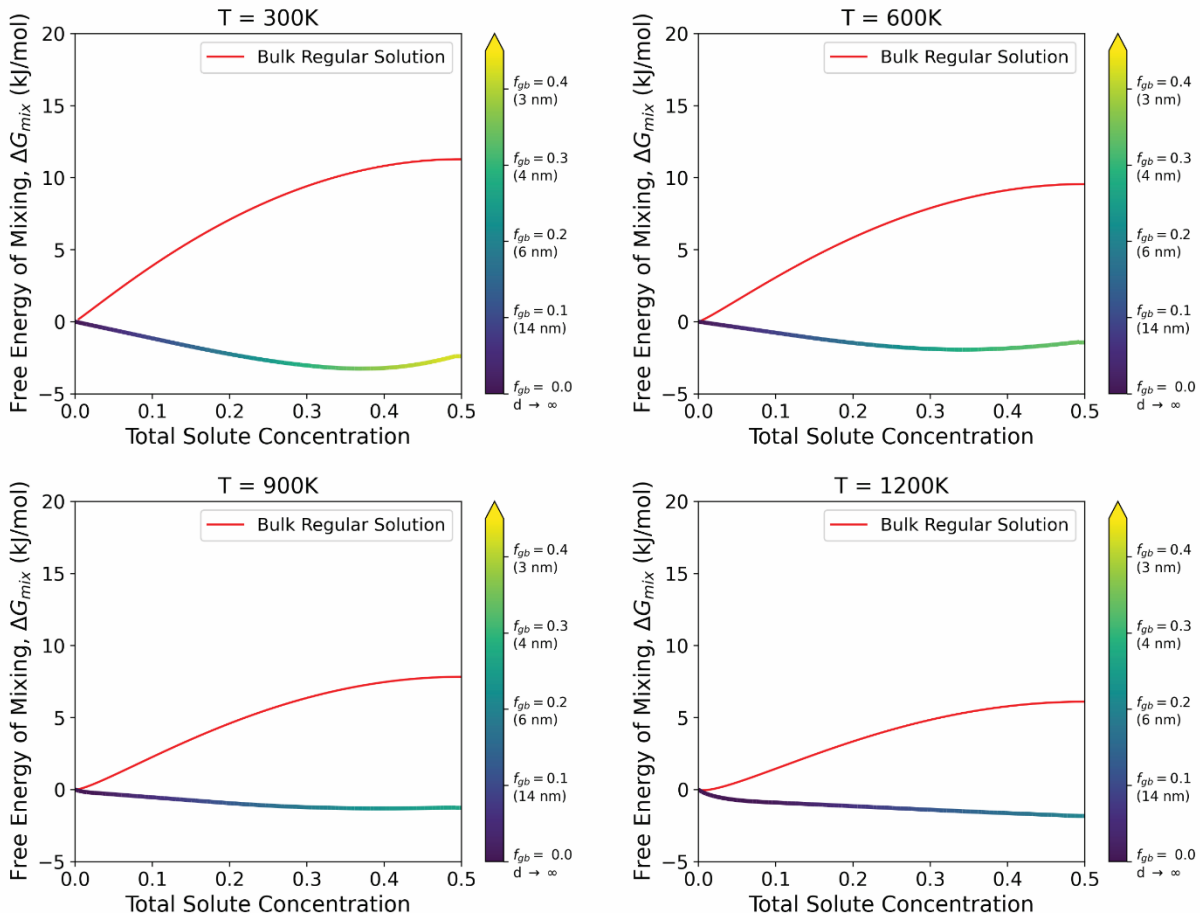

Figure 5.3. Minimum energy convex hull of the polycrystalline free energy (Equation (4.18)) across many grain sizes at 300, 600, 900, and 1200 K. The infinite grain size limit (Equation (4.1)) is shown in red for reference.

Repeating the construction of the minimum energy convex hull in Figure 5.3(b) across many temperatures, the resulting free energy curves can be used to produce a phase and defect diagram. This is shown for 300, 600, 900, and 1200 K in Figure 5.3. From this, observe that the polycrystalline state with a finite grain size is the minimum energy configuration at every observed temperature, with the grain size decreasing at higher solute concentrations, and converging to the infinite grain size limit at zero solute concentration. The amount of solute required to access smaller grain sizes increases with temperature.

The minimum energy hulls constructed above can be used to construct minimum energy grain size contours in temperature-concentration space and produce the phase and defect diagram shown in Figure 5.4. which also plots the bulk miscibility gap, determined by Equation (4.1), for comparison; note that this model predicts the replacement of bulk phase behavior with a gradually decreasing grain size as solute is introduced, without need for phase separation. For reference, I have also plotted the left-most grain size contour at f_{gb} = 0.001 (1499 nm) as an arbitrary limit to show the boundary between nanocrystalline stability and typical micron-scale polycrystalline behavior. Here, it should be reiterated that this model considers only solvent-based polycrystalline states and does not consider B-rich phases or polycrystalline states. By visual inspection of the shape of the minimum energy hulls shown in Figure 5.3, a reasonable assumption can be drawn that the A-based states considered here should be in equilibrium with either the B-rich regular solution, or a B-based polycrystalline state via a common tangent that extends beyond the 50% total solute limit imposed here. Future efforts with experimentally measured spectral inputs should consider both ends of the concentration range and enable the modeling of such behaviors.

The nanocrystalline stability regime shrinks with increasing temperature, requiring additional solute to reach stability at higher temperatures. Additionally, the equilibrium grain size decreases with additional solute, and increases with temperature, as observed above. It should be noted that the prediction for this system indicates polycrystalline stability well outside of and at higher temperatures than the bulk miscibility gap. However, this stability prediction at higher temperatures does not consider vibrational entropy, nor competition with the liquid phase. A more complete extension in the future should incorporate these effects, and the model presented here is simply designed to provide a roadmap for future phase and defect diagrams.

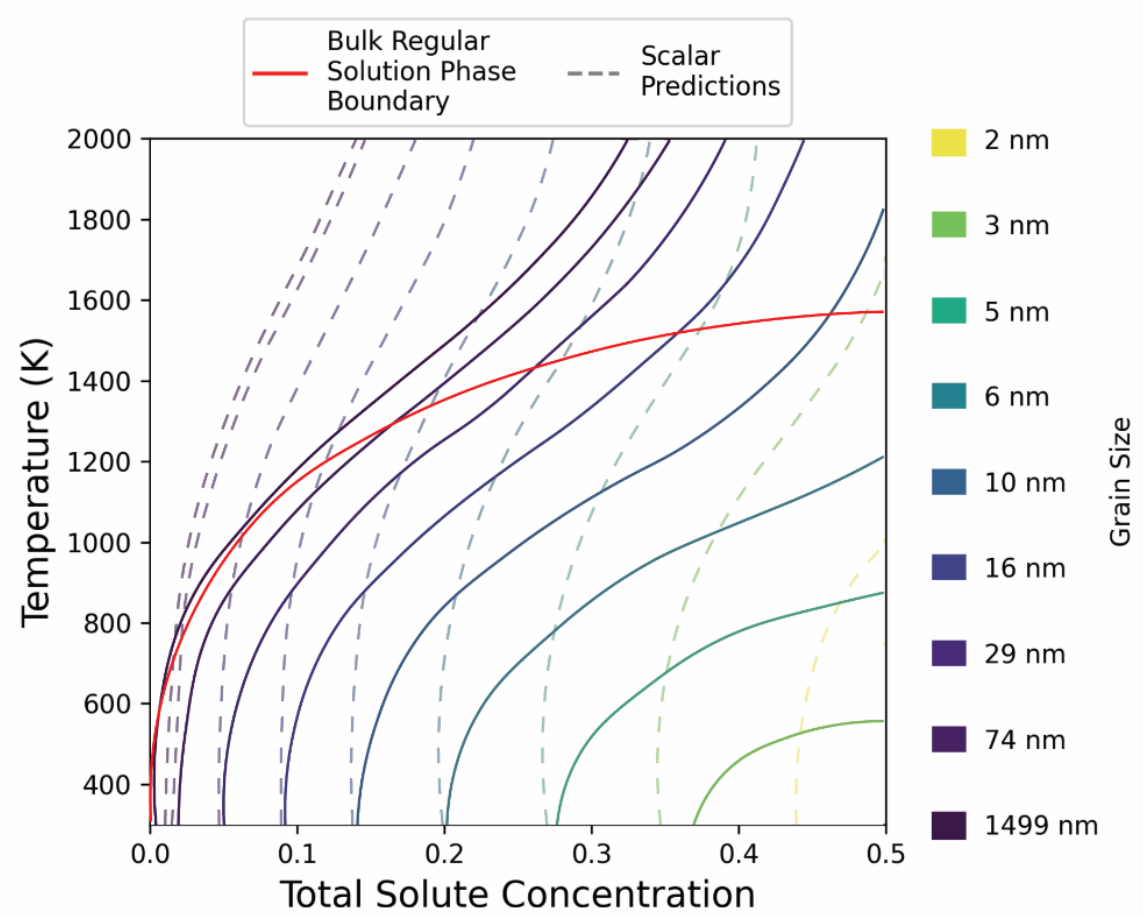

Figure 5.4. Polycrystalline phase and defect diagram, using the spectral parameters for the hypothetical system shown in Figure 5.1. The infinite grain size two-phase region is shown in red, and the minimum energy grain size contours are colored according to grain size. The polycrystalline stability boundary is given arbitrarily at f_{gb} = 0.001 (1499 nm). Scalar predictions are shown as faded dashed lines.

For comparison with previously developed non-spectral models, the solute interaction energy and grain boundary excess energy spectra in Figure 5.1 were collapsed into average parameters, and the segregation energy was taken as the average of the lower quartile of dilute limit segregation energy spectrum, to emulate the fitted effectively segregation energies generally used in scalar models [67,69,72,82]. These parameters were used as inputs for the scalar nanocrystalline regular solution model originally developed in [41], and reproduced in Appendix A, to create the phase and defect diagram shown as the faded dashed lines in Figure 5.4.

Figure 5.4 convincingly shows that a spectral approach gives rise to different states than a scalar approach. This is because effective segregation energies, which are typically fitted at fixed grain sizes with lower solute concentrations, often only account for the most favorable segregation sites. As such, when a spectrum is accounted for, the effective segregation energy can change as both a function of composition and temperature, as noted in several prior works [67,72,82]. Furthermore, the scalar nanocrystalline regular solution model, when using true averages of the spectral parameters shown in Figure 5.1, predicts no polycrystalline stability whatsoever for this system, indicating that even a true average of the full spectrum of sites fails to capture the correct behavior. This work therefore further augments recent discussion about the necessity of spectral information for the polycrystalline state to accurately produce phase and defect diagrams such as these.

While the model presented here has several limitations – its assumed random mixing in both the bulk and grain boundary, ability to handle only the regular solution complexion state, and inability to address the B-rich end of the phase diagram without additional adjustments – it does provide an initial framework for the use of spectral models in the production of phase-and-defect diagrams of segregated polycrystalline alloys. The development of these phase-and-defect diagrams will constitute a huge step forward in the potential and ease of engineering alloyed grain boundaries, providing access to information about a huge range of available alloys and properties that were previously unexplored. However, while large-scale databases for the dilute limit segregation spectra and vibrational entropy spectra of binary alloys exists [68,83,84], no such resource exists for spectral parameters beyond the dilute limit, making usage of this model inaccessible in practice. The following chapter will focus on addressing this need.

6. A Large-Scale Database of Spectral Parameters Beyond the Dilute Limit

In this chapter, I seek to develop a database of spectral grain boundary parameters at finite concentrations, to enable the population of the model described in Chapters 4 and 5. To that end, I turn towards constructing an accelerated to approach to measuring the solute interaction spectra described in Chapter 3 [69], and I seek here to find a mapping between the local atomic environment (LAE) of each GB nearest neighbor bond, depicted in Figure 3.4, and the corresponding pair-wise energetics. Section 6.1 provides a brief overview of the use of LAE representations, and the remainder of this chapter presents the development of a "bond-focused" LAE representation, which I then use to construct a database of non-dilute spectral parameters for binary alloys from almost 200 EAM potentials available on the NIST potential repository [112,113]. The work presented in this chapter is currently under review for publication in a peer reviewed journal.

6.1. Background on LAE Representations

Simplified numerical representations that capture the local atomic environment (LAE) have proven invaluable in understanding complex alloy configuration energetics in recent years, such as in high entropy alloys (HEAs) [114–116], metallic glasses [117–119], and grain boundaries [68,83,120]. Especially in topologically disordered environments (such as the grain boundaries considered in this work) these LAE representations are often constructed from basic structural features, such as coordination, atomic volume, or Voronoi parameters [121,122]. An approach that is more physics-agnostic while capturing site geometry in full detail is provided by complex descriptors, such as those often used in machine-learned interatomic potentials [123,124]. These descriptors encode the local atomic environment within a cutoff radius as a simplified feature vector and include methods such as atom-centered symmetry functions [125] or the Smooth Overlap of Atomic Positions (SOAP) [126].

The SOAP representation has recently been used to map the full distribution of local atomic environments in a polycrystalline grain boundary network onto the corresponding spectra of dilute limit segregation energies [83] and vibrational entropies [68], and both have been adapted into high throughput frameworks to produce large-scale databases of spectral information for binary grain boundary segregation. These two spectra are similar in the sense that each atomic site in the grain boundary undergoes a single solute substitution and has a unique resulting energy or entropy quantity. This facilitates the use of LAE descriptors based on a site-centered geometry; with a SOAP vector for each site in the grain boundary network, a simple regression-type model connects the LAE to the energy and entropy of segregation at that site [83].

The above examples of grain boundary environments represent a challenge to the geometric description of the LAE but are not especially chemically complicated (one solute atom always lies at the center of a solvent-based LAE). Chemically more complex environments become relevant as composition moves away from the dilute limit. This is a common problem in high entropy alloys, in which LAE representations are often required to capture a large degree of chemical complexity within an otherwise geometrically simple phase [114–116]. Often, this chemical complexity is captured using separate site-centered descriptors for each chemical species in the local environment. However, the combination of non-dilute concentrations and complex site topologies presents an interesting cross-section where new approaches to the LAE may be needed. The interaction of solutes at grain boundaries at higher concentration (which I have measured in Chapter 3, and seek to produce accelerated predictions for here), is a prime example: this is no longer strictly a site-centered problem, but one in which two key sites interact, and those sites are geometrically disordered and distinct. It is therefore the purpose of this chapter to present an approach to this problem, by developing a “bond-focused” LAE descriptor and subsequently applying it in a learning model to create a database for solute interactions at grain boundaries.

6.2. Atomistic Assessment of the Site Spectra

All atomistic simulations in this work were performed using LAMMPS [94]. The Al-Mg [127], Ag-Cu [128], Nb-Ni [129], Ni-Pt [130], and Pt-Au [131] systems were chosen as case studies to

span different crystal structures, segregation behaviors, and interaction behaviors. For each of these systems, a (10 x 10 x 10) nm^3 polycrystal of the pure solvent was produced with 10 randomly positioned and randomly oriented grains. Each polycrystal was initialized with Voronoi tessellation in the Atomsk [92] toolkit, and was then structurally relaxed with conjugant gradient minimization, followed by a thermal anneal under an isothermal-isobaric ensemble, with a Nose-Hoover thermostat at roughly 0.4 T_{melt} and barostat at zero pressure for 0.5 ns. The polycrystals were then cooled to 0 K over 0.25 ns and relaxed with a final conjugate gradient minimization. This resulted in polycrystals with an average grain size of 6 nm, and between 50,000 and 90,000 atoms and 11,000 to 20,000 GB sites, varying with lattice parameter. This results in approximately 150,000 to 300,000 nearest neighbor GB pairs.

Grain boundary sites were detected for each polycrystal using polyhedral template matching with a 0.1 RMSD cutoff [93] by selecting atoms which do not have the same crystal structure as the bulk solvent. Nearest neighbors of GB atoms were then detected via Voronoi analysis. For each grain boundary site in the (10 x 10 x 10) nm^3 polycrystals, the dilute limit segregation energy was calculated using molecular statics via Equation (2.8). The GB excess energy of site i, $\frac{V_m}{t}\gamma_{A,i}$, following from Equation (4.23), was defined and measured as the difference between the local energy of the site, E_i , and the energy of a bulk crystalline site, E_{xtal}, both composed entirely of pure solvent A [85]:

$$\frac{V_m}{t}\gamma_{A,i} = E_i \ - E_{xtal}. \tag{6.1}$$

Finally, the solute interaction parameters were calculated for each GB nearest neighbor pair and averaged for each site using molecular statics and the definitions given in Equations (2.7), (3.2), and (3.3), and these calculations were then repeated to obtain the bulk interaction parameter from a crystalline supercell.

Figure 6.1 shows an example of the spectral energetics for grain boundary sites in a (10 x 10 x 10) nm^3 Ag-Cu polycrystal simulated using the embedded-atom-method (EAM) potential by Wu and Trinkle [128]. Figure 6.1(a) shows in red the full tri-variate spectrum required to populate

the spectral nanocrystalline regular solution model presented in Chapters 4 and 5 [85], and projections of its bivariate components in blue. Figure 6.1(c) shows how the tri-variate spectrum decomposes into its measurable univariate components, including the site-wise grain boundary excess energy of the pure solvent, defined by Equation (6.1), and the dilute limit segregation energies and interaction parameters as used in Equation (3.5).

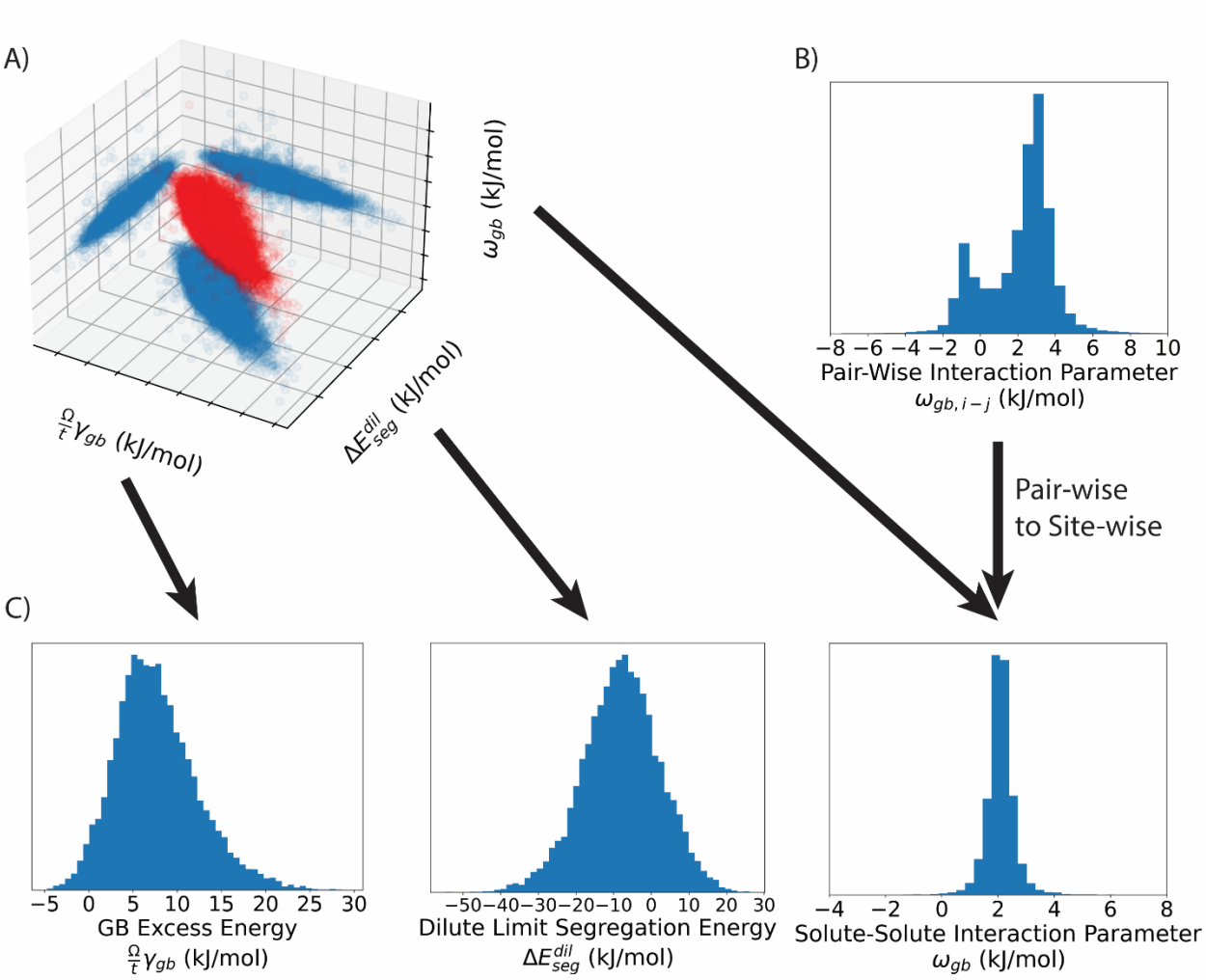

Figure 6.1. Spectral quantities for GB segregation in Ag-Cu [128]. *(a) Full site-wise tri-variate spectrum, with projections of the corresponding bi-variate distributions. (b) Pair-wise spectrum of solute interaction parameters,* $\omega_{gb,i-j}$. *(c) Univariate spectra comprising the tri-variate spectrum shown in (a), from left to right: GB excess energy of the solvent,* $\frac{V_m}{t}\gamma_{A,i}$, *dilute limit segregation energy,* $\Delta E_i^{seg,dil}$, *and the site-wise solute interaction parameter,* $\omega_{gb,i}$.

Figure 6.1(b) shows the spectrum of pair-wise interaction parameters, $\omega_{gb,i-j}$, calculated for Ag-Cu. While the site-wise parameters shown in Figure 6.1(c) have been known to follow simple skew-normal behavior as defined by Equation (2.10) [67,69,85], the pair-wise energies in this system - and many other examples studied in this chapter – demonstrate a broad, dual-peak distribution. This behavior is indicative of the more complex underlying dependence on the local atomic environment, thus necessitating a more complex LAE representation to correctly capture this behavior.

6.3. Representation of the LAE

The starting point for LAE considerations in problems of grain boundary segregation is the site-centered approach used elsewhere [68,83,84]. Here, I adopt that approach as an internal check and a touchpoint with the prior literature, as done in Figure 6.2(a). I predict the dilute limit segregation energy, $\Delta E_i^{seg,dil}$, using a site-centered descriptor constructed via the Smooth Overlap of Atomic Positions (SOAP) method [126]. SOAP produces a feature vector from the coefficients of a set of radial basis functions and spherical harmonics fitted to the local atomic environment. The feature vector size, N_{SOAP}, is determined by the maximum number of radial basis functions, n_{max}, degree of spherical harmonics, l_{max}, and the width of the gaussian functions used for fitting, σ_{at}. In this work, I have chosen to use the DScribe Python library [132] to construct the SOAP vectors, with the parameters n_{max} = 12, l_{max} = 6, and σ_{at} = 0.5, which results in a SOAP vector of length N_{SOAP} = 1016. I have chosen these parameters, in addition to a radial cutoff of 6 Å, for their generally strong performance across the several alloys which I rigorously validate in Section 6.6 below.

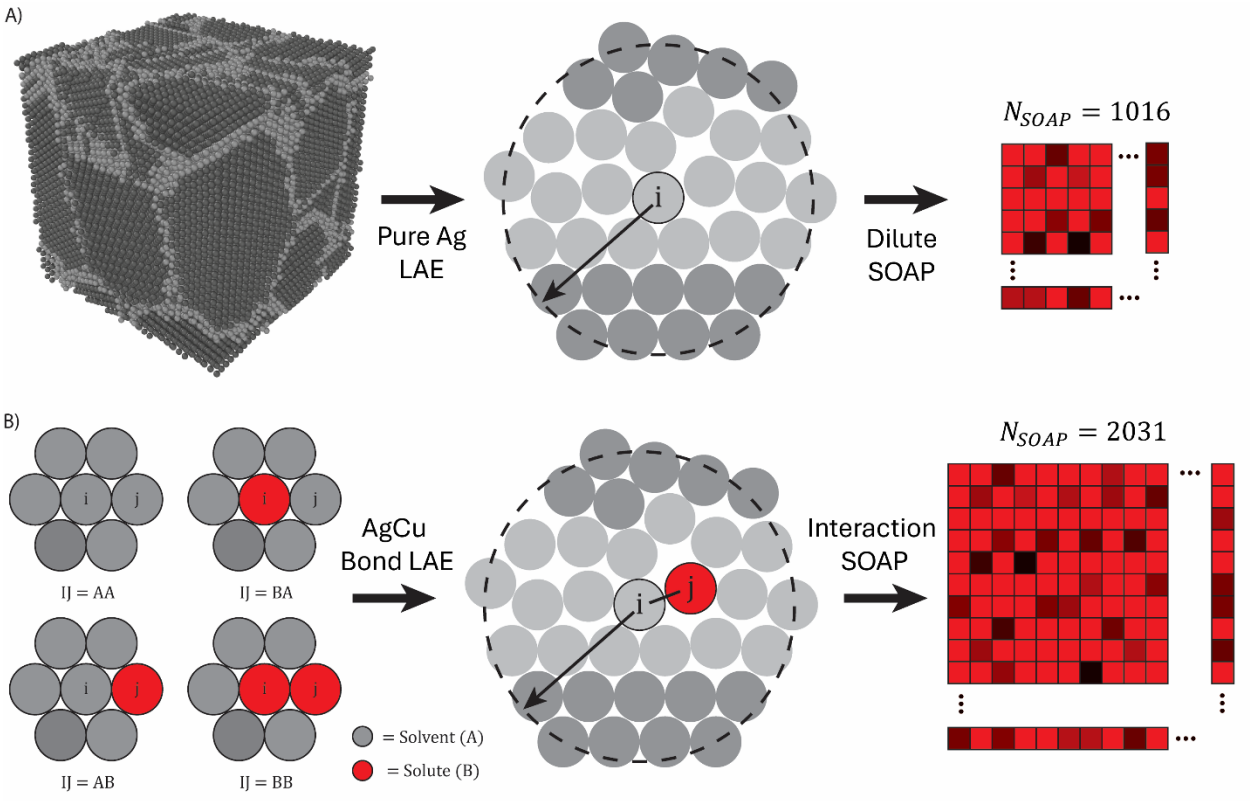

Figure 6.2. Schematic depiction of SOAP LAE descriptors. (a) Left to right: Pure polycrystal of Ag, pure solvent LAE, dilute limit SOAP matrix. (b) Left to right: required nearest neighbor solvent-solute pairs to atomistically measure $\omega_{gb,i-j}$*, a bond-focused LAE on bond i-j required to predict* $\omega_{gb,i-j}$*, non-dilute SOAP matrix.*

To predict the solute-solute interaction parameter, $\omega_{gb,i-j}$, defined in Equation (3.2), one must reflect the pair-wise nature of this quantity in the chosen LAE representation. I propose to do so by constructing a "bond-focused" SOAP embedding of the local atomic environment. For a given GB site i, this LAE has a corresponding nearest neighbor j denoted by a solute atom of a different type. Using the same parameters described above, this results in a SOAP feature vector that is approximately twice the length compared to a pure solute environment, N_{SOAP} = 2031, due to fitting an additional, separate set of functions for the second atom type. While the SOAP parameters could be individually tuned to provide the best performance when predicting solute interaction spectra for each alloy, these initial values provide a strong starting point with which I

can rapidly screen many alloys. With this construction, the LAE depicted in Figure 6.2(b) can be mapped into a SOAP feature vector, as described above and shown schematically in Figure 6.2(b).

6.4. A High-Fidelity Learning Model Based on the LAE

The adjusted LAE representation presented above provides more information than a single-component site-centered approach, in a manner that better reflects the nature of the pair-wise quantities being computed. Because of this, the corresponding SOAP vectors are larger, and present a more complex feature space that necessitates the use of more complex learning algorithms than the linear regression that was previously employed for dilute limit segregation energies [83]. In fact, my efforts seeking a simple regression-based connection between site-focused LAE and solute interaction energetics led to unacceptable results, shown for Al-Mg in Appendix B, motivating the development of more complex LAE representations, and thus more complex learning models.

I therefore use a feed-forward neural network to map the LAE representation to the solute-solute interaction parameters. This neural network was constructed using the Keras Python library [133], with a TensorFlow backend [134], and is depicted in Figure 6.3. The tapered architecture was chosen for its consistent performance across many machine learning tasks [135], and the overall number of nodes, ReLU activations, and number of layers were selected to optimize the performance of the model across the many alloys I use for validation in Section 6.6. The model was then trained for 80 epochs using a mean-squared-error loss function and an Adam optimizer with a learning rate of 0.001, and the parameters ε, β_1, and β_2 set to 0.9, 0.999, and 10^{-7}, respectively. When testing the model, the measured solute-solute interaction spectra for each alloy are randomly split into a 50/50 test-train split, for training and validation, respectively.

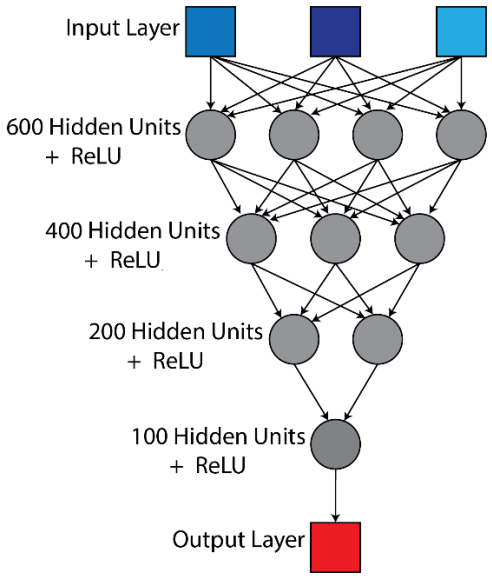

Figure 6.3. Feed-forward neural network architecture used in this work, connecting input bond-focused LAEs to the pair-wise solute interactions, $\omega_{gb,i-j}$.

6.5. Accelerated Predictions – Automatic Selection of Training Data

Using a 50/50 test/train split to train a high-fidelity model results in several hundred thousand individual calculations required before training can even begin. To reduce this cost and efficiently select a smaller training set, I follow the process depicted schematically in Figure 6.4. To begin, I map every atomic bond involving GB atoms (i.e., every nearest neighbor GB pair) into its corresponding SOAP vector, to produce a matrix which describes the feature space. I then use principal component analysis (PCA) [136] to reduce the dimensionality of the feature space, choosing here a 10-dimensional representation, which captures > 98% of the explained variance (EV), as shown in Figure 6.4(b). This approach matches the 10-dimensionial representation used by Wagih and Schuh to predict dilute limit segregation energies [83]. Next, I automatically select a representative set of nearest neighbor pairs to use as training data by clustering the reduced feature space with K-Means clustering [137]. Here, I choose to use the non-reduced feature space during training, to preserve as much information about the LAE as possible. This results in the need for a larger number of training data points on the order of 10 times the size of the input features. For this reason, I choose to use 7,000 cluster centers.

The process of constructing and selecting training data in the manner described here, as well as the training and prediction itself, is minimal compared to the cost of rigorous computation of the many energies involved, as in Chapter 3 [69]. This results in roughly an order of magnitude decrease in computational time required to predict a solute-solute interaction spectrum.

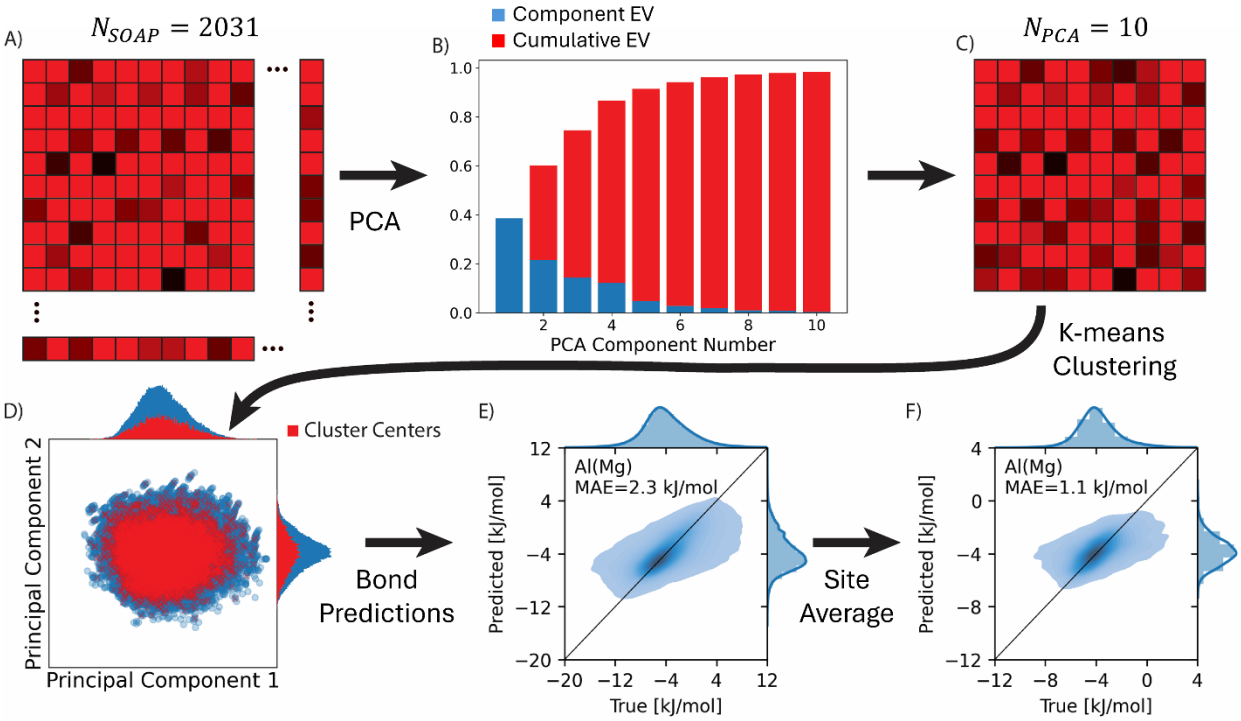

Figure 6.4. Schematic depiction of automatic training set selection. (a) Non-dilute SOAP matrix. (b) Explained variance for the first 10 components of the PCA-reduced feature space. (c) PCA-reduced feature space. (d) K-means clustering projected into the first two PCA components; cluster centers in the histograms are shown at 10x scale for clarity. (e) Pair-wise predictions of $\omega_{gb,i-j}$ *for the high-fidelity model on Al-Mg* [127]. *(f) The corresponding site-wise predictions of* $\omega_{gb,i}$.

Once the training data are chosen, they are then fed into the neural network, using the same training procedure as above, and the resulting predictions produce a pair-wise construction of the solute-solute interaction spectra, as shown in Figure 6.4(e). These pair-wise parameters can then be averaged on a site-wise basis, as in Chapter 3 [69], to produce the comparable site-wise

interaction parameters that can be used as an input for spectral thermodynamic models. Similarly, 100 training points specifically selected to learn $\Delta E_i^{seg,dil}$ are fed into a linear regression model following Wagih and Schuh [83] to reproduce the corresponding dilute limit segregation spectra.

6.6. Model Validation

To validate the performance of the model, both in its high-fidelity and accelerated forms, I begin by considering the (10x10x10) nm^3 polycrystal of Ag-Cu [128] produced in Section 6.2 above. The full solute-solute interaction spectra and dilute limit segregation energy spectra were measured exhaustively on a site-wise basis, and these spectra are shown in the first bi-variate plots in Figure 6.5(a). The same polycrystal was then used to construct bond-focused SOAP feature matrices for the GB nearest neighbor pairs and execute the learning algorithms described above. Both the high-fidelity (50/50 train/test split) and accelerated (7,000 bond) versions were then used to train the neural network model, and the resulting predicted solute-solute interaction spectra are shown on the y-axis of the parity plots in Figure 6.5(b).

To interpret the difference between the calculated and predicted spectra, I choose here to use a test case which compares the site-wise solute occupation predictions of each spectrum, under conditions of finite concentration (5 at%) and temperature (600 K). This can be done using the bivariate form of the spectral isotherm defined by Equations (3.5). These predictions are shown relative to the rigorously measured version in Figure 6.6, and the corresponding dilute limit isotherm and scalar interaction isotherm are shown for comparison.

As can be seen in the parity plots shown in Figure 6.5(b), both the high fidelity and accelerated versions of the model provide qualitatively good agreement with the solute interaction spectrum for Ag-Cu. Both models appear to accurately capture the shape and mean of the pair-wise interaction spectra, including the multi-peak behavior present in Ag-Cu. These multiple peaks are distinct from the consistently skew-normal distributions seen in the site-wise spectra, which indicates the ability of this model to correctly capture that increased complexity. Upon averaging to a site-wise value the predicted mean remains accurate, and the multi-peak distribution

correctly collapses to the expected skew-normal behavior. Once these spectra are used to evaluate site occupation in realistic conditions, the learning models produce an output that is essentially identical to the exhaustive computation, as seen in Figure 6.6.

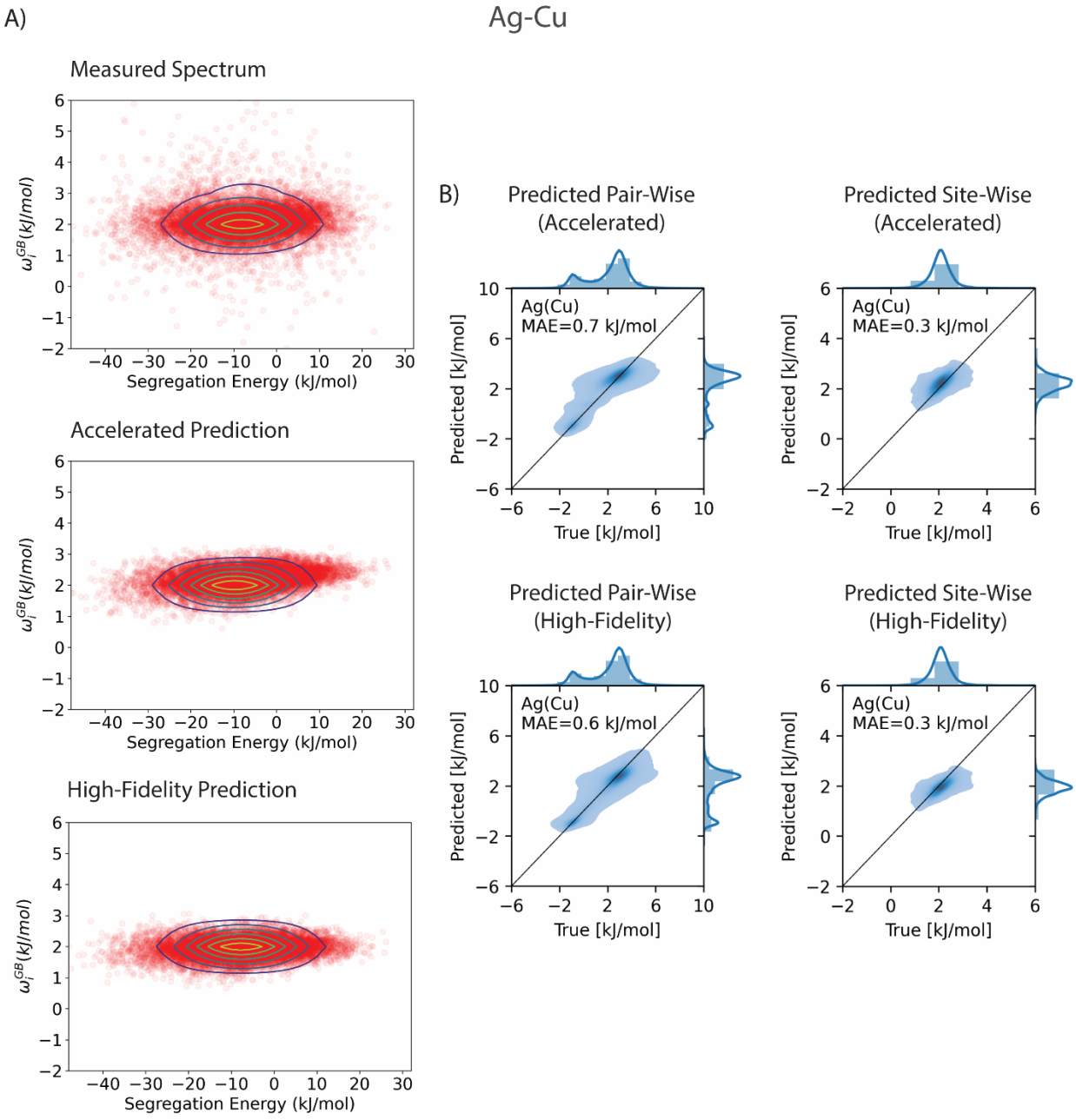

Figure 6.5. Model predictions for Ag-Cu [128]. *(a) Bivariate spectrum – measured spectrum (top), high-fidelity predicted spectrum (middle), and accelerated predicted spectrum (bottom),*

with fitted bivariate normal distributions superimposed. (b) Parity plots – accelerated pair-wise predictions (upper left), accelerated site-wise predictions (upper right), high-fidelity pair-wise predictions (bottom left), high-fidelity site-wise predictions (bottom right).

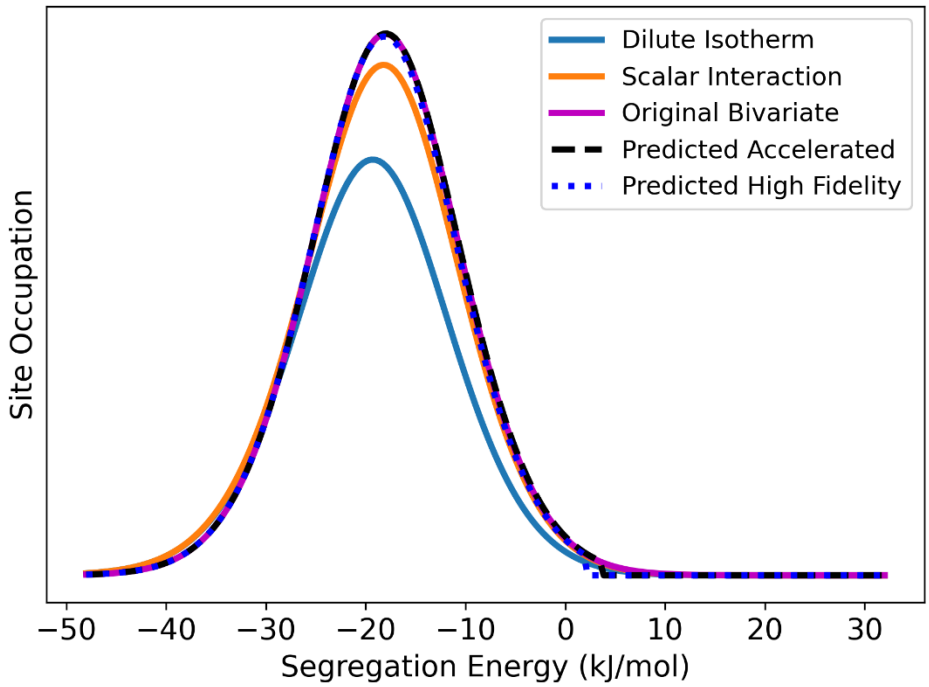

Figure 6.6. Occupation prediction plot for each model (high-fidelity in dotted blue and accelerated in dashed black), the dilute limit isotherm (light blue), an isotherm with scalar interactions(orange), and an isotherm with the measured bivariate interactions at 600 K and 5 percent total solute (pink).

Repeating the above process for the remaining polycrystals of Al-Mg [127], Nb-Ni [129], Ni-Pt [130], and Pt-Au [131] results in the predictions shown in Appendix C. These tests demonstrate that this model continues to provide qualitatively strong agreement across multiple alloys with different crystal structures and energetics. The accelerated model generally captures the correct mean and shape of the distribution, with the primary difference being the occasional narrowing of the average site-wise predictions, relative to the exhaustively calculated spectra. Despite this difference, the accelerated occupation distributions continue to provide good agreement with the

full computation, and the high fidelity and accelerated models consistently agree with one another.

Importantly, all these systems require the spectral interaction parameters to capture the true segregation response, even at relatively low total solute concentrations of 5 at%. This is because even in the global "dilute limit", segregation amplifies concentrations locally at the GBs to the point where interactions cannot be ignored. Each system correctly predicts the increase or decrease in occupation relative to that which would be expected in the dilute limit, depending on the sign of the interaction parameter. Furthermore, the effect due to the correlation between segregation energy, combined with the spread in interaction energies, requires a full spectral representation to capture correctly; some systems, such as Nb-Ni, even incorrectly exhibit little to no interaction effect when using a scalar interaction model. This is consistent with my prior observations of Al-Mg [69], and indicates that an approach such as this, which learns the full spectrum of interaction energies, is necessary to correctly capture GB energetics.

6.7. A Full Tri-Variate Database of Spectral Segregation Parameters

Having validated the accelerated method developed above, I now construct a database of spectral solute-solute interaction parameters for grain boundary segregation in binary alloys. Additionally, I reproduce the dilute limit segregation spectra using the accelerated method by Wagih and Schuh [83] and measure the excess GB energy spectra for the pure solvents via Equation (6.1). I choose here to construct this database from the available EAM potentials on the NIST Potential Repository [112,113]. To limit computational cost, I choose here to only use EAM potentials for which GPU acceleration [138–142] is available; however, this procedure can apply to any available interatomic potential.

To perform these predictions, I use (13 x 13 x 13) nm^3 polycrystals constructed using the same procedure as above, resulting in average grain sizes of 8-9 nm and a number of atoms between 120,000 and 200,000. While the 10x10x10 nm^3 polycrystals produced above are known to be sufficiently large for training purposes [69], for this step I choose to use a slightly larger polycrystal to improve the resolution of the spectra predictions available in the subsequent

database. From these polycrystals, I then detect the grain boundary sites and nearest neighbors using the method in Section 6.2, predict the site-wise solute interaction parameters using the accelerated method from Sections 6.3-6.5, predict the dilute limit segregation energies using the procedure by Wagih and Schuh [83], and measure the solvent GB excess energy spectra using Equation (6.1). The bulk interaction parameters are then calculated using the same process as Equations (2.7), (3.2), and (3.3) in a bulk crystalline supercell. An example of the solute interaction predictions, taken from Appendix D, are shown for a solvent base of Al in Figure 6.7.

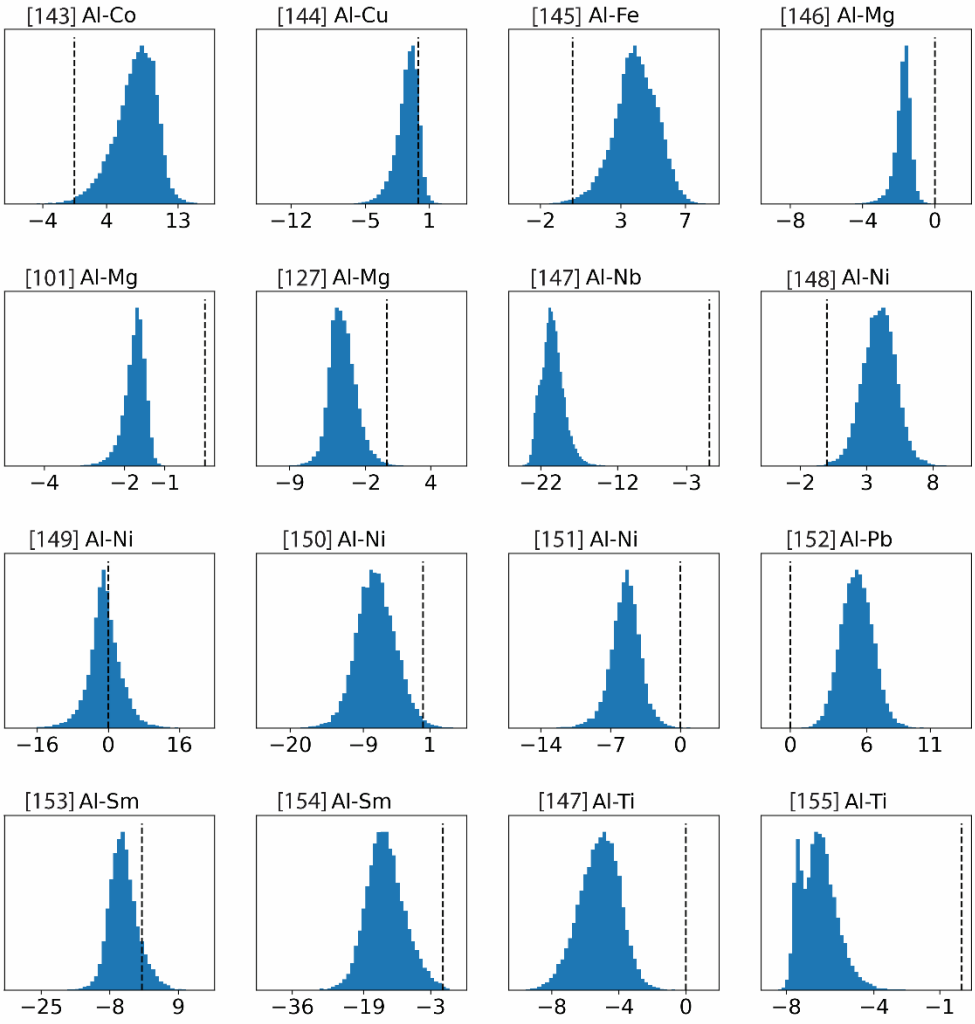

Figure 6.7. Solute interaction spectra, $\omega_{gb,i}$, in kJ/mol, for Al-based solutes, predicted using the accelerated model developed in sections 4-6. The dotted line indicates where $\omega_{gb,i}$ = 0 kJ/mol.

The results in Figure 6.7 and Appendix D are, in principle, complete and rigorous to within the accuracy of the potentials used to produce them. Used in conjunction with Equation (3.5) or (4.18), they provide accurate predictions of grain boundary segregation even down to the level of site occupancy and neighbor clustering. For ease of use, all the predicted spectra are available in a tri-variate database alongside their corresponding bulk interaction parameters; the spectra are shown in a tabulated form in Appendix D, and the complete site-wise data are available for fitting in the Supplemental Data of the corresponding publication [86]. Additionally, I have provided skew-normal parameters for each univariate distribution fitted to Equation (2.10). However, as seen in some alloys in Figure 6.7 and Appendix D, a skew-normal fit is not always appropriate. Furthermore, Equation (2.10) cannot capture the covariances between the spectra unless adjusted to higher dimensions, such as in the bivariate spectra shown in Figure 6.5. For this reason, I recommend use of the univariate distributions only for initial screening purposes and suggest that the site-wise spectra provided in the Supplemental Data [86] be used as the primary input for predictions.

I urge caution when undertaking segregation predictions; as always, energetics of atomic interactions are highly sensitive to the fitting of the corresponding interatomic potential. Particularly in the case of solute-solute interactions, interatomic potentials not explicitly fitted for disordered environments can produce non-physical results, demonstrating both predicted and measured interactions that are of a magnitude or sign that are not physically reasonable relative to the expected or observed behavior. In Appendix D and the Supplementary Data [86], I have marked examples of spectra derived from potentials that are fitted to more robust sets of complex atomic environments. These are relatively few at present, underscoring the note of caution above. Additionally, I have noted any potentials which present predictions that are of relative concern, including interactions which deviate, on average, more than 50% from the corresponding bulk interactions, those which have a different sign than the corresponding bulk interactions, those with a magnitude of greater than 10 kJ/mol, or potentials which produce negative values for the grain boundary excess energy of the solvent.

Moving forward, newly developed potentials can be easily incorporated into the present workflow to produce trustworthy grain boundary segregation spectra. Additionally, the prospect

of quantum-accurate approaches to this problem are foreshadowed by the work of Wagih and Schuh for the case of dilute-limit segregation energies [84], which may be adapted to address solute interactions in future work. The “bond-focused” LAE representation and learning algorithm presented here has opened the door to such possibilities, and has provided what is, to my knowledge, the first database of fully spectral parameters describing grain boundaries for binary alloys beyond the dilute limit, making spectral-accurate predictions of grain boundary segregation, and therefore the production of nanocrystalline phase-and-defect diagrams at finite concentrations broadly accessible for the first time.

Conclusion

Recent progress in defect engineering has focused on the incorporation of “defect states” into what I have termed here “phase-and-defect diagrams.” These diagrams seek to analyze systems containing defects with similar methodology as bulk thermodynamic phases, thus allowing for a direct comparison and mapping of the two onto a single diagram, comparable to a bulk equilibrium phase diagram [1,52–58]. These diagrams constitute a significant step forward in our ability to understand and engineer stable defect states. While significant progress has been made in this area in the case of solute segregation to relatively simple defects, such as dislocations or simple, highly symmetric brain boundaries [1,53–58], this problem has only been addressed for polycrystalline grain boundary segregation using homogenous, scalar representations of the GB energetics [52]. While spectral representations for grain boundary segregation have recently been shown to offer significant improvements, spectral representations developed prior to this work rely on thermodynamic isotherms, which cannot be used to construct phase-and-defect diagrams, and which have limited, often non-spectral options for extension beyond the dilute limit [82]. Furthermore, only dilute-limit spectral data is currently accessible to the broader community [68,83], severely restricting the usage of spectral models in predicting stable defect states, thus prevent the production of accurate nanocrystalline phase-and-defect diagrams.

To fulfill these needs, I have accomplished the following in this thesis:

1) In Chapter 3, I have explored the natural extension of the spectral model for GB segregation by assessing a comparable distribution of solute-solute interaction energies. The method presented here has provided what is, to my knowledge, the first measurement of the full spectrum of solute-solute interaction energies at the GB. The spectrum of interaction energies follows a roughly skew-normal distribution for the Al-Mg system analyzed here, and when combined with the existing segregation energy distribution constitutes a full bivariate (skew-)normal distribution that describes the GB beyond the dilute limit.

   A full bivariate normal distribution of site and interaction energies provides an excellent prediction of the solute distribution at equilibrium, as validated against rigorous hybrid Monte Carlo/ Molecular statics simulations, both on average and over the full spectrum of GB sites. Importantly, though, in the present case the interactions can be approximated by a scalar average over their full distribution and still achieve reasonable accuracy for many practical problems. This compromise is one that has the benefit of being fully atomistically informed, but less computationally intensive. This work thus paves the way to use simple, inexpensive atomistic measurement to predict solute interaction behavior during grain boundary segregation, and allows for the development of a spectral free energy model with which a spectral phase-and-defect diagram can be produced.

2) In Chapters 4 and 5, I have presented what is, to my knowledge, the first analytical model for spectral grain boundary segregation, and the first fully spectral free energy representation for the segregated polycrystalline defect state. With this spectral regular solution model, I have constructed a phase-and-defect diagram for a hypothetical system, from which I note two key points. First, the bulk two-phase behavior predicted via bulk thermodynamics has been replaced by a stable grain size that increases with temperature and decreases with solute concentration. And second, this model predicts a significant deviation from its scalar counterpart when attempting to fit an appropriate scalar segregation energy, reinforcing the need for spectral information of the polycrystalline state. The proposed model, while limited in its assumptions, provides the first framework for the production of spectral phase-and-defect diagrams, constituting a massive

improvement in our ability to engineer these defect states and access information about a broad range of alloys and properties that were previously unexplored.

3) In Chapter 6, I have presented a modified "bond-focused" LAE representation to accurately capture the pair-wise nature of grain boundary solute interactions. I then also presented a learning algorithm which takes this LAE as an input to learn the solute interaction spectra. This method is roughly an order of magnitude faster than exhaustive computation [69], enabling rapid solute interaction predictions and making solute interaction spectra accessible to quantum-accurate predictions in the future.

   And finally, I have used this "bond-focused" LAE representation and learning algorithm to produce what is, to my knowledge, the first large-scale database of spectral grain boundary parameters beyond the dilute limit, encompassing binary alloys from nearly 200 EAM potentials available on the NIST repository [112,113]. This enables broader accessibility to spectral-accurate predictions of stable segregated polycrystalline states, and thus to the production of nanocrystalline phase-and-defect diagrams.

With the completion of this thesis, I hope that the models, methods, and data presented here allow for improved access to spectral modeling of stable segregation states, enabling the production of nanocrystalline phase-and-defect diagrams and their broader adoption into existing CALPHAD methodology. In doing so, my hope is that we can achieve significant improvement in our understanding and engineering of defect states, and in our prediction and development of stable nanocrystalline alloys.

Future Outlook

The above models, methods, and data constitute a massive step forward in our understanding and ability to model spectral defect states. However, most of the work presented in this thesis suffer from limiting assumptions that, while appropriate for the steps being taken at the time of writing, will need to be stripped away and improved upon as spectral models and their corresponding phase-and-defect diagrams continue to improve. The sheer quantity of open questions in this area is staggering, and below I list but a few which I have personally spent time contemplating.

1. Quantum-Accurate Modeling of Solute Interaction Spectra

While the database of non-dilute spectral GB parameters produced in Chapter 6 is the first of its kind, it is constructed from existing interatomic potentials that are highly sensitive to the atomic configurations and material parameters with which they were fit. As noted in Chapter 6, this results in a large portion of these potentials being inappropriate for modeling polycrystalline grain boundary segregation in some or all of the required concentration range. For this reason, an ab-initio approach to measuring solute interaction spectra will be a necessary step forward.

Wagih and Schuh [84] have recently adopted a hybrid quantum mechanical-molecular mechanical (QM-MM) [156–158] approach to calculating dilute limit segregation spectra using ab-initio calculations in a “core” region around each grain boundary site and a pure-solvent interatomic potential in the remainder of the system, performing force and energy pairing through a buffer layer between the two. Even with the accelerated learning algorithm developed in Chapter 6, performing a comparable set of QM-MM calculations for the required number of nearest-neighbor pairs would prove prohibitively expensive. For this reason, further development of either the QM-MM method proposed by Wagih and Schuh, or the learning algorithm proposed here will be necessary to achieve quantum-accurate solute interaction spectra.

2. Nanocrystalline Phase-and-Defect Diagrams and CALPHAD

The phase-and-defect diagram produced in Chapter 5 is limited in the composition range and number of phases and defect states it considers. In the model proposed above, only the A-(solvent) rich polycrystalline defect state, defined by my spectral nanocrystalline regular solution model, and the A-rich bulk regular solution are considered. As such, only the A-rich side of the phase-and-defect diagram is shown. In reality, there could be any number of potential defect states, including a variety of grain boundary complexions, dislocations, etc., alongside all of the bulk ordered and solution phases spanning the entire composition range. To reliably produce a phase-and-defect diagram which contains as much of this information as possible will require the adoption of a CALPHAD [159,160] approach which incorporates as many available free energy functions as possible, including both the bulk phases and defect states. Additionally, this information will be most useful when it is derived from thermodynamically consistent sources, which will require the use of a single interatomic potential or self-consistent ab-initio calculations, both of which come with the complications discussed above. Despite this difficulty, a phase-and-defect diagram with such complete information would prove an invaluable asset to the defect engineering community.

3. Non-Ideal Configurational Entropy in the Spectral Model

Figure 1.1 shows many of the components that could be used to construct a spectral free energy function, as done in Chapter 4. Here, I have only considered the enthalpic components and the ideal configurational entropy. While the dilute limit vibrational entropy has been addressed [68] and could be easily incorporated in future works, the non-ideal configurational entropy has yet to be considered. In bulk equilibrium phases, this non-ideal behavior can be captured by analytical models (i.e. the quasi-chemical model [111]); however, it is often ignored or handled via fitted polynomials and activity coefficients [159,160]. In the case of spectral grain boundary segregation, non-ideality becomes even more significant due to the physical distribution of sites throughout the grain boundary network, and how that distribution overlaps with the spectral energetics, resulting in complex configurations of solutes which I have observed in some of my simulations with particularly strong (often attractive) solute interactions.

4. Final Thoughts

The above suggestions are only some of the possible improvements that could be made following this work, and those which I have considered personally. Other possibilities include the development of ternary and multinary spectral models, solute interactions for interstitial segregation [161], solute segregation in ordered compounds, and the translation of the thermodynamics and driving forces developed here to corresponding kinetic models. It is my hope that this work will serve as a starting point for many such developments in the future.

Appendix A – The Scalar NCRS Model

In this section I derive the scalar analog of the spectral nanocrystalline regular solution model developed in Chapter 4. This derivation is equivalent to that of Trelewicz and Schuh [41] and follows the same procedure used in the spectral derivation, assuming scalar rather than spectral bond energies for the grain boundary and transitional regions.

A1. Scalar Solution Model

Following the same procedure as shown in Chapter 4, the number of bonds and corresponding bond energies in each region are shown in Table A1. The scalar total solution energy, U_{soln}, is then given as the summation over each region, denoted by s, as:

$$U_{soln} = \sum_{s} \left[N_b^s E_b^s + N_{gb}^s E_{gb}^s + N_t^s E_t^s \right]. \qquad (A1)$$

Table A1. Bond types in each region of the scalar NCRS model – bulk (grain interior), grain boundary, and transition – along with the corresponding notation for the number of bonds and bond energies of each type.

Bond Type	**Number of Bonds**	**Bond Energies**
Bulk	$\boldsymbol{N_b^{AA}}$	$\boldsymbol{E_b^{AA}}$
	$\boldsymbol{N_b^{AB}}$	$\boldsymbol{E_b^{AB}}$
	$\boldsymbol{N_b^{BB}}$	$\boldsymbol{E_b^{BB}}$
GB-GB (Site Type i)	$\boldsymbol{N_{gb}^{AA}}$	$\boldsymbol{E_{gb}^{AA}}$
	$\boldsymbol{N_{gb}^{AB}}$	$\boldsymbol{E_{gb}^{AB}}$
	$\boldsymbol{N_{gb}^{BB}}$	$\boldsymbol{E_{gb}^{BB}}$
Transition (Site Type i)	$\boldsymbol{N_t^{AA}}$	$\boldsymbol{E_{gb}^{AA}}$
	$\boldsymbol{N_t^{AB}}$	$\boldsymbol{E_{gb}^{AB}}$
	$\boldsymbol{N_t^{BB}}$	$\boldsymbol{E_{gb}^{BB}}$

Here, N and E represent the bond numbers and energies, and b, gb, and t denote the bulk, grain boundary, and transitional bonds, respectively, and there is no longer a summation over spectral terms. The mixing energy, ΔU_{mix}, is still defined with respect to the unmixed, interface-free α phase of the same composition:

$$\Delta U_{mix} = U_{soln} - U_{ref} \tag{A2}$$

where the reference state, U_{ref}, is the same as in the spectral derivation:

$$U_{ref} = \frac{zN^A}{2} E_b^{AA} + \frac{zN^B}{2} E_b^{BB}. \tag{A3}$$

Here, N^A and N^B are the total number of A and B atoms, respectively, and z is the coordination number of the α phase. The coordination number and total number of A and B atoms are related to the number of scalar bonds given in Table A1 via:

$$zN^A = 2N_b^{AA} + N_b^{AB} + 2N_{gb}^{AA} + 2N_t^{AA} + N_{gb}^{AB} + N_t^{AB} \quad (A4)$$

$$zN^B = 2N_b^{BB} + N_b^{AB} + 2N_{gb}^{BB} + 2N_t^{BB} + N_{gb}^{AB} + N_t^{AB}. \quad (A5)$$

Combining these relationships with Equations (A1) – (A3), the scalar change in internal energy upon mixing becomes:

$$\begin{aligned}\Delta U_{mix} = \quad & N_b^{AB}\left(E_b^{AB} - \frac{E_b^{AA} + E_b^{BB}}{2}\right) + \left(N_{t,i}^{AA} + N_{gb,i}^{AA}\right)\left(E_{gb,i}^{AA} - E_b^{AA}\right) \\ & + \left(N_{t,i}^{BB} + N_{gb,i}^{BB}\right)\left(E_{gb,i}^{BB} - E_b^{BB}\right) + \left(N_{t,i}^{AB} + N_{gb,i}^{AB}\right)\left(E_{gb,i}^{AB} - \frac{E_b^{AA} + E_b^{BB}}{2}\right)\end{aligned} \quad (A6)$$

which is functionally identical to Equation (4.8), without the summation over spectral terms.

A2. Scalar Bond Distributions

The number of bulk, transition, and grain boundary bonds, P_r, where r is the region, are given as:

$$P_b = \left(\frac{z}{2}\left(1 - f_{gb}\right) - \frac{zv}{2} f_{gb}\right) N \quad (A7)$$

$$P_{gb} = \left(\frac{z}{2} f_{gb} - \frac{zv}{2} f_{gb}\right) N \quad (A8)$$

$$P_t = \left(\frac{zv}{2} f_{gb}\right) N \quad (A9)$$

where N is the total number of atoms, f_{gb} is the grain boundary volume fraction, z is the coordination number, and v is the geometric parameter that described the fraction of bonds attached to GB atoms which are transitional bonds. These are the same values of P_r from Equations (4.9)-(4.11); however, they do not need to be weighted by a spectral site probability for this scalar derivation.

Table A2. Bond types in each region of the scalar NCRS model – bulk (grain interior), grain boundary, and transition. Additionally, the corresponding notation for the number of bonds and bond energies of each type, the concentration-dependent probabilities assigned of each bond type, and the total number of bonds in each region.

Bond Type	**Number of Bonds**	**Bond Energies**	**Probabilities**	**Bonds in Region**
Bulk	$\boldsymbol{N_b^{AB}}$	$\boldsymbol{E_b^{AB}}$	$\boldsymbol{2X_b(1-X_b)}$	$\boldsymbol{P_b}$
GB-GB	$\boldsymbol{N_{gb}^{AA}}$	$\boldsymbol{E_{gb}^{AA}}$	$\boldsymbol{(1-\overline{X}_{gb})^2}$	$\boldsymbol{P_{gb}}$
	$\boldsymbol{N_{gb}^{AB}}$	$\boldsymbol{E_{gb}^{AB}}$	$\boldsymbol{2\overline{X}_{gb}(1-\overline{X}_{gb})}$	
	$\boldsymbol{N_{gb}^{BB}}$	$\boldsymbol{E_{gb}^{BB}}$	$\boldsymbol{\overline{X}_{gb}{}^2}$	
Transition	$\boldsymbol{N_t^{AA}}$	$\boldsymbol{E_{gb}^{AA}}$	$\boldsymbol{(1-X_b)(1-\overline{X}_{gb})}$	$\boldsymbol{P_t}$
	$\boldsymbol{N_t^{AB}}$	$\boldsymbol{E_{gb}^{AB}}$	$\boldsymbol{X_b(1-\overline{X}_{gb})+\overline{X}_{gb}(1-X_b)}$	
	$\boldsymbol{N_t^{BB}}$	$\boldsymbol{E_{gb}^{BB}}$	$\boldsymbol{X_b(\overline{X}_{gb})}$	

As above, I model the geometric effect of triple junctions and quadruple nodes by scaling v with the volume fraction of triple junctions and quadruple nodes, f_{tj}, given relative to the total intergranular volume fraction f_{gb} by the Palumbo polynomial [31,107–110]:

$$f_{tj} = f_{gb} - \frac{3t(d-t)^2}{d^3} \tag{A10}$$

and the fraction of grain boundary bonds that are then transitional bonds is given as:

$$v = v_0\left(1 - \frac{f_{tj}}{f_{gb}}\right) \tag{A11}$$

where v_0 is the value of v for a grain boundary with no triple junctions or quadruple nodes, which I approximate as 0.33 as in Chapter 4.

For this scalar derivation, I assume standard random mixing in both the grain boundary and the bulk, resulting in the bond probabilities shown in Table A2. The probabilities and number of bonds in the region are then combined to determine the number of bonds of each type and populate Equation (S6) to determine the total scalar change in internal energy upon mixing.

A3. Scalar Free Energy Functions

The scalar free energy of mixing, ΔG_{mix}, can be constructed from the internal energy of mixing and entropic contribution due to mixing assumptions using the same construction as in Chapter 4. Given the random mixing assumptions here, the entropic contribution, ΔS_{mix}, becomes:

$$\begin{aligned}\Delta S_{mix} = -RN[&\left(1-f_{gb}\right)(X_b \ln(X_b) + (1-X_b)\ln(1-X_b)) \\ &+\left(\bar{X}_{gb}\ln\left(\bar{X}_{gb}\right) + \left(1-\bar{X}_{gb}\right)\ln\left(1-\bar{X}_{gb}\right)\right)].\end{aligned} \tag{A12}$$

Combining Equations (A6) and (A12) with the definition for ΔG_{mix} from Equation (4.16), and normalizing by N results in the molar free energy of mixing for the scalar nanocrystalline state:

$$\Delta G_{mix} = (1-f_{gb})\Delta G^{b}_{mix} + f_{gb}\Delta G^{gb}_{mix} + v f_{gb}\begin{bmatrix}\frac{z}{2}\omega_{gb}\left(X_b - \bar{X}_{gb}\right)\left(2\bar{X}_{gb}-1\right) \\ -z\omega_b X_b(1-X_b) \\ +\frac{1}{2}\frac{V_m}{t}(\gamma_B - \gamma_A)\left(X_b - \bar{X}_{gb}\right)\end{bmatrix}. \tag{A13}$$

Note that this form is functionally the same as that derived in Chapter 4, except all the spectral terms have been replaced by a single scalar value with no need for an integral. Additionally, this form of the free energy of mixing is functionally the same as that derived previously by Trelewicz and Schuh [41].

The bulk mixing energy, ΔG^{b}_{mix}, is the same as derived in Equation (4.19) and is given as:

$$\Delta G_{mix}^{b} = zX_b(1-X_b)\left(E_b^{AB} - \frac{E_b^{AA}+E_b^{BB}}{2}\right) + RT(X_b \ln(X_b) + (1-X_b)\ln(1-X_b)) \quad (A14)$$

with the same bulk regular-solution interaction parameter, ω_b:

$$\omega_b = \left(E_b^{AB} - \frac{E_b^{AA}+E_b^{BB}}{2}\right). \quad (A15)$$

The scalar "amorphous limit", ΔG_{mix}^{gb}, is given as:

$$\begin{aligned}\Delta G_{mix}^{gb} = \; & \frac{z}{2}\{(1-\bar{X}_{gb})(E_{gb}^{AA} - E_b^{AA}) + \bar{X}_{gb}(E_{gb}^{BB} - E_b^{BB}) \\ & + \left(E_{gb}^{AB} - \frac{E_{gb}^{AA}+E_{gb}^{BB}}{2}\right)(\bar{X}_{gb})(1-\bar{X}_{gb})\} \\ & + RT(\bar{X}_{gb}\ln(\bar{X}_{gb}) + (1-\bar{X}_{gb})\ln(1-\bar{X}_{gb}))\end{aligned} \quad (A16)$$

where the scalar GB analogue to the bulk regular-solution parameter, ω_{gb}, emerges as:

$$\omega_{gb} = \left(E_{gb}^{AB} - \frac{E_{gb}^{AA}+E_{gb}^{BB}}{2}\right). \quad (A17)$$

The first two terms of Equation (S16) and are related to the scalar versions of the conventional grain boundary energies of the solvent, γ_A, and of the solute, γ_B, by the relationship:

$$\gamma_A = \frac{z}{2}\frac{t}{V_m}(E_{gb}^{AA} - E_b^{AA}) \quad (A18)$$

$$\gamma_B = \frac{z}{2}\frac{t}{V_m}(E_{gb}^{BB} - E_b^{BB}) \quad (A19)$$

where $\frac{t}{V_m}$ converts the grain boundary excess energy to a molar quantity by normalizing with the thickness of the boundary, t, and the molar volume, V_m.

Combining these definitions with Equation (A16), the scalar free energy contribution due to the grain boundary region is thus:

$$\begin{aligned}\Delta G_{mix}^{gb} = \quad & \frac{z}{2}\{(1-\bar{X}_{gb})\gamma_A + (\bar{X}_{gb})\gamma_B \\ & + \omega_{gb}(\bar{X}_{gb})(1-\bar{X}_{gb})\} \\ & + RT\left(\bar{X}_{gb}\ln(\bar{X}_{gb}) + (1-\bar{X}_{gb})\ln(1-\bar{X}_{gb})\right)\end{aligned} \tag{A16}$$

which is the same as Equation (4.25) after brief rearrangement, when the spectral terms are replaced with their scalar counterparts, and the integral is removed.

A4. Scalar Equilibrium Conditions and the Scalar Isotherm Model

As discussed in Chapter 4, the equilibrium condition of the scalar nanocrystalline state can be readily solved via analytical minimization with respect to both grain size, d (or equivalently, the grain boundary volume fraction, f_{gb}), and the average solute concentration at the grain boundary, $\bar{X}_{gb}$, assuming a closed system with constant total concentration, X_{tot}. Given the numerical framework used to find the equilibrium condition of the spectral model derived above, I neglect the rigorous minimization here, and refer readers to the original derivation by Trelewicz and Schuh for the complete procedure [41]. Here, I minimize only with respect to solute concentration to reveal the scalar isotherm model from which I constructed the spectral counterpart above. This minimization can be constructed by setting the following derivative of Equation (A13) equal to zero:

$$\left.\frac{d\Delta G_{mix}}{d\bar{X}_{gb}}\right|_{f_{gb}} = 0. \tag{A17}$$

From the construction, the relationship between the bulk and grain boundary concentrations is revealed to follow a Fowler-type isotherm:

$$\frac{X_{gb}}{1-X_{gb}} = \frac{X_b}{1-X_b}\exp\left(\frac{-\Delta H^{seg}}{kT}\right) \tag{A18}$$

where the scalar segregation energy, ΔH^{seg}, is given as:

$$\begin{aligned}\Delta H^{seg} = & \left(\frac{vf_{gb}}{1-f_{gb}}-1\right)z\omega_b + \left(1+\frac{v}{2}\left(1+\frac{f_{gb}}{1-f_{gb}}\right)\right)z\omega_{gb} \\ & + \frac{V_m}{t}\left(1-\frac{v}{2}\left(1+\frac{f_{gb}}{1-f_{gb}}\right)\right)(\gamma_B-\gamma_A) \\ & + 2z\left(\left(1-\frac{vf_{gb}}{1-f_{gb}}\right)w_bX_b - \left(1+\frac{v}{2}\left(1+\frac{f_{gb}}{1-f_{gb}}\right)\right)\omega_{gb}\bar{X}_{gb} + \frac{v}{2}\omega_{gb}(X_b-\bar{X}_{gb})\right)\end{aligned} \tag{A19}$$

Appendix B – Solute Interaction Predictions from a "Site-Focused" LAE

The site-wise solute interaction parameter, $\omega_{gb,i}$, predicted following the procedure of Wagih and Schuh using a site-focused LAE [83], is shown in Figure B1. The site-focused LAE, combined with the relatively simple linear-regression type learning model fails to accurately capture the behavior of the solute interaction parameter.

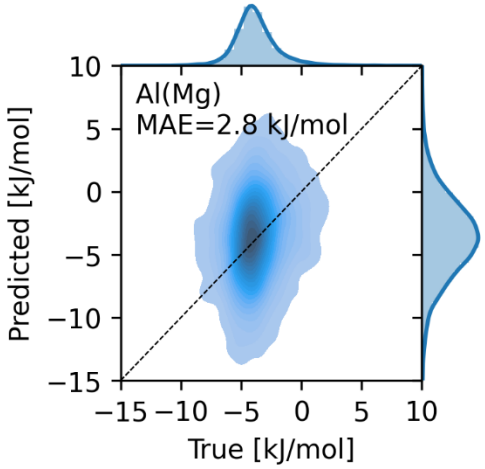

Figure B1. Site-wise solute interaction parameter, $\omega_{gb,i}$, predicted using a site-focused LAE.

Appendix C – Accelerated Model Validation

Table C1. Accelerated Model Validation on Al-Mg, Nb-Ni, Ni-Pt, and Pt-Au, showing the rigorously measured and predicted spectra, parity plots, and occupation predictions from the dilute limit isotherm, scalar interaction isotherm, rigorously measured bivariate isotherm, and the accelerated and high-fidelity learning models.

.

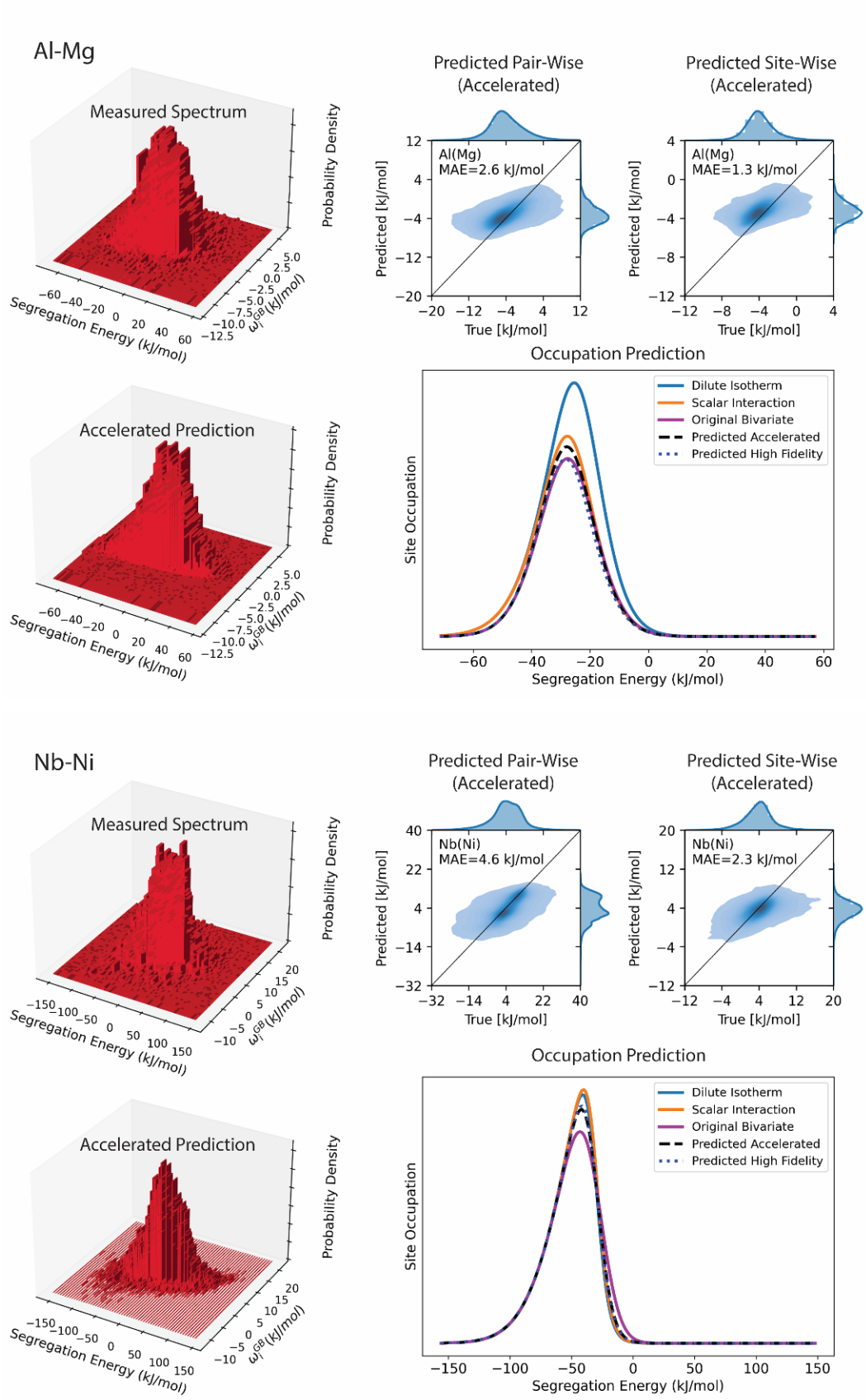
Al-Mg
Measured Spectrum
Probability Density
Segregation Energy (kJ/mol)
Predicted Pair-Wise (Accelerated)
Predicted Site-Wise (Accelerated)
Al(Mg)
MAE=2.6 kJ/mol
Al(Mg)
MAE=1.3 kJ/mol
Predicted [kJ/mol]
True [kJ/mol]
Accelerated Prediction
Occupation Prediction
Dilute Isotherm
Scalar Interaction
Original Bivariate
Predicted Accelerated
Predicted High Fidelity
Site Occupation
Nb-Ni
Nb(Ni)
MAE=4.6 kJ/mol
Nb(Ni)
MAE=2.3 kJ/mol

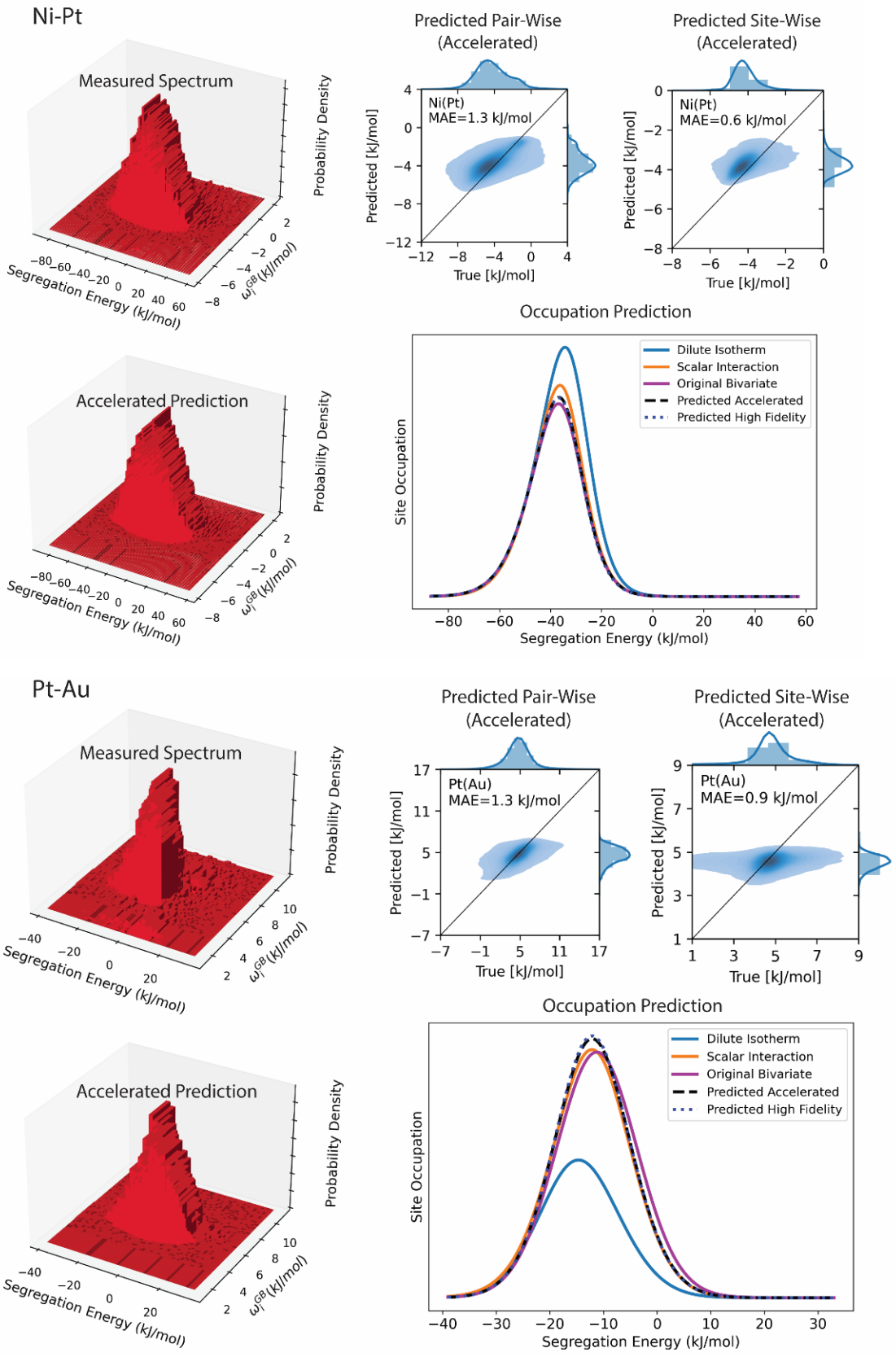
Ni-Pt
Measured Spectrum
Probability Density
Segregation Energy (kJ/mol)
ω_i^{GB}(kJ/mol)
Predicted Pair-Wise (Accelerated)
Predicted Site-Wise (Accelerated)
Ni(Pt)
MAE=1.3 kJ/mol
Ni(Pt)
MAE=0.6 kJ/mol
Predicted [kJ/mol]
True [kJ/mol]
Accelerated Prediction
Occupation Prediction
Dilute Isotherm
Scalar Interaction
Original Bivariate
Predicted Accelerated
Predicted High Fidelity
Site Occupation
Segregation Energy (kJ/mol)
Pt-Au
Measured Spectrum
Predicted Pair-Wise (Accelerated)
Predicted Site-Wise (Accelerated)
Pt(Au)
MAE=1.3 kJ/mol
Pt(Au)
MAE=0.9 kJ/mol
Accelerated Prediction
Occupation Prediction

Appendix D - Full Tri-Variate Database of Spectral Segregation Parameters

In this section, I provide individual spectra, including the solvent excess grain boundary enthalpy, dilute limit segregation energy, and solute interaction energy, for each binary alloy calculated in Chapter 6. Additionally, I provide the bulk interaction parameter. This data includes approximately 200 binary systems with EAM potentials available on the NIST potential repository [112,113]. The following data are depicted as separate single parameter spectra for easy viewing. For the complete tri-variate distribution, please refer to the site-wise values published in the Supplemental Data of the corresponding publication [86]. In the following, I have marked examples of potentials calibrated against more robust atomic environments, including amorphous environments. Additionally, I have marked any potentials which have produced energetics that are of concern when considering their physical reasonability. This includes potentials which predict GB solute interactions which deviate, on average, more than 50% from the bulk interaction, GB interactions which have a different sign than that in the bulk, those with a magnitude of greater than 10 kJ/mol, or those that produce a solvent grain boundary excess enthalpy which is negative on average. For a more viewable list of these criteria, I refer the reader to the tabulated data published in the Supplemental Data [86].

Table D1. Database of spectral GB parameters beyond the dilute limit, constructed for approximately 200 binary systems with EAM potentials from the NIST potential repository [112,113].

☑ Fitted to complex and/or amorphous atomic environments

☒ Produced energetics of concerning physical reasonability

Ag-based Alloys

Ag-Au [130]

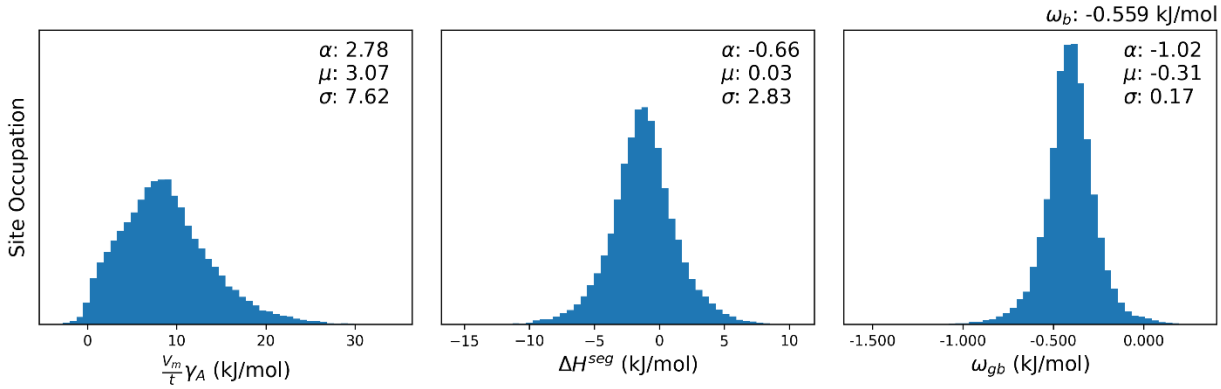

Ag-Au [162]

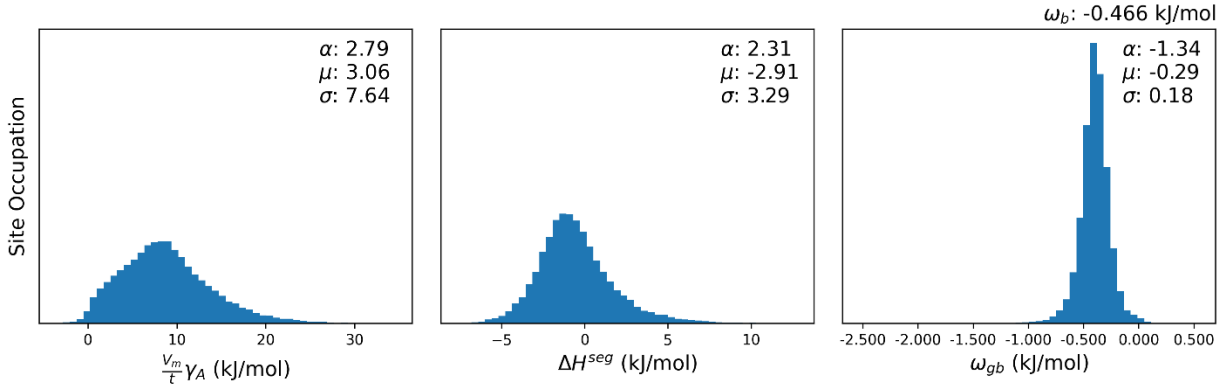

Ag-Au [163]

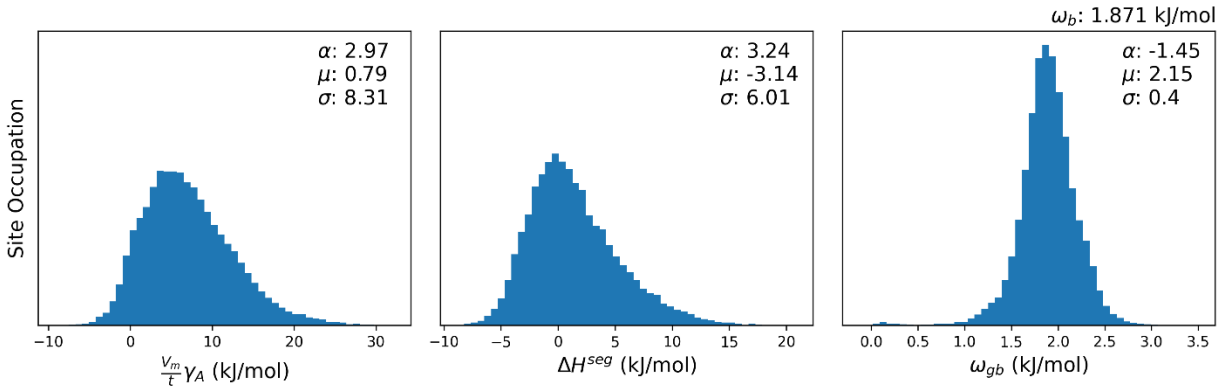

Ag-Cu [130]

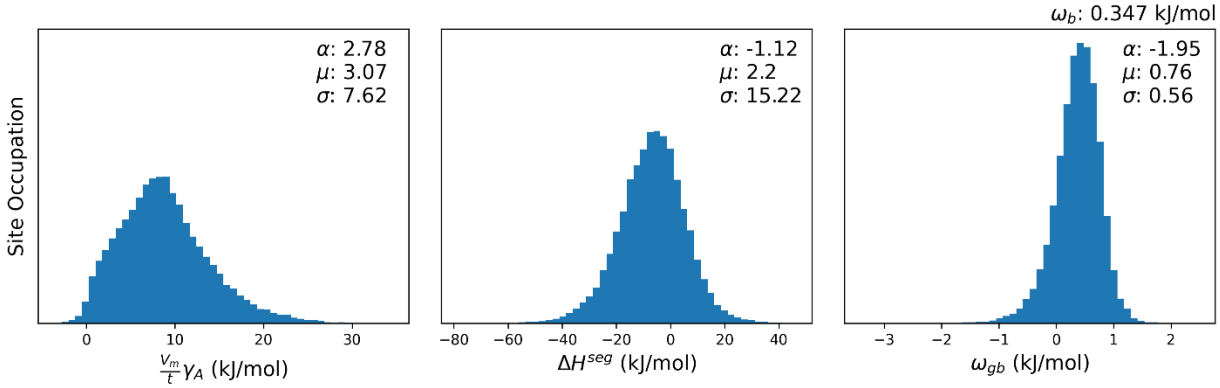

☒ Ag-Cu [162]

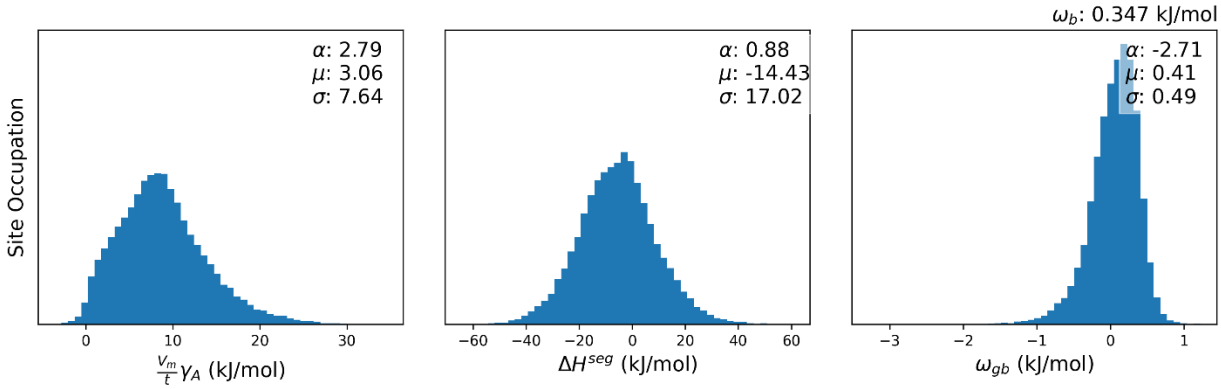

☒ Ag-Cu [163]

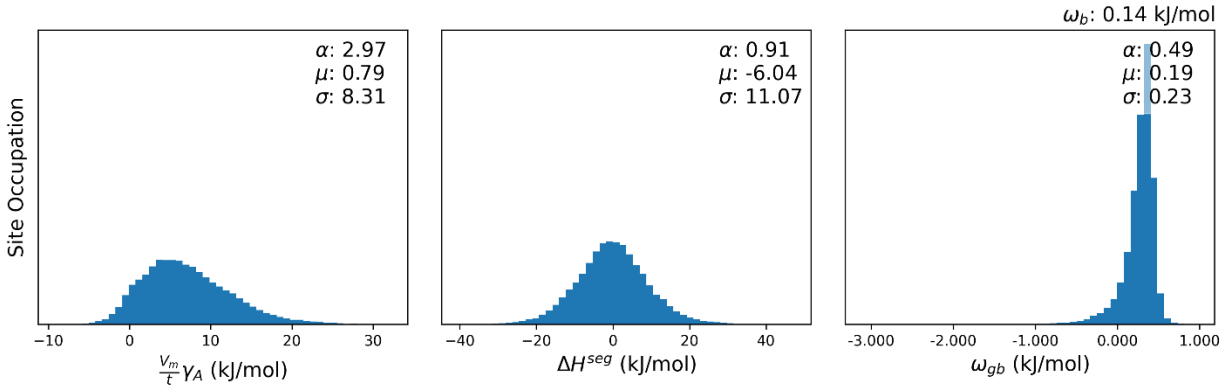

Ag-Cu [164]

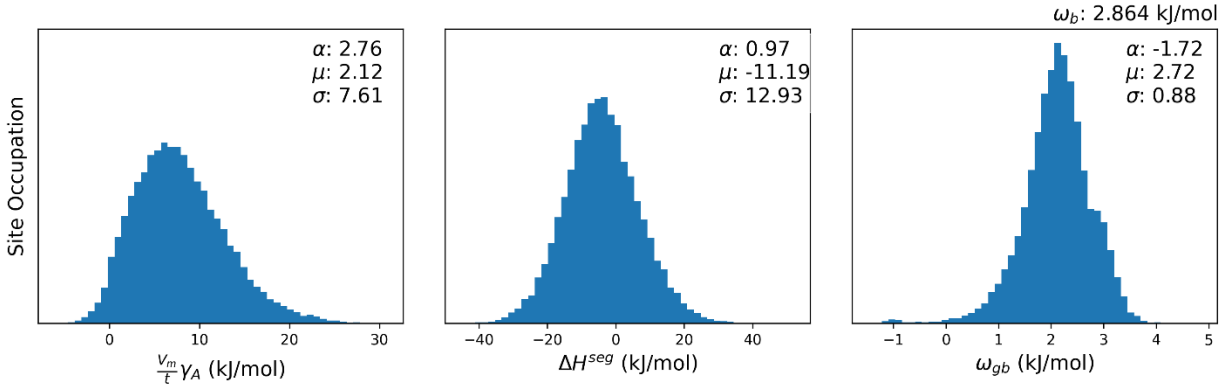

☒ Ag-Cu [128]

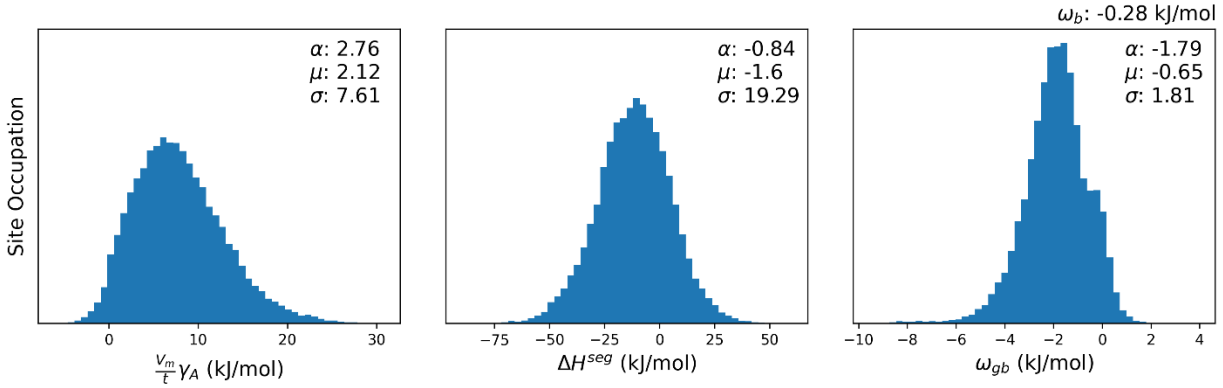

Ag-Ni [130]

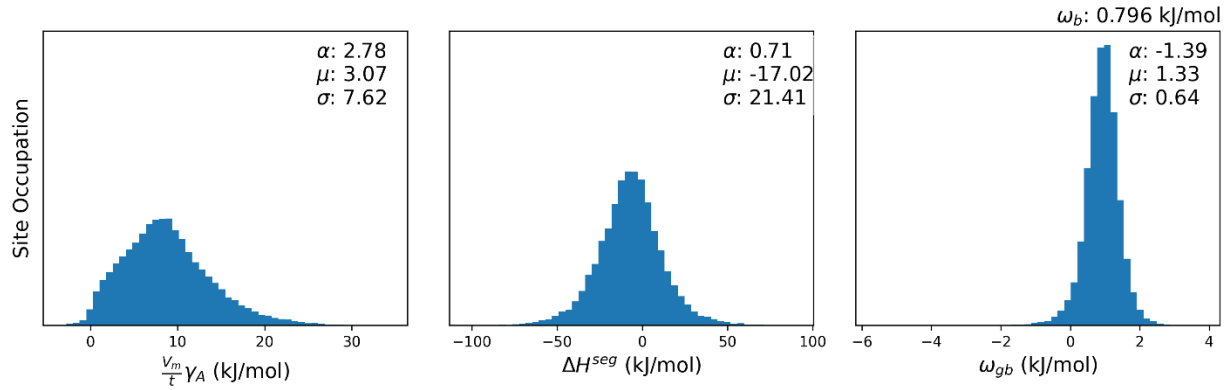

Ag-Ni [162]

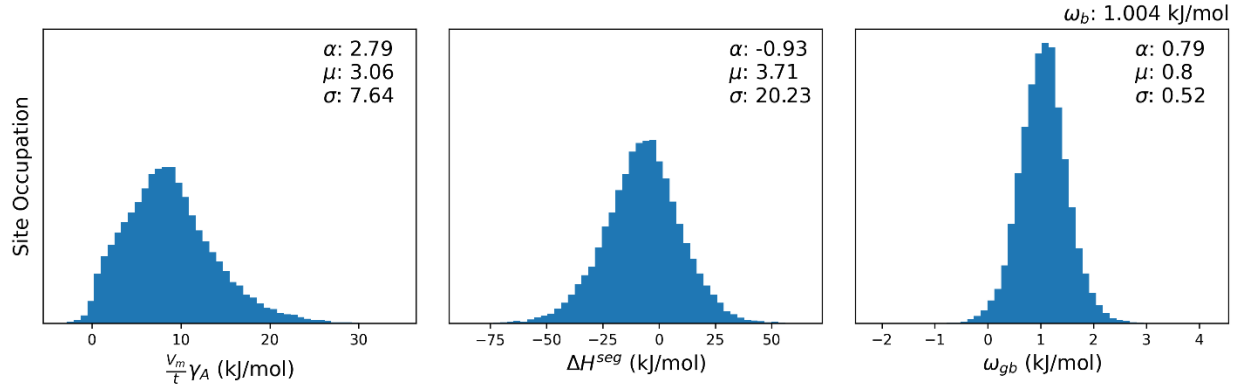

☑ Ag-Ni [165]

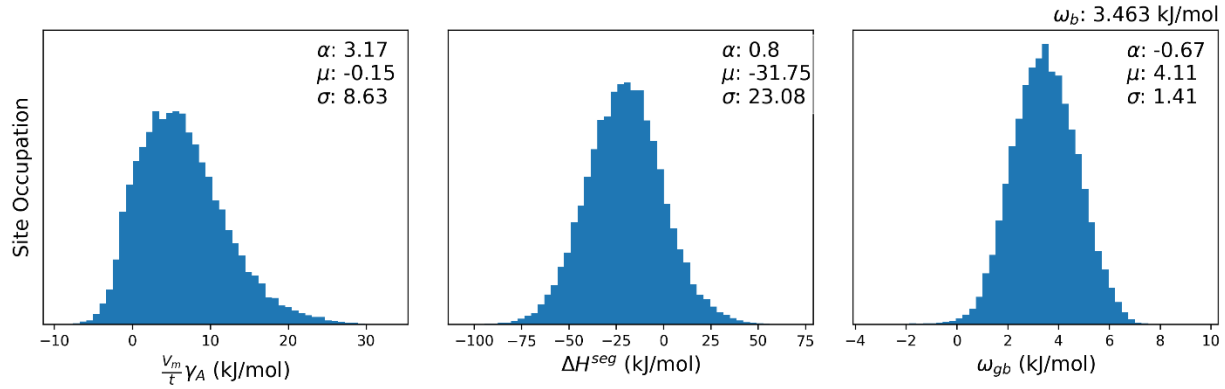

☒ Ag-Pd [130]

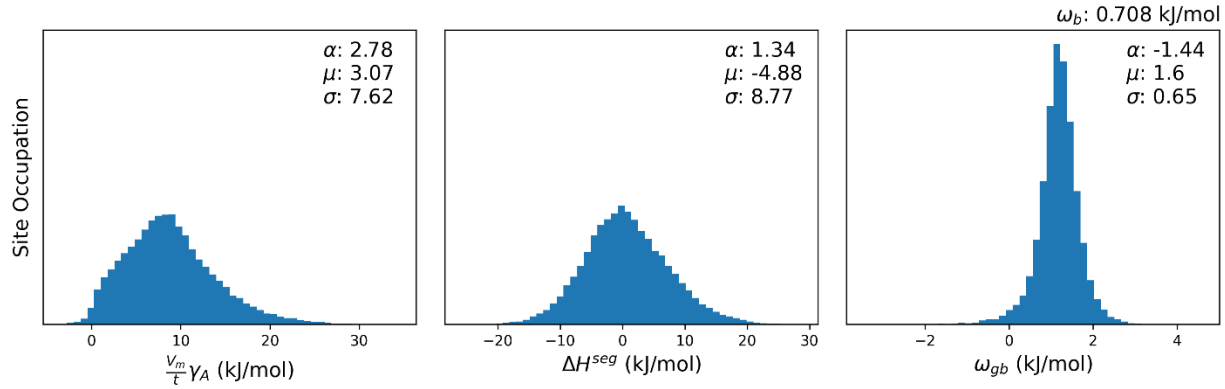

Ag-Pd [162]

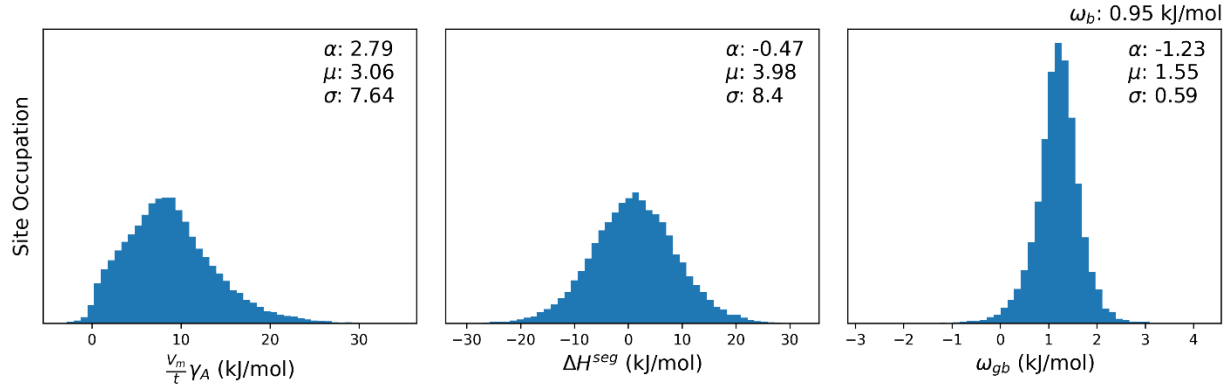

Ag-Pt [130]

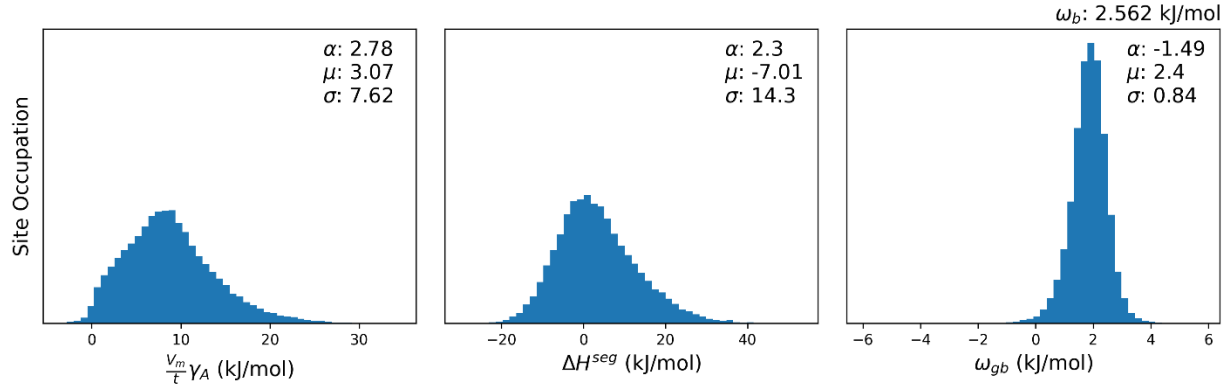

Ag-Pt [162]

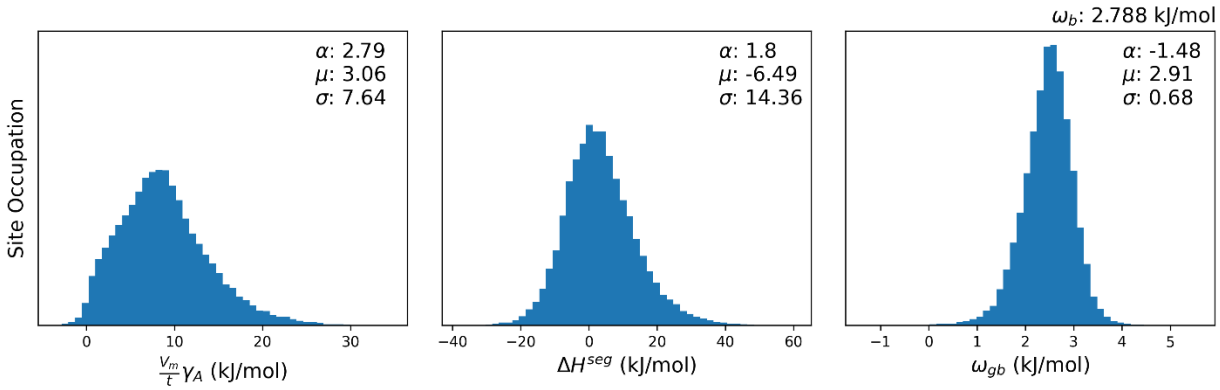

Al-based Alloys

☒ Al-Co [143]

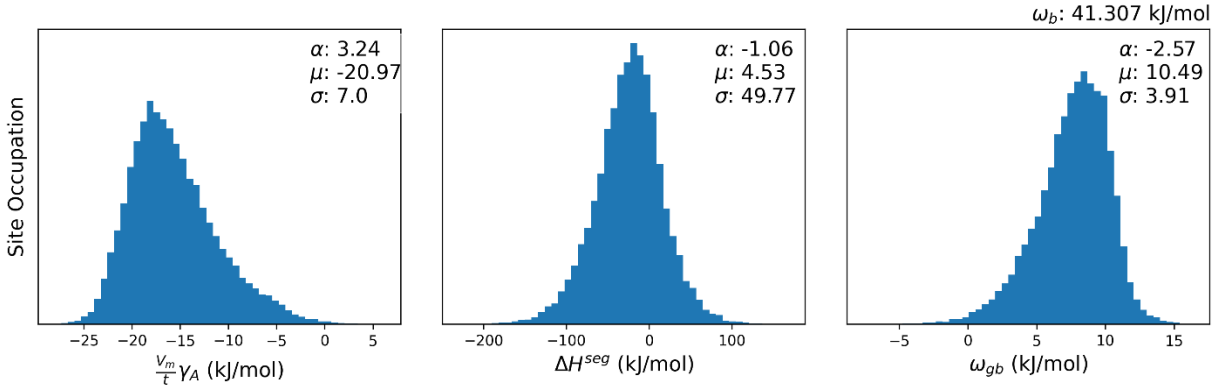

☑☒ Al-Cu [144]

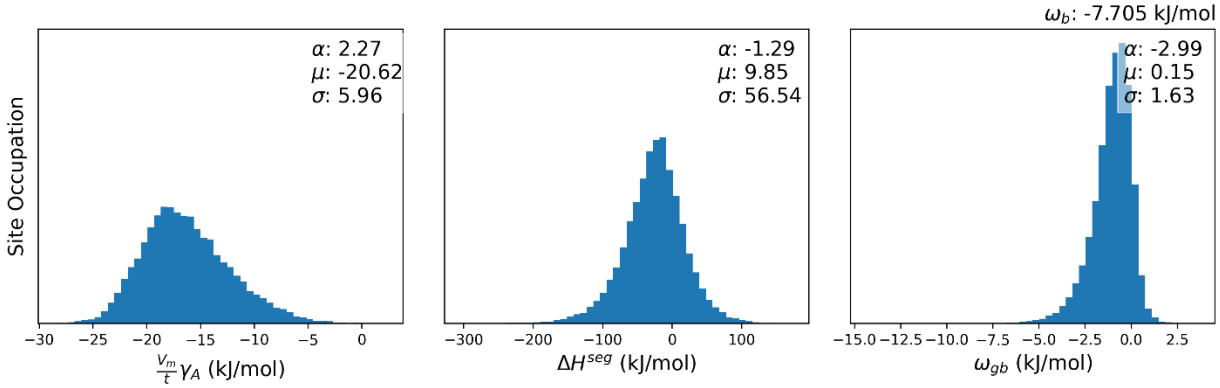

☑☒ Al-Fe [145]

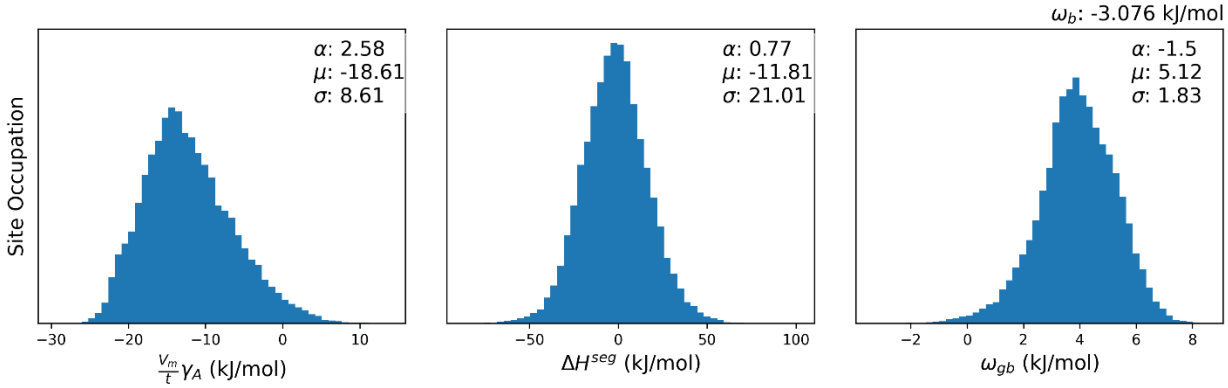

☒ Al-Mg [146]

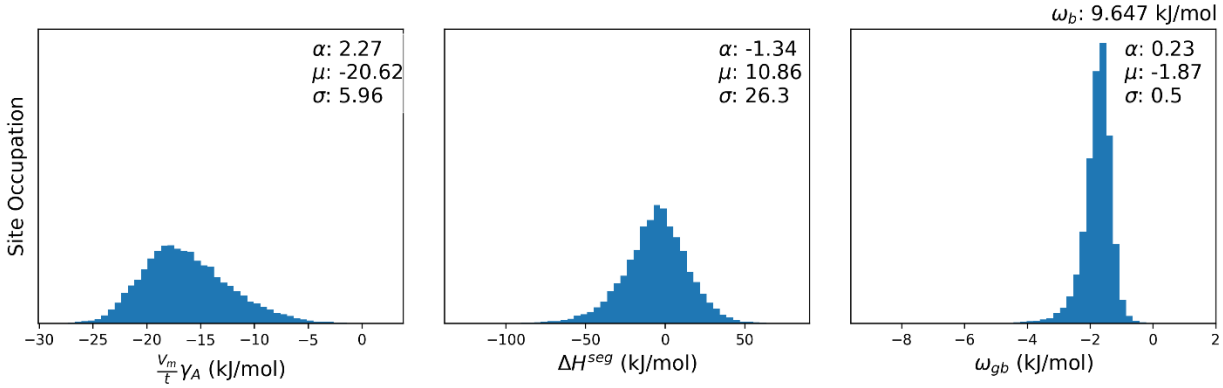

☑☒ Al-Mg [101]

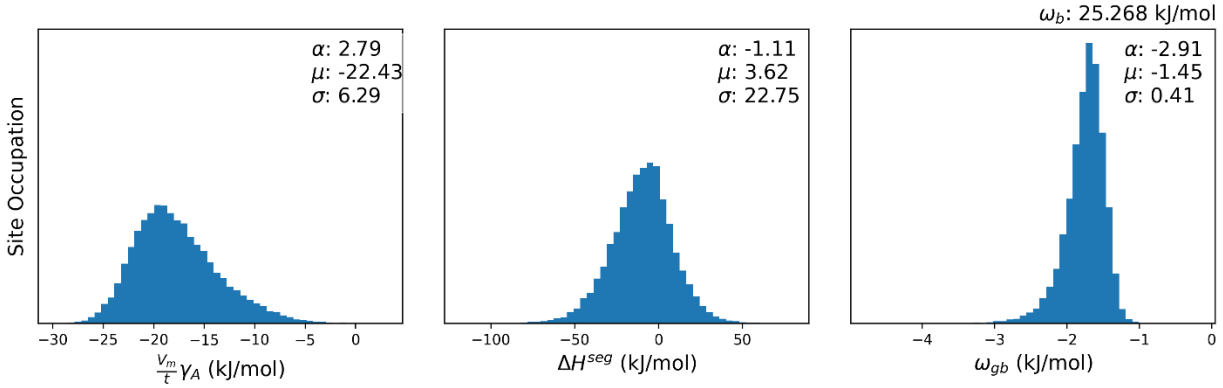

☑☒ Al-Mg [127]

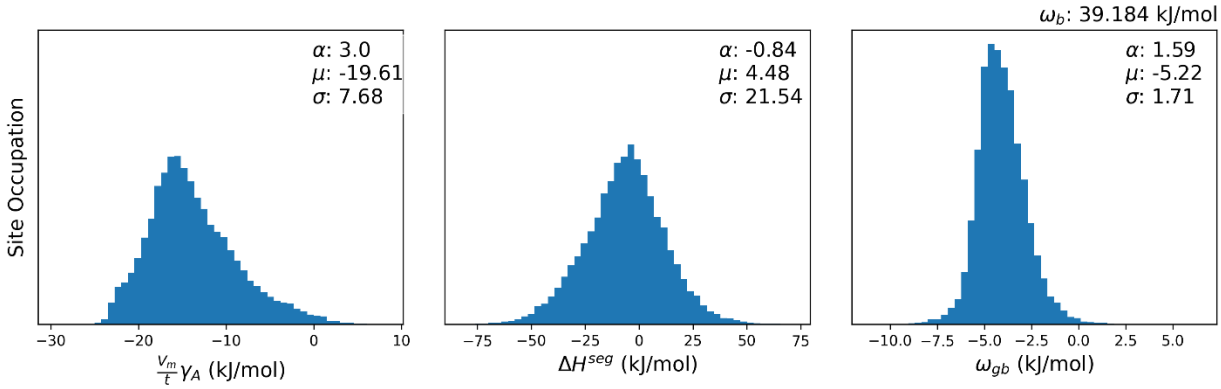

☒ Al-Nb [147]

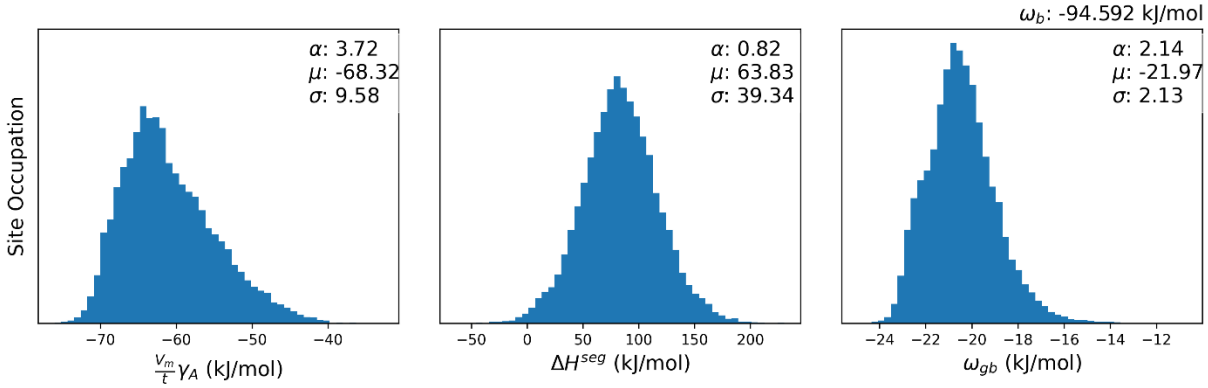

☒ Al-Ni [148]

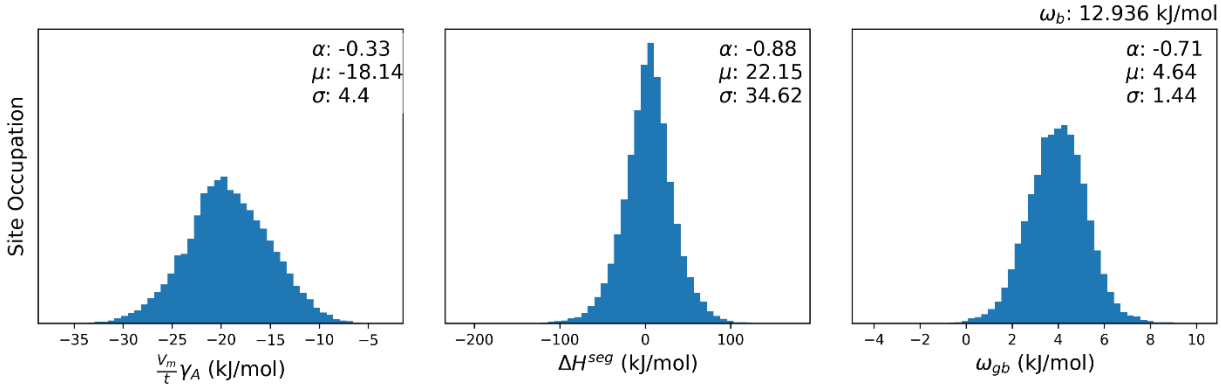

☒ Al-Ni [149]

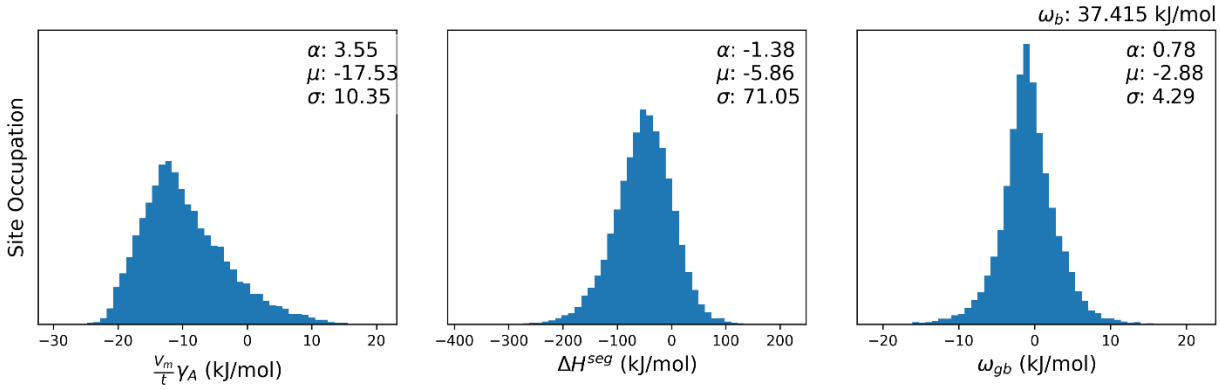

☒ Al-Ni [150]

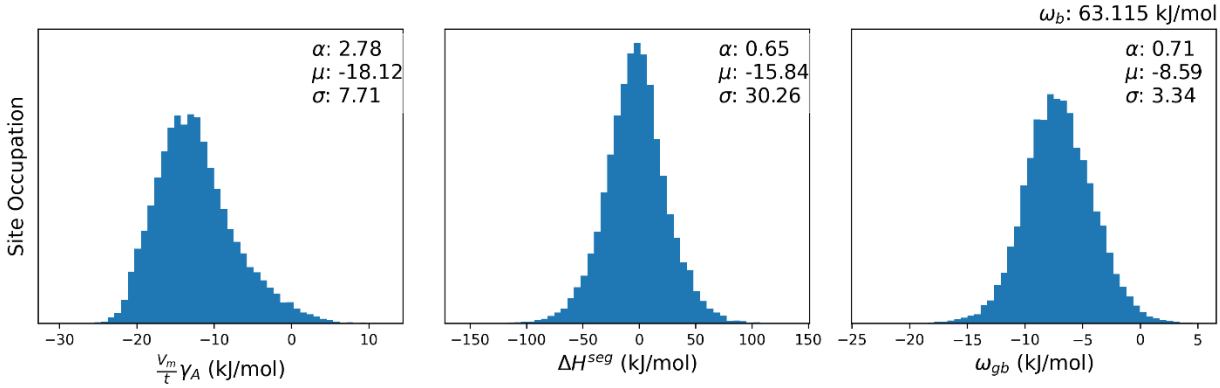

☒ Al-Ni [151]

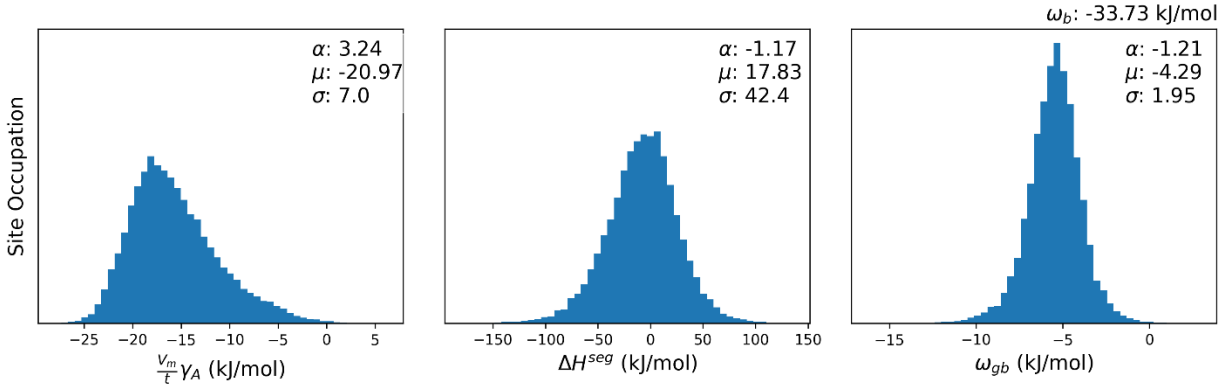

☑☒ Al-Pb [152]

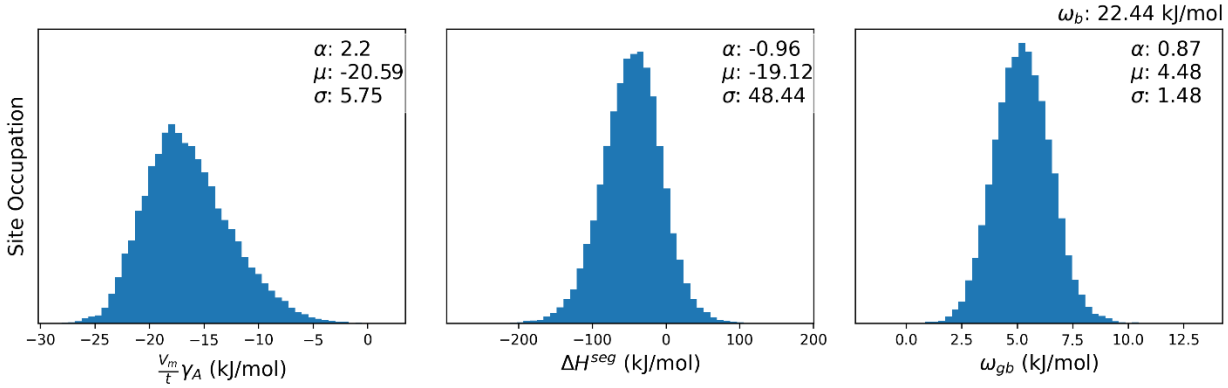

☑☒ Al-Sm [153]

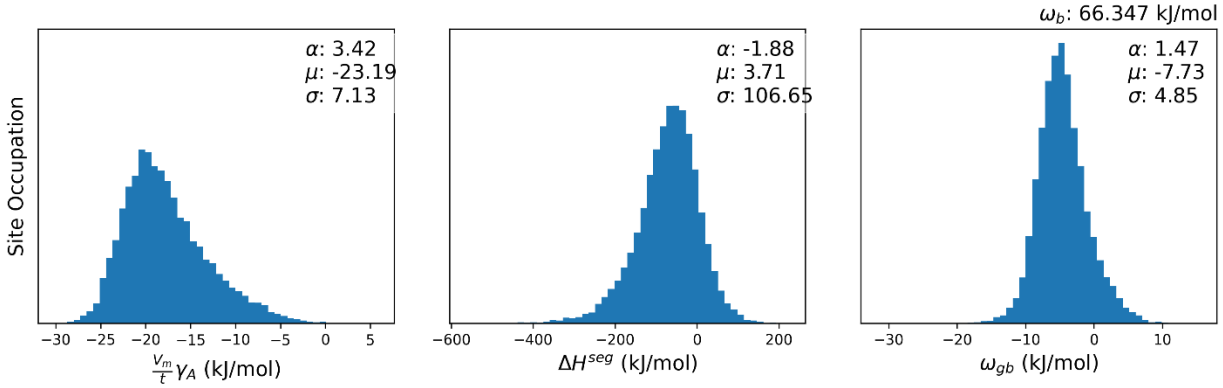

☑☒ Al-Sm [154]

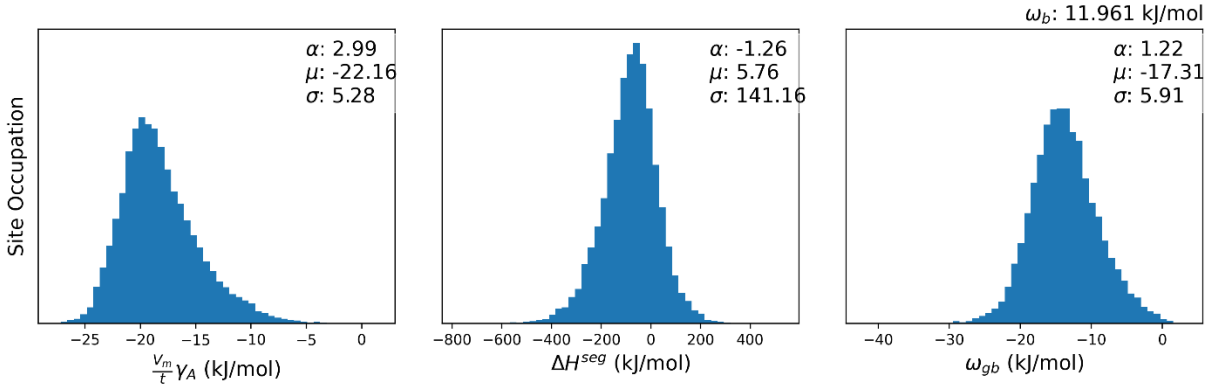

☒ Al-Ti [147]

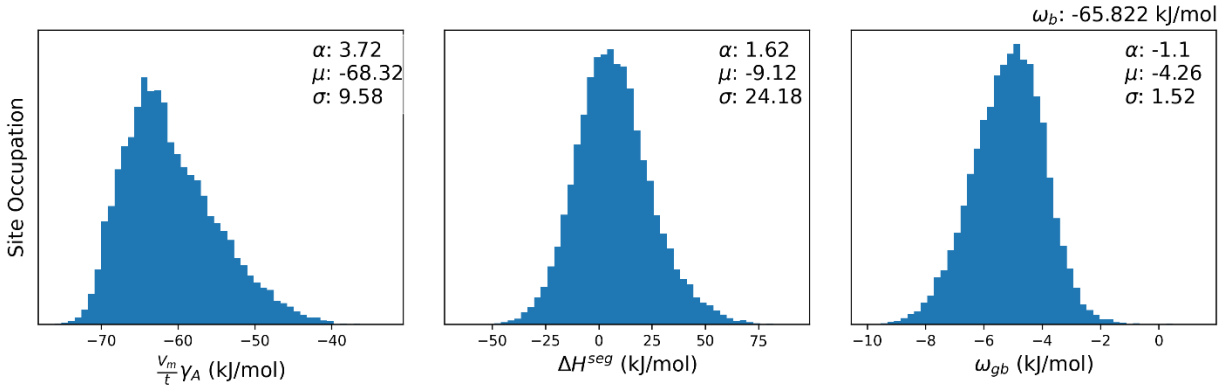

☒ Al-Ti [155]

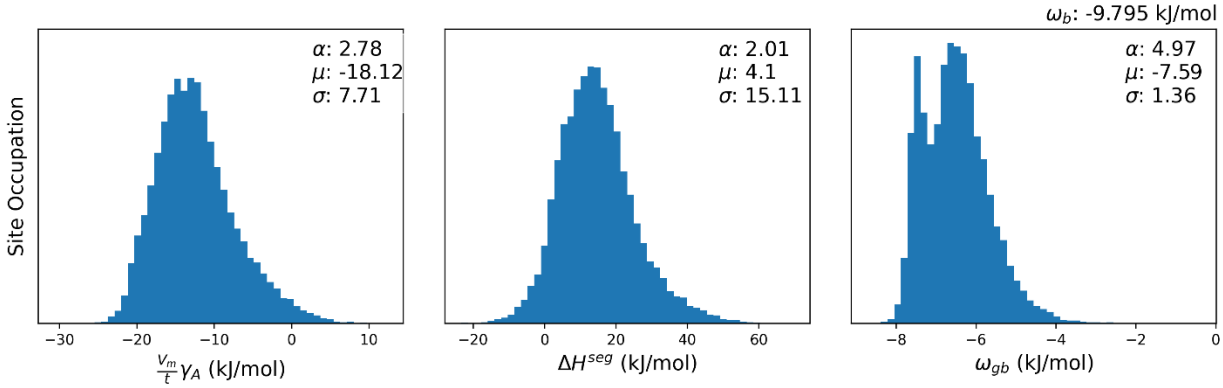

Au-based Alloys

Au-Ag [130]

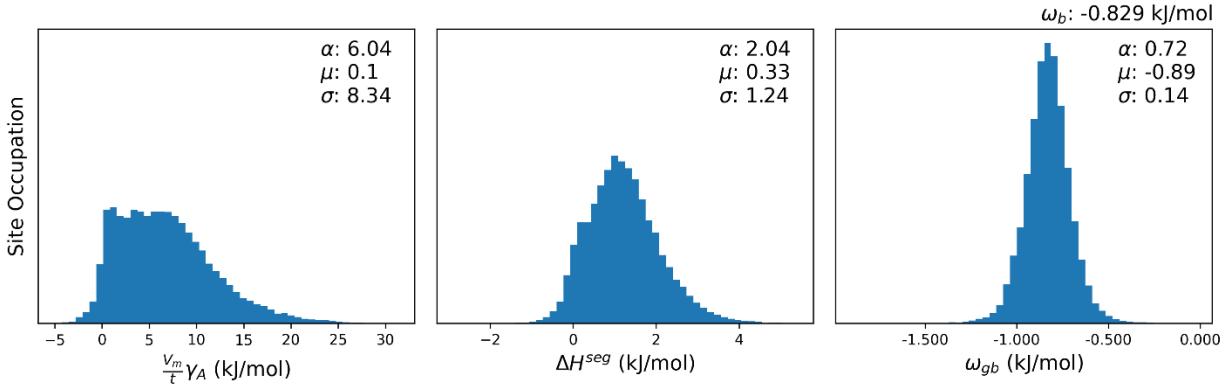

Au-Ag [162]

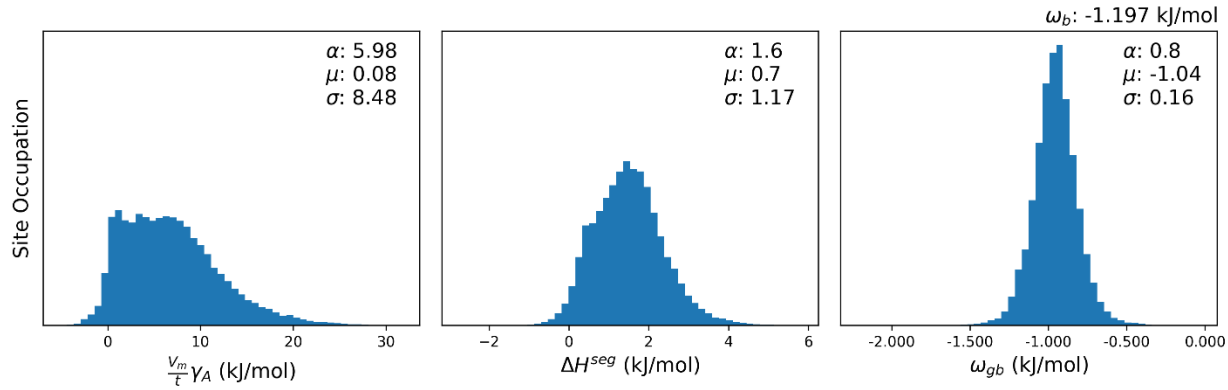

☒ Au-Ag [163]

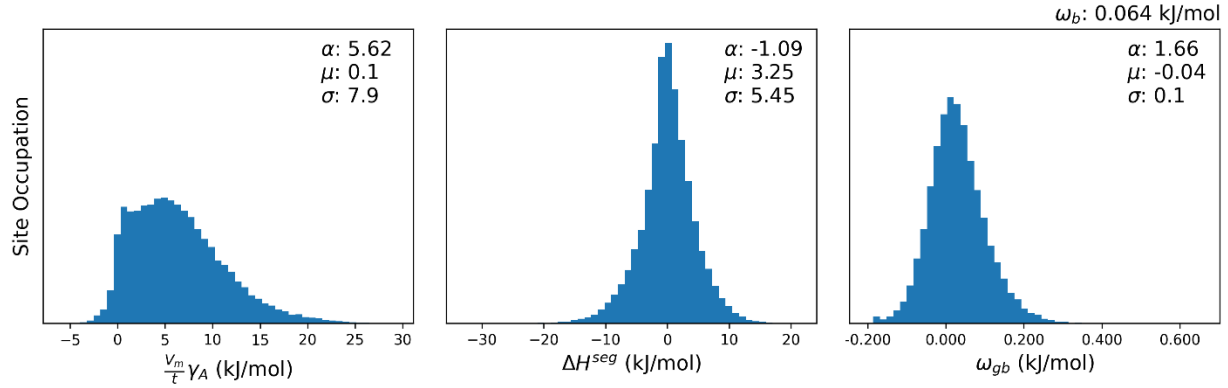

Au-Cu [130]

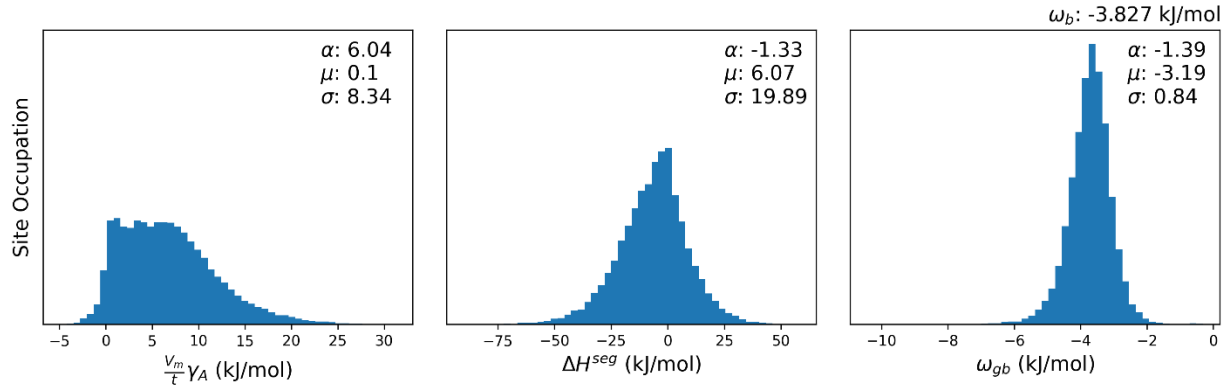

Au-Cu [162]

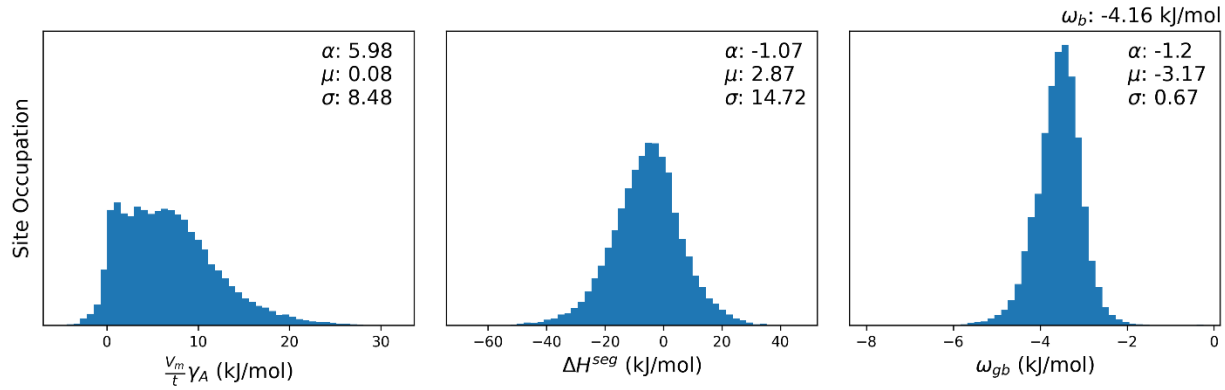

Au-Cu [163]

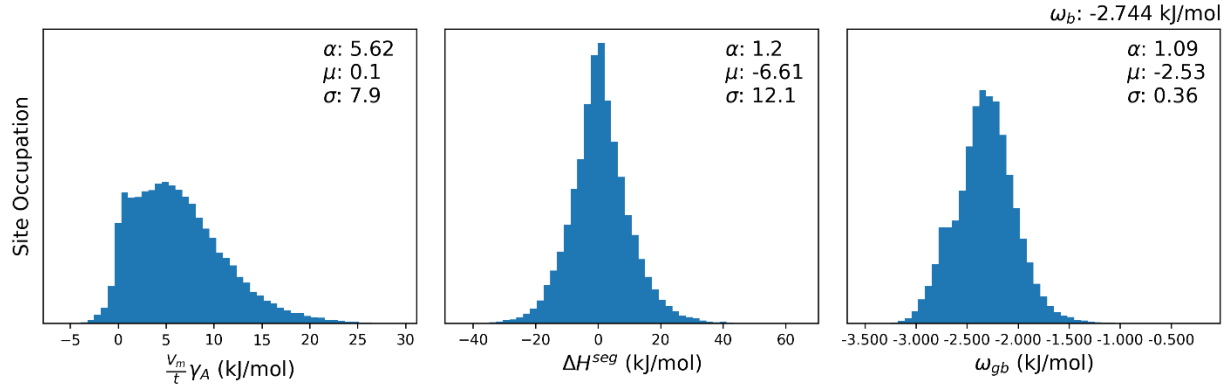

Au-Ni [130]

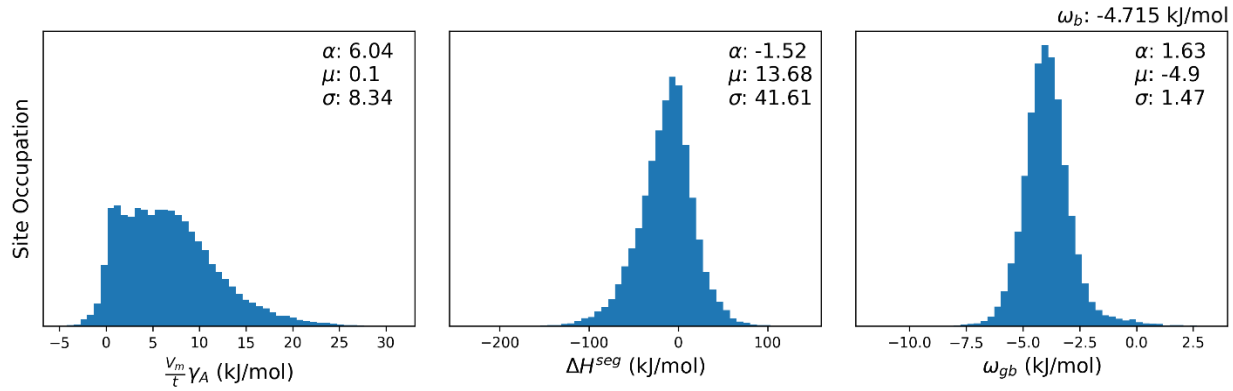

Au-Ni [162]

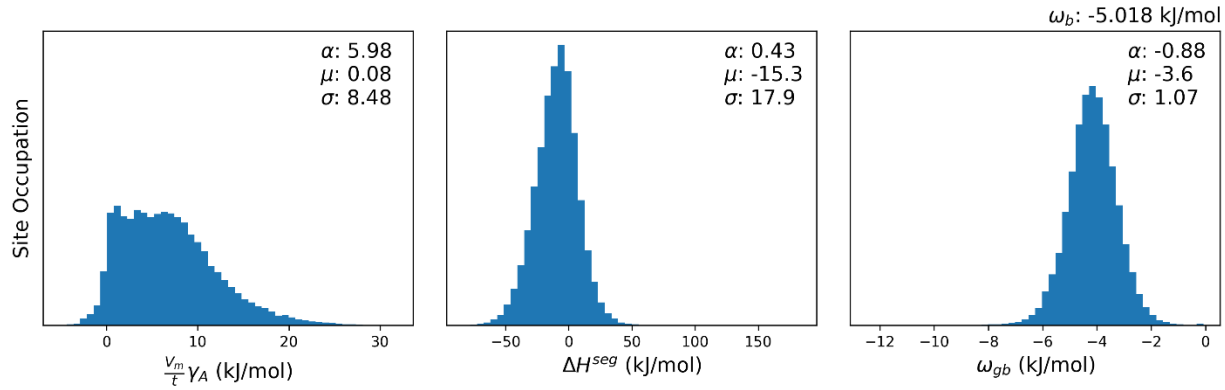

☒ Au-Pd [130]

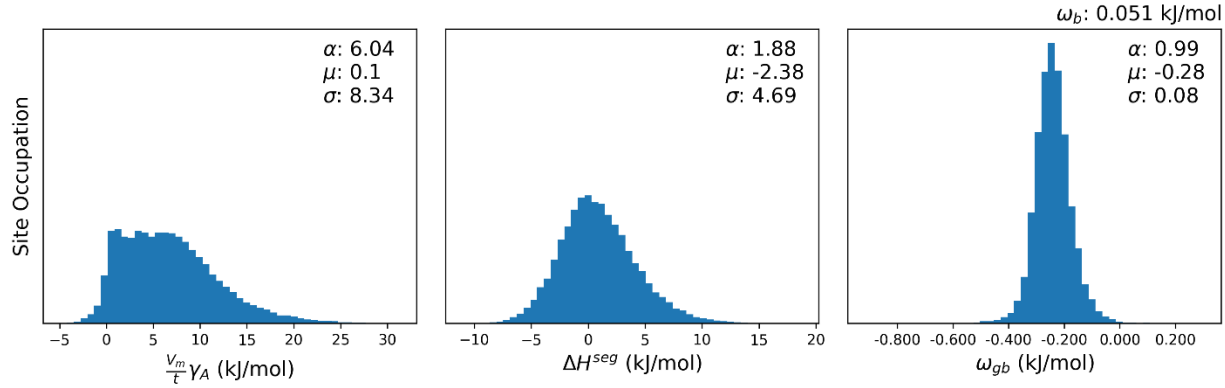

Au-Pd [162]

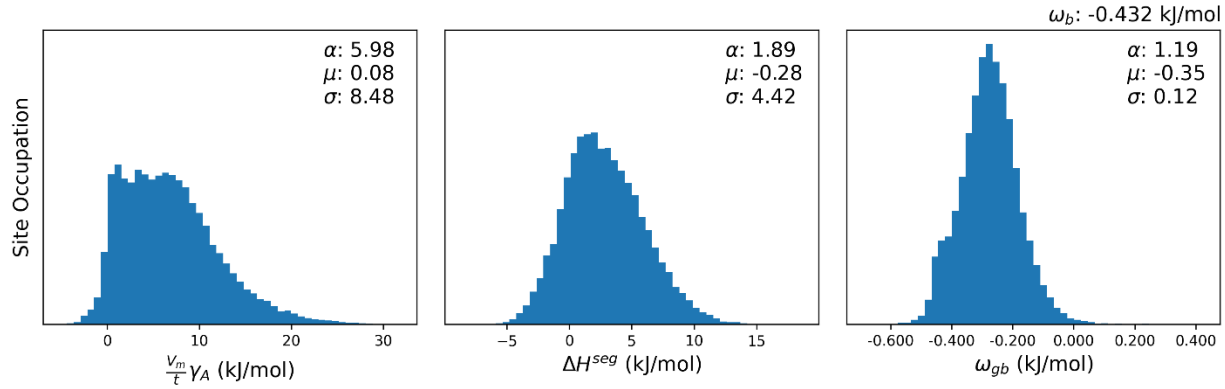

Au-Pt [130]

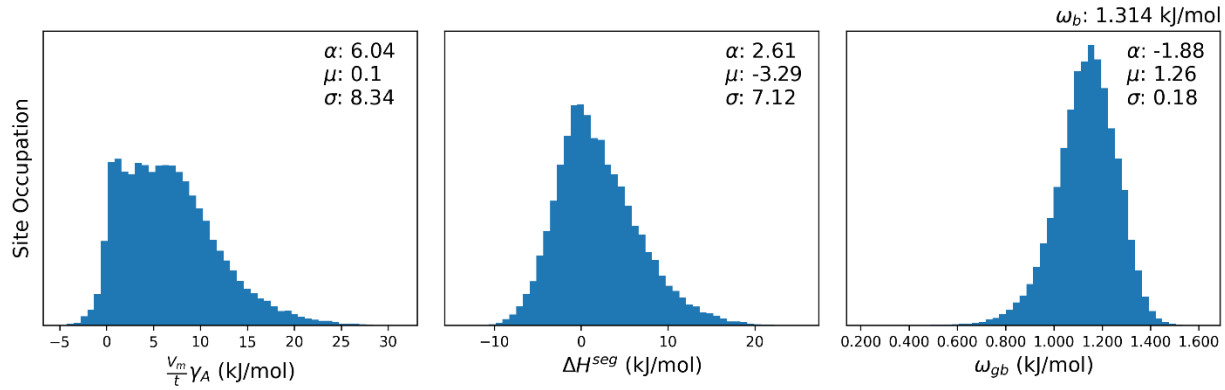

Au-Pt [162]

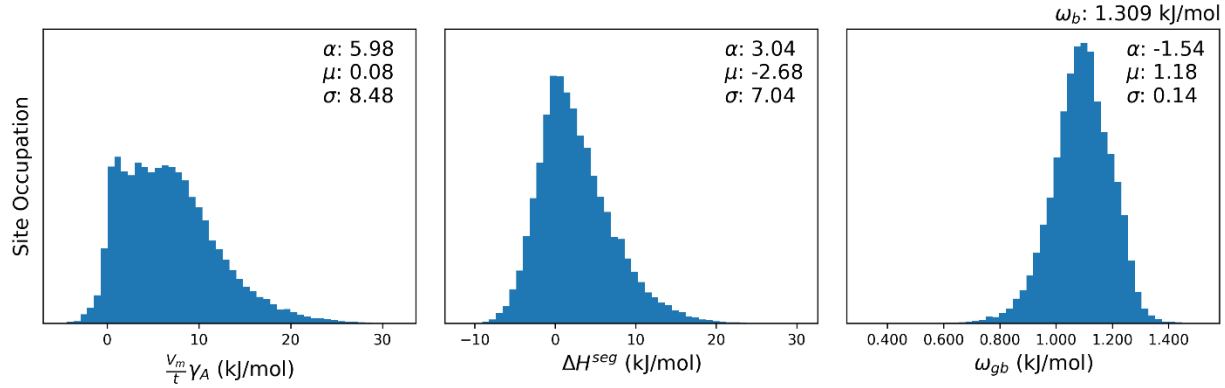

☑☒ Au-Pt [131]

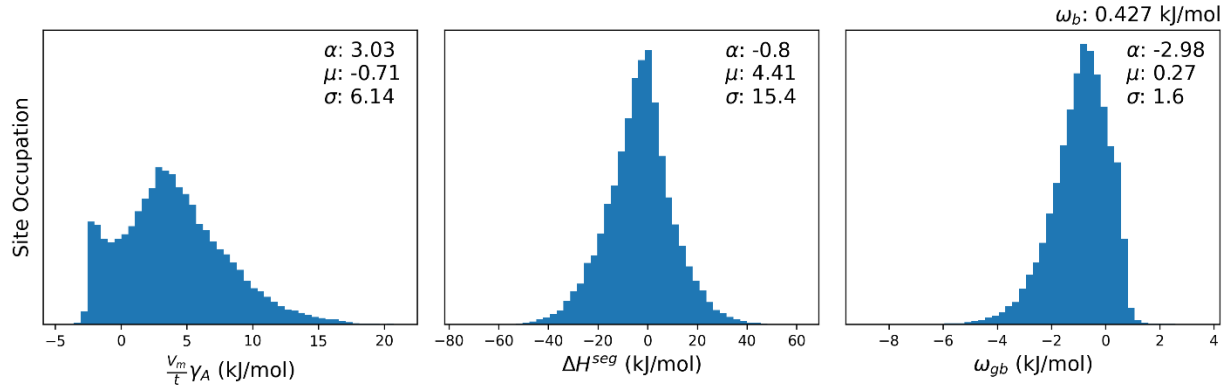

Co-based Alloys

Co-Al [143]

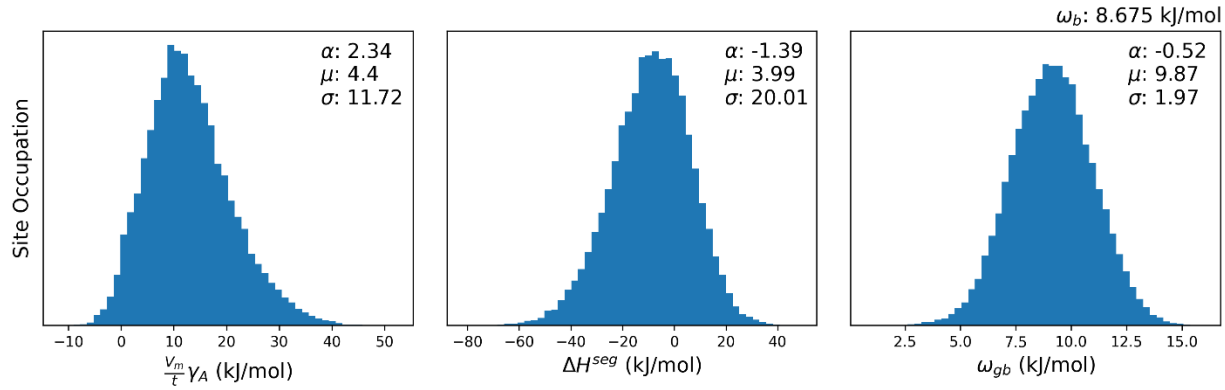

Co-Al [143]

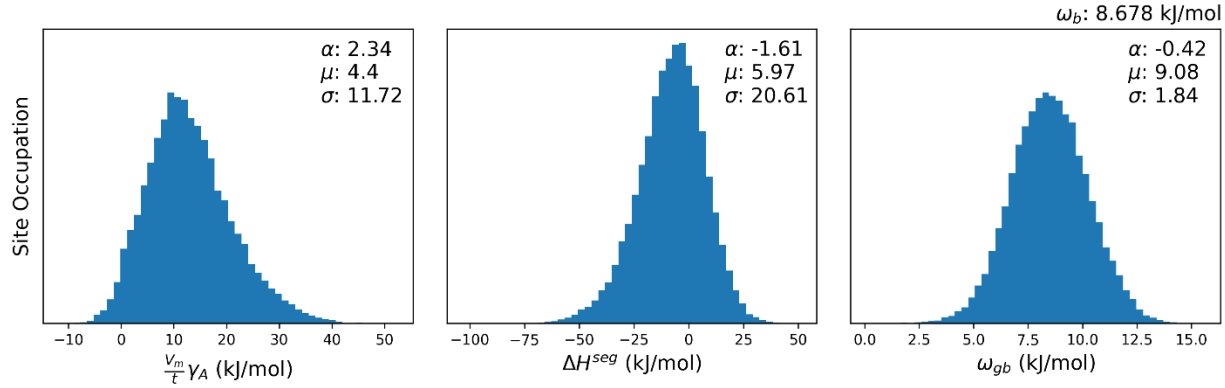

Co-Al [166]

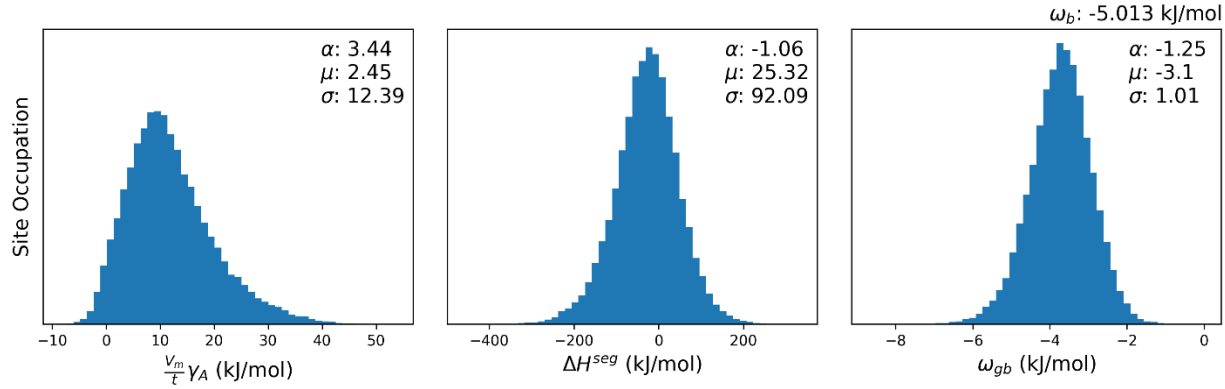

☒ Co-Cr [167]

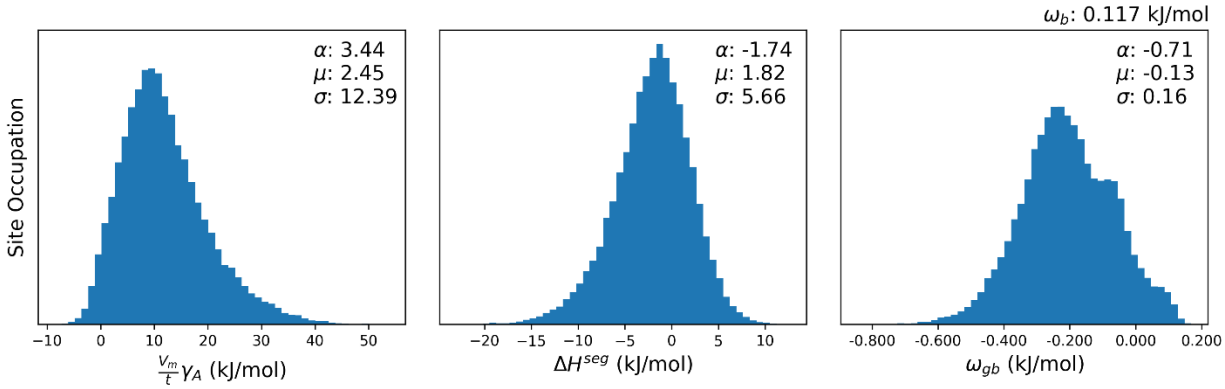

☒ Co-Cr [166]

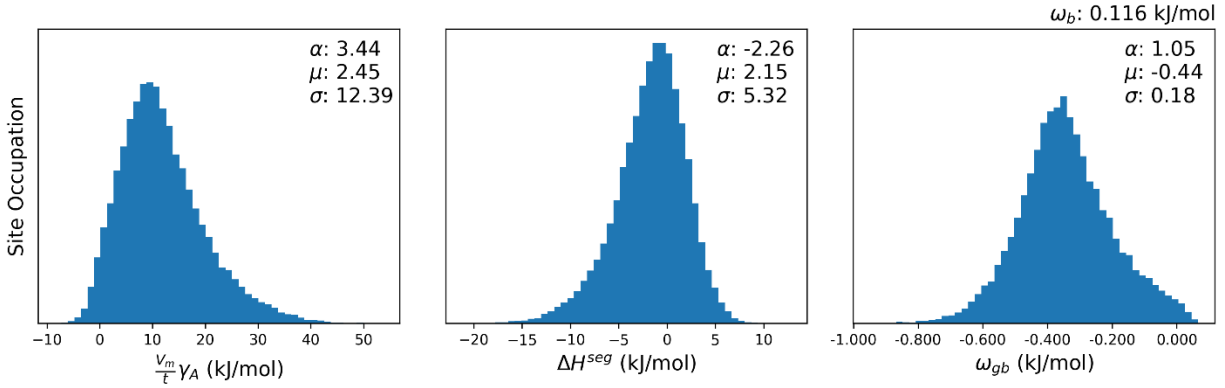

☒ Co-Cr [168]

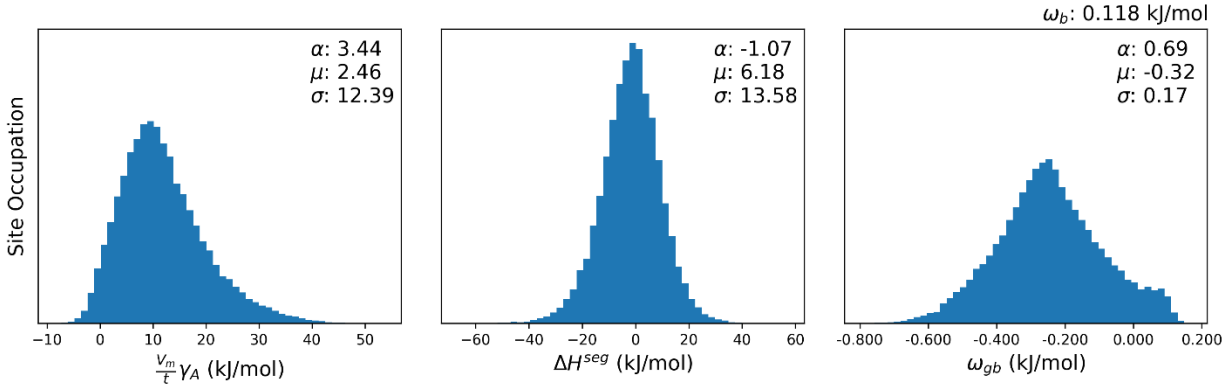

☒ Co-Cu [167]

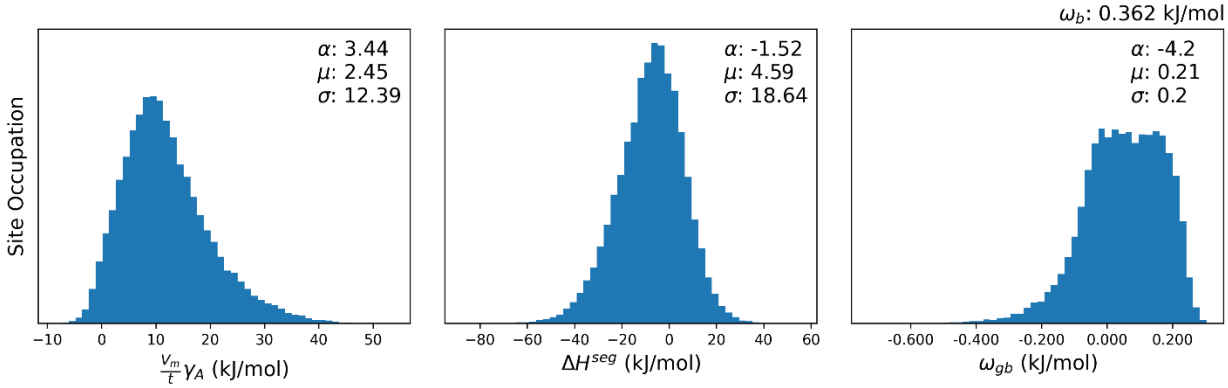

☒ Co-Cu [168]

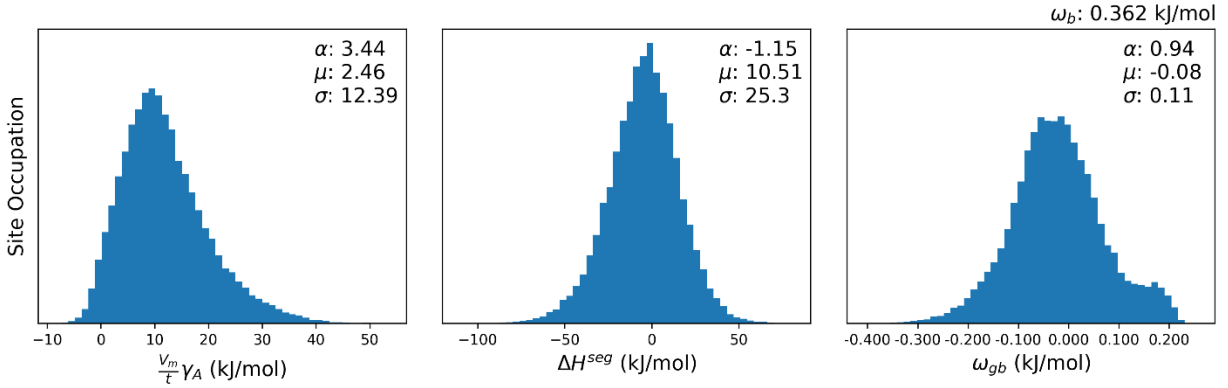

☒ Co-Fe [167]

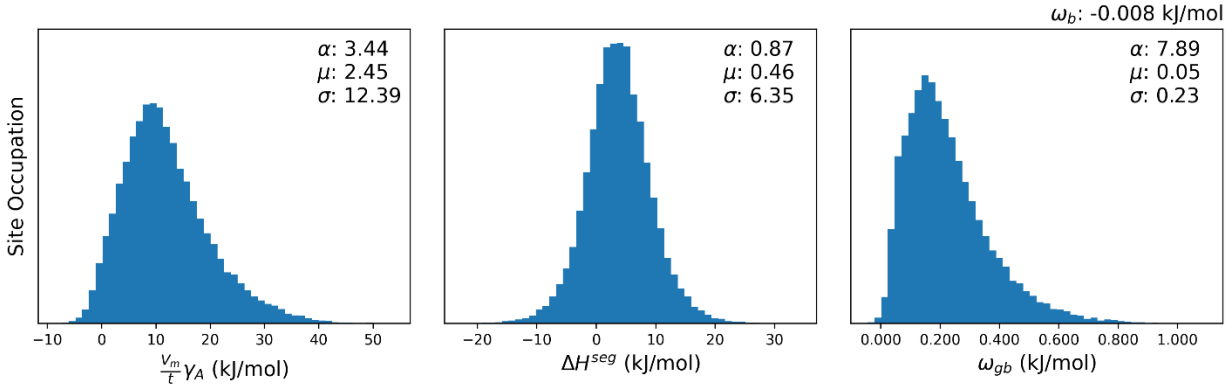

☒ Co-Fe [166]

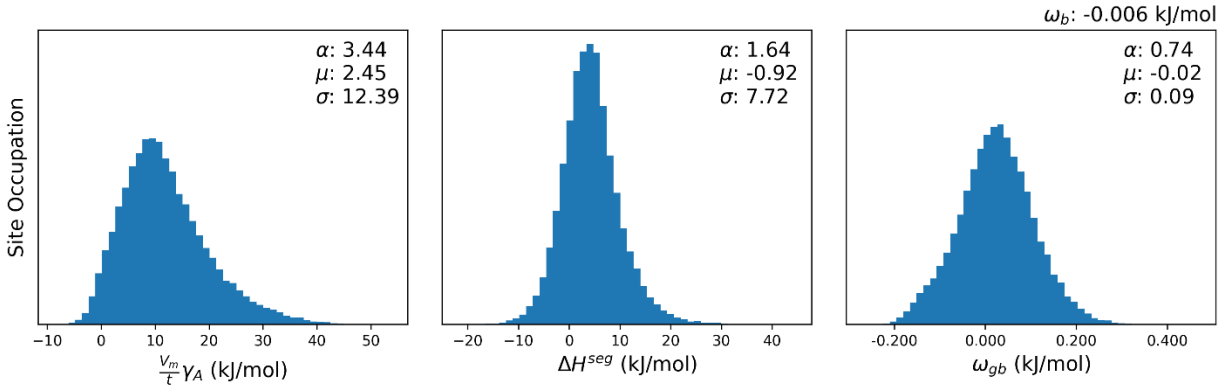

☒ Co-Fe [168]

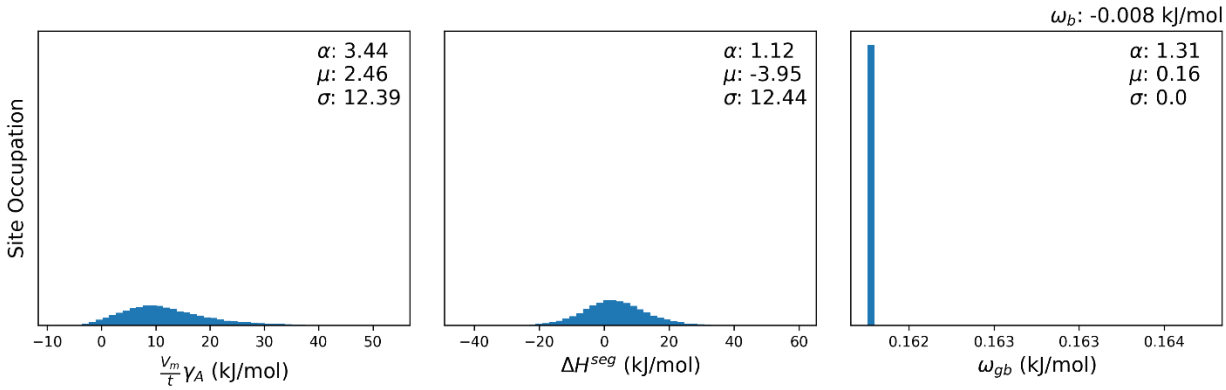

Co-Ni [143]

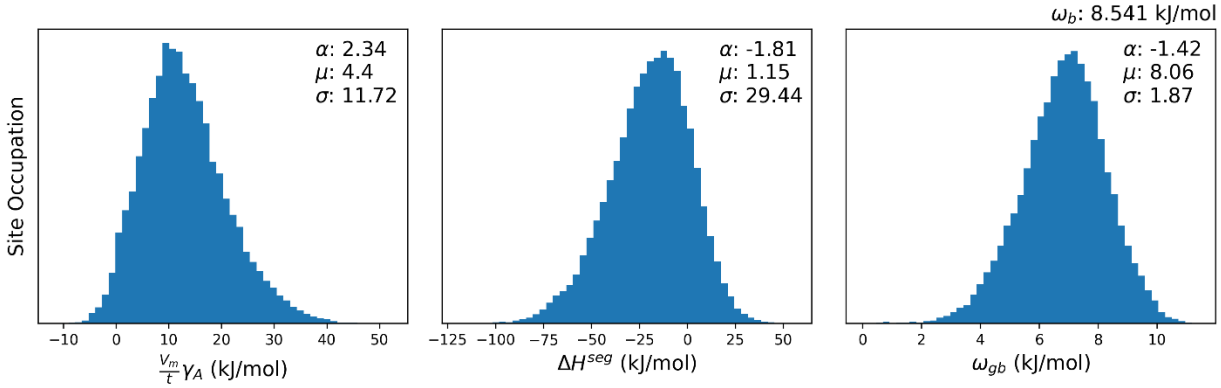

Co-Ni [143]

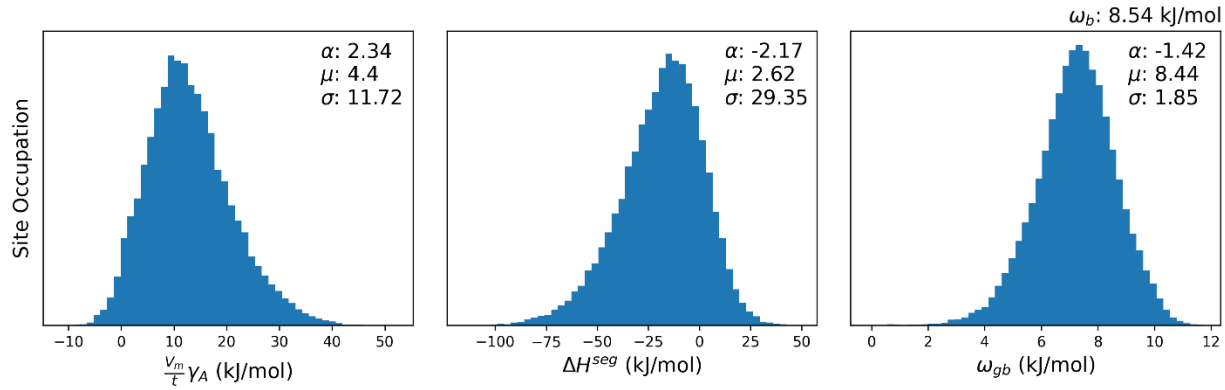

☒ Co-Ni [169]

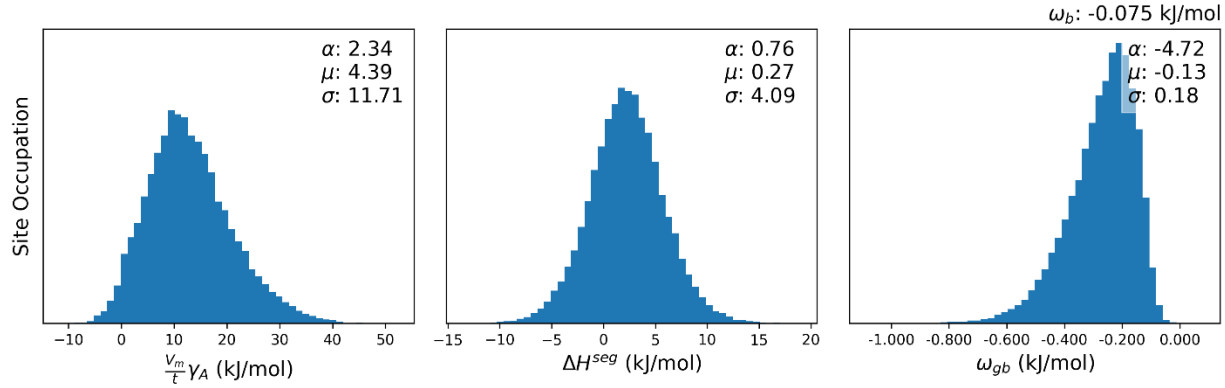

☒ Co-Ni [167]

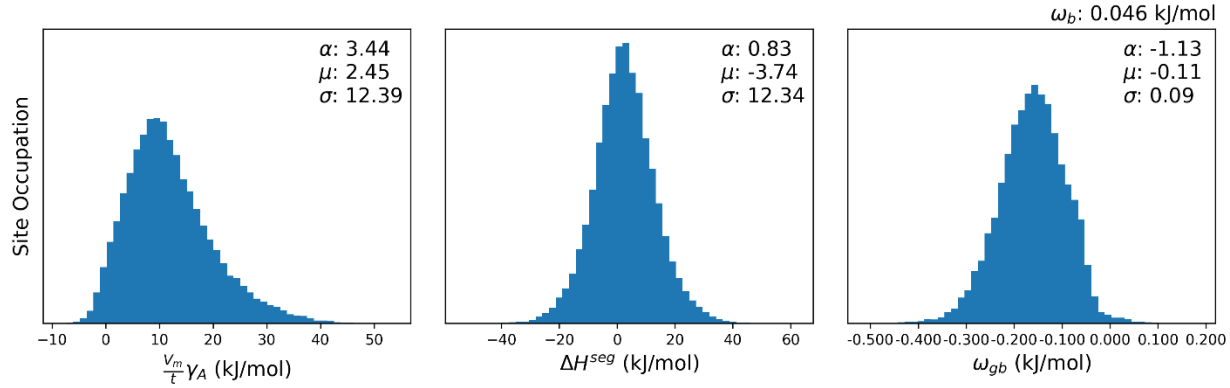

☒ Co-Ni [166]

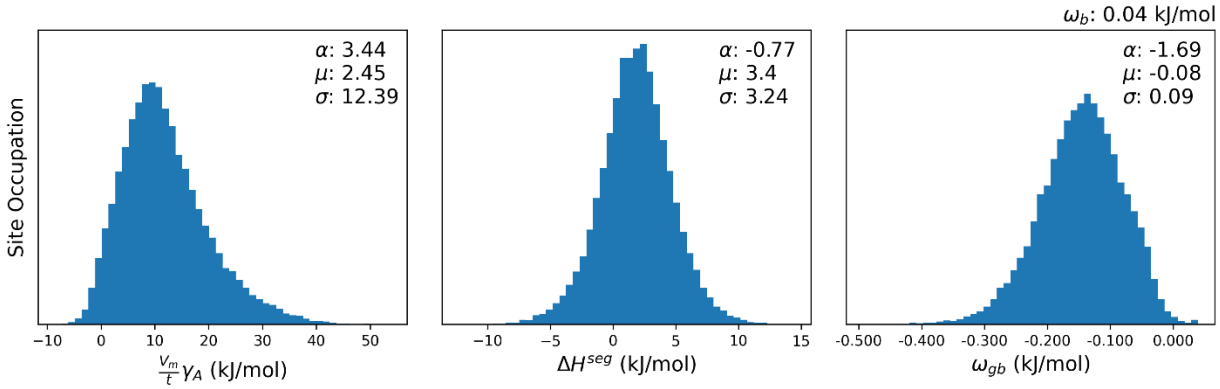

☒ Co-Ni [168]

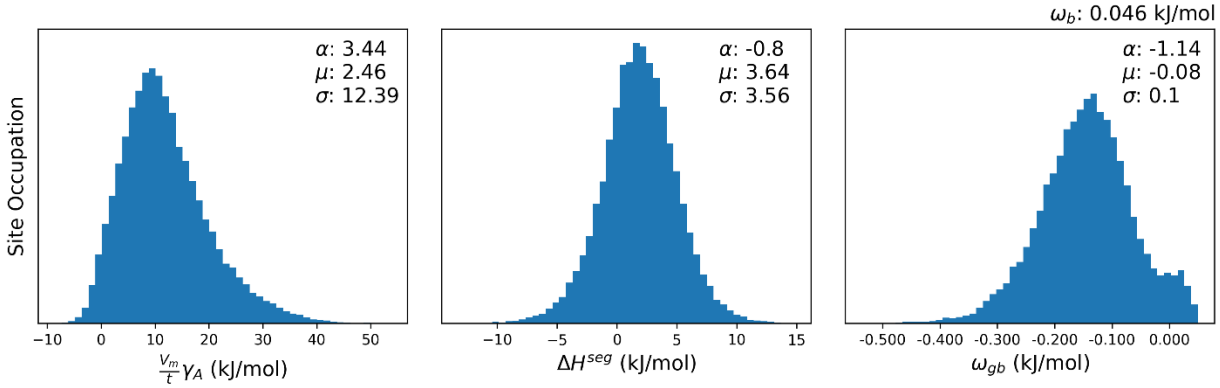

Cr-based Alloys

☒ Cr-Fe [170]

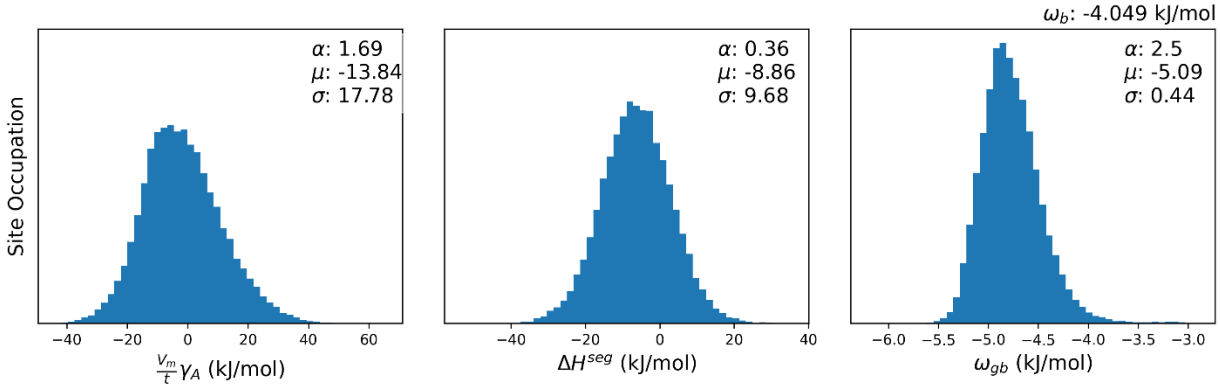

☒ Cr-Ni [170]

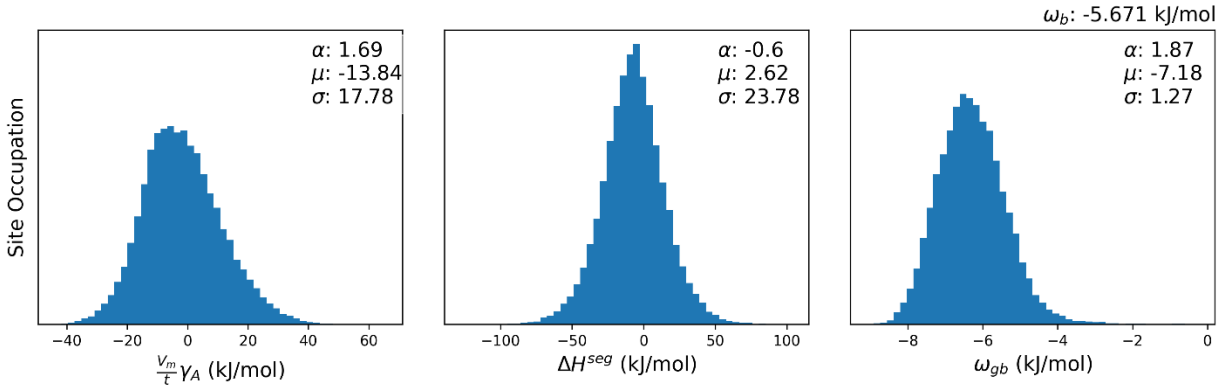

Cu-based Alloys

☒ Cu-Ag [130]

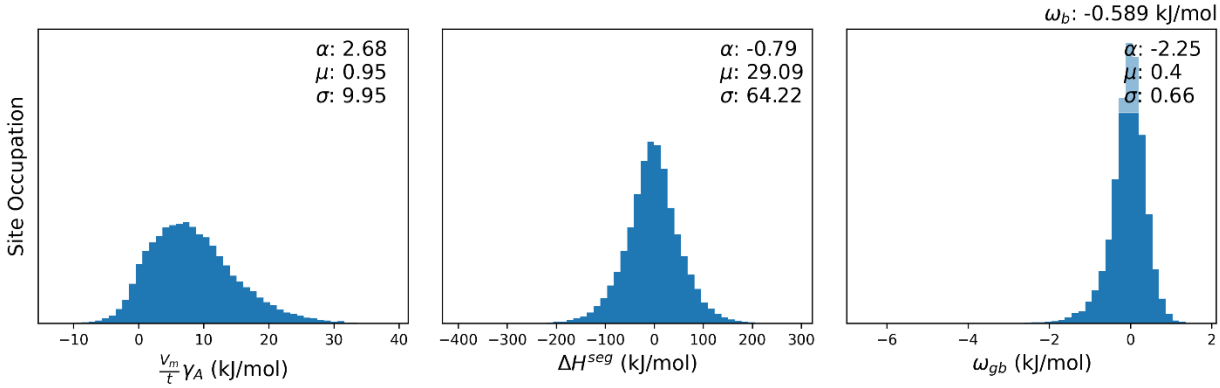

☒ Cu-Ag [162]

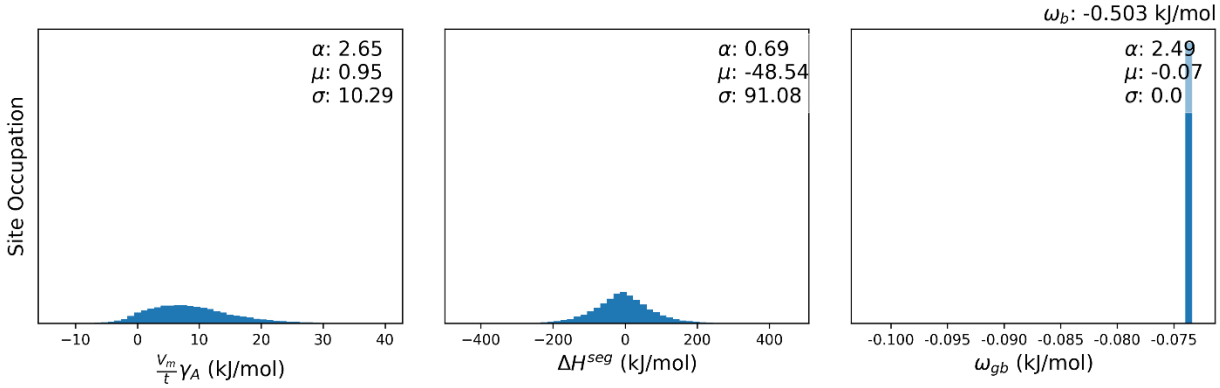

Cu-Ag [164]

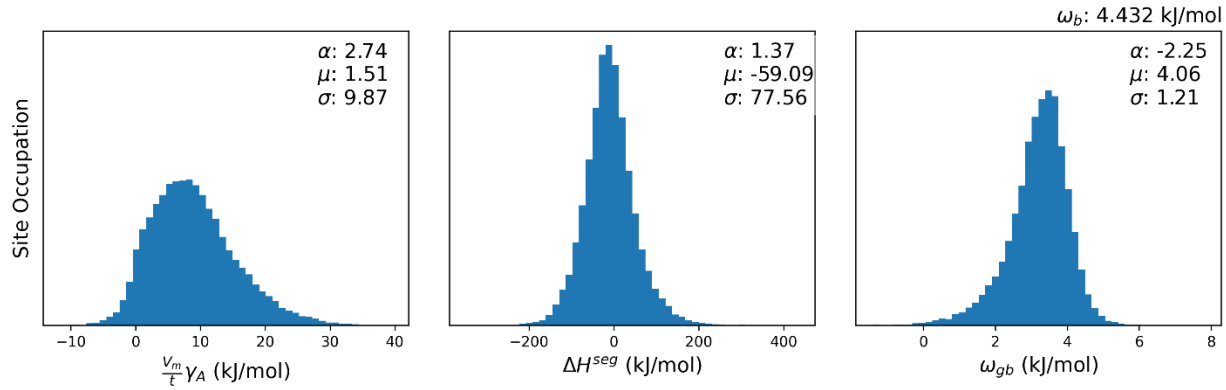

Cu-Ag [128]

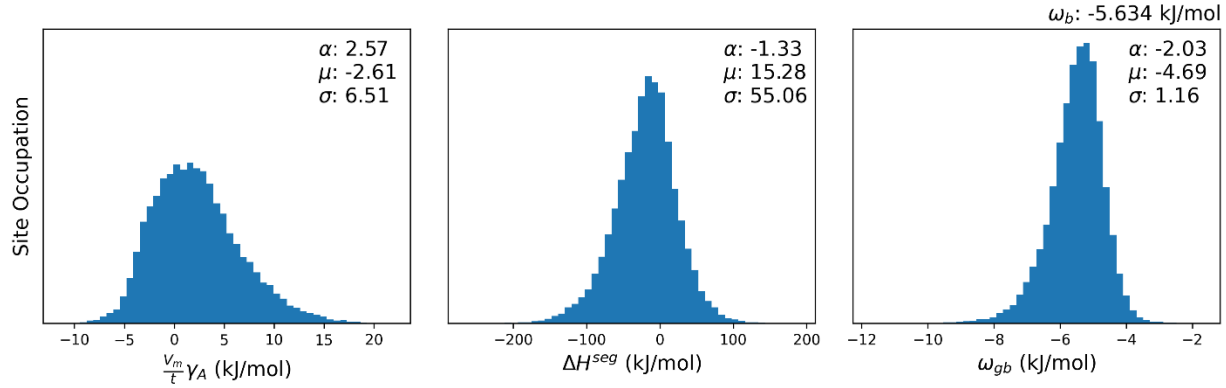

☒ Cu-Ag [163]

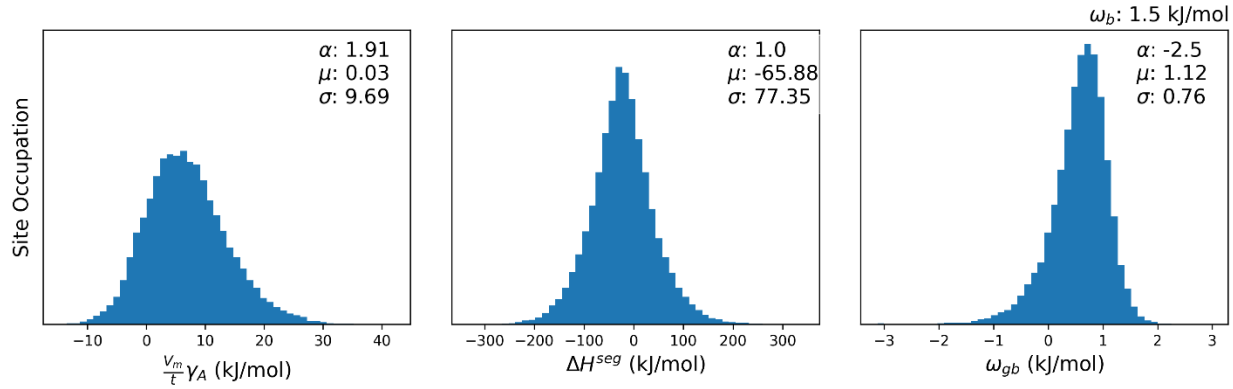

☑ Cu-Al [144]

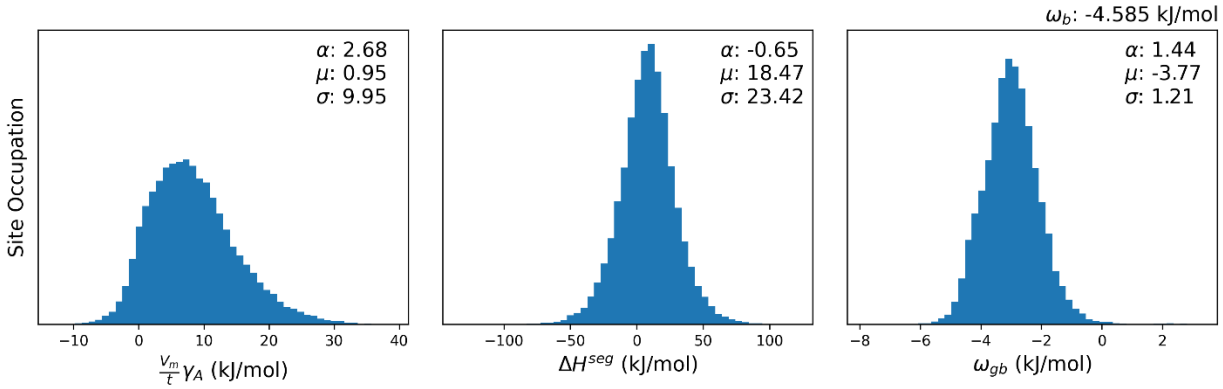

Cu-Au [130]

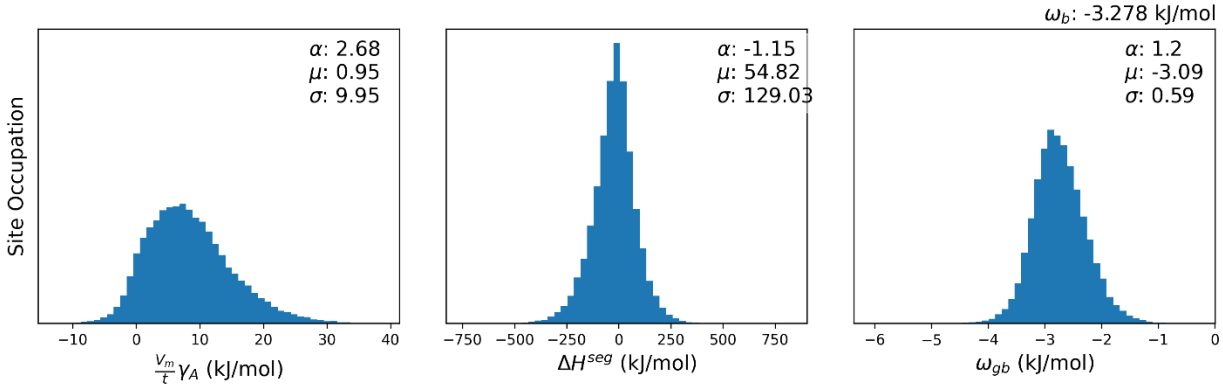

Cu-Au [162]

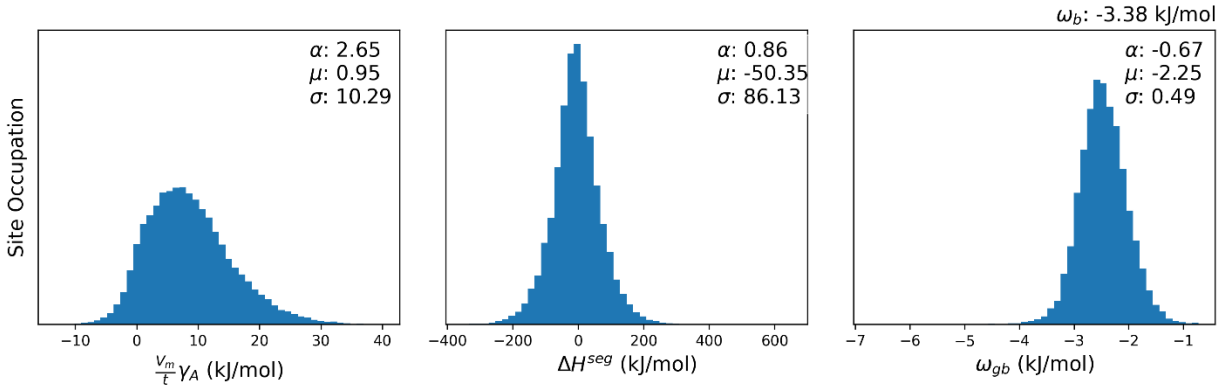

☒ Cu-Co [167]

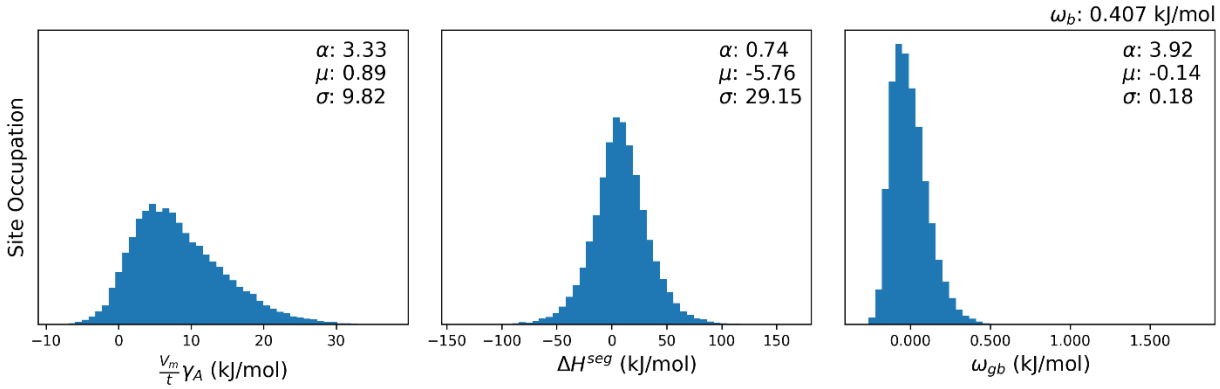

☒ Cu-Co [168]

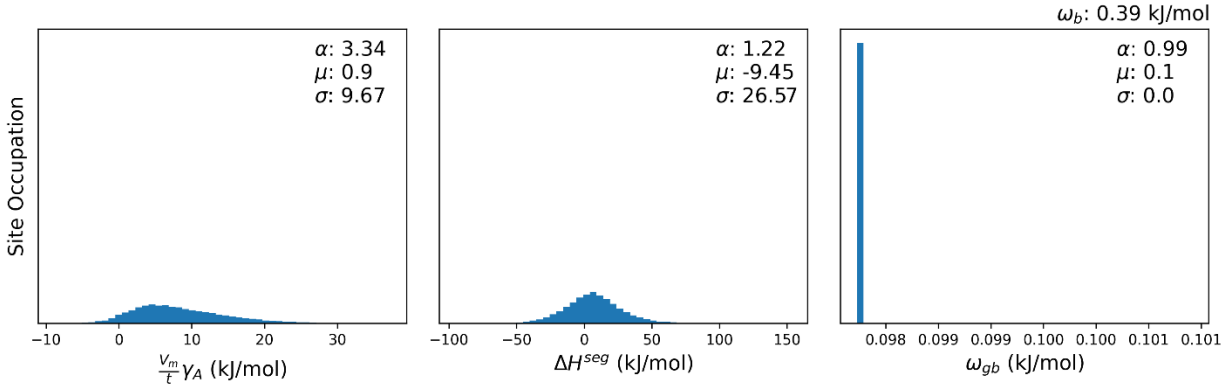

Cu-Cr [167]

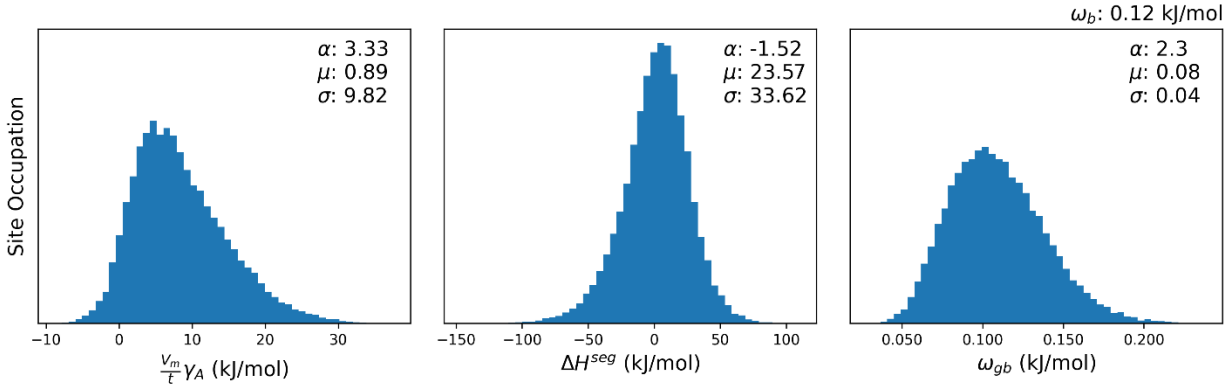

Cu-Cr [168]

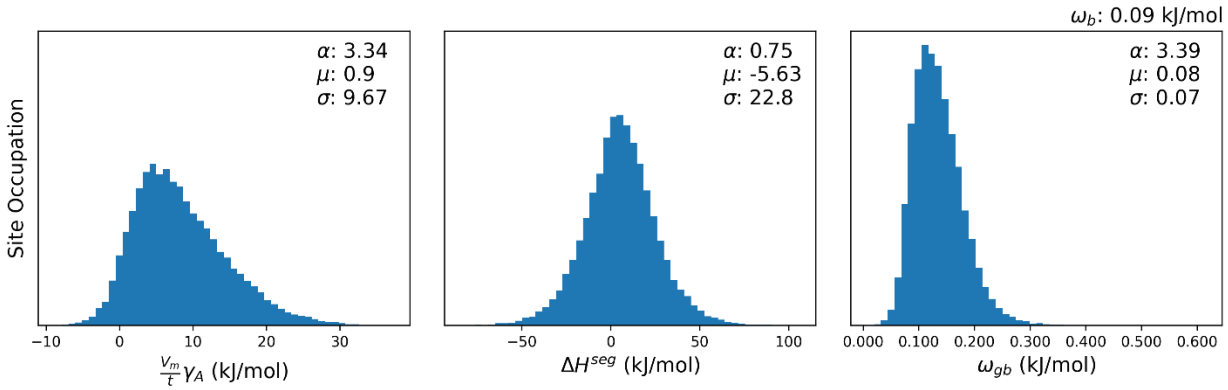

☒ Cu-Fe [171]

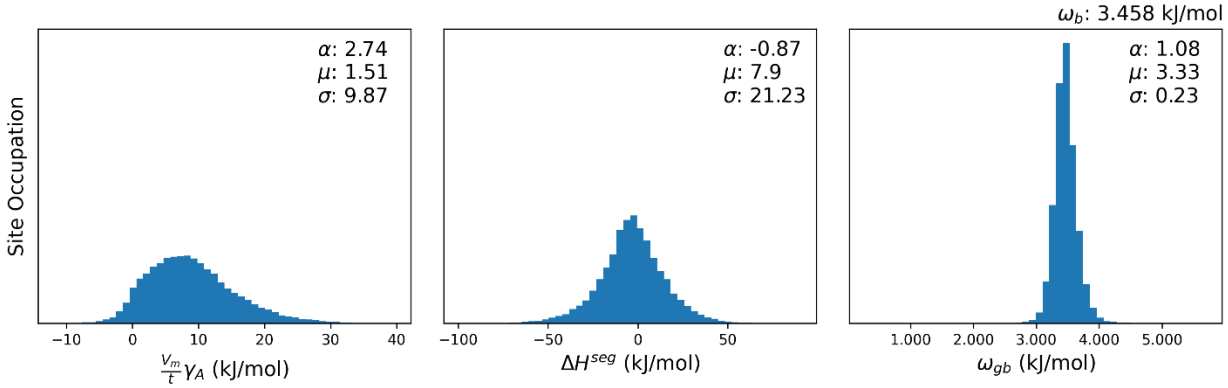

Cu-Fe [167]

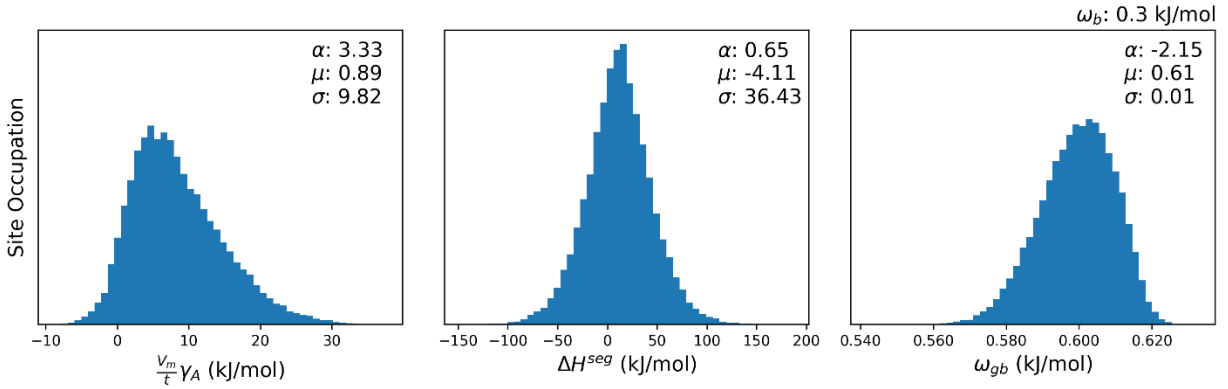

☒ Cu-Fe [168]

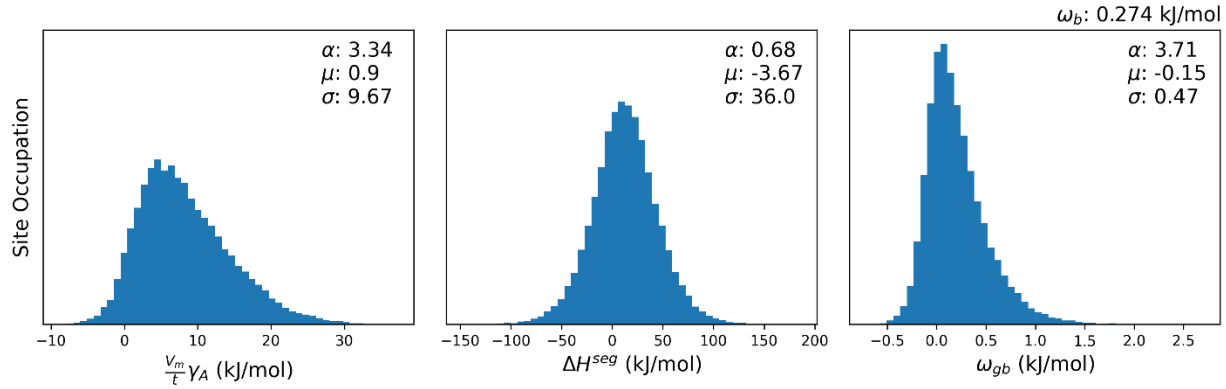

Cu-Ni [172]

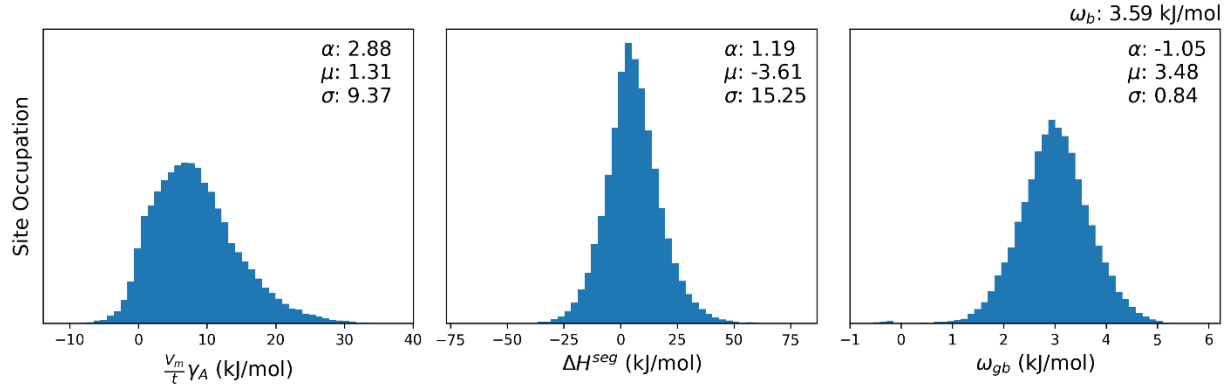

Cu-Ni [130]

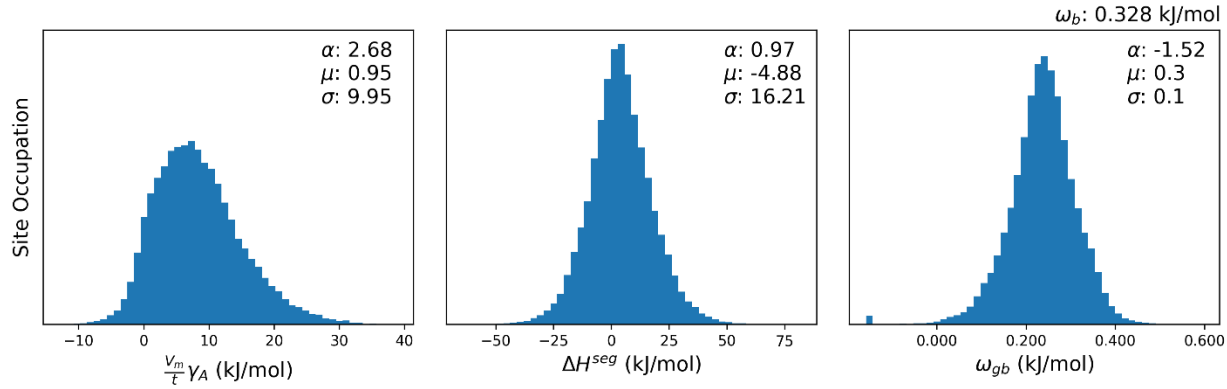

Cu-Ni [162]

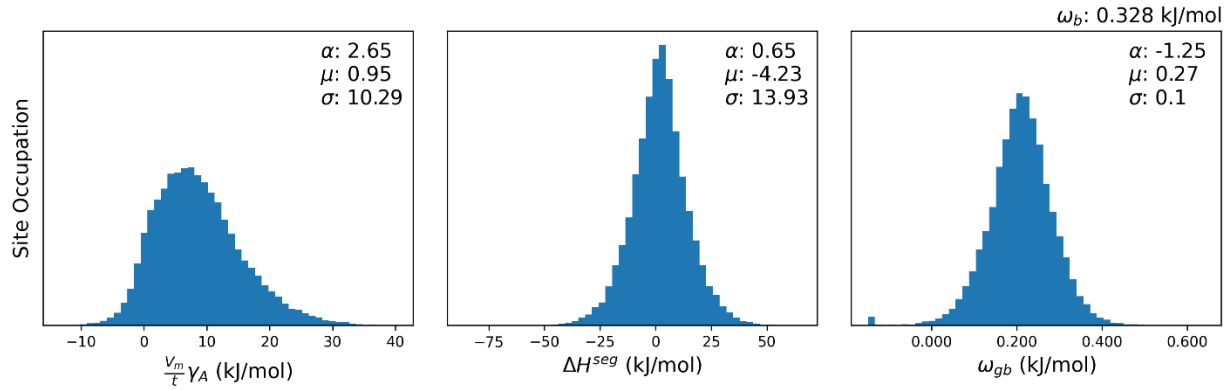

Cu-Ni [171]

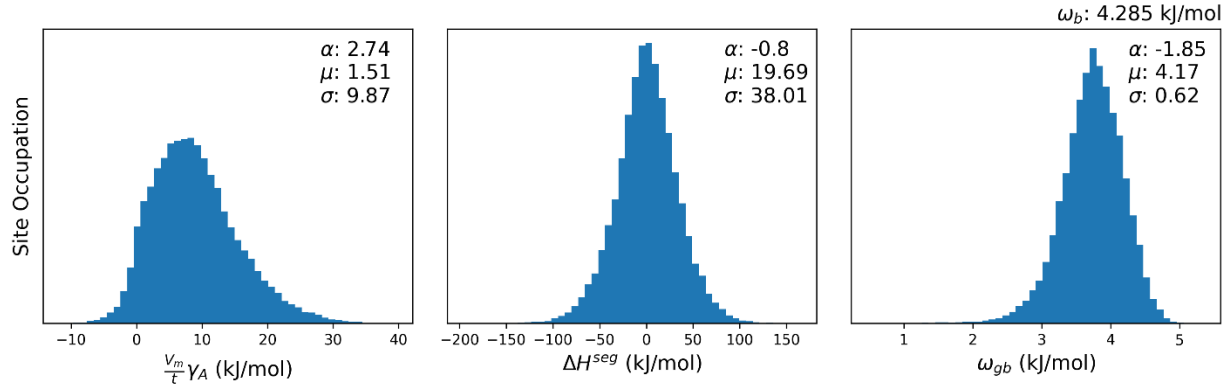

Cu-Ni [173]

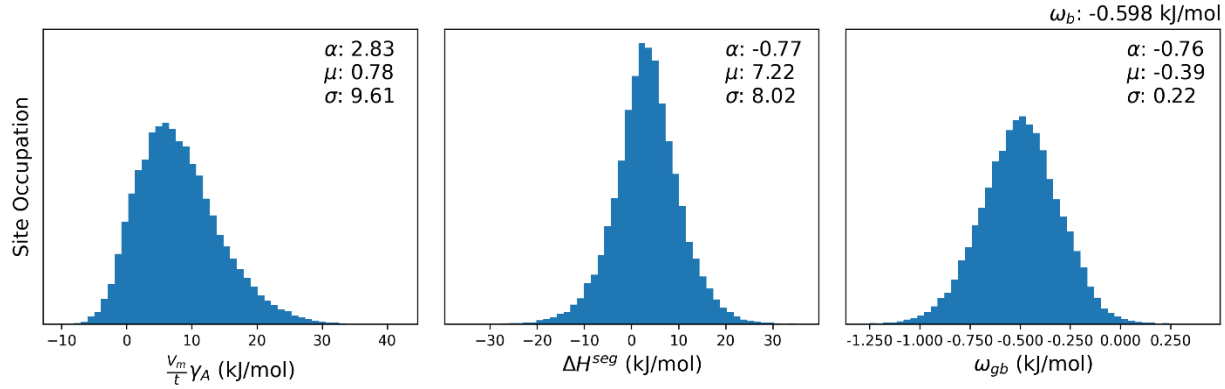

Cu-Ni [167]

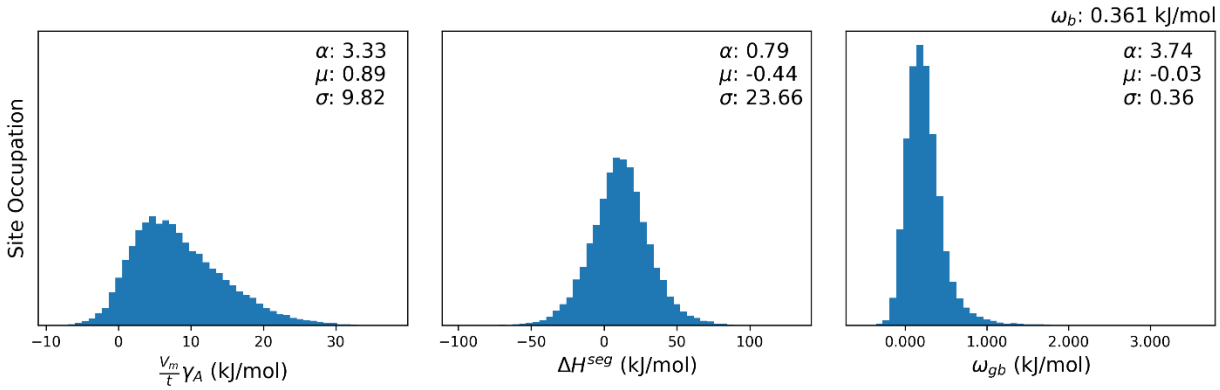

☑ Cu-Ni [174]

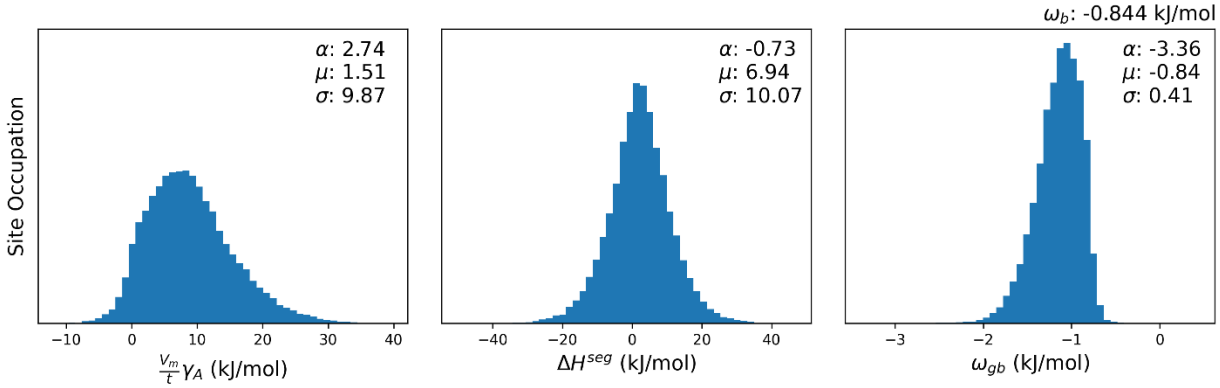

Cu-Ni [168]

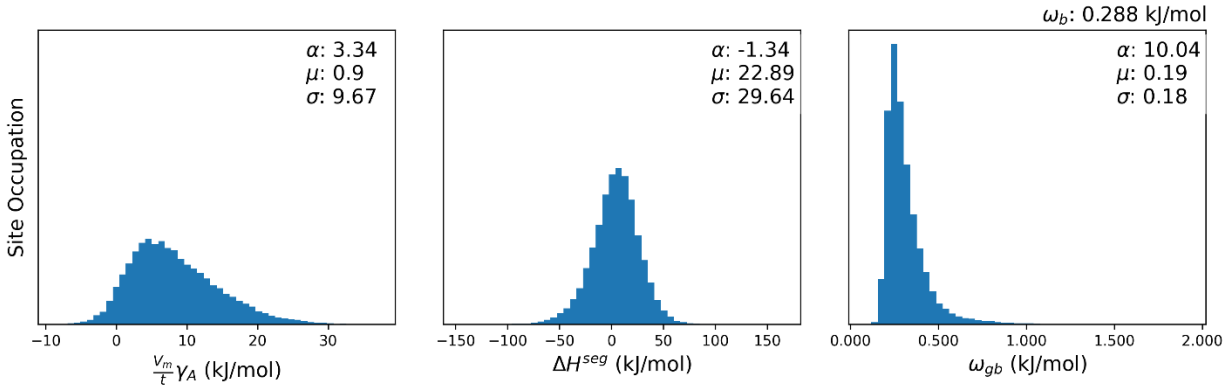

☑ Cu-Pb [175]

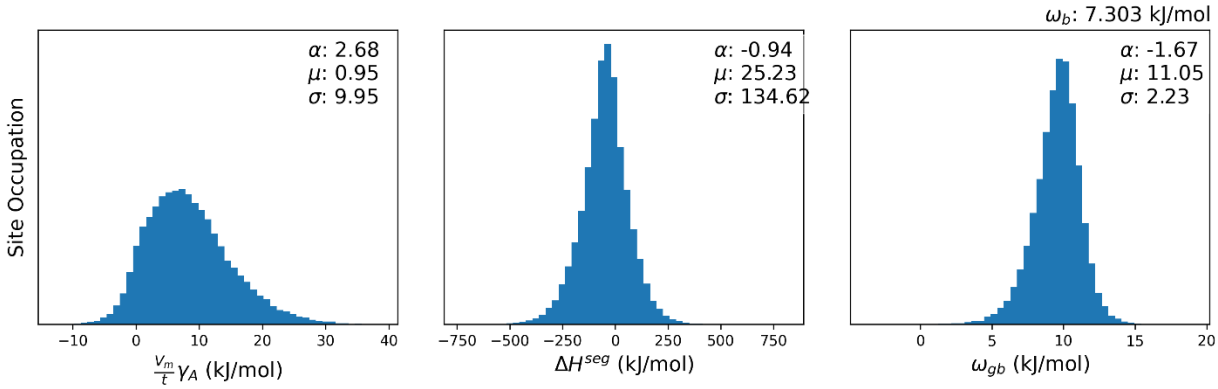

Cu-Pd [130]

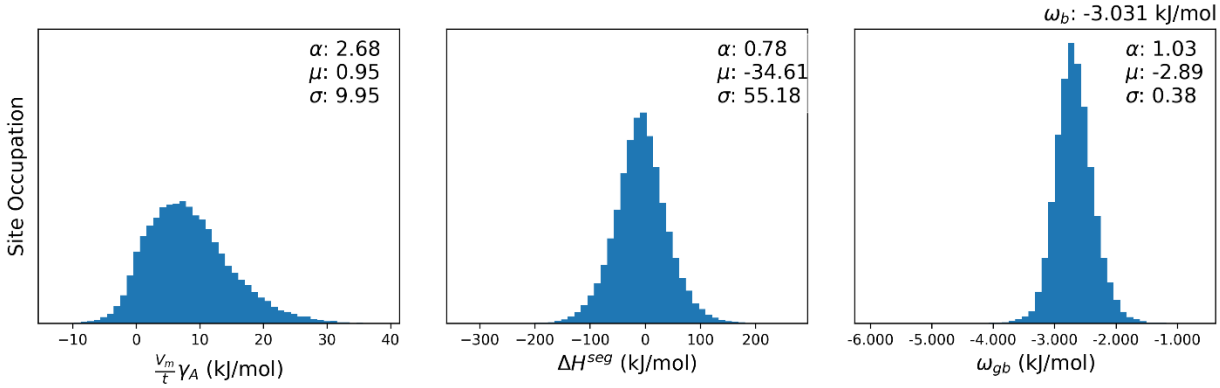

Cu-Pd [162]

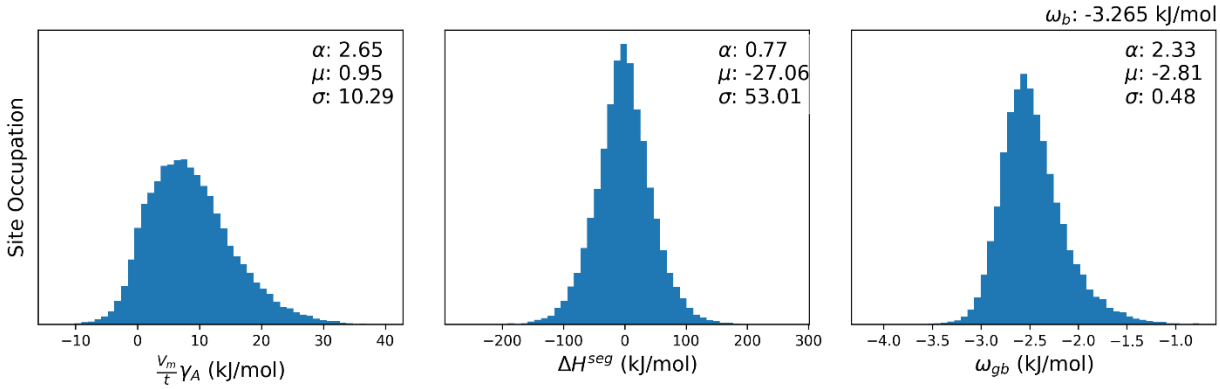

Cu-Pt [130]

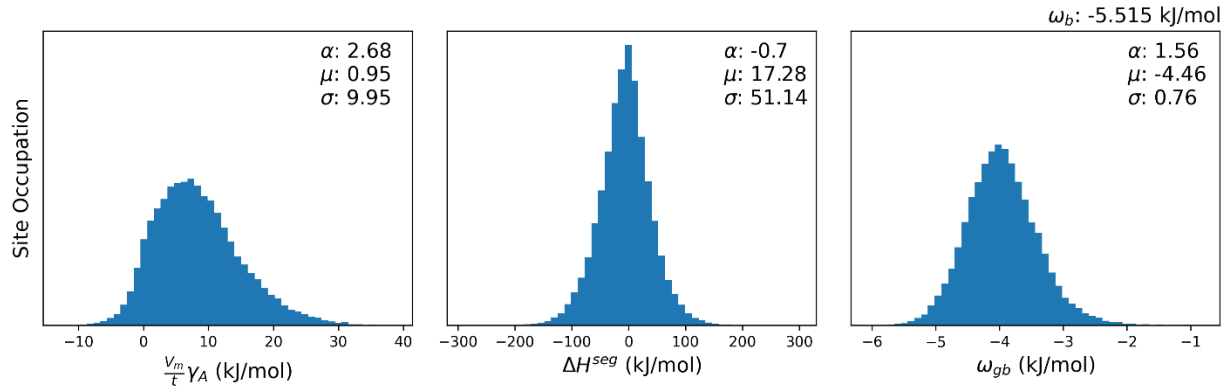

Cu-Pt [162]

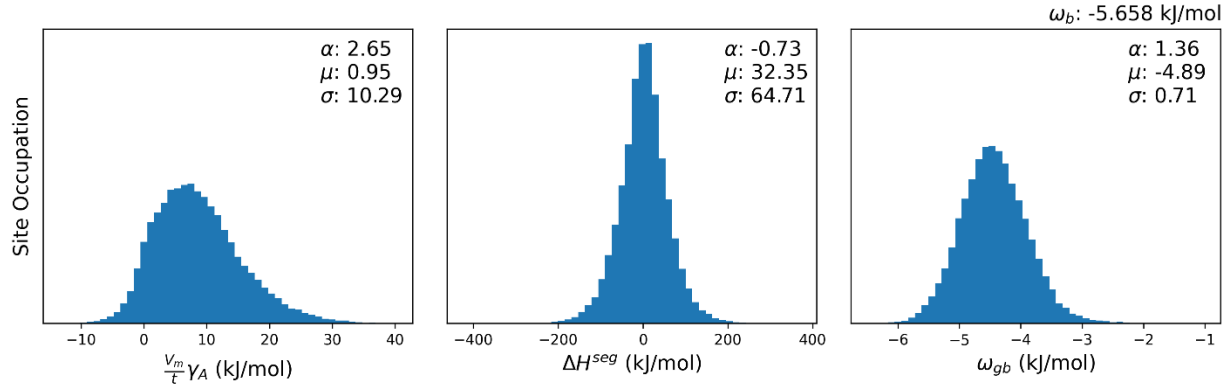

☒ Cu-Ta [163]

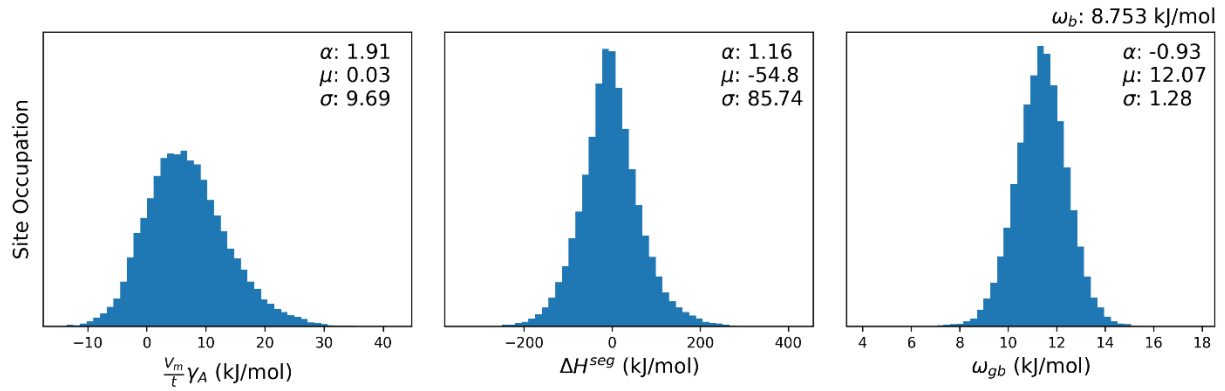

☑☒ Cu-Zr [176]

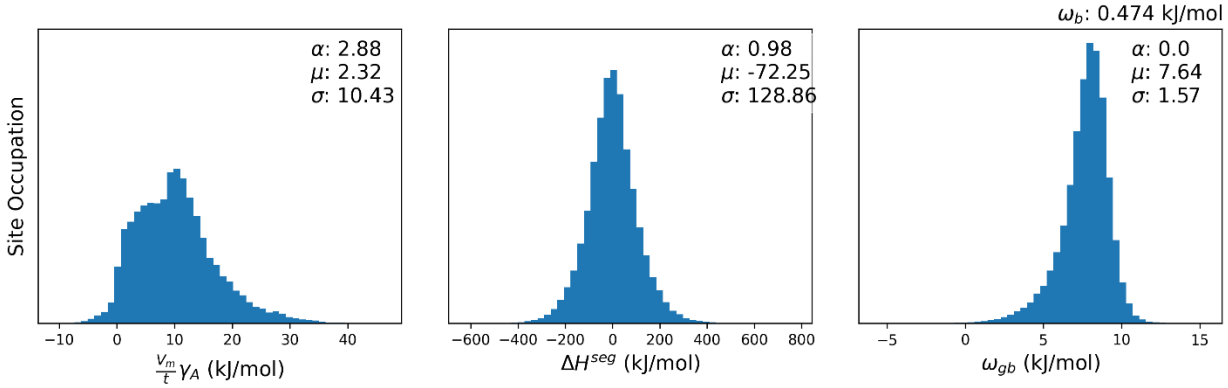

☑☒ Cu-Zr [177]

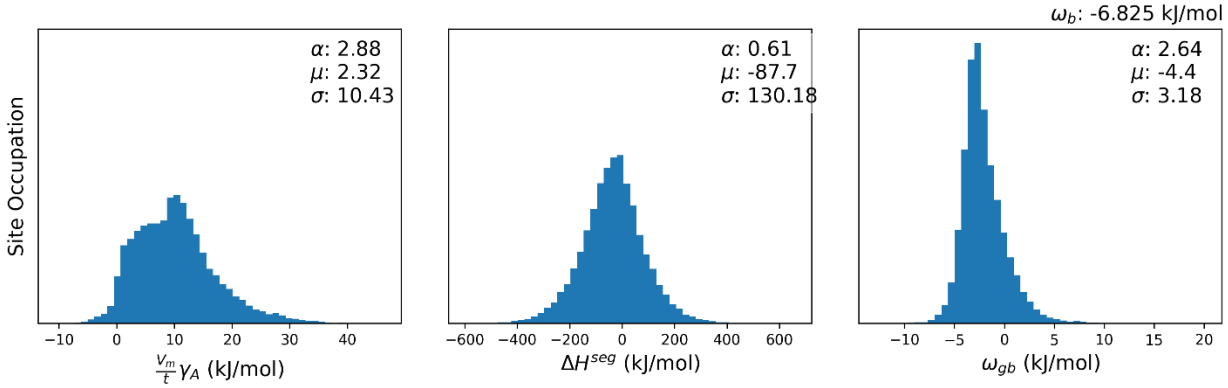

☑ Cu-Zr [178]

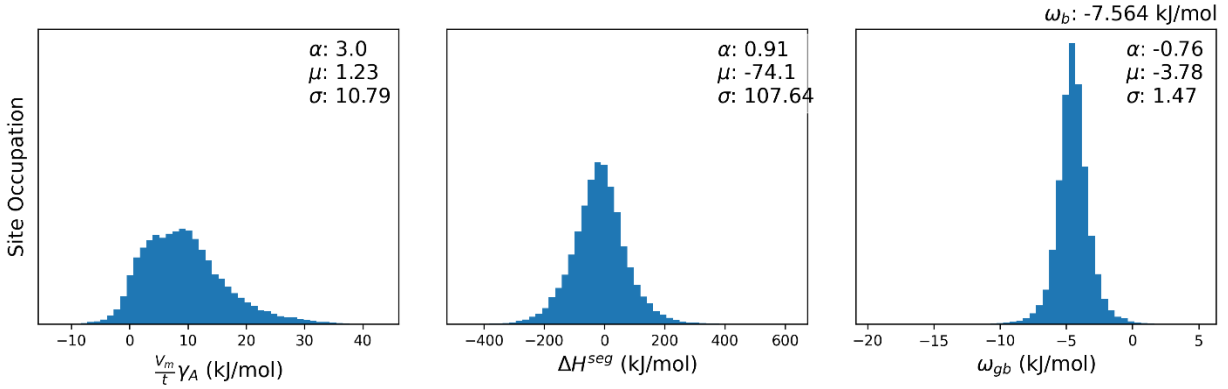

☑☒ Cu-Zr

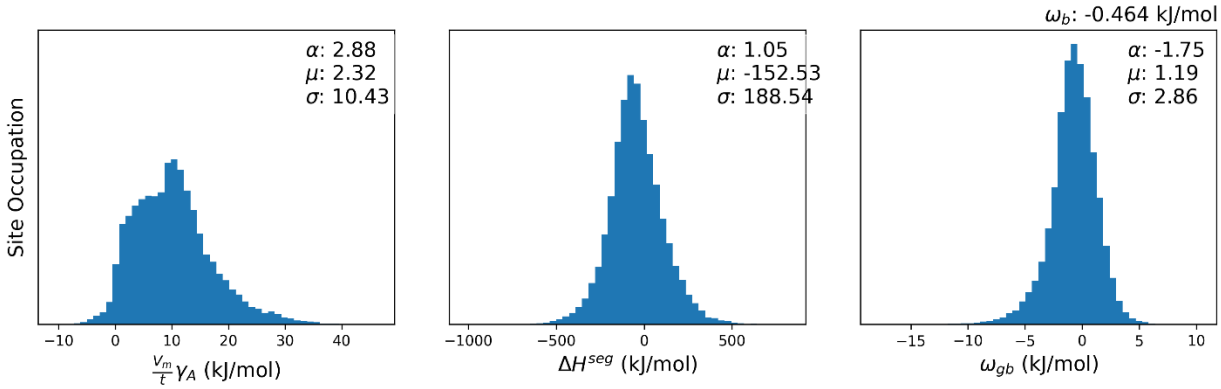

Fe-based Alloys

☑☒ Fe-Al [145]

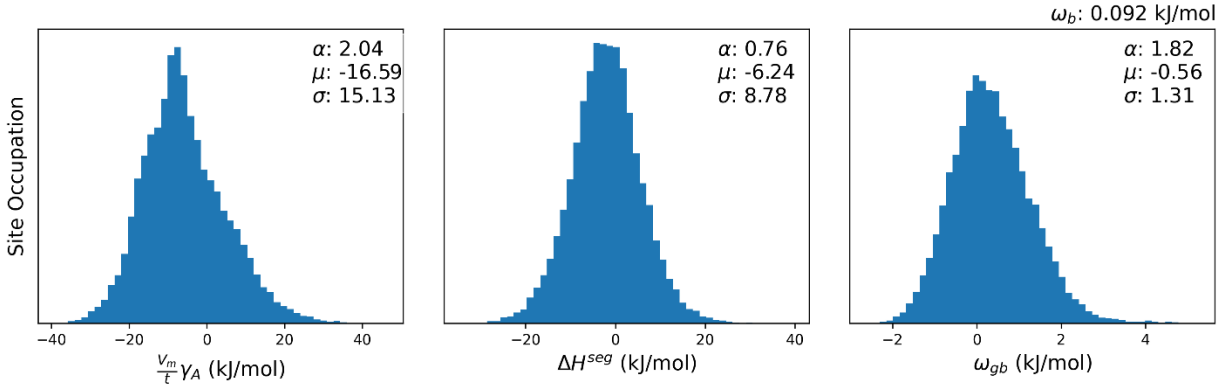

☒ Fe-Cr [170]

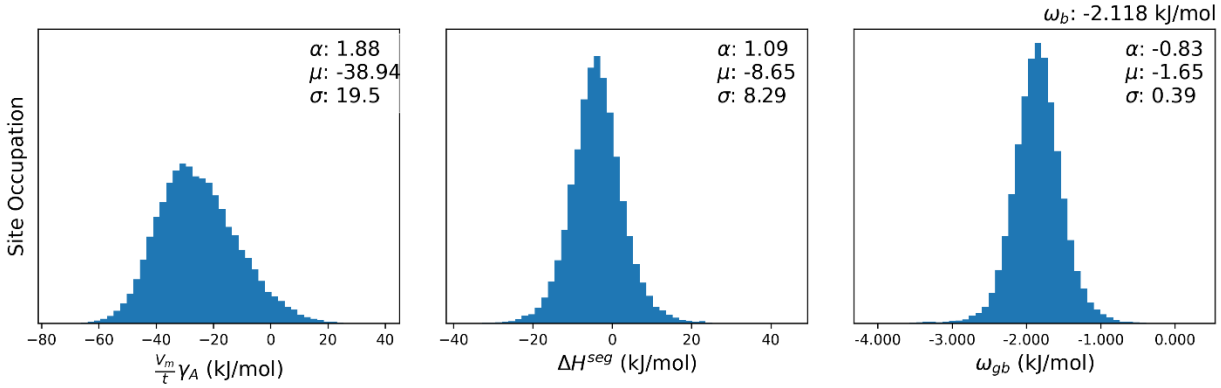

☒ Fe-Cu [171]

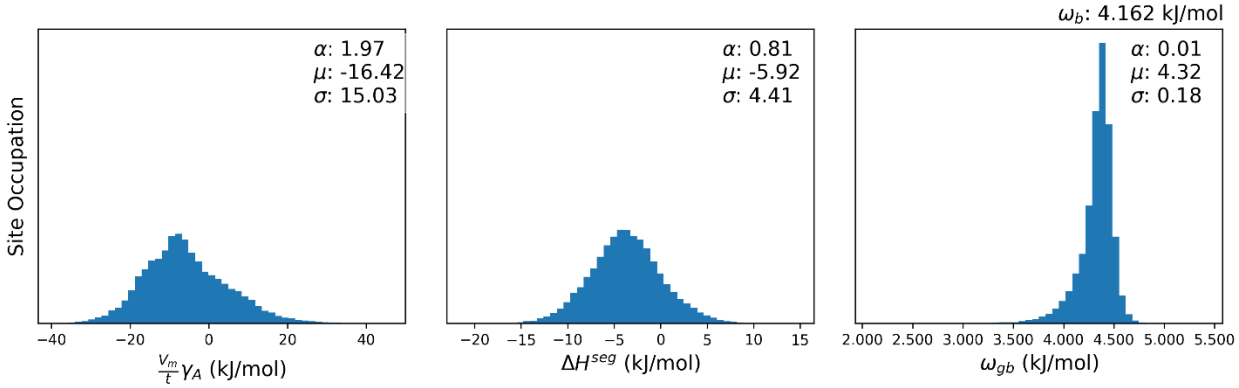

☒ Fe-H [179]

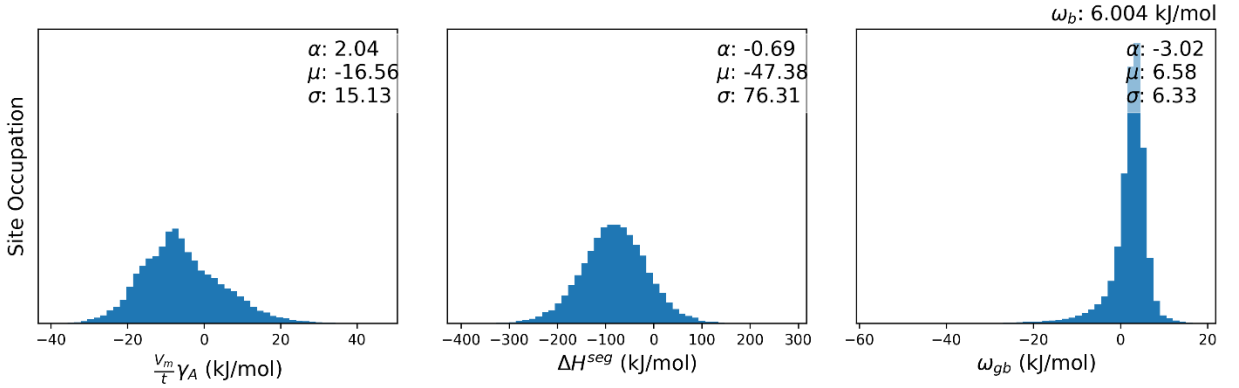

☒ Fe-Ni [171]

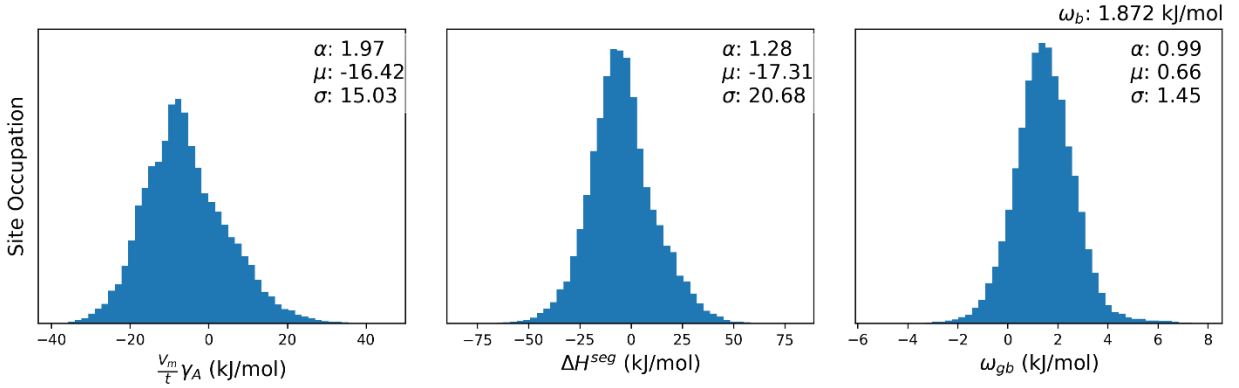

☒ Fe-Ni [180]

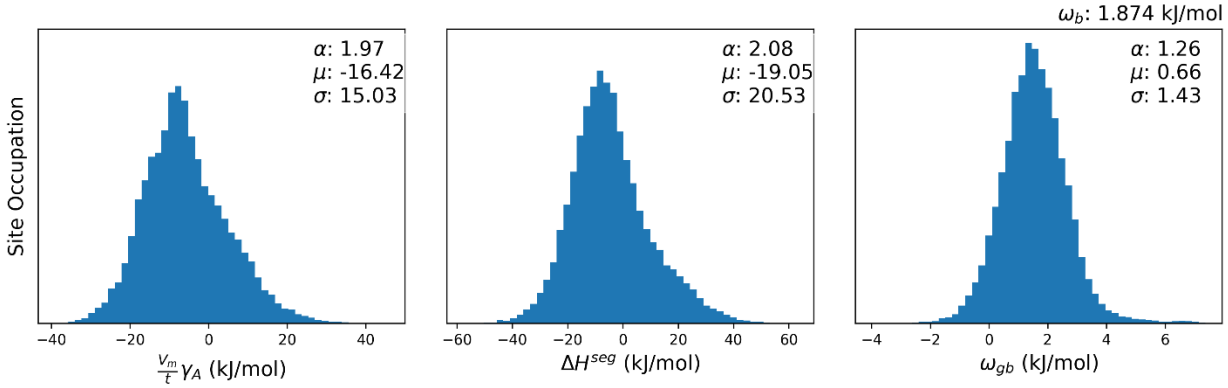

☒ Fe-Ni [170]

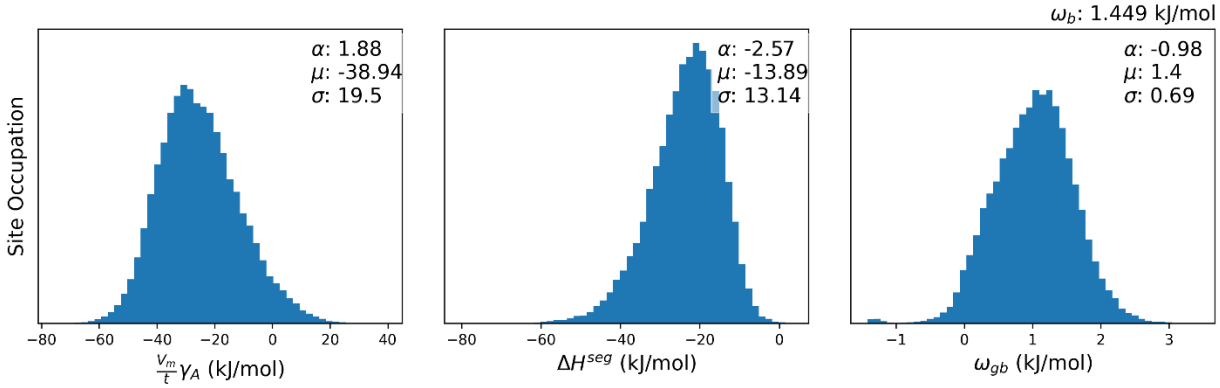

☒ Fe-P [181]

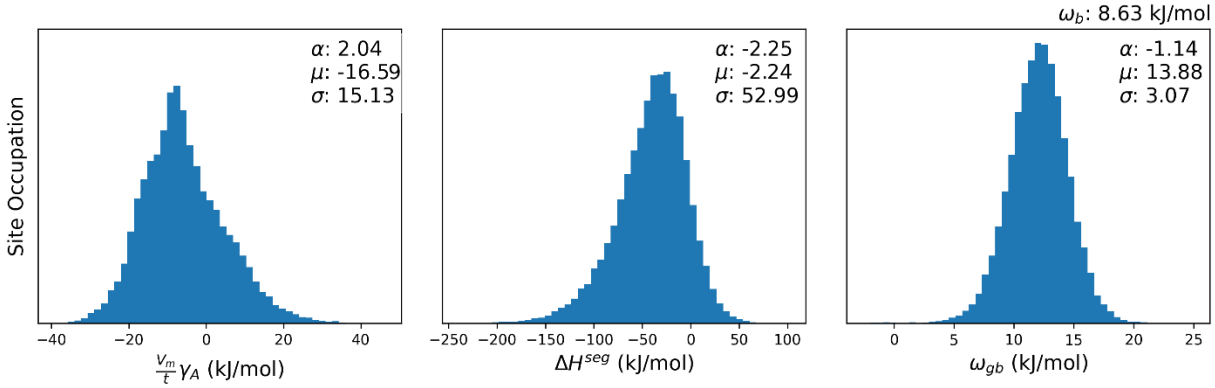

☒ Fe-V [182]

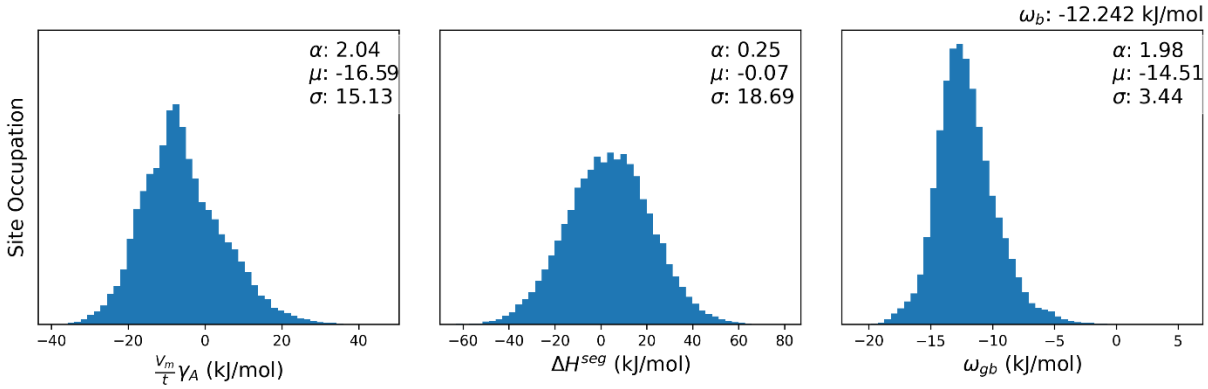

☒ Fe-W [183]

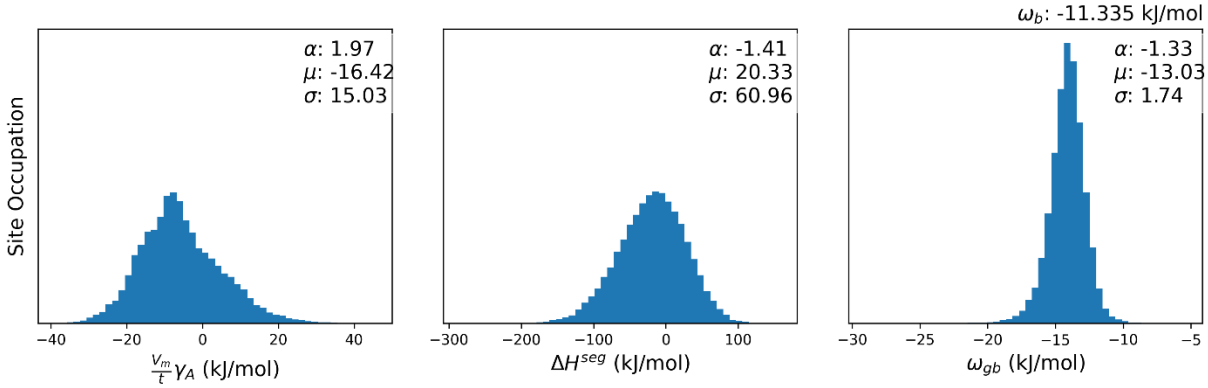

Mg-based Alloys

☒ Mg-Al [146]

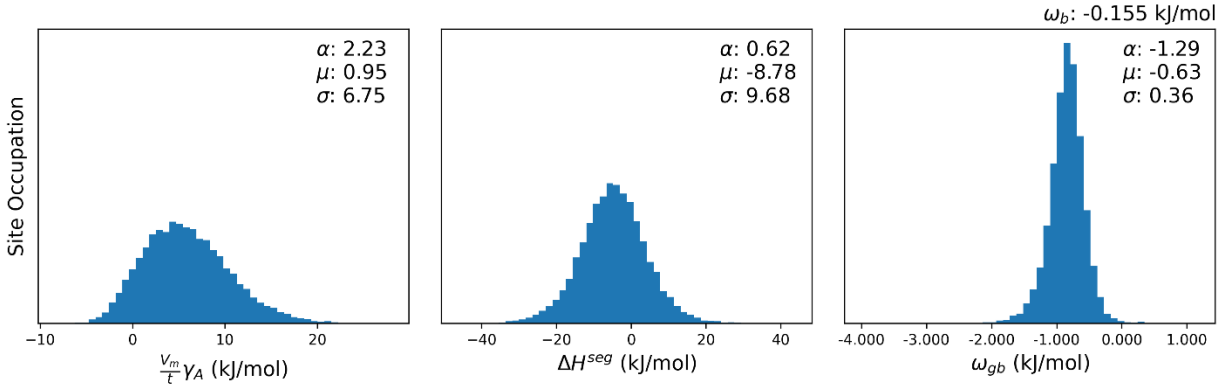

☑ Mg-Al [101]

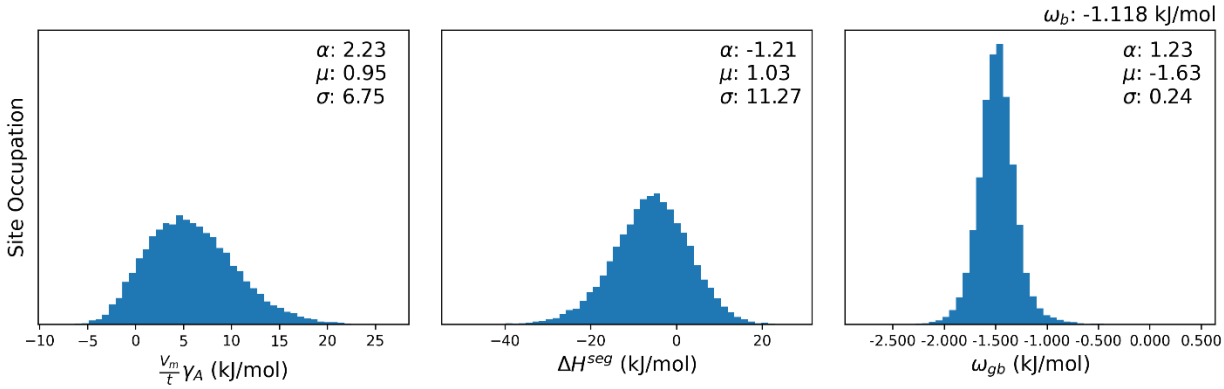

☑☒ Mg-Al [127]

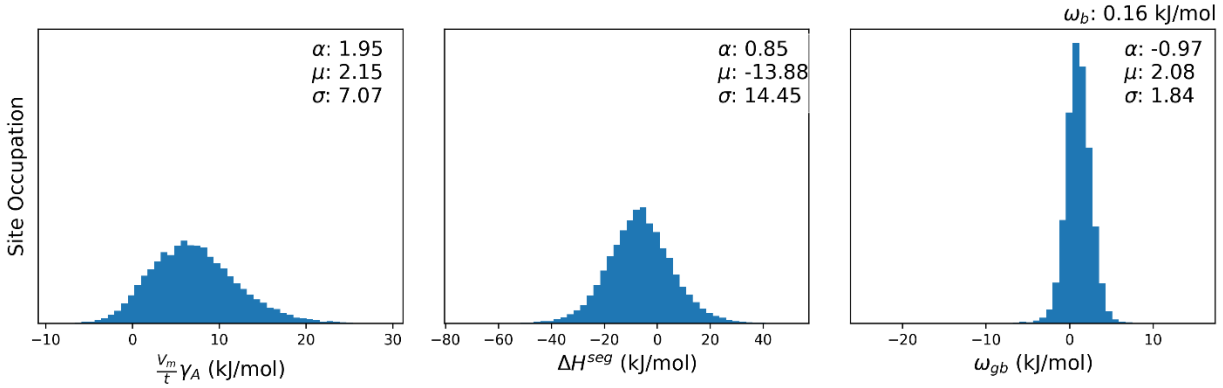

Nb-based Alloys

☒ Nb-Al [147]

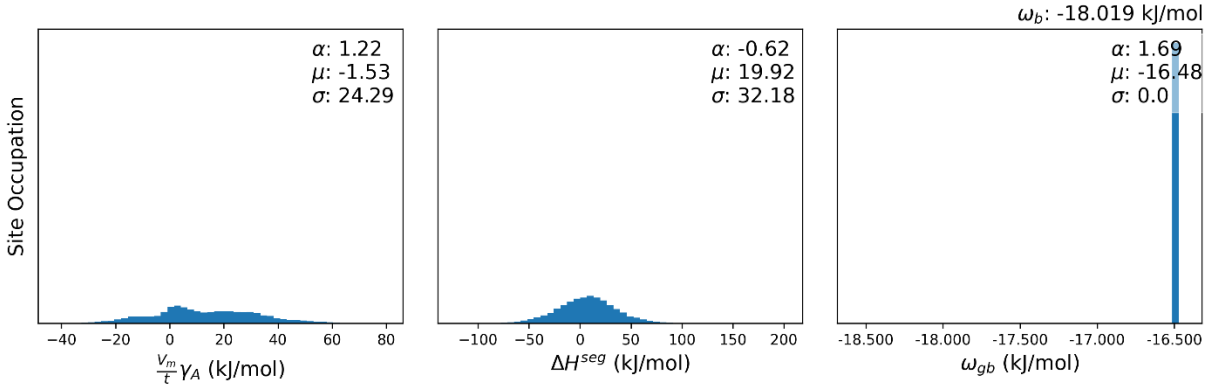

☑ Nb-Ni [129]

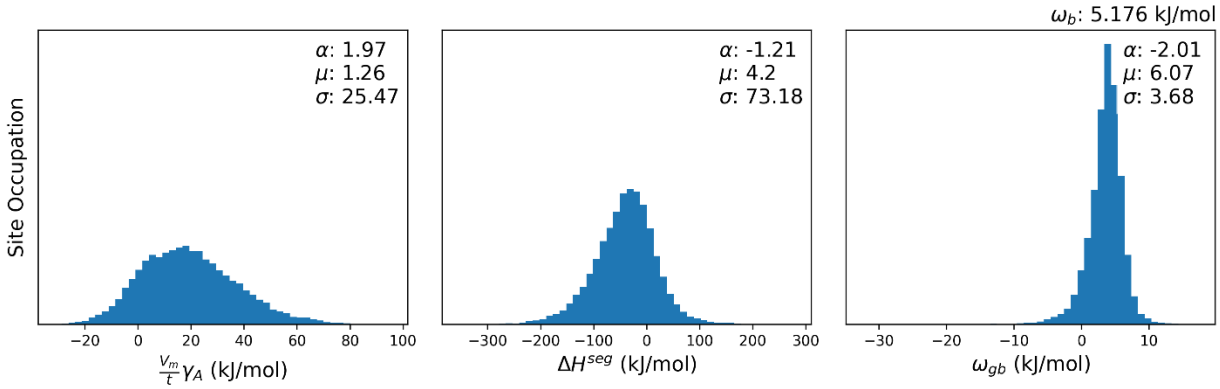

☒ Nb-Ti [147]

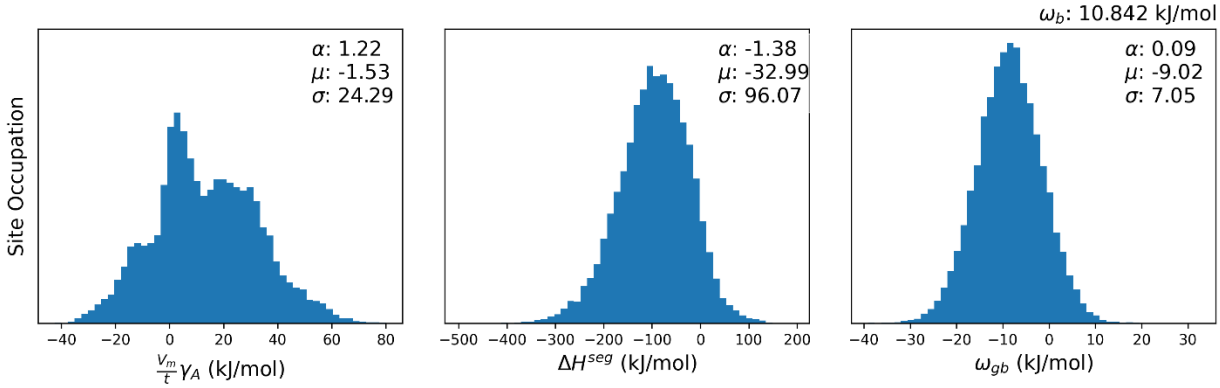

Ni-based Alloys

☒ Ni-Ag [130]

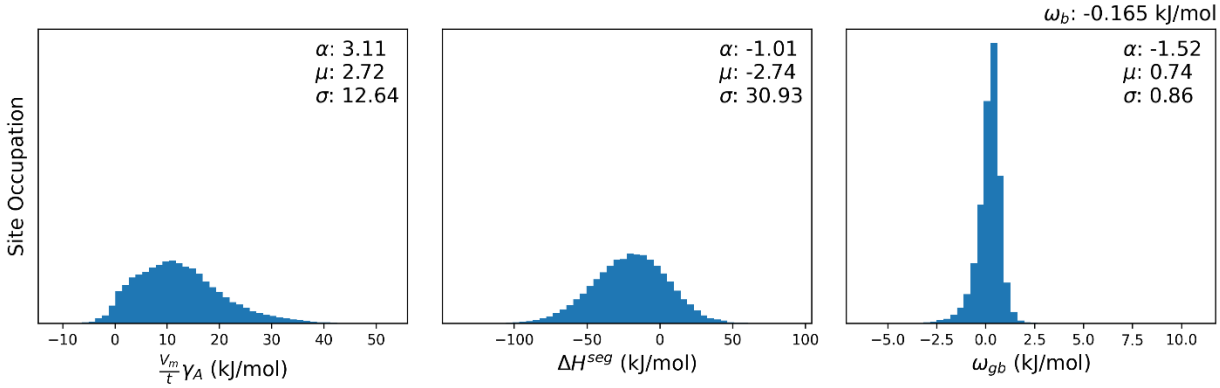

☒ Ni-Ag [162]

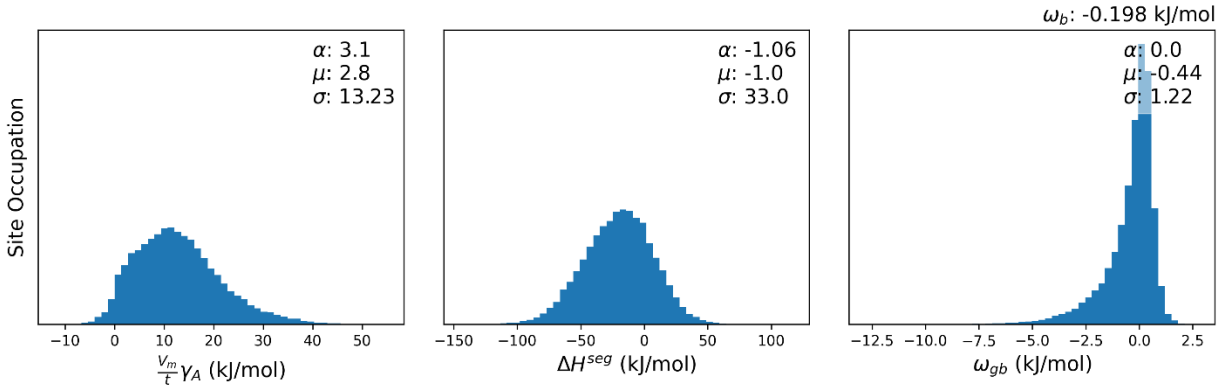

☑ Ni-Ag [165]

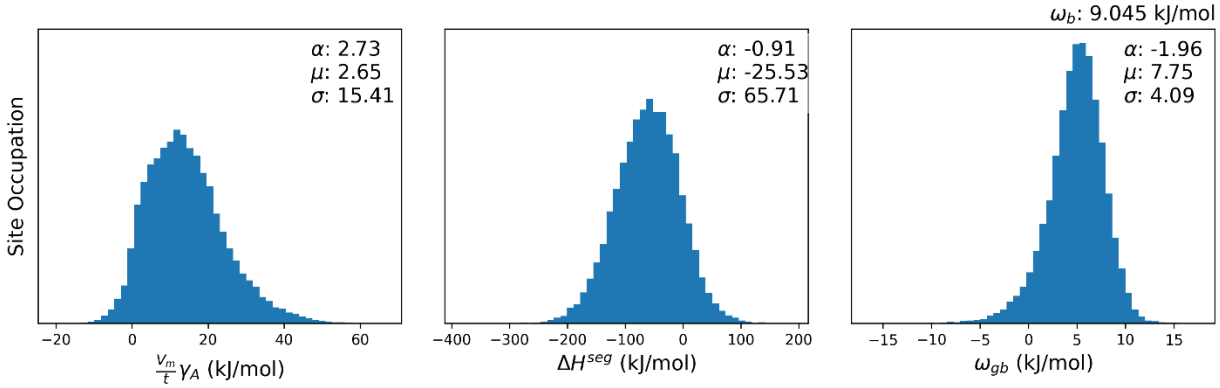

☒ Ni-Al [148]

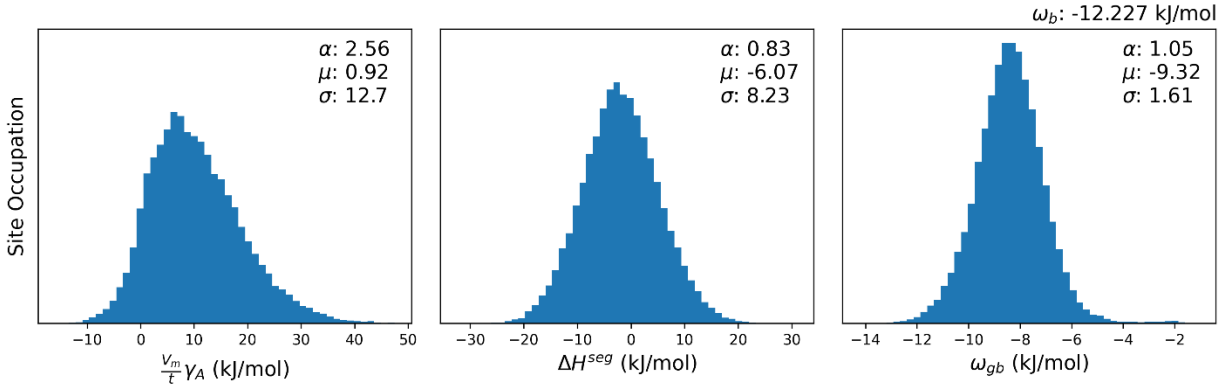

☒ Ni-Al [149]

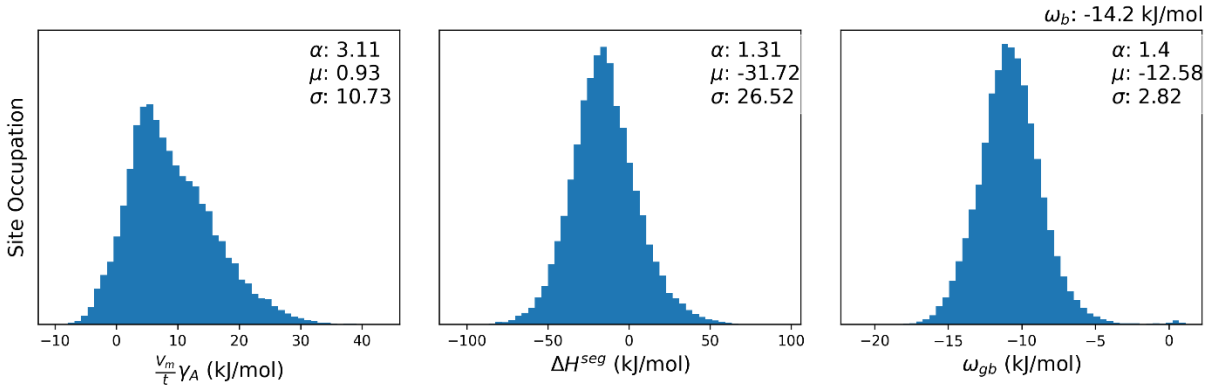

☒ Ni-Al [150]

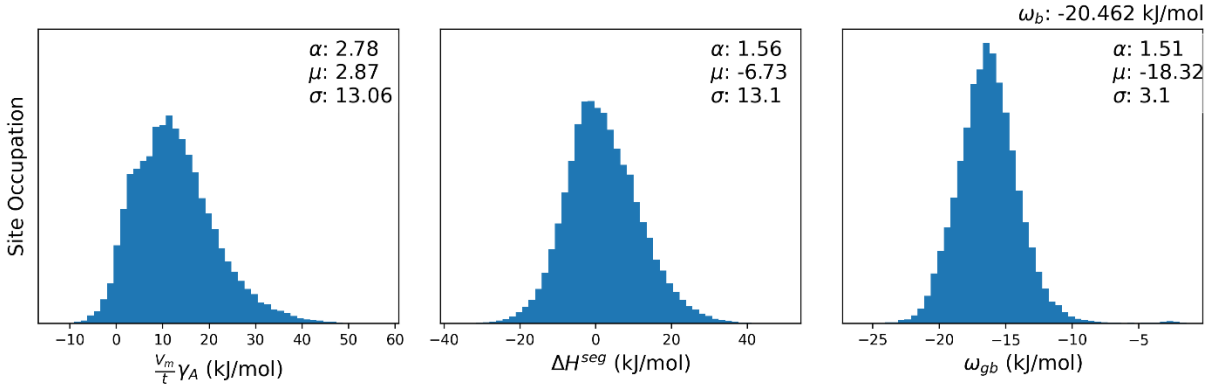

☒ Ni-Al [151]

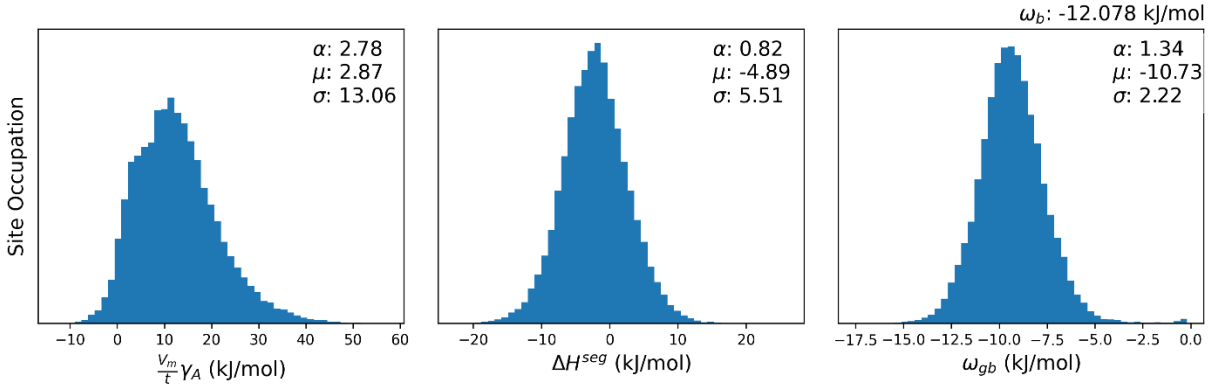

Ni-Al [166]

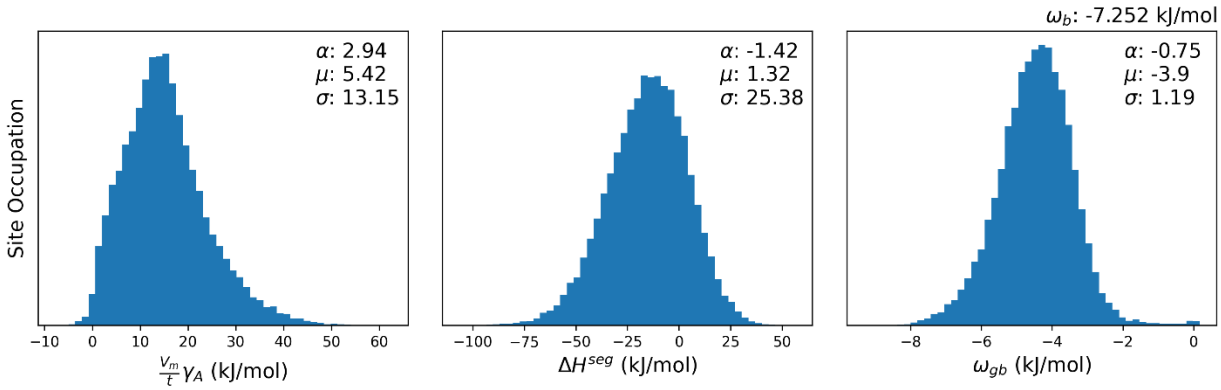

Ni-Au [130]

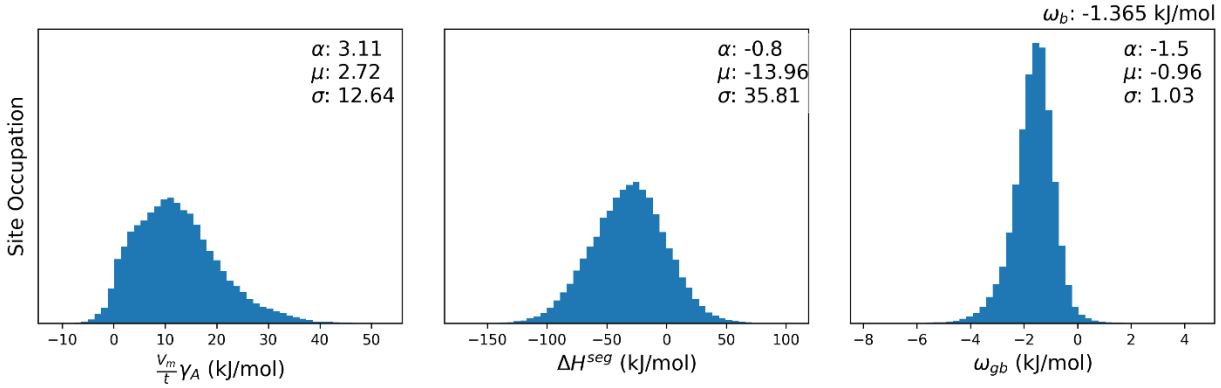

Ni-Au [162]

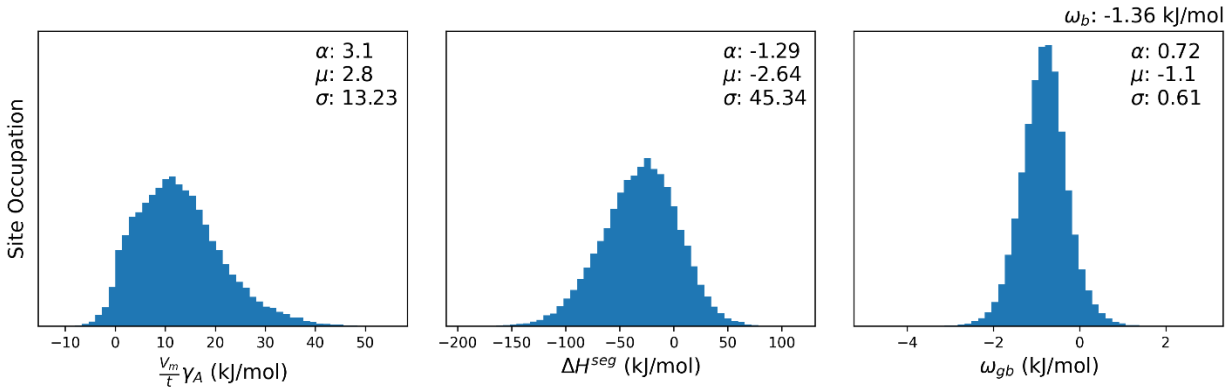

Ni-Co [143]

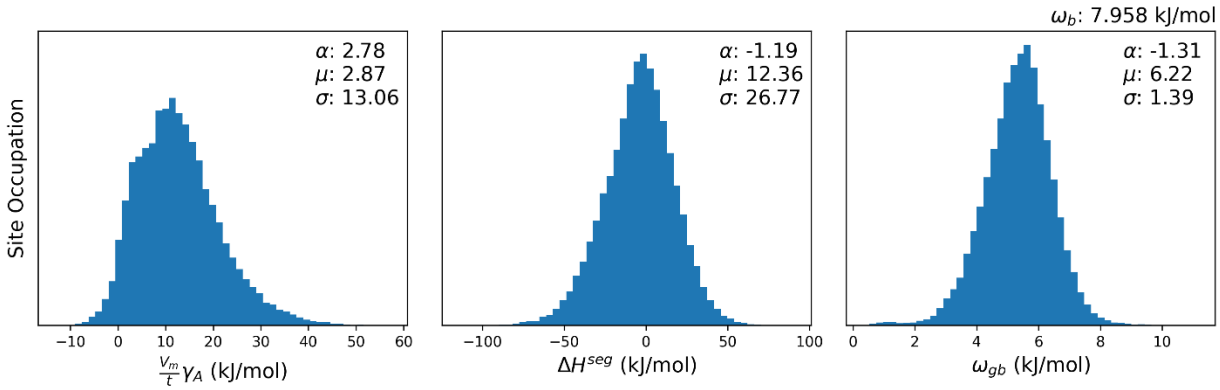

Ni-Co [169]

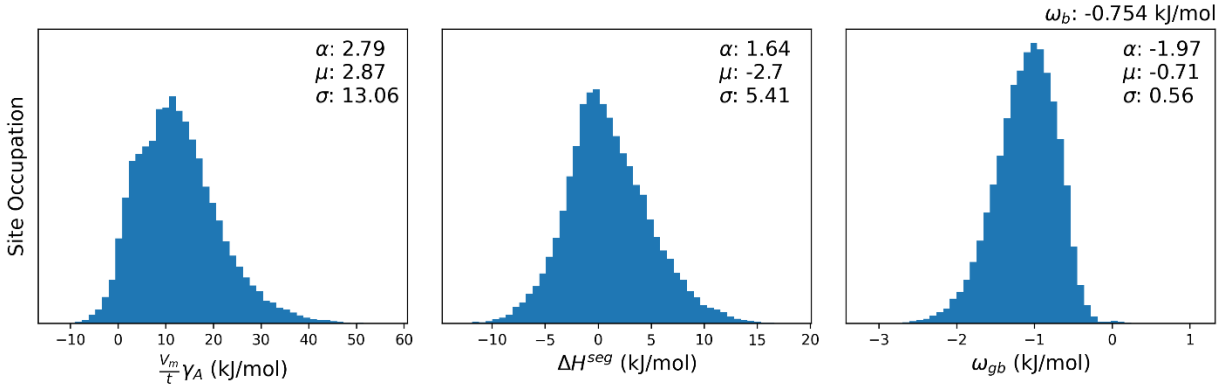

☒ Ni-Co [167]

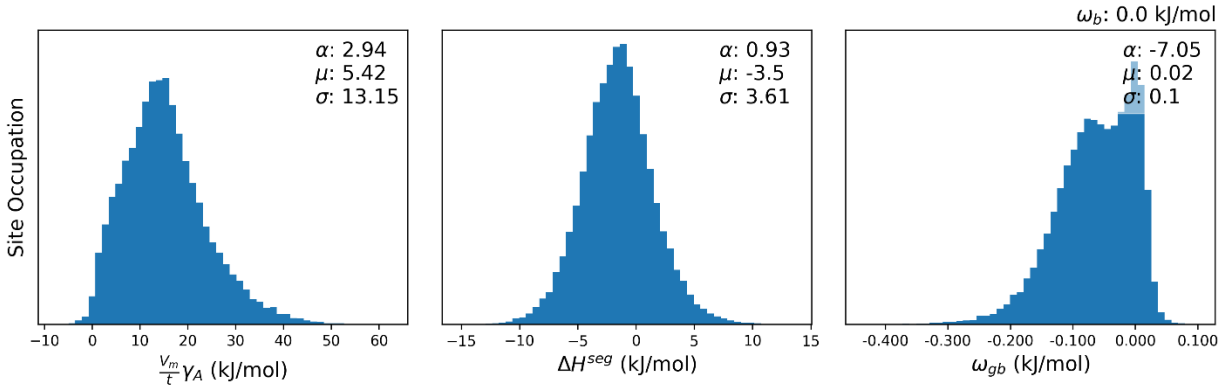

☒ Ni-Co [166]

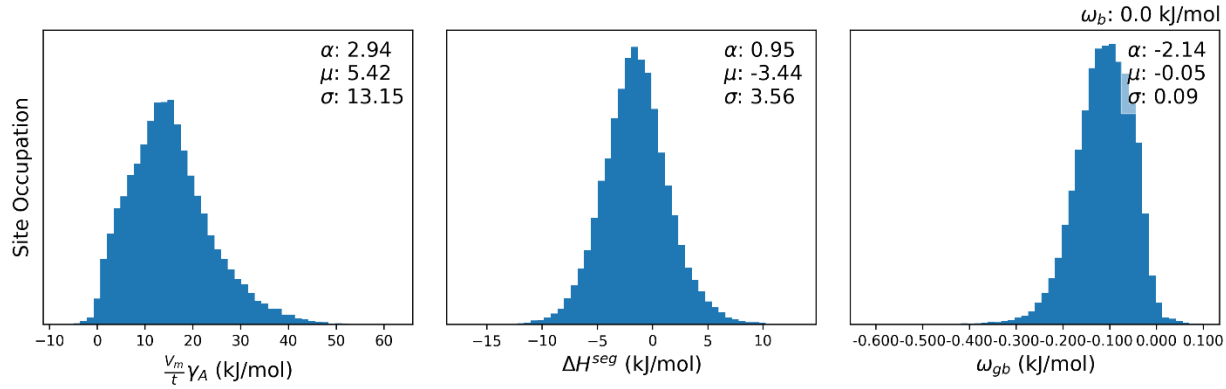

Ni-Cr [184]

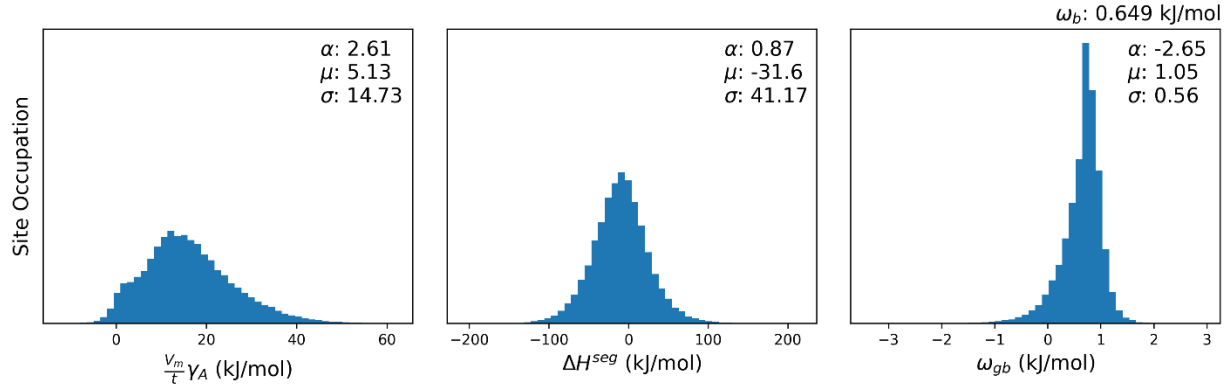

Ni-Cr [185]

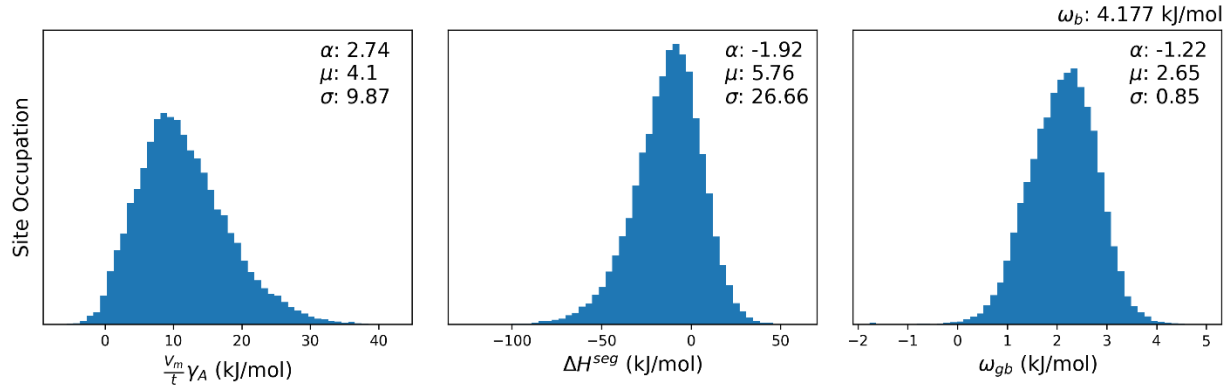

Ni-Cr [186]

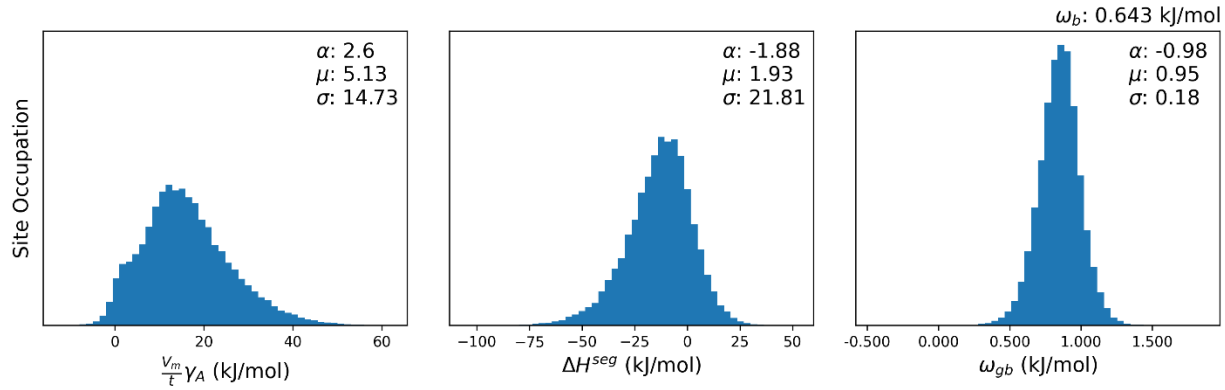

☒ Ni-Cr [167]

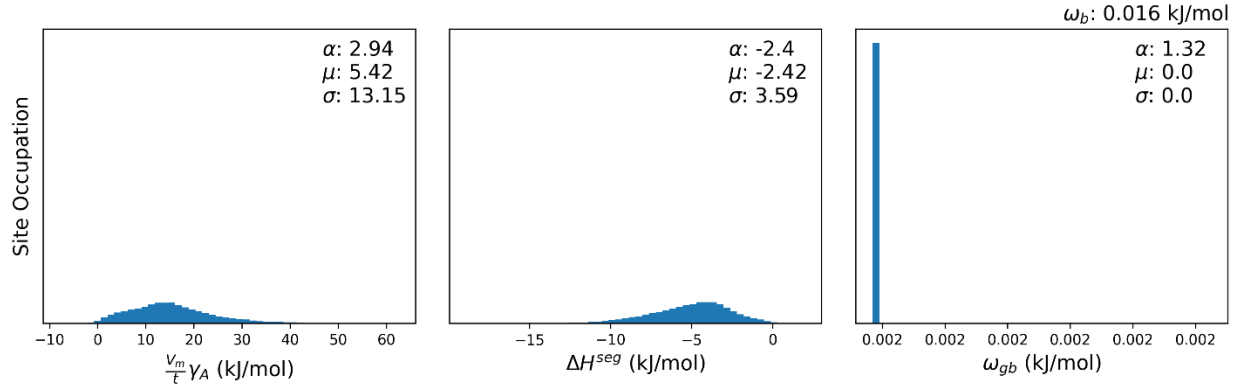

☒ Ni-Cr [170]

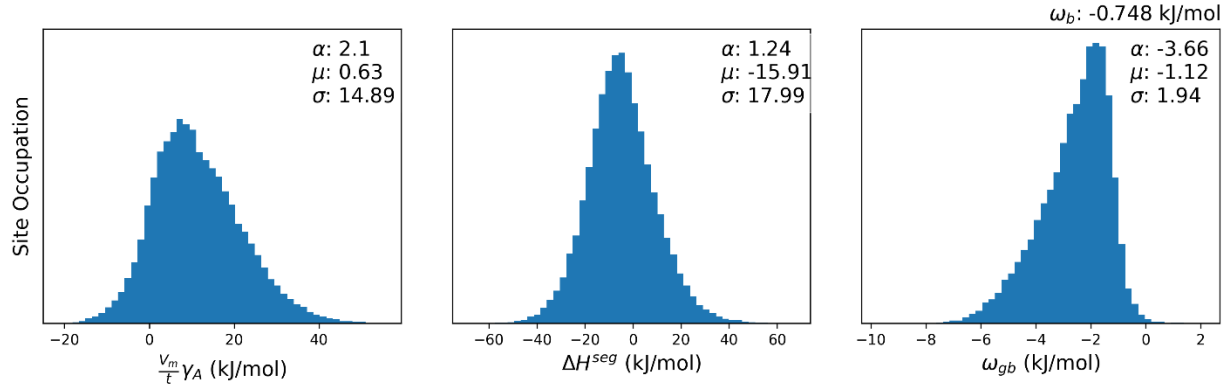

☒ Ni-Cr [166]

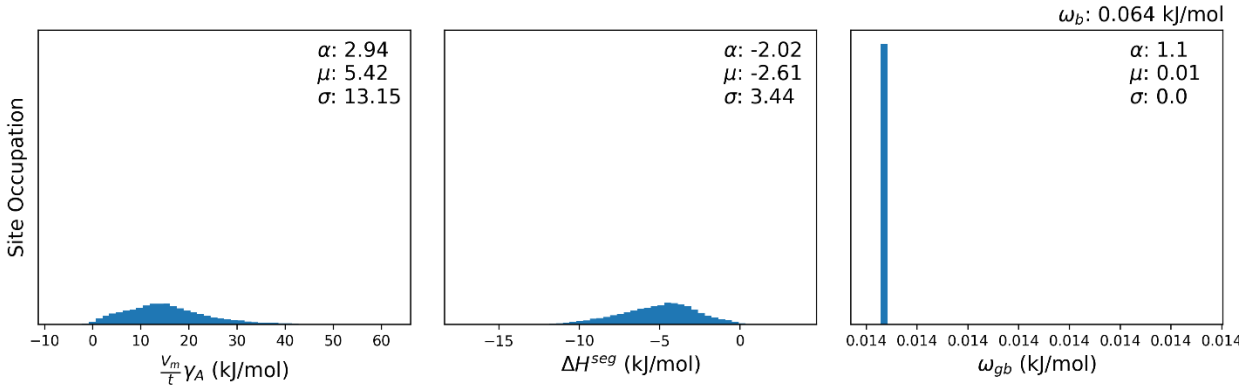

☒ Ni-Cu [172]

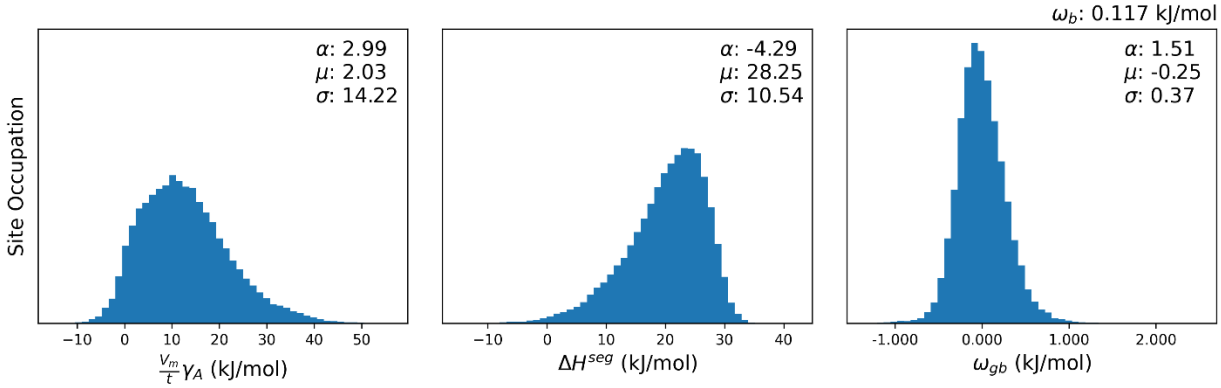

Ni-Cu [130]

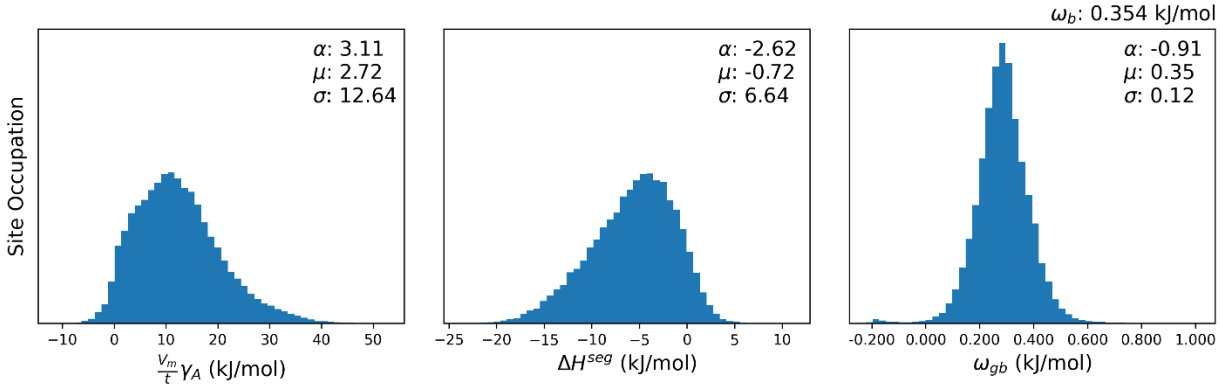

Ni-Cu [162]

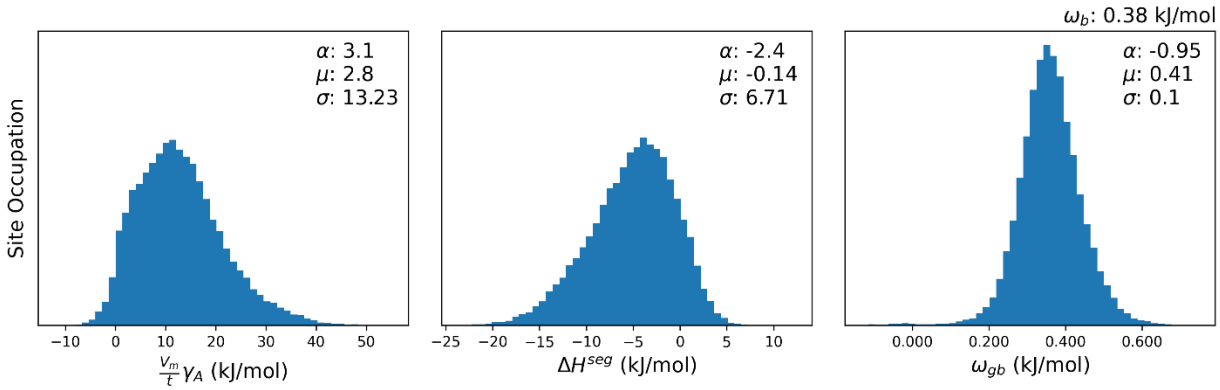

Ni-Cu [171]

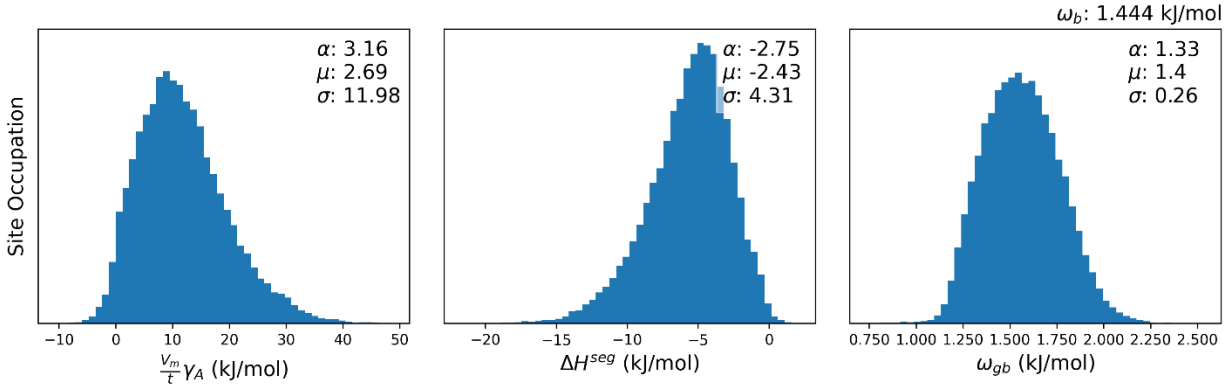

Ni-Cu [173]

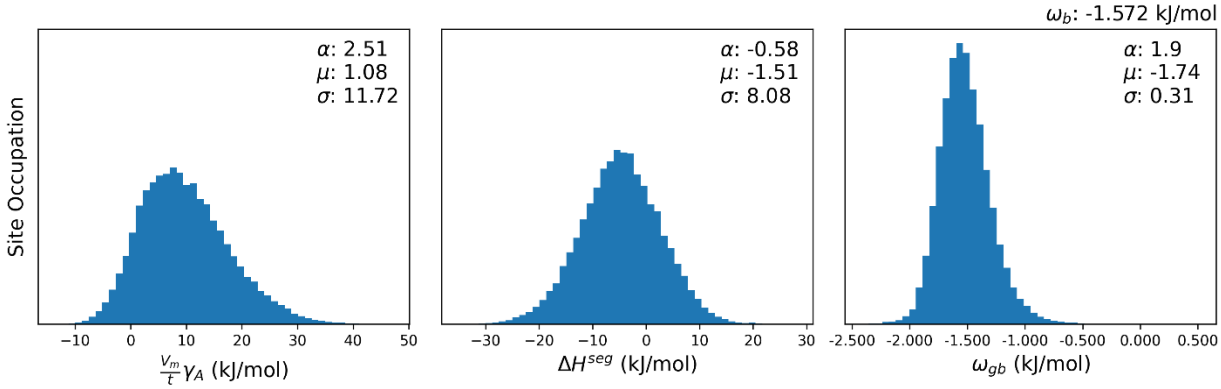

Ni-Cu [167]

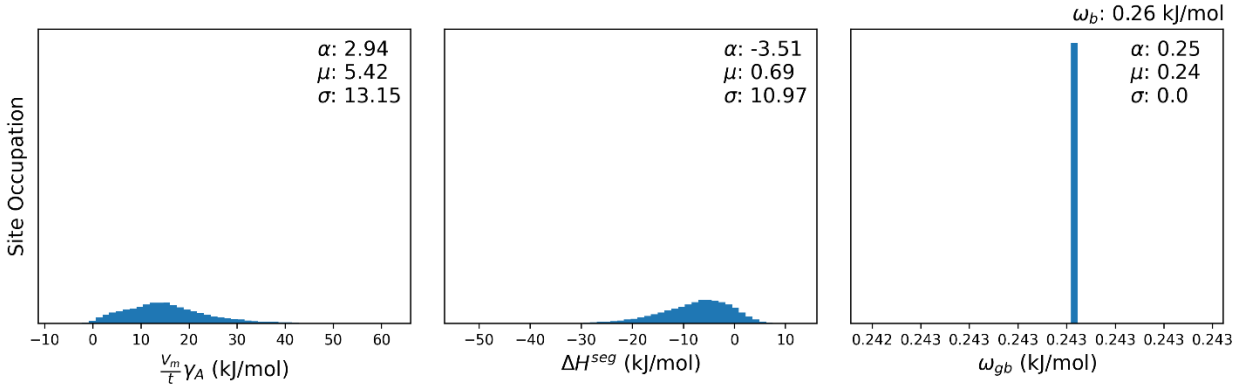

☑☒ Ni-Cu [174]

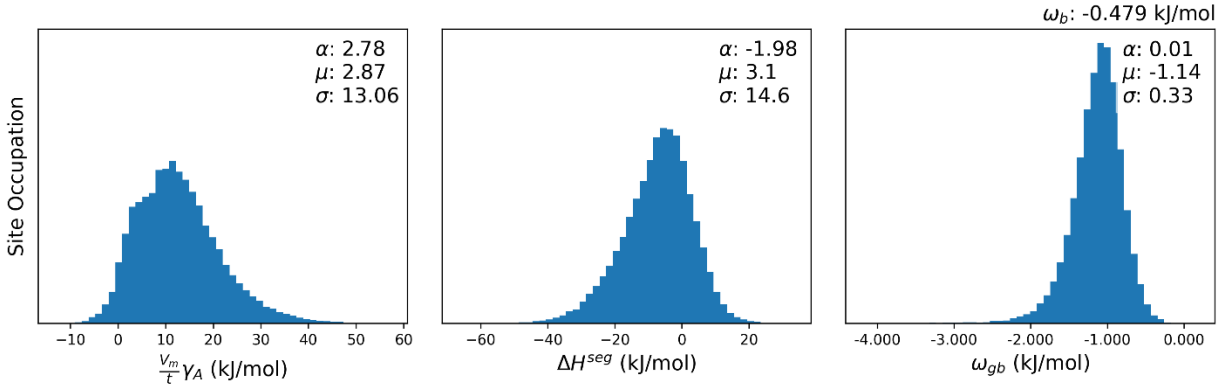

☒ Ni-Fe [171]

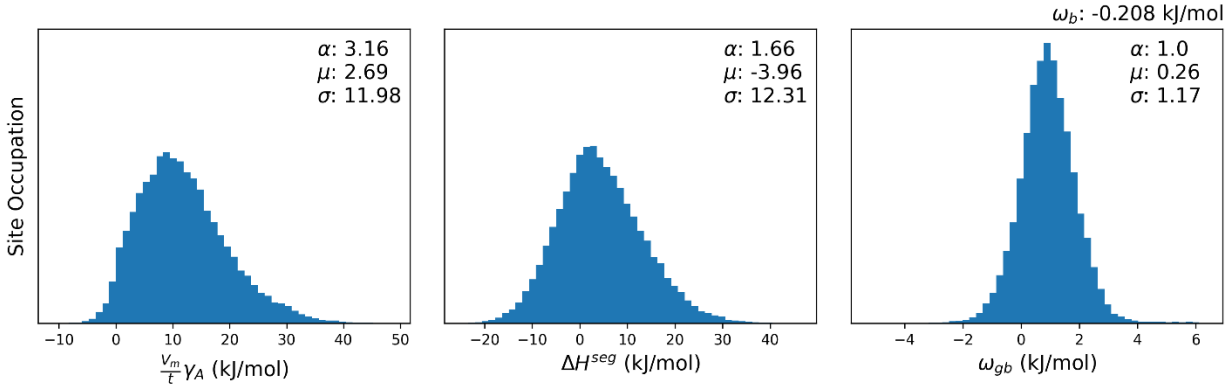

☒ Ni-Fe [184]

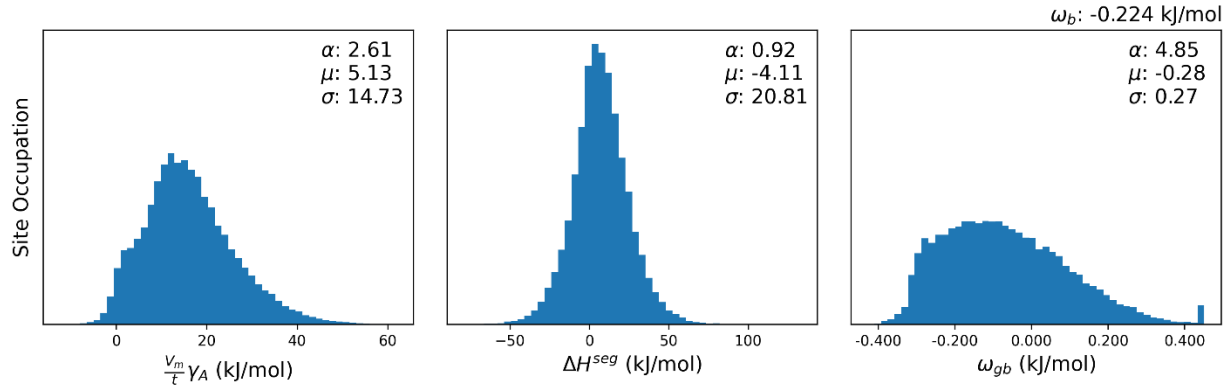

Ni-Fe [185]

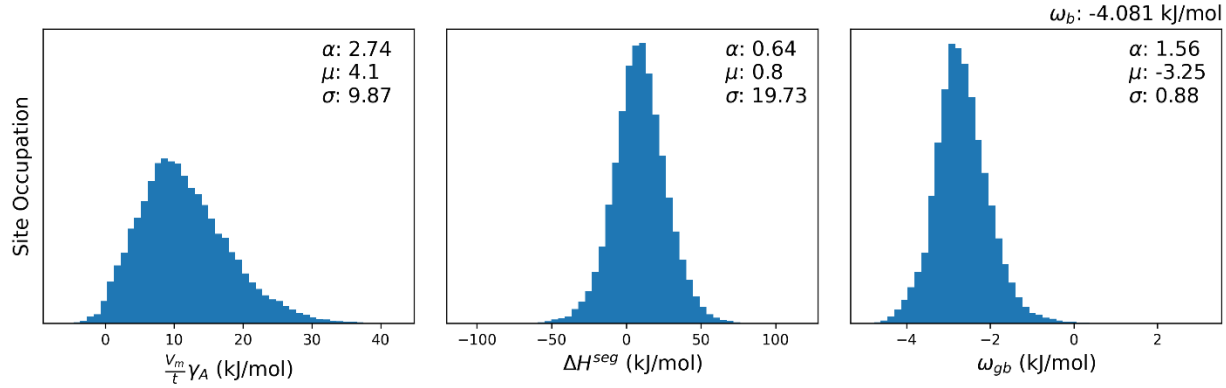

☒ Ni-Fe [186]

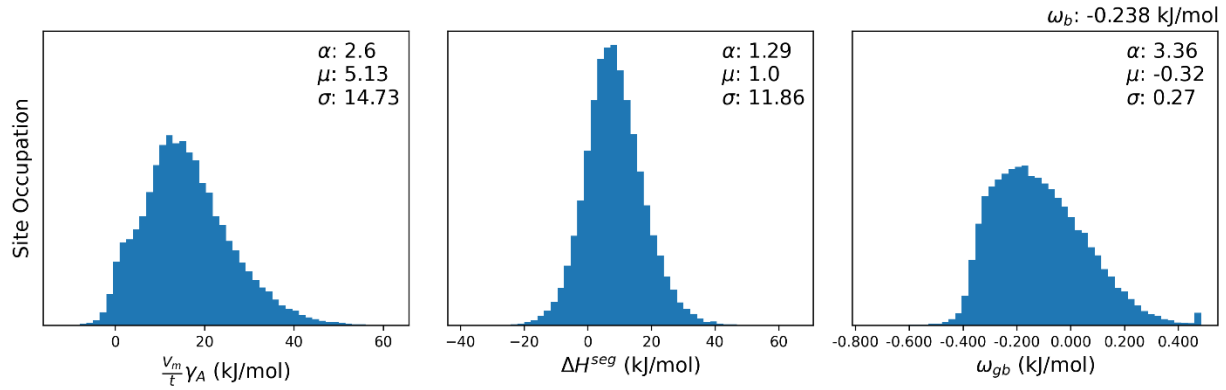

☒ Ni-Fe [167]

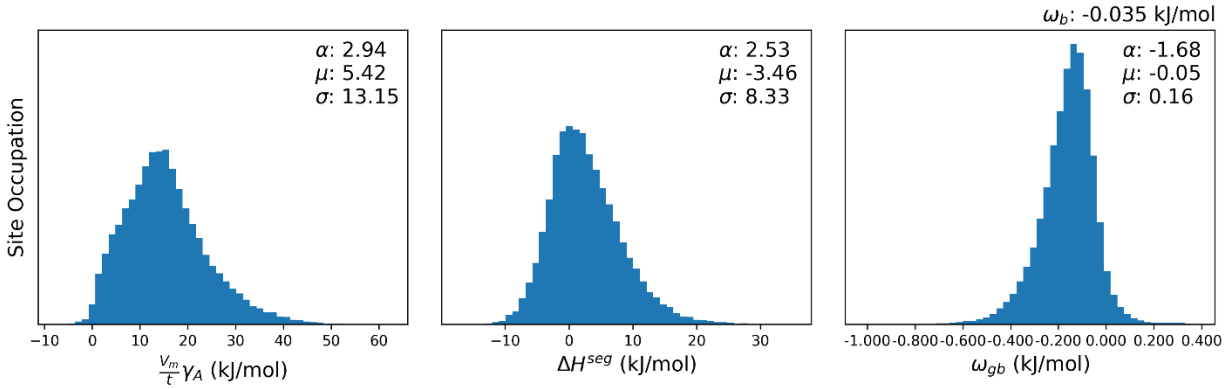

Ni-Fe [170]

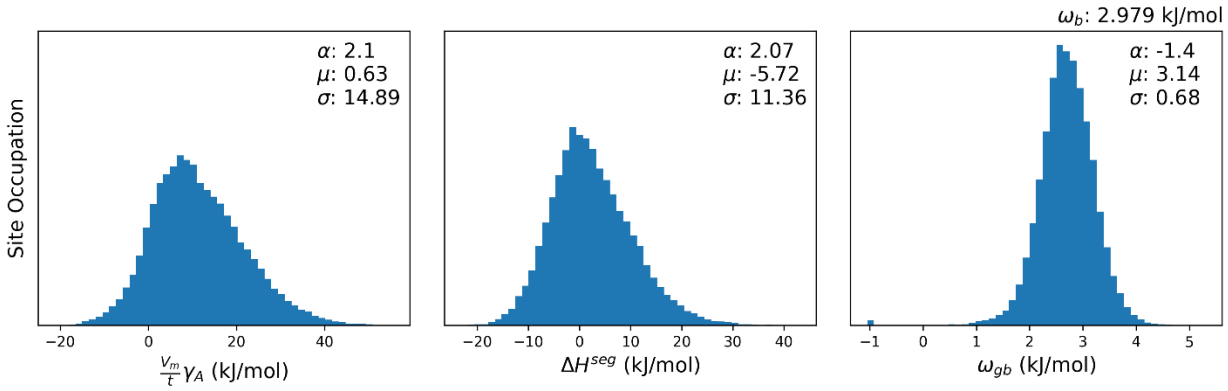

☒ Ni-Fe [166]

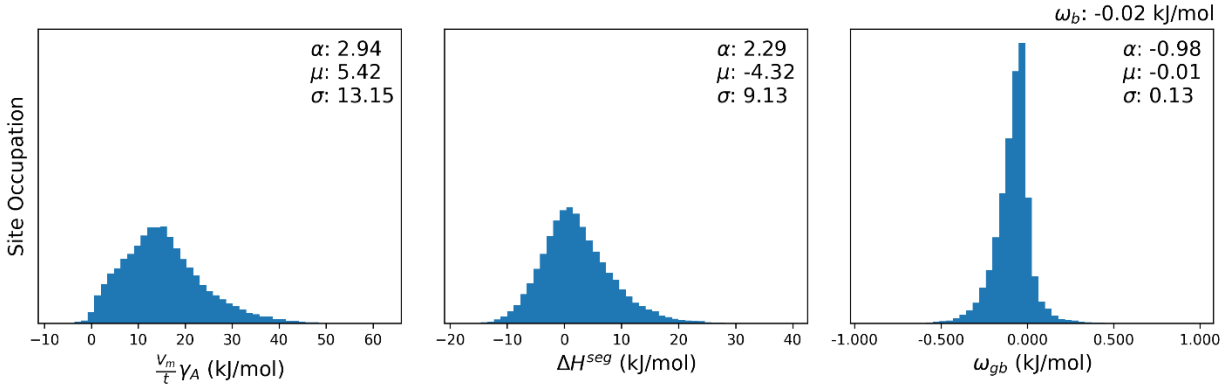

☑☒ Ni-Nb [129]

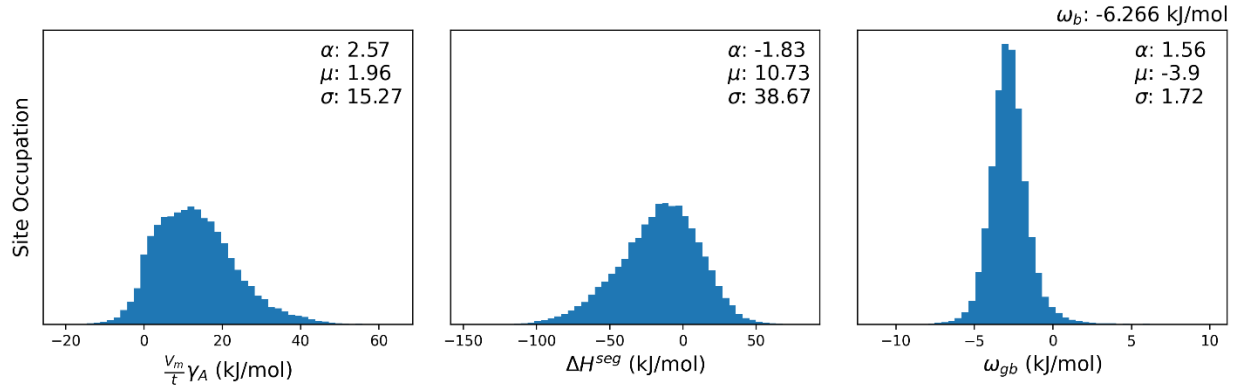

Ni-Pd [130]

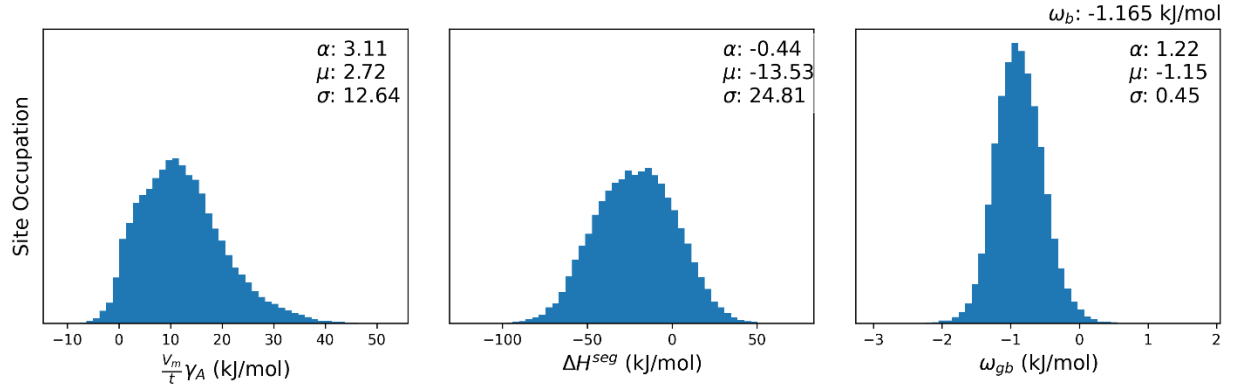

Ni-Pd [162]

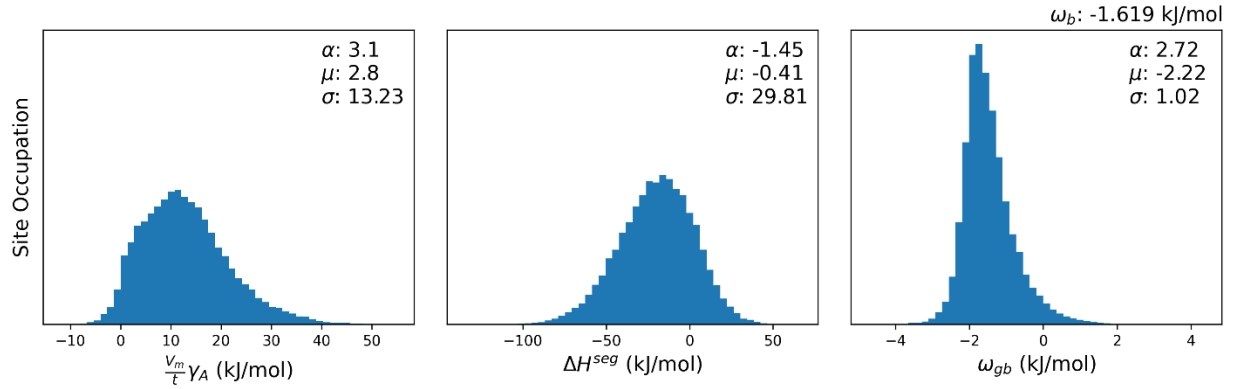

Ni-Pd [187]

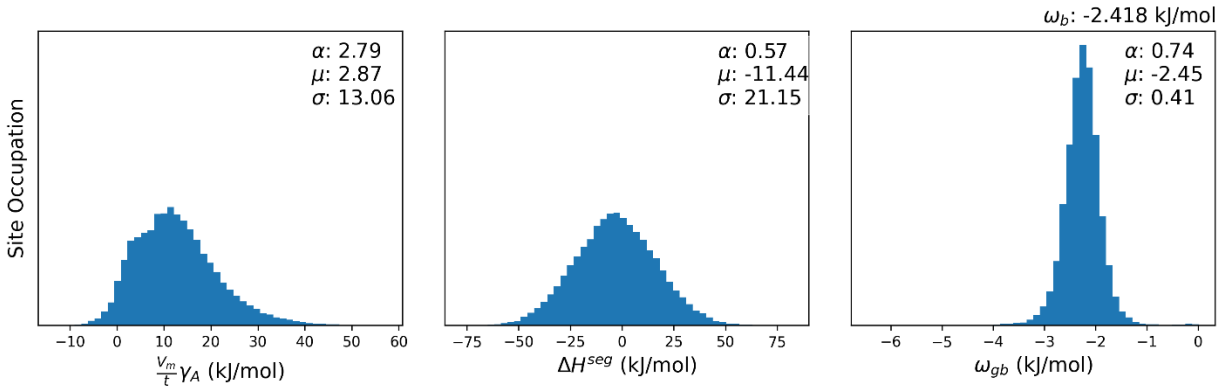

Ni-Pt [130]

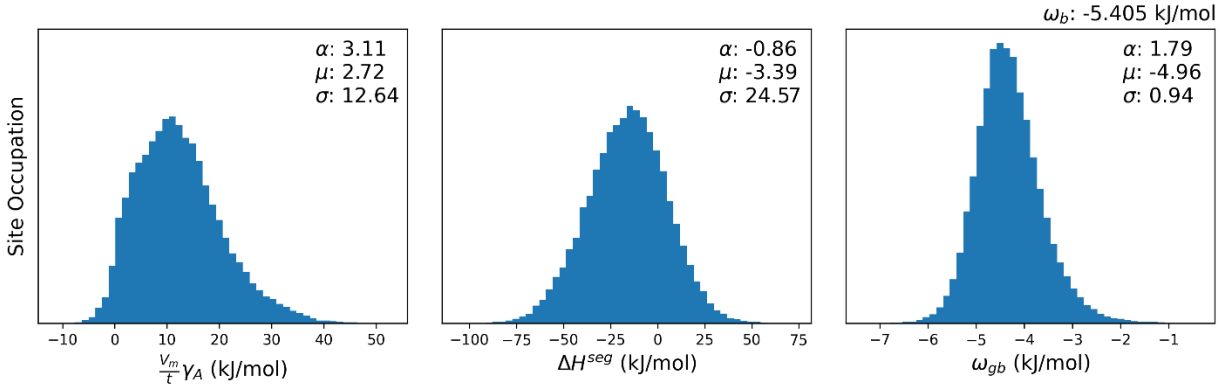

Ni-Pt [162]

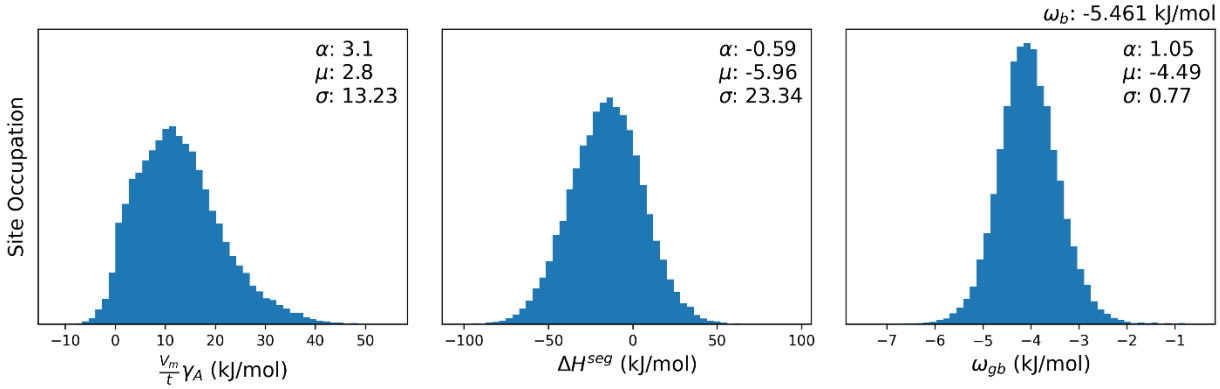

Ni-W [188]

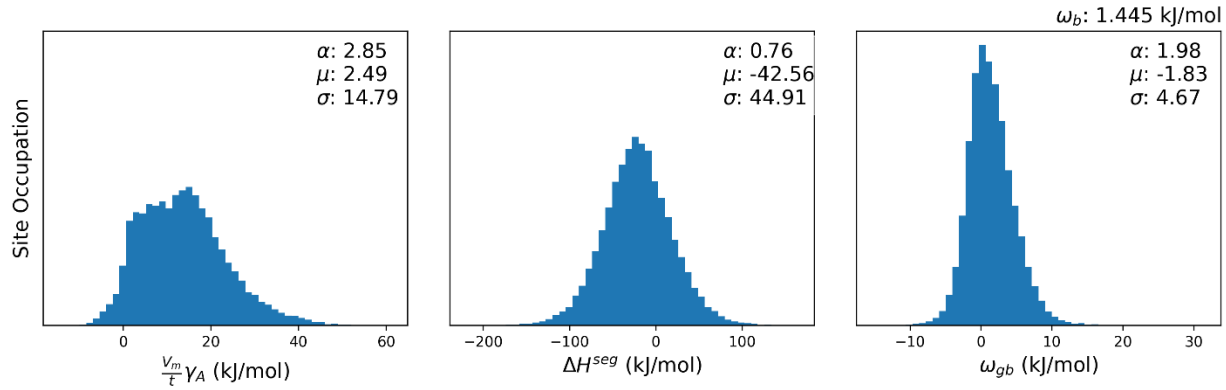

☑☒ Ni-Zr [189]

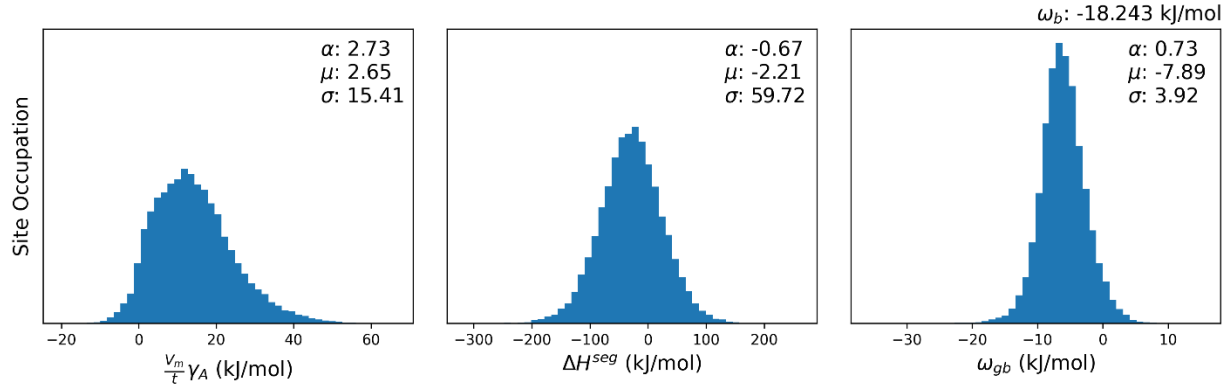

☑☒ Ni-Zr [190]

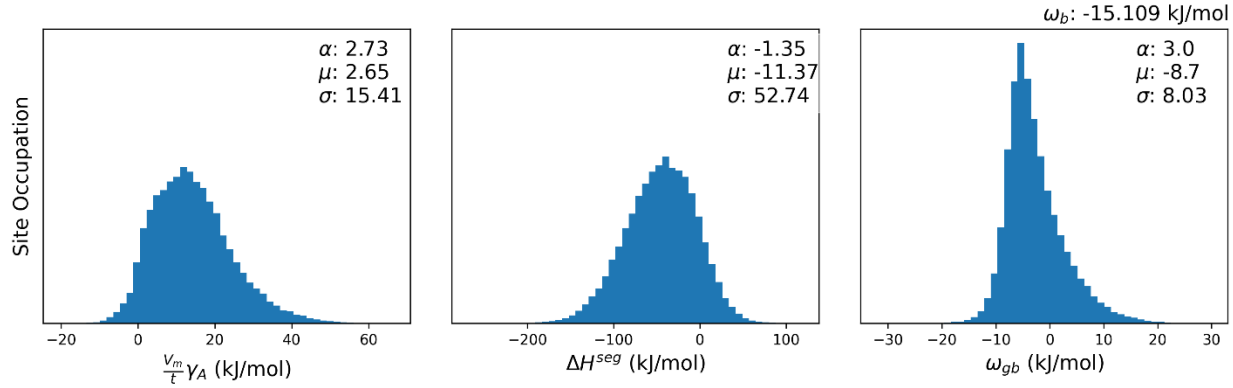

Pd-based Alloys

Pd-Ag [130]

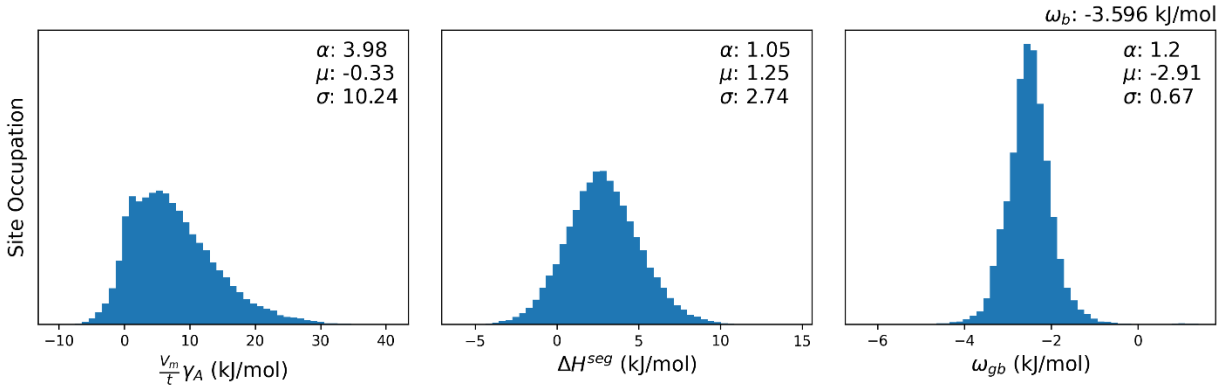

Pd-Ag [162]

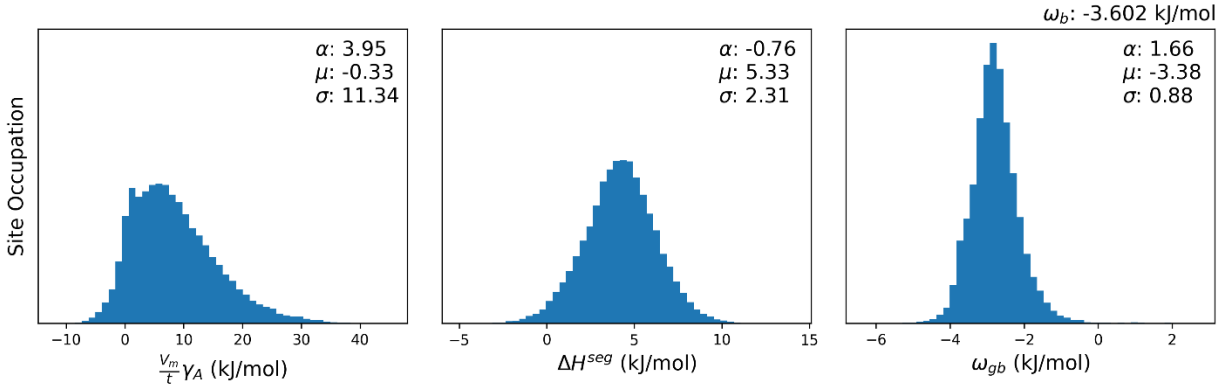

☒ Pd-Ag [191]

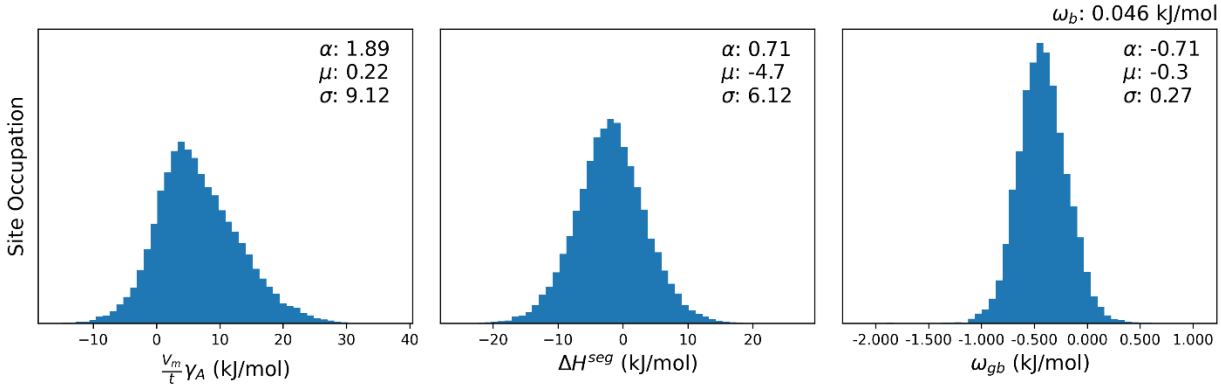

☒ Pd-Ag [191]

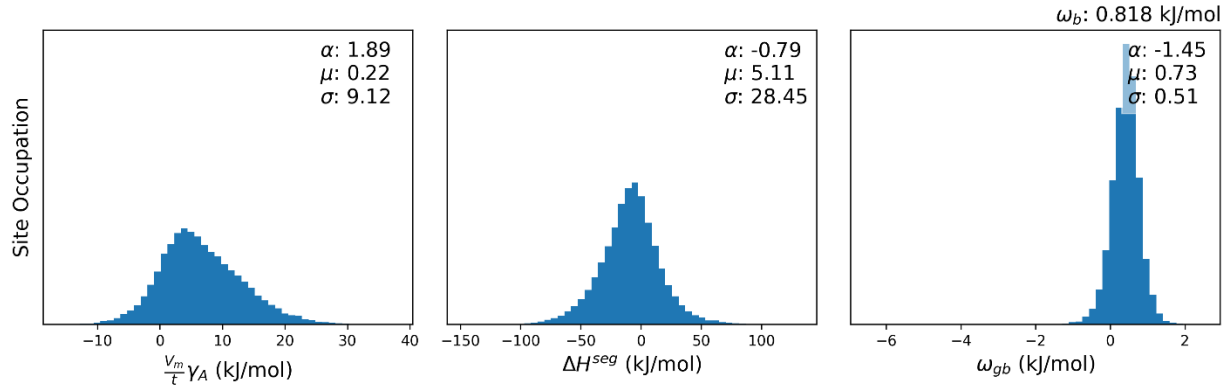

Pd-Au [130]

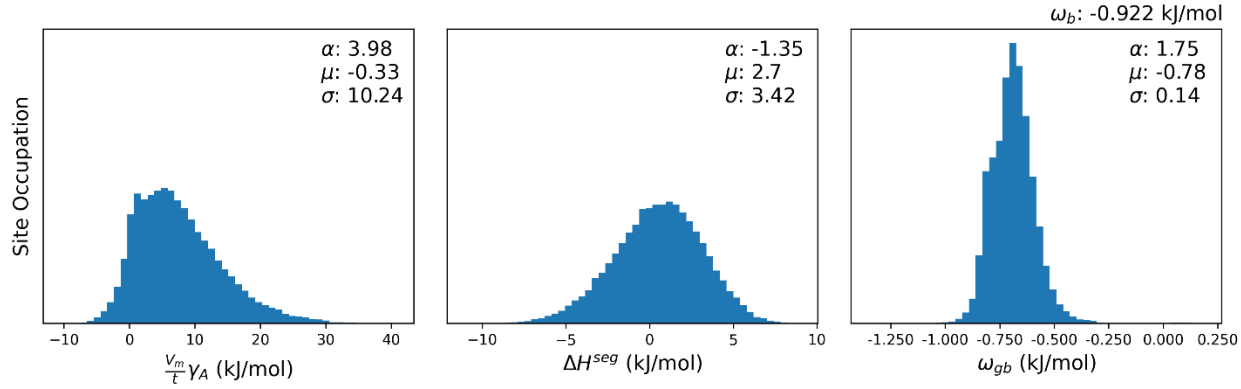

Pd-Au [162]

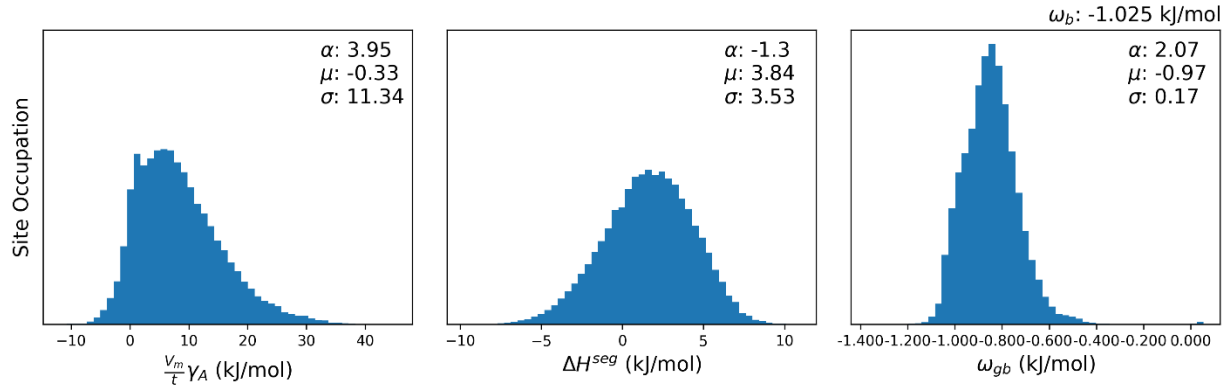

Pd-Cu [130]

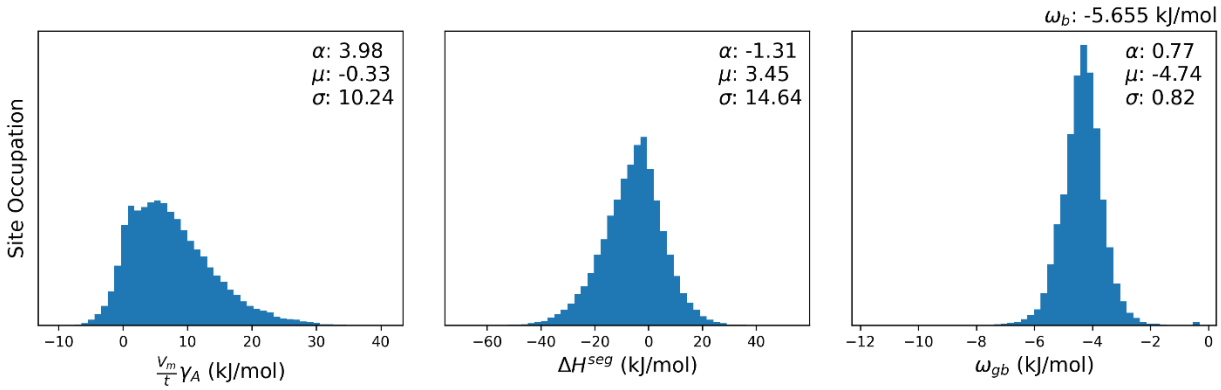

Pd-Cu [162]

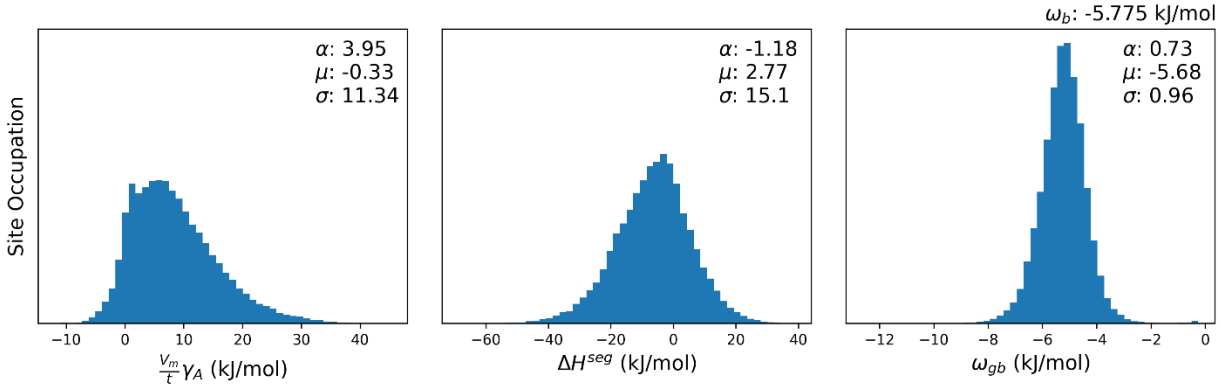

☒ Pd-H [191]

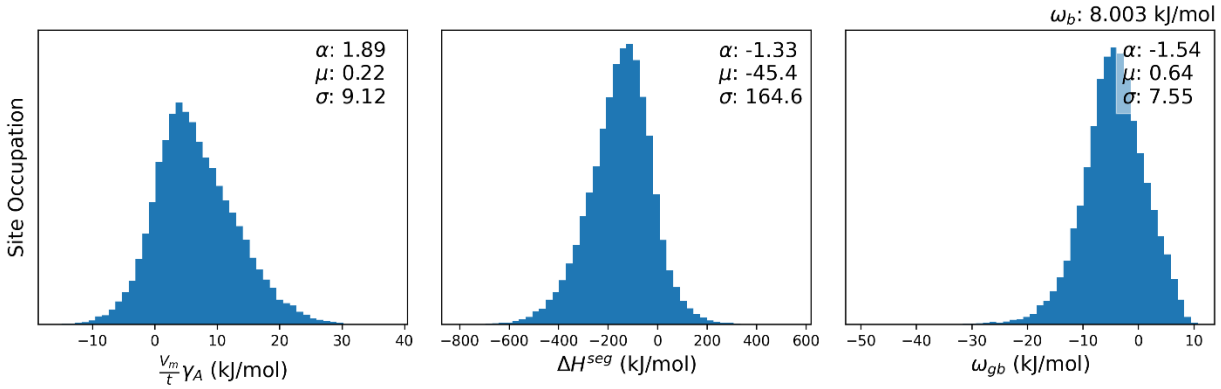

☒ Pd-H [191]

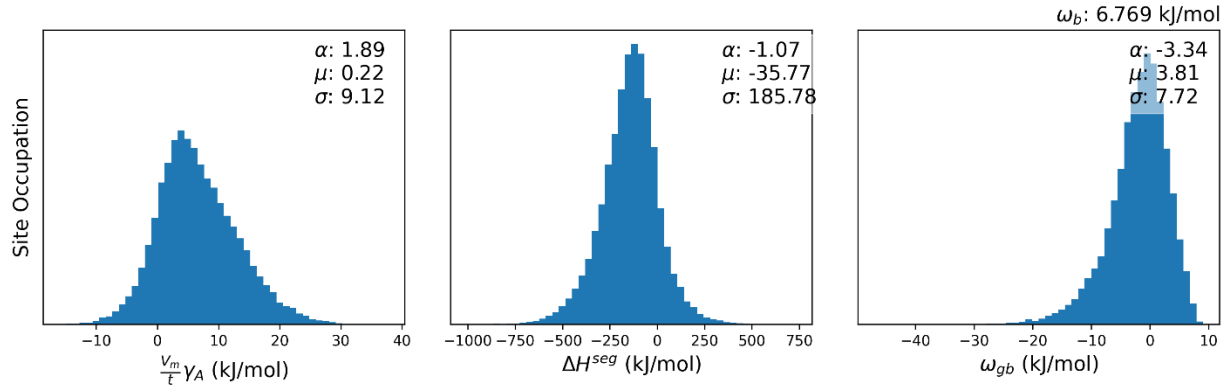

Pd-Ni [130]

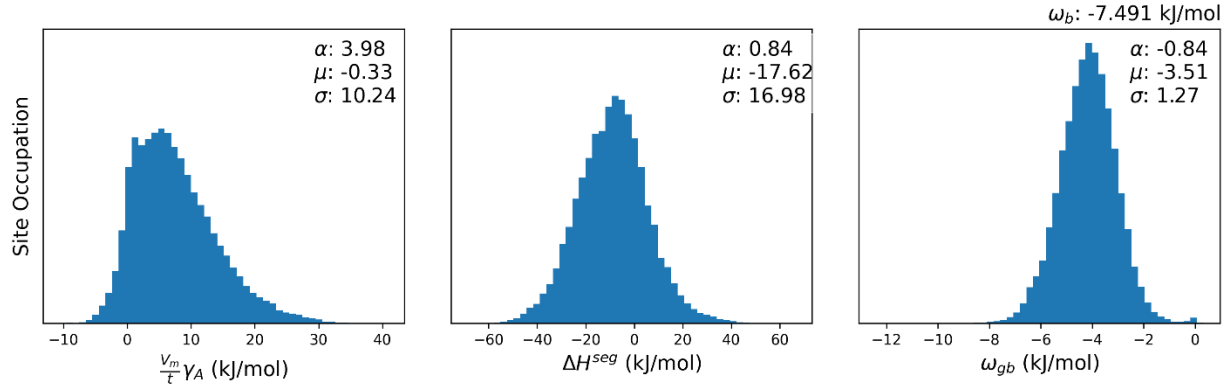

Pd-Ni [162]

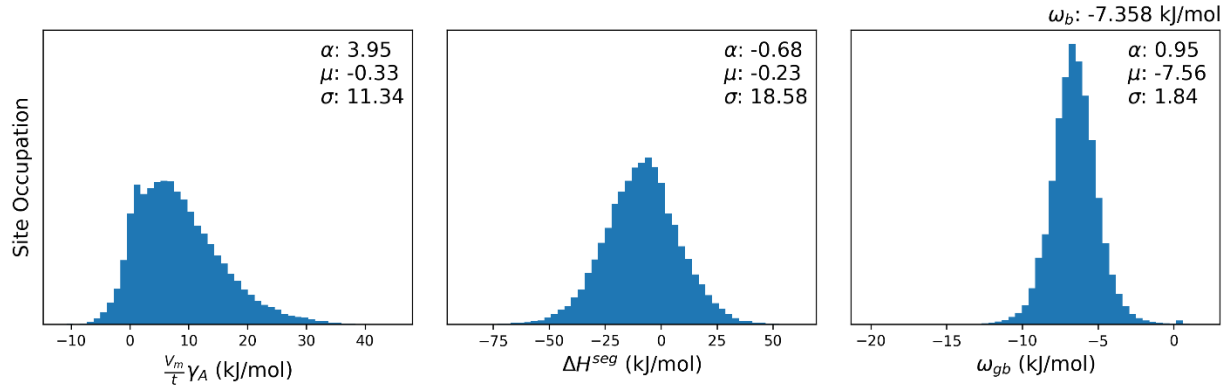

Pd-Ni [187]

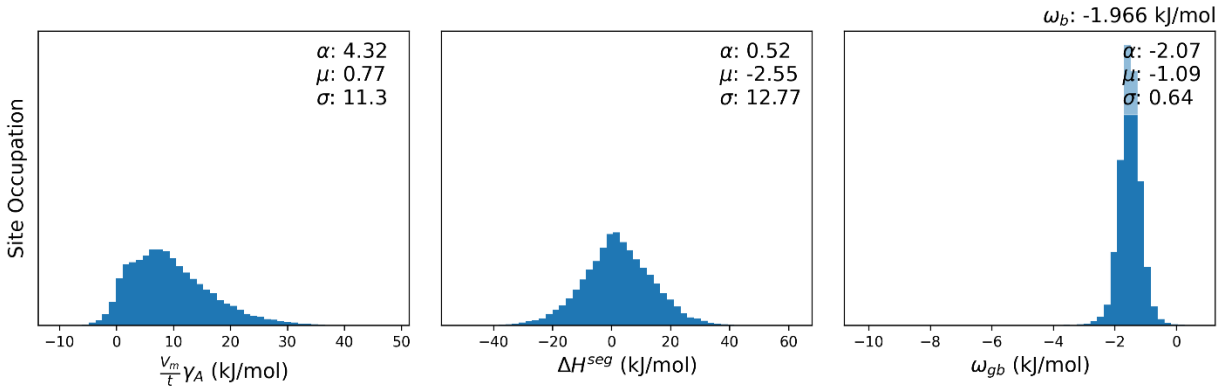

Pd-Pt [130]

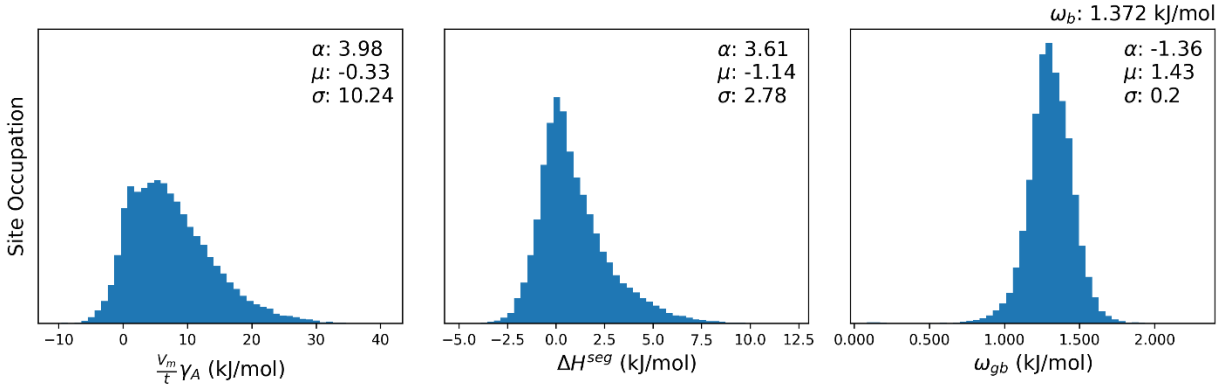

Pd-Pt [162]

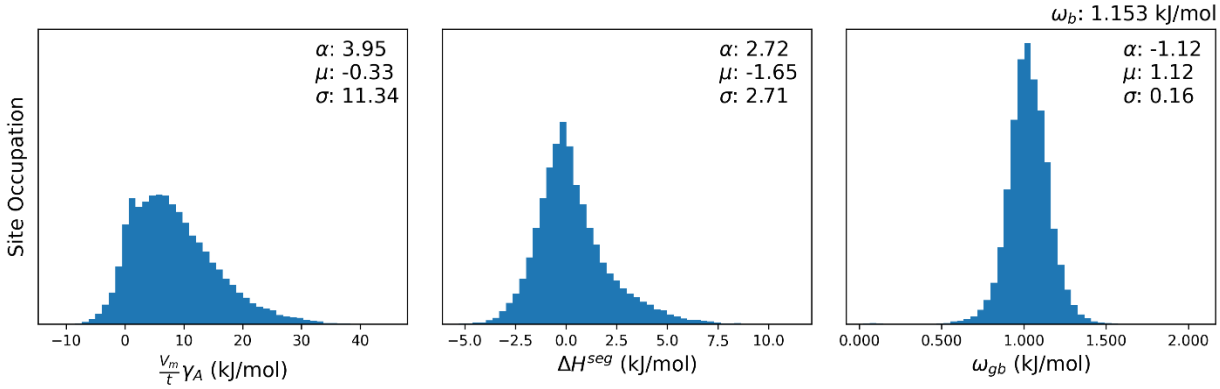

Pt-Based Alloys

☒ Pt-Ag [130]

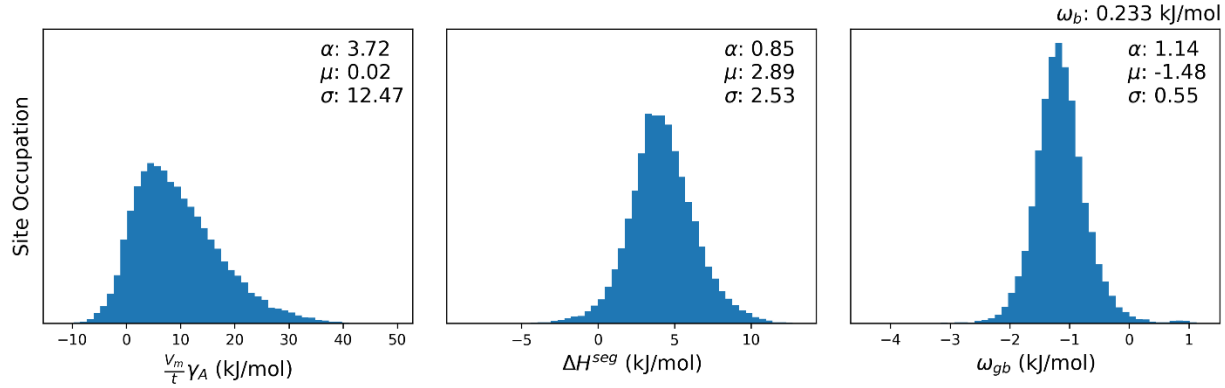

Pt-Ag [162]

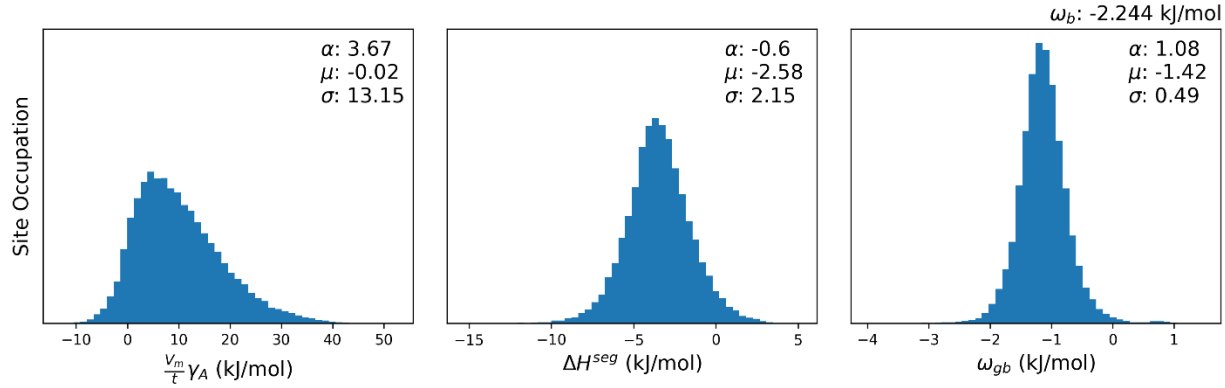

Pt-Au [130]

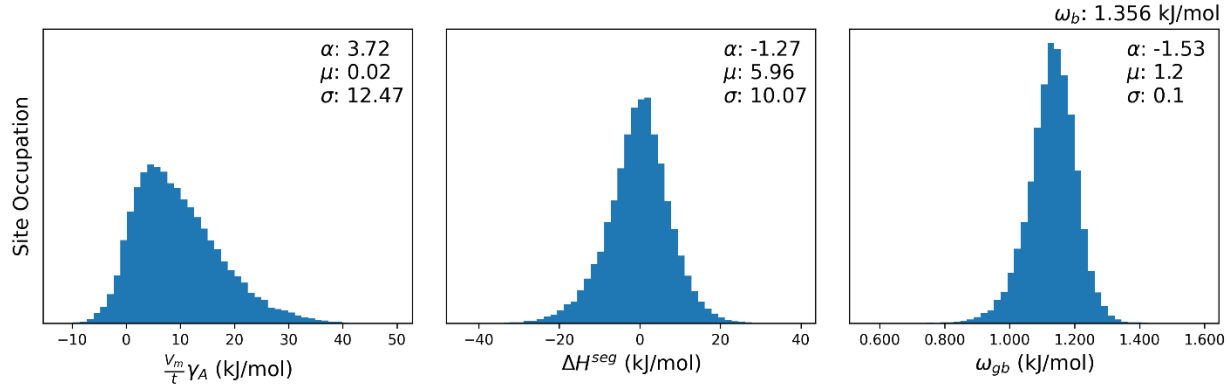

Pt-Au [162]

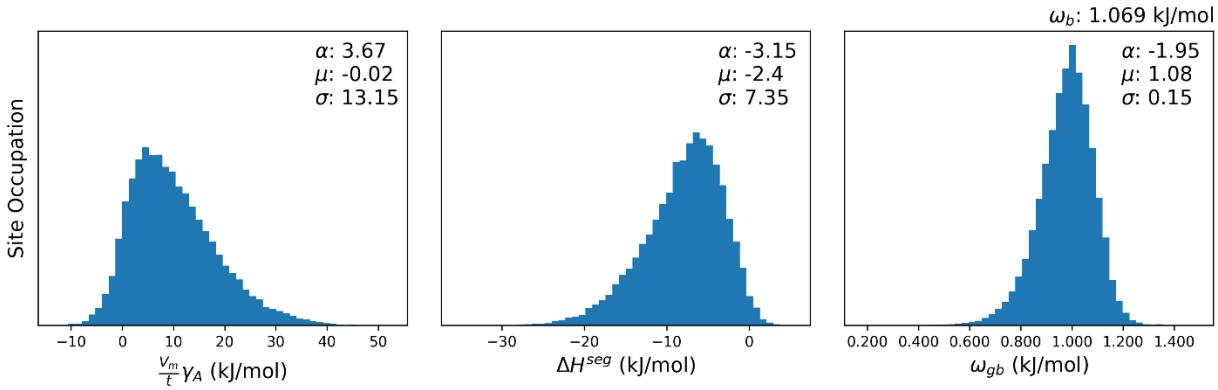

☑ Pt-Au [131]

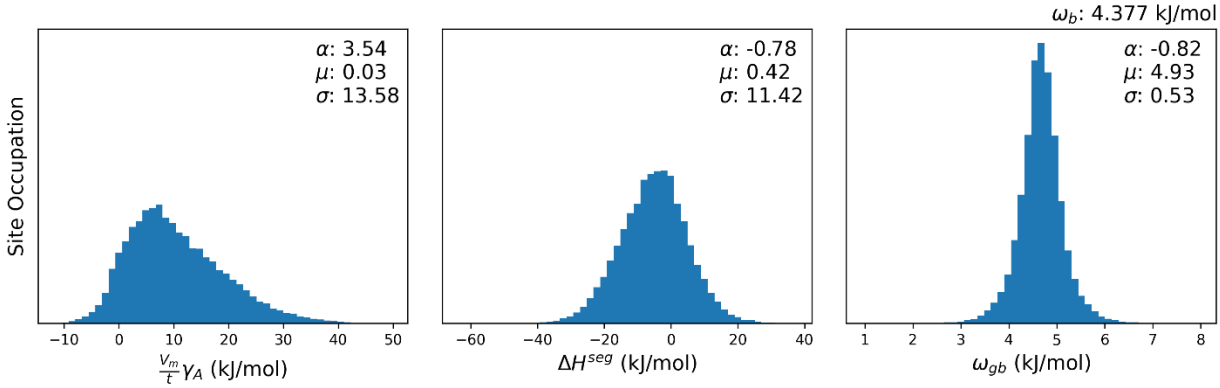

Pt-Cu [130]

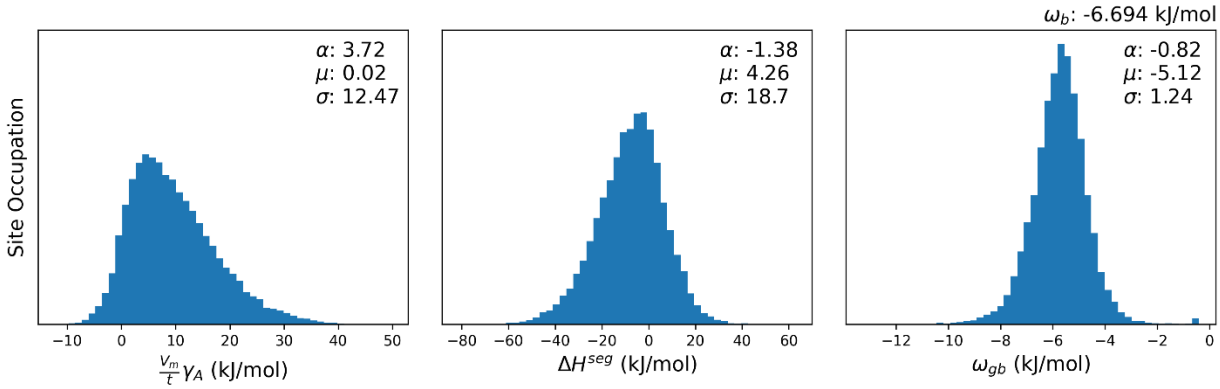

Pt-Cu [162]

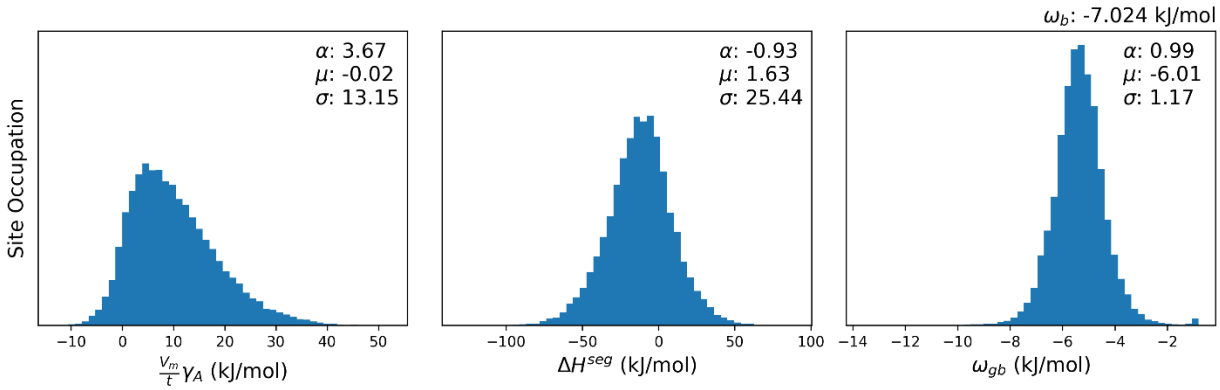

Pt-Ni [130]

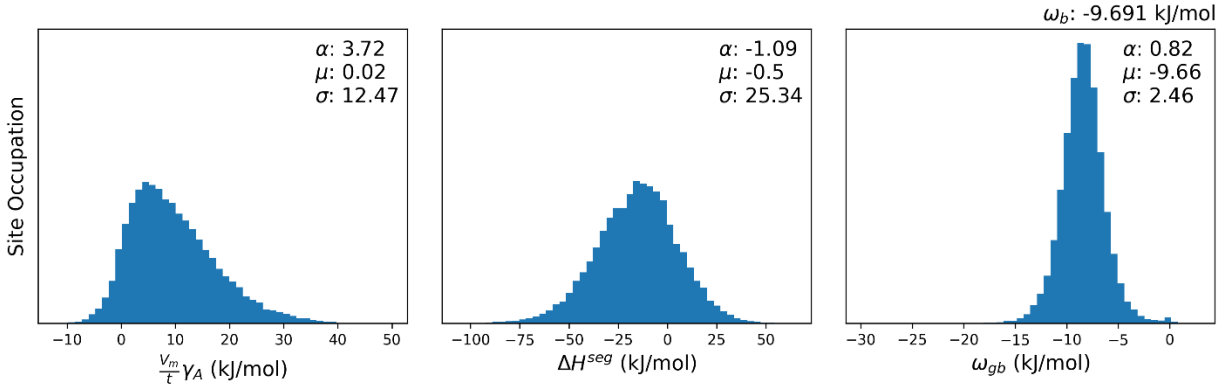

Pt-Ni [162]

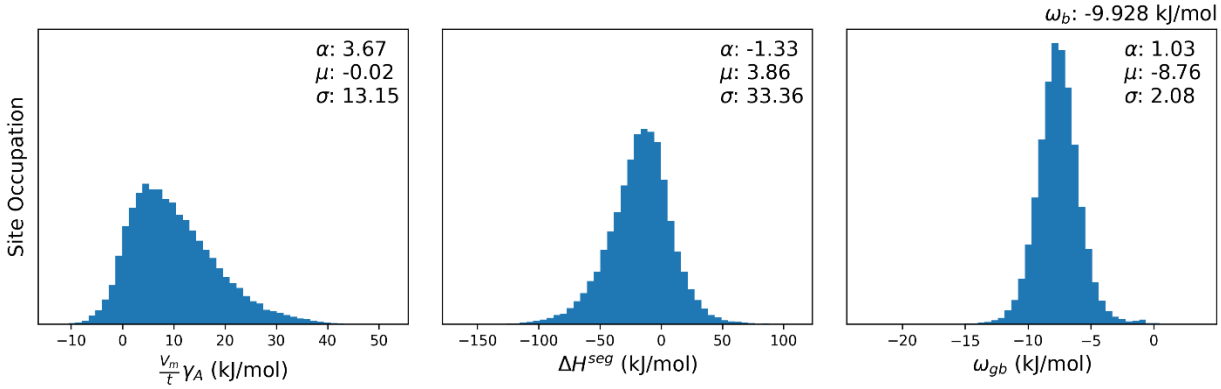

Pt-Pd [130]

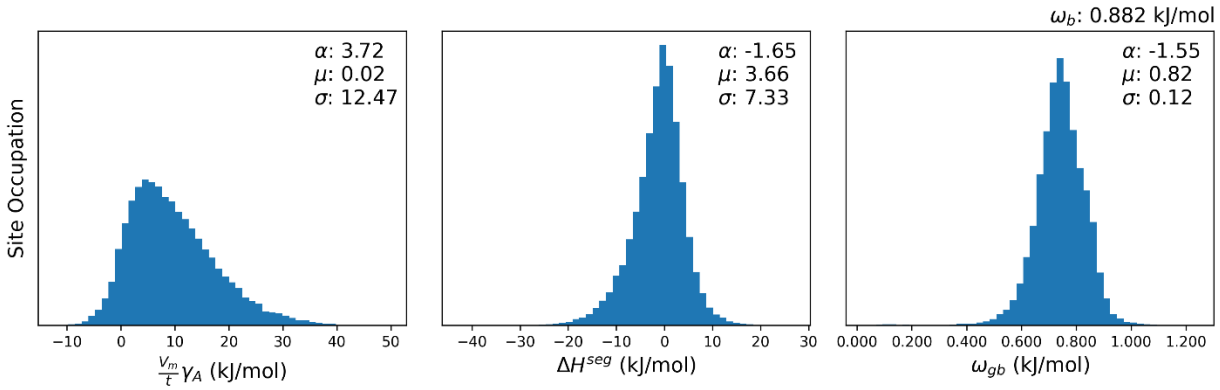

Pt-Pd [162]

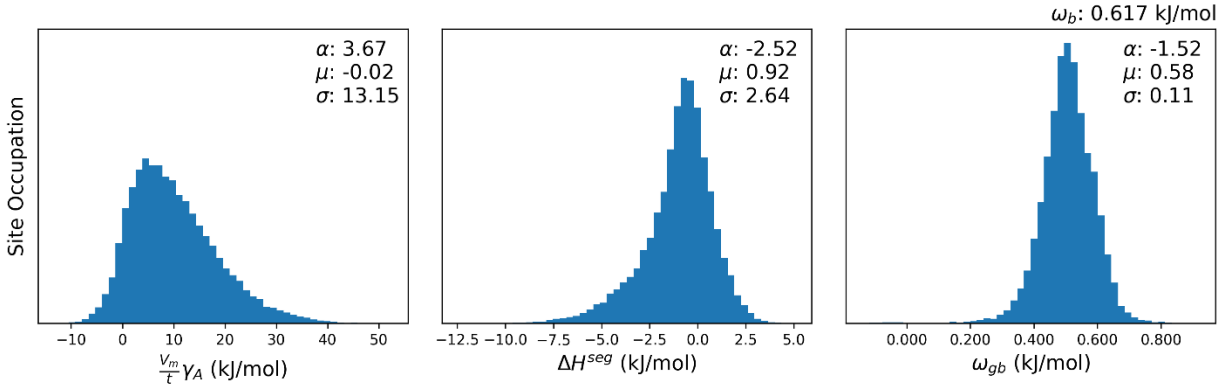

Re-based Alloys

Re-W [192]

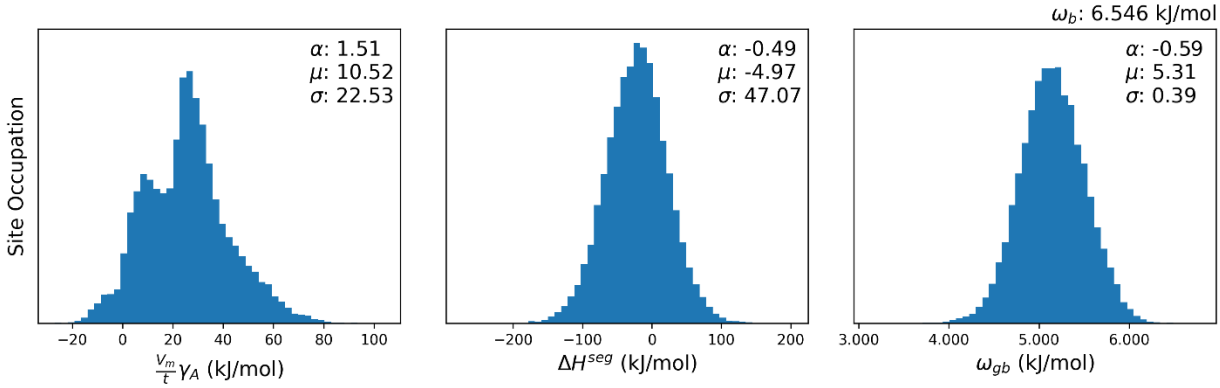

Re-W [193]

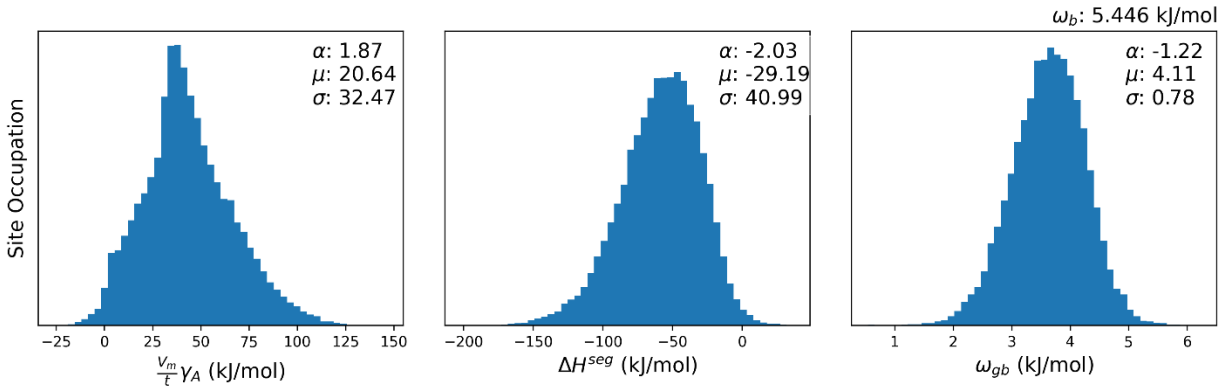

Ta-based Alloys

Ta-Cu [163]

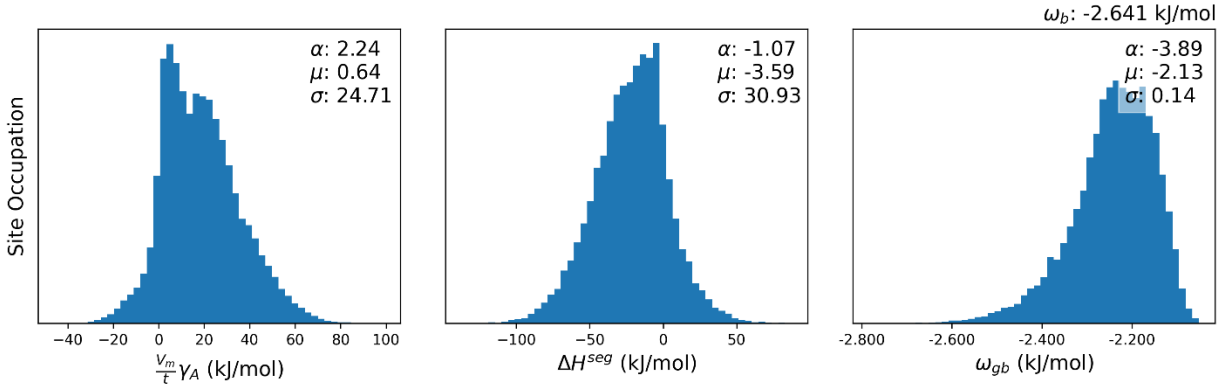

☒ Ta-W [194]

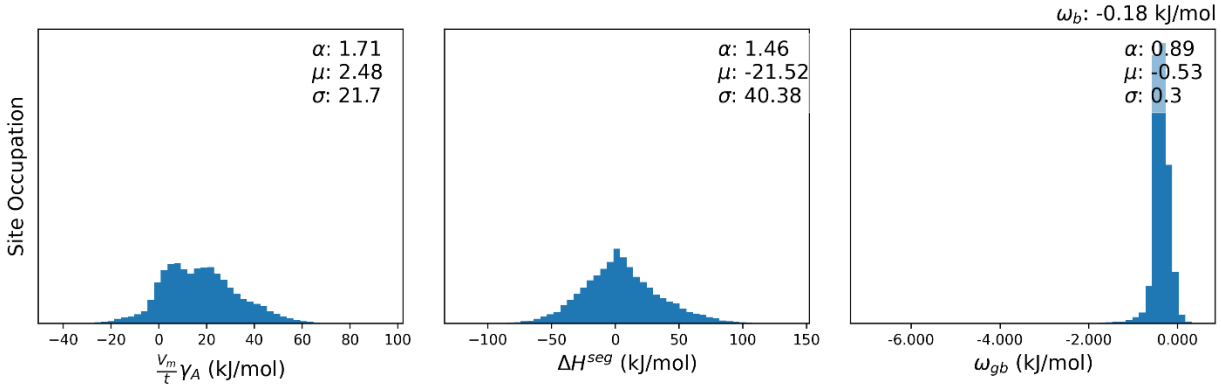

Ti-based Alloys

Ti-Al [147]

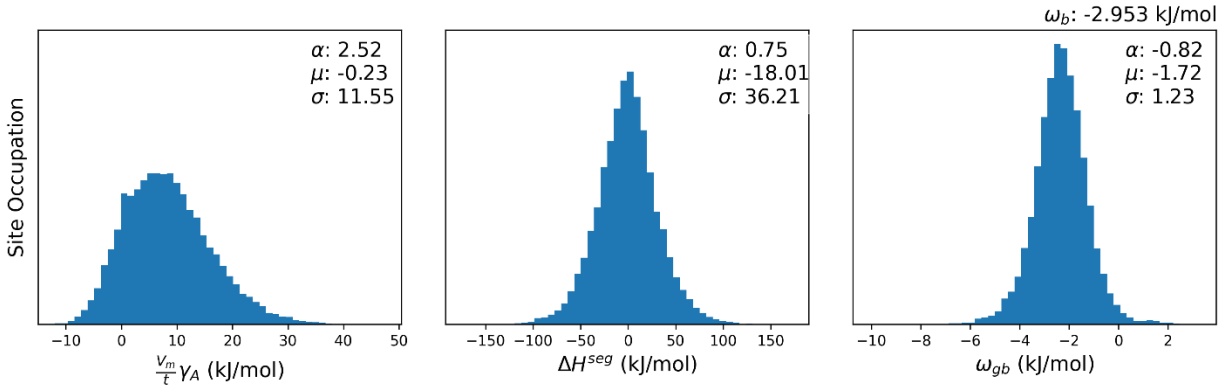

Ti-Al [155]

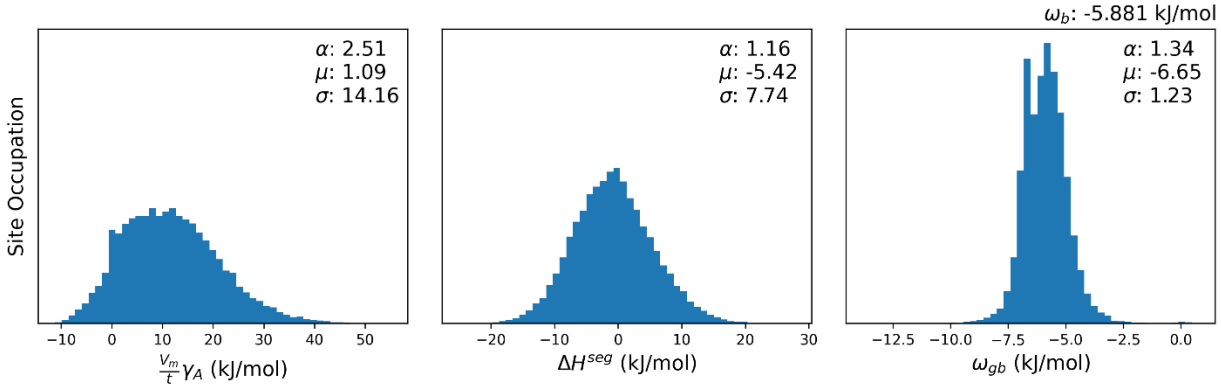

☒ Ti-Nb [147]

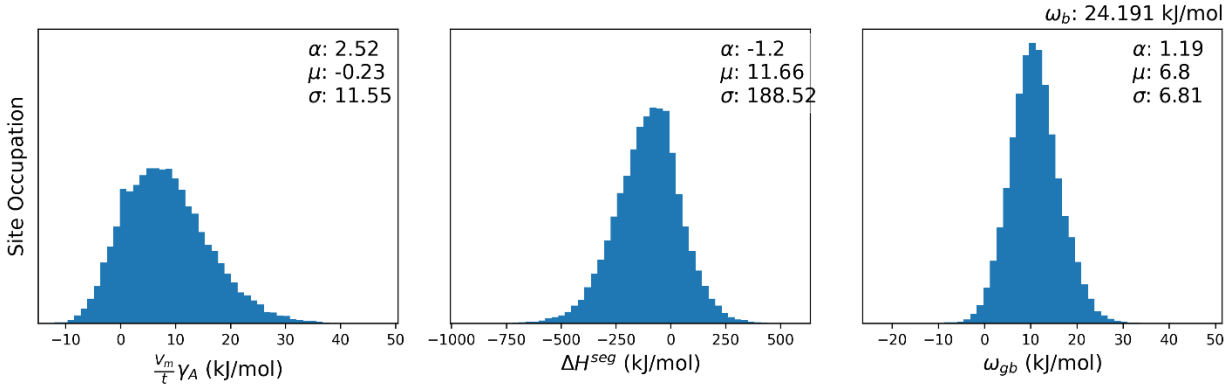

V-based Alloys

V-Fe [182]

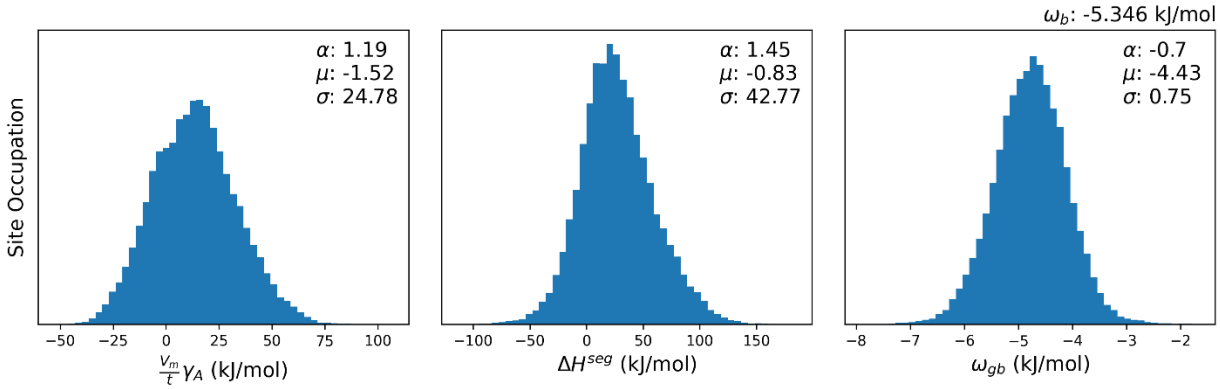

W-based Alloys

W-Fe [183]

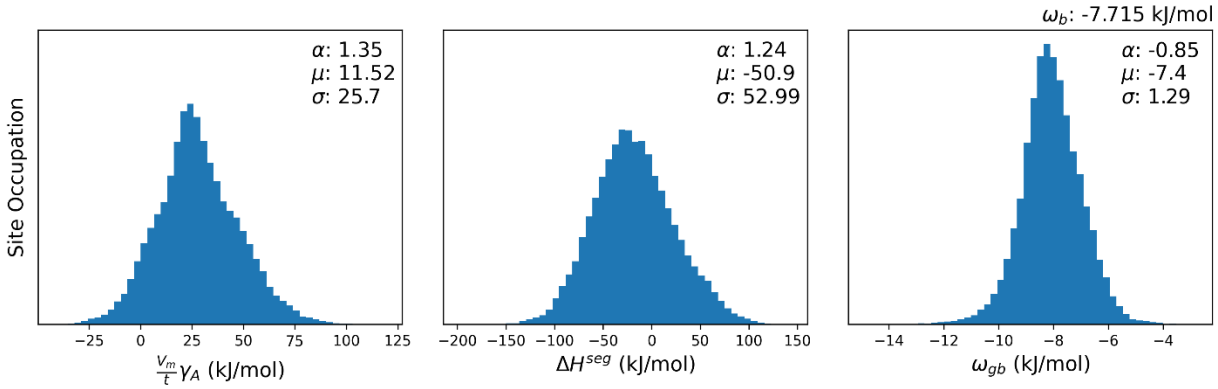

☒ W-Ni [188]

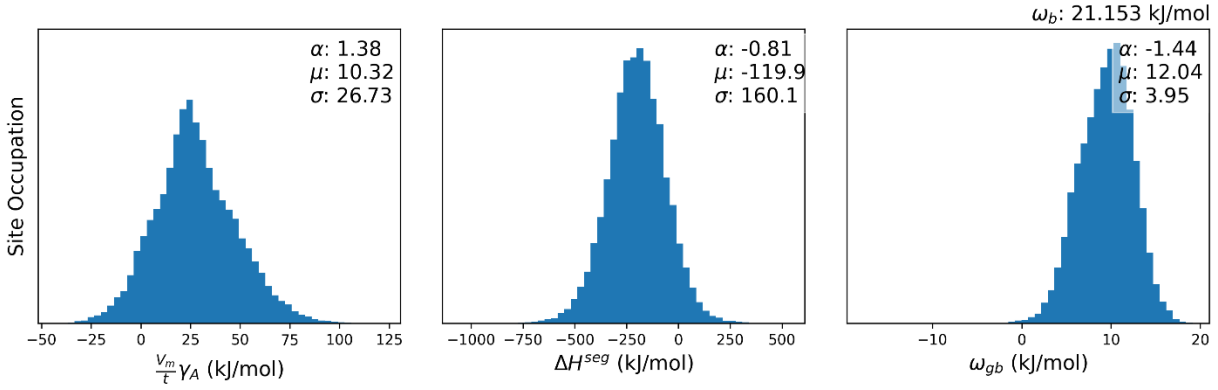

W-Re [192]

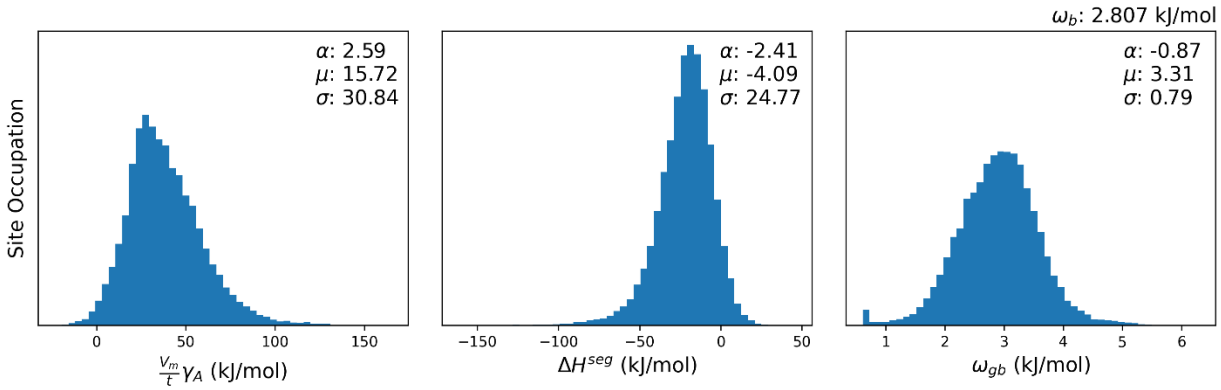

☒ W-Re [193]

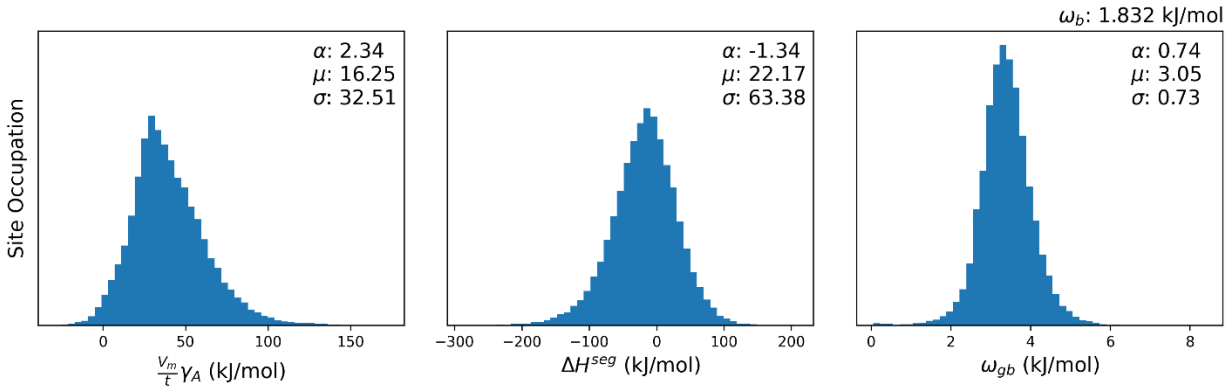

☒ W-Ta [194]

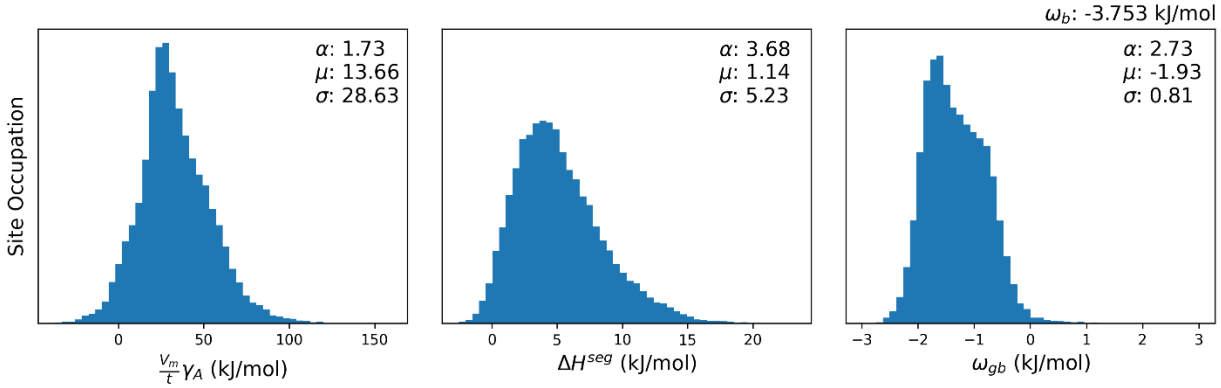

Zr-based Alloys

☑☒ Zr-Cu [176]

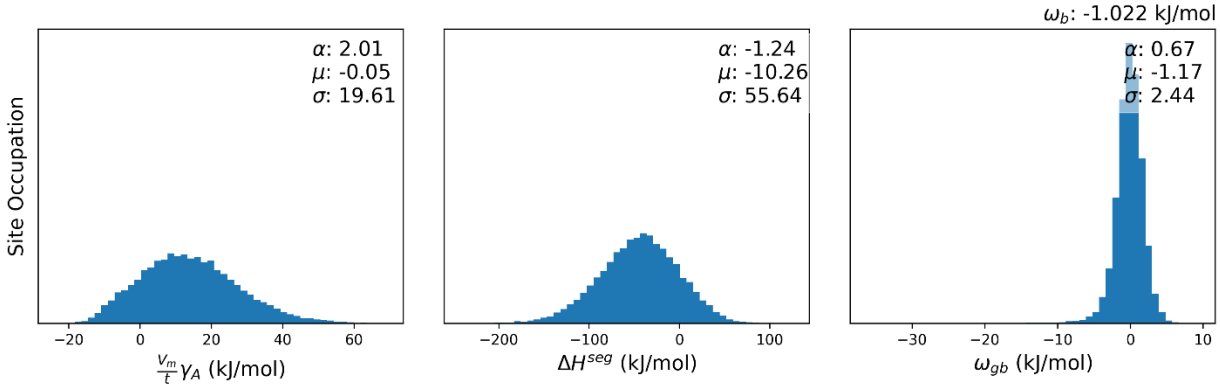

☑☒ Zr-Cu [177]

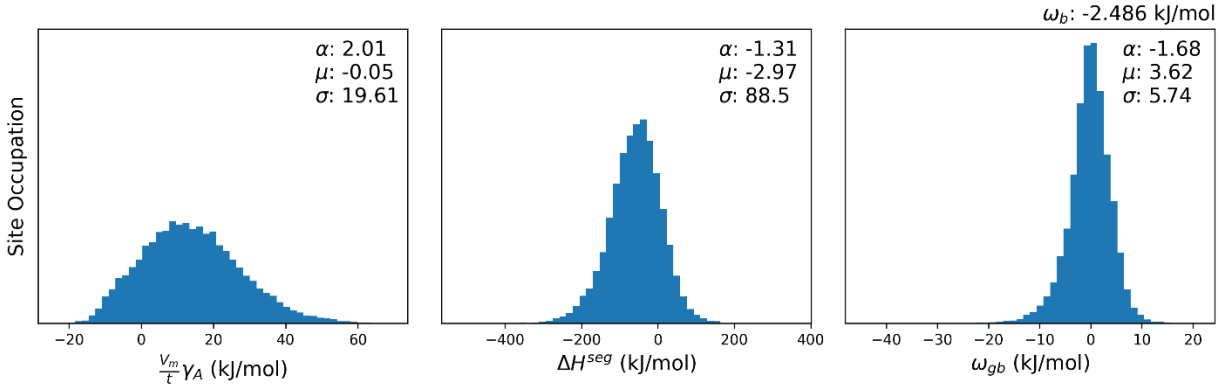

☑ Zr-Cu [178]

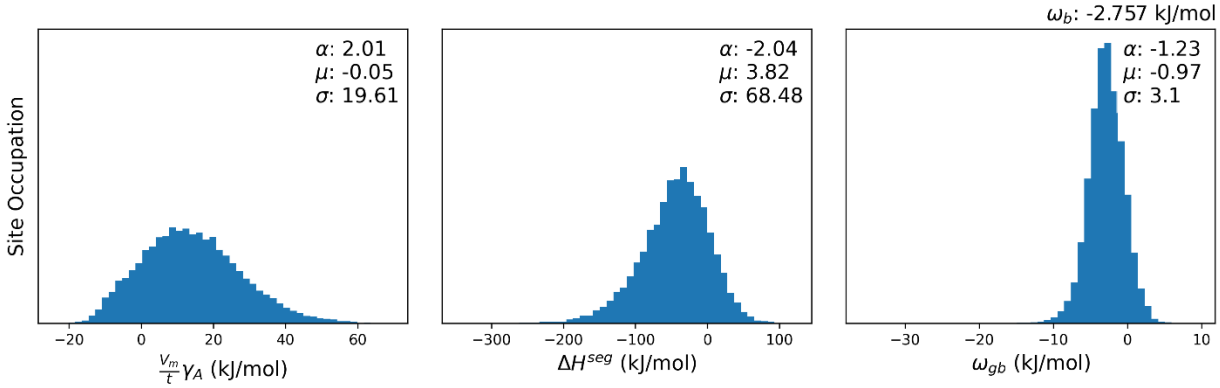

☑☒ Zr-Ni [189]

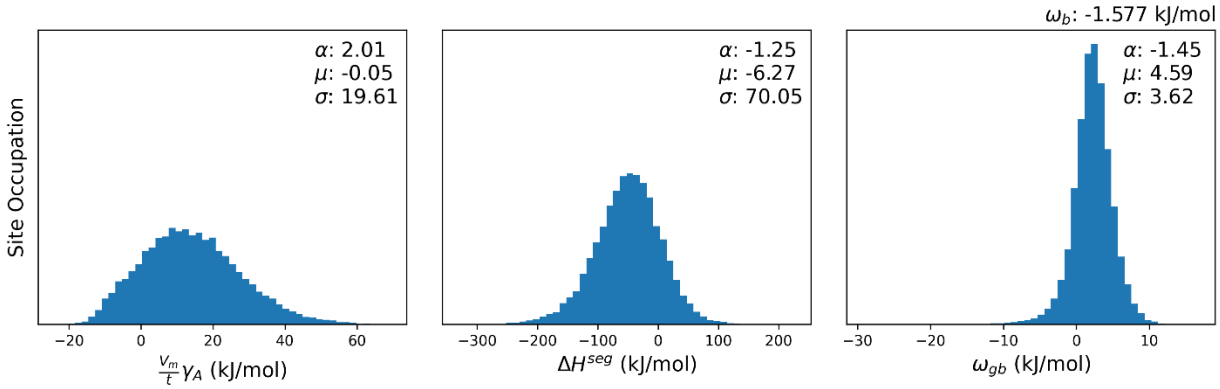

☑☒ Zr-Ni [190]

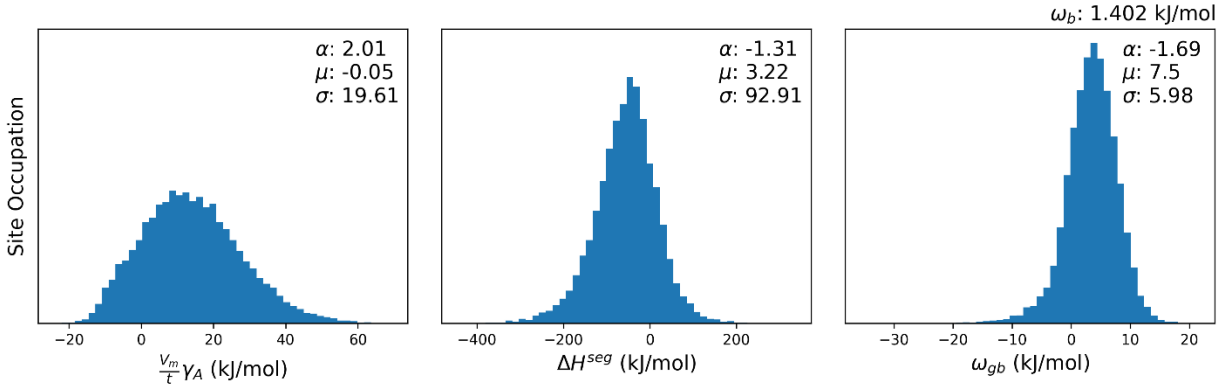

References

[1] P.R. Cantwell, M. Tang, S.J. Dillon, J. Luo, G.S. Rohrer, M.P. Harmer, Grain boundary complexions, Acta Materialia 62 (2014) 1–48. https://doi.org/10.1016/j.actamat.2013.07.037.

[2] P.R. Cantwell, T. Frolov, T.J. Rupert, A.R. Krause, C.J. Marvel, G.S. Rohrer, J.M. Rickman, M.P. Harmer, Grain Boundary Complexion Transitions, Annu. Rev. Mater. Res. 50 (2020) 465–492. https://doi.org/10.1146/annurev-matsci-081619-114055.

[3] A.R. Krause, P.R. Cantwell, C.J. Marvel, C. Compson, J.M. Rickman, M.P. Harmer, Review of grain boundary complexion engineering: Know your boundaries, J Am Ceram Soc 102 (2019) 778–800. https://doi.org/10.1111/jace.16045.

[4] J.P. Male, L. Abdellaoui, Y. Yu, S. Zhang, N. Pieczulewski, O. Cojocaru-Mirédin, C. Scheu, G.J. Snyder, Dislocations Stabilized by Point Defects Increase Brittleness in PbTe, Adv Funct Materials 31 (2021) 2108006. https://doi.org/10.1002/adfm.202108006.

[5] N.A. Sobolev, Defect engineering in implantation technology of silicon light-emitting structures with dislocation-related luminescence, Semiconductors 44 (2010) 1–23. https://doi.org/10.1134/S106378261001001X.

[6] Y. Zheng, T.J. Slade, L. Hu, X.Y. Tan, Y. Luo, Z.-Z. Luo, J. Xu, Q. Yan, M.G. Kanatzidis, Defect engineering in thermoelectric materials: what have we learned?, Chem. Soc. Rev. 50 (2021) 9022–9054. https://doi.org/10.1039/D1CS00347J.

[7] V. Gurylev, T.P. Perng, Defect engineering of ZnO: Review on oxygen and zinc vacancies, Journal of the European Ceramic Society 41 (2021) 4977–4996. https://doi.org/10.1016/j.jeurceramsoc.2021.03.031.

[8] S. Bai, N. Zhang, C. Gao, Y. Xiong, Defect engineering in photocatalytic materials, Nano Energy 53 (2018) 296–336. https://doi.org/10.1016/j.nanoen.2018.08.058.

[9] J. Xiong, J. Di, J. Xia, W. Zhu, H. Li, Surface Defect Engineering in 2D Nanomaterials for Photocatalysis, Adv Funct Materials 28 (2018) 1801983. https://doi.org/10.1002/adfm.201801983.

[10] M.P. Harmer, The Phase Behavior of Interfaces, Science 332 (2011) 182–183. https://doi.org/10.1126/science.1204204.

[11] S.J. Dillon, M. Tang, W.C. Carter, M.P. Harmer, Complexion: A new concept for kinetic engineering in materials science, Acta Materialia 55 (2007) 6208–6218. https://doi.org/10.1016/j.actamat.2007.07.029.

[12] A. Gupta, X. Zhou, G.B. Thompson, G.J. Tucker, Role of grain boundary character and its evolution on interfacial solute segregation behavior in nanocrystalline Ni-P, Acta Materialia 190 (2020) 113–123. https://doi.org/10.1016/j.actamat.2020.03.012.

[13] S.J. Dillon, K. Tai, S. Chen, The importance of grain boundary complexions in affecting physical properties of polycrystals, Current Opinion in Solid State and Materials Science 20 (2016) 324–335. https://doi.org/10.1016/j.cossms.2016.06.003.

[14] J. Luo, H. Cheng, K.M. Asl, C.J. Kiely, M.P. Harmer, The Role of a Bilayer Interfacial Phase on Liquid Metal Embrittlement, Science 333 (2011) 1730–1733. https://doi.org/10.1126/science.1208774.

[15] K.A. Darling, M. Rajagopalan, M. Komarasamy, M.A. Bhatia, B.C. Hornbuckle, R.S. Mishra, K.N. Solanki, Extreme creep resistance in a microstructurally stable nanocrystalline alloy, Nature 537 (2016) 378–381. https://doi.org/10.1038/nature19313.

[16] H. Kotan, M. Saber, C.C. Koch, R.O. Scattergood, Effect of annealing on microstructure, grain growth, and hardness of nanocrystalline Fe–Ni alloys prepared by mechanical alloying,

Materials Science and Engineering: A 552 (2012) 310–315. https://doi.org/10.1016/j.msea.2012.05.045.
[17] K.S. Kumar, H. Van Swygenhoven, S. Suresh, Mechanical behavior of nanocrystalline metals and alloys, Acta Materialia 51 (2003) 5743–5774. https://doi.org/10.1016/j.actamat.2003.08.032.
[18] G. Liu, G.J. Zhang, F. Jiang, X.D. Ding, Y.J. Sun, J. Sun, E. Ma, Nanostructured high-strength molybdenum alloys with unprecedented tensile ductility, Nature Mater 12 (2013) 344–350. https://doi.org/10.1038/nmat3544.
[19] M.A. Meyers, A. Mishra, D.J. Benson, Mechanical properties of nanocrystalline materials, Progress in Materials Science 51 (2006) 427–556. https://doi.org/10.1016/j.pmatsci.2005.08.003.
[20] M.S. Dresselhaus, G. Chen, M.Y. Tang, R.G. Yang, H. Lee, D.Z. Wang, Z.F. Ren, J.-P. Fleurial, P. Gogna, New Directions for Low-Dimensional Thermoelectric Materials, Adv. Mater. 19 (2007) 1043–1053. https://doi.org/10.1002/adma.200600527.
[21] G. Herzer, Grain size dependence of coercivity and permeability in nanocrystalline ferromagnets, IEEE Trans. Magn. 26 (1990) 1397–1402. https://doi.org/10.1109/20.104389.
[22] A. Manaf, R.A. Buckley, H.A. Davies, New nanocrystalline high-remanence Nd-Fe-B alloys by rapid solidification, Journal of Magnetism and Magnetic Materials 128 (1993) 302–306. https://doi.org/10.1016/0304-8853(93)90475-H.
[23] H. Tuller, Ionic conduction in nanocrystalline materials, Solid State Ionics 131 (2000) 143–157. https://doi.org/10.1016/S0167-2738(00)00629-9.
[24] Y. Xijuan, X. Pingbo, S. Qingde, Size-dependent optical properties of nanocrystalline CeO2 :Er obtained by combustion synthesis, Phys. Chem. Chem. Phys. 3 (2001) 5266–5269. https://doi.org/10.1039/b105890h.
[25] K.A. Darling, B.K. VanLeeuwen, C.C. Koch, R.O. Scattergood, Thermal stability of nanocrystalline Fe–Zr alloys, Materials Science and Engineering: A 527 (2010) 3572–3580. https://doi.org/10.1016/j.msea.2010.02.043.
[26] V.Y. Gertsman, R. Birringer, On the room-temperature grain growth in nanocrystalline copper, Scripta Metallurgica et Materialia 30 (1994) 577–581. https://doi.org/10.1016/0956-716X(94)90432-4.
[27] H. Natter, M. Schmelzer, R. Hempelmann, Nanocrystalline nickel and nickel-copper alloys: Synthesis, characterization, and thermal stability, J. Mater. Res. 13 (1998) 1186–1197. https://doi.org/10.1557/JMR.1998.0169.
[28] M. Thuvander, M. Abraham, A. Cerezo, G.D.W. Smith, Thermal stability of electrodeposited nanocrystalline nickel and iron–nickel alloys, Materials Science and Technology 17 (2001) 961–970. https://doi.org/10.1179/026708301101510799.
[29] K.A. Darling, B.K. VanLeeuwen, J.E. Semones, C.C. Koch, R.O. Scattergood, L.J. Kecskes, S.N. Mathaudhu, Stabilized nanocrystalline iron-based alloys: Guiding efforts in alloy selection, Materials Science and Engineering: A 528 (2011) 4365–4371. https://doi.org/10.1016/j.msea.2011.02.080.
[30] A. Detor, C. Schuh, Grain boundary segregation, chemical ordering and stability of nanocrystalline alloys: Atomistic computer simulations in the Ni–W system, Acta Materialia 55 (2007) 4221–4232. https://doi.org/10.1016/j.actamat.2007.03.024.
[31] A.J. Detor, C.A. Schuh, Microstructural evolution during the heat treatment of nanocrystalline alloys, J. Mater. Res. 22 (2007) 3233–3248. https://doi.org/10.1557/JMR.2007.0403.

[32] T. Hentschel, D. Isheim, R. Kirchheim, F. Müller, H. Kreye, Nanocrystalline Ni–3.6 at.% P and its transformation sequence studied by atom-probe field-ion microscopy, Acta Materialia 48 (2000) 933–941. https://doi.org/10.1016/S1359-6454(99)00371-7.
[33] M. Saber, H. Kotan, C.C. Koch, R.O. Scattergood, Thermal stability of nanocrystalline Fe–Cr alloys with Zr additions, Materials Science and Engineering: A 556 (2012) 664–670. https://doi.org/10.1016/j.msea.2012.07.045.
[34] S.C. Mehta, D.A. Smith, U. Erb, Study of grain growth in electrodeposited nanocrystalline nickel-1.2 wt.% phosphorus alloy, Materials Science and Engineering: A 204 (1995) 227–232. https://doi.org/10.1016/0921-5093(95)09966-2.
[35] W. Xing, S.A. Kube, A.R. Kalidindi, D. Amram, J. Schroers, C.A. Schuh, Stability of ternary nanocrystalline alloys in the Pt–Pd–Au system, Materialia 8 (2019) 100449. https://doi.org/10.1016/j.mtla.2019.100449.
[36] T. Chookajorn, C.A. Schuh, Thermodynamics of stable nanocrystalline alloys: A Monte Carlo analysis, Phys. Rev. B 89 (2014) 064102. https://doi.org/10.1103/PhysRevB.89.064102.
[37] A.R. Kalidindi, C.A. Schuh, Stability criteria for nanocrystalline alloys, Acta Materialia 132 (2017) 128–137. https://doi.org/10.1016/j.actamat.2017.03.029.
[38] R. Kirchheim, Reducing grain boundary, dislocation line and vacancy formation energies by solute segregation. I. Theoretical background, Acta Materialia 55 (2007) 5129–5138. https://doi.org/10.1016/j.actamat.2007.05.047.
[39] H.A. Murdoch, C.A. Schuh, Stability of binary nanocrystalline alloys against grain growth and phase separation, Acta Materialia 61 (2013) 2121–2132. https://doi.org/10.1016/j.actamat.2012.12.033.
[40] M. Saber, H. Kotan, C.C. Koch, R.O. Scattergood, A predictive model for thermodynamic stability of grain size in nanocrystalline ternary alloys, Journal of Applied Physics 114 (2013) 103510. https://doi.org/10.1063/1.4821040.
[41] J.R. Trelewicz, C.A. Schuh, Grain boundary segregation and thermodynamically stable binary nanocrystalline alloys, Phys. Rev. B 79 (2009) 094112. https://doi.org/10.1103/PhysRevB.79.094112.
[42] J. Weissmüller, Alloy effects in nanostructures, Nanostructured Materials 3 (1993) 261–272. https://doi.org/10.1016/0965-9773(93)90088-S.
[43] A.R. Kalidindi, T. Chookajorn, C.A. Schuh, Nanocrystalline Materials at Equilibrium: A Thermodynamic Review, JOM 67 (2015) 2834–2843. https://doi.org/10.1007/s11837-015-1636-9.
[44] K. Boylan, D. Ostrander, U. Erb, G. Palumbo, K.T. Aust, An in-situ tem study of the thermal stability of nanocrystalline NiP, Scripta Metallurgica et Materialia 25 (1991) 2711–2716. https://doi.org/10.1016/0956-716X(91)90144-P.
[45] F.J. Humphreys, M. Hatherly, in: Recrystallization and Related Annealing Phenomena, Pergamon Press, Oxford, United Kingdom, 1995: pp. 121–167.
[46] P. Knauth, A. Charaï, P. Gas, Grain growth of pure nickel and of a Ni-Si solid solution studied by differential scanning calorimetry on nanometer-sized crystals, Scripta Metallurgica et Materialia 28 (1993) 325–330. https://doi.org/10.1016/0956-716X(93)90436-V.
[47] K. Lücke, K. Detert, A quantitative theory of grain-boundary motion and recrystallization in metals in the presence of impurities, Acta Metallurgica 5 (1957) 628–637. https://doi.org/10.1016/0001-6160(57)90109-8.
[48] R.J. Perez, H.G. Jiang, E.J. Lavernia, C.P. Dogan, Grain growth of nanocrystalline cryomilled Fe-Al powders, Metall and Mat Trans A 29 (1998) 2469–2475. https://doi.org/10.1007/s11661-998-0218-7.

[49] L. Shaw, H. Luo, J. Villegas, D. Miracle, Thermal stability of nanostructured Al93Fe3Cr2Ti2 alloys prepared via mechanical alloying, Acta Materialia 51 (2003) 2647–2663. https://doi.org/10.1016/S1359-6454(03)00075-2.
[50] T. Chookajorn, H.A. Murdoch, C.A. Schuh, Design of Stable Nanocrystalline Alloys, Science 337 (2012) 951–954. https://doi.org/10.1126/science.1224737.
[51] C.M. Barr, S.M. Foiles, M. Alkayyali, Y. Mahmood, P.M. Price, D.P. Adams, B.L. Boyce, F. Abdeljawad, K. Hattar, The role of grain boundary character in solute segregation and thermal stability of nanocrystalline Pt–Au, Nanoscale 13 (2021) 3552–3563. https://doi.org/10.1039/D0NR07180C.
[52] A.R. Kalidindi, C.A. Schuh, Phase transitions in stable nanocrystalline alloys, J. Mater. Res. 32 (2017) 1993–2002. https://doi.org/10.1557/jmr.2017.188.
[53] X. Shi, J. Luo, Developing grain boundary diagrams as a materials science tool: A case study of nickel-doped molybdenum, Phys. Rev. B 84 (2011) 014105. https://doi.org/10.1103/PhysRevB.84.014105.
[54] N. Zhou, J. Luo, Developing grain boundary diagrams for multicomponent alloys, Acta Materialia 91 (2015) 202–216. https://doi.org/10.1016/j.actamat.2015.03.013.
[55] V. Turlo, T.J. Rupert, Prediction of a wide variety of linear complexions in face centered cubic alloys, Acta Materialia 185 (2020) 129–141. https://doi.org/10.1016/j.actamat.2019.11.069.
[56] S.A.E. Johansson, G. Wahnström, First-principles derived complexion diagrams for phase boundaries in doped cemented carbides, (2016). https://doi.org/10.48550/ARXIV.1601.01588.
[57] S. Korte-Kerzel, T. Hickel, L. Huber, D. Raabe, S. Sandlöbes-Haut, M. Todorova, J. Neugebauer, Defect phases – thermodynamics and impact on material properties, International Materials Reviews 67 (2022) 89–117. https://doi.org/10.1080/09506608.2021.1930734.
[58] A. Tehranchi, S. Zhang, A. Zendegani, C. Scheu, T. Hickel, J. Neugebauer, Metastable defect phase diagrams as a tool to describe chemically driven defect formation: Application to planar defects, (2023). https://doi.org/10.48550/ARXIV.2303.07504.
[59] K.L. Merkle, D.J. Smith, Atomic Structure of Symmetric Tilt Grain Boundaries in NiO, Phys. Rev. Lett. 59 (1987) 2887–2890. https://doi.org/10.1103/PhysRevLett.59.2887.
[60] K. Sickafus, S.L. Sass, Observation of a grain boundary phase transformation induced by solute segregation, Journal of Vacuum Science & Technology A: Vacuum, Surfaces, and Films 3 (1985) 1525–1530. https://doi.org/10.1116/1.573156.
[61] S. Divinski, M. Lohmann, C. Herzig, B. Straumal, B. Baretzky, W. Gust, Grain-boundary melting phase transition in the Cu − Bi system, Phys. Rev. B 71 (2005) 104104. https://doi.org/10.1103/PhysRevB.71.104104.
[62] S.V. Divinski, H. Edelhoff, S. Prokofjev, Diffusion and segregation of silver in copper Σ 5(310) grain boundary, Phys. Rev. B 85 (2012) 144104. https://doi.org/10.1103/PhysRevB.85.144104.
[63] R. Freitas, R.E. Rudd, M. Asta, T. Frolov, Free energy of grain boundary phases: Atomistic calculations for Σ 5 (310) [001] grain boundary in Cu, Phys. Rev. Materials 2 (2018) 093603. https://doi.org/10.1103/PhysRevMaterials.2.093603.
[64] D. Frenkel, A.J.C. Ladd, New Monte Carlo method to compute the free energy of arbitrary solids. Application to the fcc and hcp phases of hard spheres, The Journal of Chemical Physics 81 (1984) 3188–3193. https://doi.org/10.1063/1.448024.
[65] R. Freitas, M. Asta, M. De Koning, Nonequilibrium free-energy calculation of solids using LAMMPS, Computational Materials Science 112 (2016) 333–341. https://doi.org/10.1016/j.commatsci.2015.10.050.

[66] D. Udler, D.N. Seidman, Solute segregation at [001] tilt boundaries in dilute f.c.c. alloys, Acta Materialia 46 (1998) 1221–1233. https://doi.org/10.1016/S1359-6454(97)00297-8.
[67] M. Wagih, C.A. Schuh, Spectrum of grain boundary segregation energies in a polycrystal, Acta Materialia 181 (2019) 228–237. https://doi.org/10.1016/j.actamat.2019.09.034.
[68] N. Tuchinda, C.A. Schuh, The vibrational entropy spectra of grain boundary segregation in polycrystals, Acta Materialia 245 (2023) 118630. https://doi.org/10.1016/j.actamat.2022.118630.
[69] T.P. Matson, C.A. Schuh, Atomistic Assessment of Solute-Solute Interactions during Grain Boundary Segregation, Nanomaterials 11 (2021) 2360. https://doi.org/10.3390/nano11092360.
[70] T. Nenninger, F. Sansoz, Local atomic environment analysis of short and long-range solute-solute interactions in a symmetric tilt grain boundary, Scripta Materialia 222 (2023) 115045. https://doi.org/10.1016/j.scriptamat.2022.115045.
[71] P. Lejček, M. Šob, V. Paidar, Interfacial segregation and grain boundary embrittlement: An overview and critical assessment of experimental data and calculated results, Progress in Materials Science 87 (2017) 83–139. https://doi.org/10.1016/j.pmatsci.2016.11.001.
[72] N. Tuchinda, C.A. Schuh, Triple junction solute segregation in Al-based polycrystals, Phys. Rev. Materials 7 (2023) 023601. https://doi.org/10.1103/PhysRevMaterials.7.023601.
[73] P. Wynblatt, D. Chatain, Anisotropy of segregation at grain boundaries and surfaces, Metall and Mat Trans A 37 (2006) 2595–2620. https://doi.org/10.1007/BF02586096.
[74] R. Kikuchi, J.W. Cahn, Grain boundaries with impurities in a two-dimensional lattice-gas model, Phys. Rev. B 36 (1987) 418–428. https://doi.org/10.1103/PhysRevB.36.418.
[75] M. Wagih, C.A. Schuh, Thermodynamics and design of nanocrystalline alloys using grain boundary segregation spectra, Acta Materialia 217 (2021) 117177. https://doi.org/10.1016/j.actamat.2021.117177.
[76] D.A. Steigerwald, P. Wynblatt, Calculation of the anisotropy of equilibrium surface composition in metallic solid solutions using the embedded atom method, Surface Science 193 (1988) 287–303. https://doi.org/10.1016/0039-6028(88)90337-8.
[77] J. Creuze, F. Berthier, R. Tétot, B. Legrand, Intergranular segregation and ordering effect: A mixed Monte Carlo mean-field approach, Phys. Rev. B 62 (2000) 2813–2824. https://doi.org/10.1103/PhysRevB.62.2813.
[78] P. Lejcek, in: Grain Boundary Segregation in Metals, Springer Berlin Heidelberg, Berlin, Heidelberg, Germany, 2010: pp. 51–102. https://doi.org/10.1007/978-3-642-12505-8.
[79] C.L. White, D.F. Stein, Sulfur segregation to grain boundaries in Ni3Al and Ni3(Al,Ti) alloys, MTA 9 (1978) 13–22. https://doi.org/10.1007/BF02647165.
[80] R. Kirchheim, Hydrogen solubility and diffusivity in defective and amorphous metals, Progress in Materials Science 32 (1988) 261–325. https://doi.org/10.1016/0079-6425(88)90010-2.
[81] T. Mütschele, R. Kirchheim, Segregation and diffusion of hydrogen in grain boundaries of palladium, Scripta Metallurgica 21 (1987) 135–140. https://doi.org/10.1016/0036-9748(87)90423-6.
[82] M. Wagih, C.A. Schuh, Grain boundary segregation beyond the dilute limit: Separating the two contributions of site spectrality and solute interactions, Acta Materialia 199 (2020) 63–72. https://doi.org/10.1016/j.actamat.2020.08.022.
[83] M. Wagih, P.M. Larsen, C.A. Schuh, Learning grain boundary segregation energy spectra in polycrystals, Nat Commun 11 (2020) 6376. https://doi.org/10.1038/s41467-020-20083-6.

[84] M. Wagih, C.A. Schuh, Learning Grain-Boundary Segregation: From First Principles to Polycrystals, Phys. Rev. Lett. 129 (2022) 046102. https://doi.org/10.1103/PhysRevLett.129.046102.
[85] T.P. Matson, C.A. Schuh, Phase and defect diagrams based on spectral grain boundary segregation: A regular solution approach, Acta Materialia 265 (2024) 119584. https://doi.org/10.1016/j.actamat.2023.119584.
[86] T. Matson, A "Bond-Focused" Local Atomic Environment Representation for a High Throughput Solute Interaction Spectrum Analysis: Supplemental Data, (2024). https://doi.org/10.17632/HRV39BZ4K6.1.
[87] D. McLean, in: Grain Boundaries in Metals, Clarendon Press, Oxford, United Kingdom, 1957: pp. 116–150.
[88] R.H. Fowler, E.A. Guggenheim, Statistical Thermodynamics: A Version of Staistical Mechanics for Students of Physics and Chemistry, Cambridge University Press, Cambridge, United Kingdom, 1939.
[89] P. Lejček, L. Zheng, S. Hofmann, M. Šob, Applied Thermodynamics: Grain Boundary Segregation, Entropy 16 (2014) 1462–1483. https://doi.org/10.3390/e16031462.
[90] K. Ishida, Effect of grain size on grain boundary segregation, Journal of Alloys and Compounds 235 (1996) 244–249. https://doi.org/10.1016/0925-8388(95)02094-2.
[91] M.I. Mendelev, M. Asta, M.J. Rahman, J.J. Hoyt, Development of interatomic potentials appropriate for simulation of solid–liquid interface properties in Al–Mg alloys, Philosophical Magazine 89 (2009) 3269–3285. https://doi.org/10.1080/14786430903260727.
[92] P. Hirel, Atomsk: A tool for manipulating and converting atomic data files, Computer Physics Communications 197 (2015) 212–219. https://doi.org/10.1016/j.cpc.2015.07.012.
[93] A. Stukowski, Visualization and analysis of atomistic simulation data with OVITO–the Open Visualization Tool, Modelling Simul. Mater. Sci. Eng. 18 (2010) 015012. https://doi.org/10.1088/0965-0393/18/1/015012.
[94] S. Plimpton, Fast Parallel Algorithms for Short-Range Molecular Dynamics, Journal of Computational Physics 117 (1995) 1–19. https://doi.org/10.1006/jcph.1995.1039.
[95] L. Huber, B. Grabowski, M. Militzer, J. Neugebauer, J. Rottler, Ab initio modelling of solute segregation energies to a general grain boundary, Acta Materialia 132 (2017) 138–148. https://doi.org/10.1016/j.actamat.2017.04.024.
[96] B. Sadigh, P. Erhart, A. Stukowski, A. Caro, E. Martinez, L. Zepeda-Ruiz, Scalable parallel Monte Carlo algorithm for atomistic simulations of precipitation in alloys, Phys. Rev. B 85 (2012) 184203. https://doi.org/10.1103/PhysRevB.85.184203.
[97] N. Metropolis, A.W. Rosenbluth, M.N. Rosenbluth, A.H. Teller, E. Teller, Equation of State Calculations by Fast Computing Machines, The Journal of Chemical Physics 21 (1953) 1087–1092. https://doi.org/10.1063/1.1699114.
[98] A. Seki, D.N. Seidman, Y. Oh, S.M. Foiles, Monte Carlo simulations of segregation at [001] twist boundaries in a Pt(Au) alloy—II. Discussion, Acta Metallurgica et Materialia 39 (1991) 3179–3185. https://doi.org/10.1016/0956-7151(91)90052-3.
[99] M. Menyhard, M. Yan, V. Vitek, Atomistic vs phenomenological approaches to grain boundary segregation: Computer modeling of Cu□Ag alloys, Acta Metallurgica et Materialia 42 (1994) 2783–2796. https://doi.org/10.1016/0956-7151(94)90219-4.
[100] S.M. Foiles, Calculation of grain-boundary segregation in Ni-Cu alloys, Phys. Rev. B 40 (1989) 11502–11506. https://doi.org/10.1103/PhysRevB.40.11502.
[101] X.-Y. Liu, J.B. Adams, Grain-boundary segregation in Al–10%Mg alloys at hot working temperatures, Acta Materialia 46 (1998) 3467–3476. https://doi.org/10.1016/S1359-6454(98)00038-X.

[102] A. Seki, D.N. Seidman, Y. Oh, S.M. Foiles, Monte Carlo simulations of segregation at [001] twist boundaries in a Pt(Au) alloy—I. Results, Acta Metallurgica et Materialia 39 (1991) 3167–3177. https://doi.org/10.1016/0956-7151(91)90051-2.
[103] The Collected Works of J. Willard Gibbs, Nature 124 (1929) 119–120. https://doi.org/10.1038/124119a0.
[104] J.W. Cahn, Thermodynamics of Solid and Fluid Surfaces, in: W.C. Carter, W.C. Johnson (Eds.), The Selected Works of John W. Cahn, 1st ed., Wiley, 1998: pp. 379–399. https://doi.org/10.1002/9781118788295.ch39.
[105] A. Azzalini, The multivariate skew-normal distribution, Biometrika 83 (1996) 715–726. https://doi.org/10.1093/biomet/83.4.715.
[106] M. Hillert, The compound energy formalism, Journal of Alloys and Compounds 320 (2001) 161–176. https://doi.org/10.1016/S0925-8388(00)01481-X.
[107] A. Detor, C. Schuh, Grain boundary segregation, chemical ordering and stability of nanocrystalline alloys: Atomistic computer simulations in the Ni–W system, Acta Materialia 55 (2007) 4221–4232. https://doi.org/10.1016/j.actamat.2007.03.024.
[108] S.C. Pun, W. Wang, A. Khalajhedayati, J.D. Schuler, J.R. Trelewicz, T.J. Rupert, Nanocrystalline Al-Mg with extreme strength due to grain boundary doping, Materials Science and Engineering: A 696 (2017) 400–406. https://doi.org/10.1016/j.msea.2017.04.095.
[109] M. Kapoor, G.B. Thompson, Role of atomic migration in nanocrystalline stability: Grain size and thin film stress states, Current Opinion in Solid State and Materials Science 19 (2015) 138–146. https://doi.org/10.1016/j.cossms.2014.11.001.
[110] K. Ito, H. Sawada, S. Ogata, Theoretical Prediction of Grain Boundary Segregation Using Nano-Polycrystalline Grain Boundary Model, Mater. Trans. 62 (2021) 575–581. https://doi.org/10.2320/matertrans.MT-M2020352.
[111] J.W. Gibbs, The Collected Works, Yale University Press, New Haven, CT, 1957.
[112] C.A. Becker, F. Tavazza, Z.T. Trautt, R.A. Buarque De Macedo, Considerations for choosing and using force fields and interatomic potentials in materials science and engineering, Current Opinion in Solid State and Materials Science 17 (2013) 277–283. https://doi.org/10.1016/j.cossms.2013.10.001.
[113] L.M. Hale, Z.T. Trautt, C.A. Becker, Evaluating variability with atomistic simulations: the effect of potential and calculation methodology on the modeling of lattice and elastic constants, Modelling Simul. Mater. Sci. Eng. 26 (2018) 055003. https://doi.org/10.1088/1361-651X/aabc05.
[114] A.A. Mirzoev, B.R. Gelchinski, A.A. Rempel, Neural Network Prediction of Interatomic Interaction in Multielement Substances and High-Entropy Alloys: A Review, Dokl Phys Chem 504 (2022) 51–77. https://doi.org/10.1134/S0012501622700026.
[115] M.S. Farnell, Z.D. McClure, S. Tripathi, A. Strachan, Modeling environment-dependent atomic-level properties in complex-concentrated alloys, The Journal of Chemical Physics 156 (2022) 114102. https://doi.org/10.1063/5.0076584.
[116] A. Roy, G. Balasubramanian, Predictive descriptors in machine learning and data-enabled explorations of high-entropy alloys, Computational Materials Science 193 (2021) 110381. https://doi.org/10.1016/j.commatsci.2021.110381.
[117] D. Coslovich, R.L. Jack, J. Paret, Dimensionality reduction of local structure in glassy binary mixtures, The Journal of Chemical Physics 157 (2022) 204503. https://doi.org/10.1063/5.0128265.

[118] D. Wei, J. Yang, M.-Q. Jiang, B.-C. Wei, Y.-J. Wang, L.-H. Dai, Revisiting the structure–property relationship of metallic glasses: Common spatial correlation revealed as a hidden rule, Phys. Rev. B 99 (2019) 014115. https://doi.org/10.1103/PhysRevB.99.014115.
[119] A.R. Ferreira, Chemical bonding in metallic glasses from machine learning and crystal orbital Hamilton population, Phys. Rev. Materials 4 (2020) 113603. https://doi.org/10.1103/PhysRevMaterials.4.113603.
[120] C. Dösinger, M. Hodapp, O. Peil, A. Reichmann, V. Razumovskiy, D. Scheiber, L. Romaner, Efficient descriptors and active learning for grain boundary segregation, Phys. Rev. Materials 7 (2023) 113606. https://doi.org/10.1103/PhysRevMaterials.7.113606.
[121] L. Huber, B. Grabowski, M. Militzer, J. Neugebauer, J. Rottler, Ab initio modelling of solute segregation energies to a general grain boundary, Acta Materialia 132 (2017) 138–148. https://doi.org/10.1016/j.actamat.2017.04.024.
[122] L. Huber, R. Hadian, B. Grabowski, J. Neugebauer, A machine learning approach to model solute grain boundary segregation, Npj Comput Mater 4 (2018) 64. https://doi.org/10.1038/s41524-018-0122-7.
[123] Y. Mishin, Machine-learning interatomic potentials for materials science, Acta Materialia 214 (2021) 116980. https://doi.org/10.1016/j.actamat.2021.116980.
[124] V.L. Deringer, M.A. Caro, G. Csányi, Machine Learning Interatomic Potentials as Emerging Tools for Materials Science, Advanced Materials 31 (2019) 1902765. https://doi.org/10.1002/adma.201902765.
[125] J. Behler, M. Parrinello, Generalized Neural-Network Representation of High-Dimensional Potential-Energy Surfaces, Phys. Rev. Lett. 98 (2007) 146401. https://doi.org/10.1103/PhysRevLett.98.146401.
[126] A.P. Bartók, R. Kondor, G. Csányi, On representing chemical environments, Phys. Rev. B 87 (2013) 184115. https://doi.org/10.1103/PhysRevB.87.184115.
[127] M.I. Mendelev, M. Asta, M.J. Rahman, J.J. Hoyt, Development of interatomic potentials appropriate for simulation of solid–liquid interface properties in Al–Mg alloys, Philosophical Magazine 89 (2009) 3269–3285. https://doi.org/10.1080/14786430903260727.
[128] H.H. Wu, D.R. Trinkle, Cu/Ag EAM potential optimized for heteroepitaxial diffusion from ab initio data, Computational Materials Science 47 (2009) 577–583. https://doi.org/10.1016/j.commatsci.2009.09.026.
[129] Y. Zhang, R. Ashcraft, M.I. Mendelev, C.Z. Wang, K.F. Kelton, Experimental and molecular dynamics simulation study of structure of liquid and amorphous Ni62Nb38 alloy, The Journal of Chemical Physics 145 (2016) 204505. https://doi.org/10.1063/1.4968212.
[130] S.M. Foiles, M.I. Baskes, M.S. Daw, Embedded-atom-method functions for the fcc metals Cu, Ag, Au, Ni, Pd, Pt, and their alloys, Phys. Rev. B 33 (1986) 7983–7991. https://doi.org/10.1103/PhysRevB.33.7983.
[131] C.J. O'Brien, C.M. Barr, P.M. Price, K. Hattar, S.M. Foiles, Grain boundary phase transformations in PtAu and relevance to thermal stabilization of bulk nanocrystalline metals, J Mater Sci 53 (2018) 2911–2927. https://doi.org/10.1007/s10853-017-1706-1.
[132] L. Himanen, M.O.J. Jäger, E.V. Morooka, F. Federici Canova, Y.S. Ranawat, D.Z. Gao, P. Rinke, A.S. Foster, DScribe: Library of descriptors for machine learning in materials science, Computer Physics Communications 247 (2020) 106949. https://doi.org/10.1016/j.cpc.2019.106949.
[133] F. Chollet, others, Keras, (2015). https://keras.io.
[134] TensorFlow Developers, TensorFlow, (2023). https://doi.org/10.5281/ZENODO.4724125.

[135] D. Svozil, V. Kvasnicka, J. Pospichal, Introduction to multi-layer feed-forward neural networks, Chemometrics and Intelligent Laboratory Systems 39 (1997) 43–62. https://doi.org/10.1016/S0169-7439(97)00061-0.
[136] M.E. Tipping, C.M. Bishop, Probabilistic Principal Component Analysis, Journal of the Royal Statistical Society Series B: Statistical Methodology 61 (1999) 611–622. https://doi.org/10.1111/1467-9868.00196.
[137] S. Lloyd, Least squares quantization in PCM, IEEE Trans. Inform. Theory 28 (1982) 129–137. https://doi.org/10.1109/TIT.1982.1056489.
[138] W.M. Brown, M. Yamada, Implementing molecular dynamics on hybrid high performance computers—Three-body potentials, Computer Physics Communications 184 (2013) 2785–2793. https://doi.org/10.1016/j.cpc.2013.08.002.
[139] W.M. Brown, A. Kohlmeyer, S.J. Plimpton, A.N. Tharrington, Implementing molecular dynamics on hybrid high performance computers – Particle–particle particle-mesh, Computer Physics Communications 183 (2012) 449–459. https://doi.org/10.1016/j.cpc.2011.10.012.
[140] W.M. Brown, P. Wang, S.J. Plimpton, A.N. Tharrington, Implementing molecular dynamics on hybrid high performance computers – short range forces, Computer Physics Communications 182 (2011) 898–911. https://doi.org/10.1016/j.cpc.2010.12.021.
[141] T.D. Nguyen, GPU-accelerated Tersoff potentials for massively parallel Molecular Dynamics simulations, Computer Physics Communications 212 (2017) 113–122. https://doi.org/10.1016/j.cpc.2016.10.020.
[142] T.D. Nguyen, S.J. Plimpton, Accelerating dissipative particle dynamics simulations for soft matter systems, Computational Materials Science 100 (2015) 173–180. https://doi.org/10.1016/j.commatsci.2014.10.068.
[143] G.P. Purja Pun, V. Yamakov, Y. Mishin, Interatomic potential for the ternary Ni–Al–Co system and application to atomistic modeling of the B2–L1 $_0$ martensitic transformation, Modelling Simul. Mater. Sci. Eng. 23 (2015) 065006. https://doi.org/10.1088/0965-0393/23/6/065006.
[144] X.-Y. Liu, C.-L. Liu, L.J. Borucki, A new investigation of copper's role in enhancing Al–Cu interconnect electromigration resistance from an atomistic view, Acta Materialia 47 (1999) 3227–3231. https://doi.org/10.1016/S1359-6454(99)00186-X.
[145] M.I. Mendelev, D.J. Srolovitz, G.J. Ackland, S. Han, Effect of Fe Segregation on the Migration of a Non-Symmetric Σ5 Tilt Grain Boundary in Al, J. Mater. Res. 20 (2005) 208–218. https://doi.org/10.1557/JMR.2005.0024.
[146] X.-Y. Liu, P.P. Ohotnicky, J.B. Adams, C.L. Rohrer, R.W. Hyland, Anisotropic surface segregation in Al□Mg alloys, Surface Science 373 (1997) 357–370. https://doi.org/10.1016/S0039-6028(96)01154-5.
[147] D. Farkas, C. Jones, Interatomic potentials for ternary Nb - Ti - Al alloys, Modelling Simul. Mater. Sci. Eng. 4 (1996) 23–32. https://doi.org/10.1088/0965-0393/4/1/004.
[148] J.E. Angelo, N.R. Moody, M.I. Baskes, Trapping of hydrogen to lattice defects in nickel, Modelling Simul. Mater. Sci. Eng. 3 (1995) 289–307. https://doi.org/10.1088/0965-0393/3/3/001.
[149] Y. Mishin, M.J. Mehl, D.A. Papaconstantopoulos, Embedded-atom potential for B 2 − NiAl, Phys. Rev. B 65 (2002) 224114. https://doi.org/10.1103/PhysRevB.65.224114.
[150] Y. Mishin, Atomistic modeling of the γ and γ'-phases of the Ni–Al system, Acta Materialia 52 (2004) 1451–1467. https://doi.org/10.1016/j.actamat.2003.11.026.
[151] G.P. Purja Pun, Y. Mishin, Development of an interatomic potential for the Ni-Al system, Philosophical Magazine 89 (2009) 3245–3267. https://doi.org/10.1080/14786430903258184.

[152] A. Landa, P. Wynblatt, D.J. Siegel, J.B. Adams, O.N. Mryasov, X.-Y. Liu, Development of glue-type potentials for the Al–Pb system: phase diagram calculation, Acta Materialia 48 (2000) 1753–1761. https://doi.org/10.1016/S1359-6454(00)00002-1.
[153] M.I. Mendelev, F. Zhang, Z. Ye, Y. Sun, M.C. Nguyen, S.R. Wilson, C.Z. Wang, K.M. Ho, Development of interatomic potentials appropriate for simulation of devitrification of $Al_{90}Sm_{10}$ alloy, Modelling Simul. Mater. Sci. Eng. 23 (2015) 045013. https://doi.org/10.1088/0965-0393/23/4/045013.
[154] H. Song, M.I. Mendelev, Molecular Dynamics Study of Mechanism of Solid–Liquid Interface Migration and Defect Formation in Al3Sm Alloy, JOM 73 (2021) 2312–2319. https://doi.org/10.1007/s11837-021-04733-8.
[155] R.R. Zope, Y. Mishin, Interatomic potentials for atomistic simulations of the Ti-Al system, Phys. Rev. B 68 (2003) 024102. https://doi.org/10.1103/PhysRevB.68.024102.
[156] N. Bernstein, J.R. Kermode, G. Csányi, Hybrid atomistic simulation methods for materials systems, Rep. Prog. Phys. 72 (2009) 026501. https://doi.org/10.1088/0034-4885/72/2/026501.
[157] R.E. Rudd, J.Q. Broughton, Concurrent Coupling of Length Scales in Solid State Systems, in: P. Deák, T. Frauenheim, M.R. Pederson (Eds.), Computer Simulation of Materials at Atomic Level, 1st ed., Wiley, 2000: pp. 251–291. https://doi.org/10.1002/3527603107.ch11.
[158] N. Choly, G. Lu, W. E, E. Kaxiras, Multiscale simulations in simple metals: A density-functional-based methodology, Phys. Rev. B 71 (2005) 094101. https://doi.org/10.1103/PhysRevB.71.094101.
[159] P.J. Spencer, A brief history of CALPHAD, Calphad 32 (2008) 1–8. https://doi.org/10.1016/j.calphad.2007.10.001.
[160] Y.A. Chang, S. Chen, F. Zhang, X. Yan, F. Xie, R. Schmid-Fetzer, W.A. Oates, Phase diagram calculation: past, present and future, Progress in Materials Science 49 (2004) 313–345. https://doi.org/10.1016/S0079-6425(03)00025-2.
[161] M. Wagih, C.A. Schuh, The Spectrum of Interstitial Solute Energies in Polycrystals, (2023). https://doi.org/10.48550/ARXIV.2304.07343.
[162] J.B. Adams, S.M. Foiles, W.G. Wolfer, Self-diffusion and impurity diffusion of fee metals using the five-frequency model and the Embedded Atom Method, J. Mater. Res. 4 (1989) 102–112. https://doi.org/10.1557/JMR.1989.0102.
[163] X.W. Zhou, R.A. Johnson, H.N.G. Wadley, Misfit-energy-increasing dislocations in vapor-deposited CoFe/NiFe multilayers, Phys. Rev. B 69 (2004) 144113. https://doi.org/10.1103/PhysRevB.69.144113.
[164] P.L. Williams, Y. Mishin, J.C. Hamilton, An embedded-atom potential for the Cu–Ag system, Modelling Simul. Mater. Sci. Eng. 14 (2006) 817–833. https://doi.org/10.1088/0965-0393/14/5/002.
[165] Z. Pan, V. Borovikov, M.I. Mendelev, F. Sansoz, Development of a semi-empirical potential for simulation of Ni solute segregation into grain boundaries in Ag, Modelling Simul. Mater. Sci. Eng. 26 (2018) 075004. https://doi.org/10.1088/1361-651X/aadea3.
[166] D. Farkas, A. Caro, Model interatomic potentials for Fe–Ni–Cr–Co–Al high-entropy alloys, J. Mater. Res. 35 (2020) 3031–3040. https://doi.org/10.1557/jmr.2020.294.
[167] D. Farkas, A. Caro, Model interatomic potentials and lattice strain in a high-entropy alloy, J. Mater. Res. 33 (2018) 3218–3225. https://doi.org/10.1557/jmr.2018.245.
[168] O.R. Deluigi, R.C. Pasianot, F.J. Valencia, A. Caro, D. Farkas, E.M. Bringa, Simulations of primary damage in a High Entropy Alloy: Probing enhanced radiation resistance, Acta Materialia 213 (2021) 116951. https://doi.org/10.1016/j.actamat.2021.116951.

[169] L.K. Béland, C. Lu, Y.N. Osetskiy, G.D. Samolyuk, A. Caro, L. Wang, R.E. Stoller, Features of primary damage by high energy displacement cascades in concentrated Ni-based alloys, Journal of Applied Physics 119 (2016) 085901. https://doi.org/10.1063/1.4942533.
[170] X.W. Zhou, M.E. Foster, R.B. Sills, An Fe-Ni-Cr embedded atom method potential for austenitic and ferritic systems, J Comput Chem 39 (2018) 2420–2431. https://doi.org/10.1002/jcc.25573.
[171] G. Bonny, R.C. Pasianot, N. Castin, L. Malerba, Ternary Fe–Cu–Ni many-body potential to model reactor pressure vessel steels: First validation by simulated thermal annealing, Philosophical Magazine 89 (2009) 3531–3546. https://doi.org/10.1080/14786430903299824.
[172] S.M. Foiles, Calculation of the surface segregation of Ni-Cu alloys with the use of the embedded-atom method, Phys. Rev. B 32 (1985) 7685–7693. https://doi.org/10.1103/PhysRevB.32.7685.
[173] B. Onat, S. Durukanoğlu, An optimized interatomic potential for Cu–Ni alloys with the embedded-atom method, J. Phys.: Condens. Matter 26 (2014) 035404. https://doi.org/10.1088/0953-8984/26/3/035404.
[174] F. Fischer, G. Schmitz, S.M. Eich, A systematic study of grain boundary segregation and grain boundary formation energy using a new copper–nickel embedded-atom potential, Acta Materialia 176 (2019) 220–231. https://doi.org/10.1016/j.actamat.2019.06.027.
[175] J.J. Hoyt, J.W. Garvin, E.B. Webb, M. Asta, An embedded atom method interatomic potential for the Cu Pb system, Modelling Simul. Mater. Sci. Eng. 11 (2003) 287–299. https://doi.org/10.1088/0965-0393/11/3/302.
[176] M.I. Mendelev, D.J. Sordelet, M.J. Kramer, Using atomistic computer simulations to analyze x-ray diffraction data from metallic glasses, Journal of Applied Physics 102 (2007) 043501. https://doi.org/10.1063/1.2769157.
[177] M.I. Mendelev, M.J. Kramer, R.T. Ott, D.J. Sordelet, D. Yagodin, P. Popel, Development of suitable interatomic potentials for simulation of liquid and amorphous Cu–Zr alloys, Philosophical Magazine 89 (2009) 967–987. https://doi.org/10.1080/14786430902832773.
[178] V. Borovikov, M.I. Mendelev, A.H. King, Effects of stable and unstable stacking fault energy on dislocation nucleation in nano-crystalline metals, Modelling Simul. Mater. Sci. Eng. 24 (2016) 085017. https://doi.org/10.1088/0965-0393/24/8/085017.
[179] M. Wen, A new interatomic potential describing Fe-H and H-H interactions in bcc iron, Computational Materials Science 197 (2021) 110640. https://doi.org/10.1016/j.commatsci.2021.110640.
[180] G. Bonny, R.C. Pasianot, L. Malerba, Fe–Ni many-body potential for metallurgical applications, Modelling Simul. Mater. Sci. Eng. 17 (2009) 025010. https://doi.org/10.1088/0965-0393/17/2/025010.
[181] G.J. Ackland, M.I. Mendelev, D.J. Srolovitz, S. Han, A.V. Barashev, Development of an interatomic potential for phosphorus impurities in -iron, J. Phys.: Condens. Matter 16 (2004) S2629–S2642. https://doi.org/10.1088/0953-8984/16/27/003.
[182] M.I. Mendelev, S. Han, W. Son, G.J. Ackland, D.J. Srolovitz, Simulation of the interaction between Fe impurities and point defects in V, Phys. Rev. B 76 (2007) 214105. https://doi.org/10.1103/PhysRevB.76.214105.
[183] G. Bonny, N. Castin, J. Bullens, A. Bakaev, T.C.P. Klaver, D. Terentyev, On the mobility of vacancy clusters in reduced activation steels: an atomistic study in the Fe–Cr–W model alloy, J. Phys.: Condens. Matter 25 (2013) 315401. https://doi.org/10.1088/0953-8984/25/31/315401.

[184] G. Bonny, D. Terentyev, R.C. Pasianot, S. Poncé, A. Bakaev, Interatomic potential to study plasticity in stainless steels: the FeNiCr model alloy, Modelling Simul. Mater. Sci. Eng. 19 (2011) 085008. https://doi.org/10.1088/0965-0393/19/8/085008.
[185] G. Bonny, N. Castin, D. Terentyev, Interatomic potential for studying ageing under irradiation in stainless steels: the FeNiCr model alloy, Modelling Simul. Mater. Sci. Eng. 21 (2013) 085004. https://doi.org/10.1088/0965-0393/21/8/085004.
[186] L.K. Béland, A. Tamm, S. Mu, G.D. Samolyuk, Y.N. Osetsky, A. Aabloo, M. Klintenberg, A. Caro, R.E. Stoller, Accurate classical short-range forces for the study of collision cascades in Fe–Ni–Cr, Computer Physics Communications 219 (2017) 11–19. https://doi.org/10.1016/j.cpc.2017.05.001.
[187] G.D. Samolyuk, L.K. Béland, G.M. Stocks, R.E. Stoller, Electron–phonon coupling in Ni-based binary alloys with application to displacement cascade modeling, J. Phys.: Condens. Matter 28 (2016) 175501. https://doi.org/10.1088/0953-8984/28/17/175501.
[188] L.T. Kong, J.B. Liu, W.S. Lal, B.X. Liu, Correlation of lattice constant versus tungsten concentration of the Ni-based solid solution examined by molecular dynamics simulation, Journal of Alloys and Compounds 337 (2002) 143–147. https://doi.org/10.1016/S0925-8388(01)01932-6.
[189] M.I. Mendelev, M.J. Kramer, S.G. Hao, K.M. Ho, C.Z. Wang, Development of interatomic potentials appropriate for simulation of liquid and glass properties of $NiZr_2$ alloy, Philosophical Magazine 92 (2012) 4454–4469. https://doi.org/10.1080/14786435.2012.712220.
[190] S.R. Wilson, M.I. Mendelev, Anisotropy of the solid–liquid interface properties of the Ni–Zr B33 phase from molecular dynamics simulation, Philosophical Magazine 95 (2015) 224–241. https://doi.org/10.1080/14786435.2014.995742.
[191] L.M. Hale, B.M. Wong, J.A. Zimmerman, X.W. Zhou, Atomistic potentials for palladium–silver hydrides, Modelling Simul. Mater. Sci. Eng. 21 (2013) 045005. https://doi.org/10.1088/0965-0393/21/4/045005.
[192] G. Bonny, A. Bakaev, D. Terentyev, Yu.A. Mastrikov, Interatomic potential to study plastic deformation in tungsten-rhenium alloys, Journal of Applied Physics 121 (2017) 165107. https://doi.org/10.1063/1.4982361.
[193] W. Setyawan, N. Gao, R.J. Kurtz, A tungsten-rhenium interatomic potential for point defect studies, Journal of Applied Physics 123 (2018) 205102. https://doi.org/10.1063/1.5030113.
[194] Y. Chen, J. Fang, L. Liu, W. Hu, N. Gao, F. Gao, H. Deng, Development of the interatomic potentials for W-Ta system, Computational Materials Science 163 (2019) 91–99. https://doi.org/10.1016/j.commatsci.2019.03.021.